



Molecular modeling of Bcl-xL post-translational modifications and of keteniminium salts

Gamze Tanriver

► To cite this version:

Gamze Tanriver. Molecular modeling of Bcl-xL post-translational modifications and of keteniminium salts. Chemical Sciences. Université de Lorraine; Boğaziçi üniversitesi (Istanbul), 2021. English. NNT : 2021LORR0302 . tel-03703094

HAL Id: tel-03703094

<https://hal.univ-lorraine.fr/tel-03703094>

Submitted on 20 Oct 2022

HAL is a multi-disciplinary open access archive for the deposit and dissemination of scientific research documents, whether they are published or not. The documents may come from teaching and research institutions in France or abroad, or from public or private research centers.

L'archive ouverte pluridisciplinaire **HAL**, est destinée au dépôt et à la diffusion de documents scientifiques de niveau recherche, publiés ou non, émanant des établissements d'enseignement et de recherche français ou étrangers, des laboratoires publics ou privés.



**UNIVERSITÉ
DE LORRAINE**

**BIBLIOTHÈQUES
UNIVERSITAIRES**

AVERTISSEMENT

Ce document est le fruit d'un long travail approuvé par le jury de soutenance et mis à disposition de l'ensemble de la communauté universitaire élargie.

Il est soumis à la propriété intellectuelle de l'auteur. Ceci implique une obligation de citation et de référencement lors de l'utilisation de ce document.

D'autre part, toute contrefaçon, plagiat, reproduction illicite encourt une poursuite pénale.

Contact bibliothèque : ddoc-theses-contact@univ-lorraine.fr
(Cette adresse ne permet pas de contacter les auteurs)

LIENS

Code de la Propriété Intellectuelle. articles L 122. 4

Code de la Propriété Intellectuelle. articles L 335.2- L 335.10

http://www.cfcopies.com/V2/leg/leg_droi.php

<http://www.culture.gouv.fr/culture/infos-pratiques/droits/protection.htm>

**Modélisation moléculaire des
modifications post-translationnelles
dans Bcl-x_L et des sels de céténiminium**

*Molecular modeling of Bcl-x_L post-translational
modifications and of keteniminium salts*

THÈSE

présentée et soutenue publiquement le 17 decembre 2021

pour l'obtention du

Doctorat de l'Université de Lorraine

(Mention Chimie)

par

Gamze Tanriver

Composition du jury

Président : Dr. Mounir Tarek, Université de Lorraine, Nancy, France

Rapporteurs : Prof. Fethiye Aylin Sungur, Istanbul Technical University, Istanbul, Turquie
Dr. Florent Barbault, Université de Paris, Paris, France

Examineur : Assoc. Prof. Başak Kayıtmazer, Boğaziçi University, Istanbul, Turquie

Encadrants : Prof. Gérard Monard, Université de Lorraine, Nancy, France
Prof. Şaron Çatak, Boğaziçi University, Istanbul, Turquie

Mis en page avec la classe thesul.

Contents

Acknowledgments	v
Abbreviations	vii
Résumé	1
1 Introduction	11
2 Objective and scope	13
3 Theoretical Background	15
3.1 Molecular Mechanics (MM)	15
3.1.1 Newton's equation of motion	16
3.1.2 Integration of Newton's equations of motion	16
3.1.3 Molecular dynamics simulations	16
3.1.4 Replica Exchange Molecular dynamics (REMD)	18
3.1.5 Principal components analysis (PCA)	19
3.1.6 Clustering Analysis	19
3.2 Quantum Mechanics (QM)	20
3.2.1 The Schrödinger Equation	20
3.2.2 The Hartree-Fock (HF) Theory	21
3.2.3 Semi-Empirical Methods	22
3.2.4 Density Functional Theory	23
3.2.5 Non-covalent Interaction Analysis (NCIs)	28
3.2.6 Conceptual Density Functional Theory (CDFT)	28
4 Impact of deamidation on the structure and function of anti-apoptotic Bcl-x_L in water	31
4.1 Introduction	31

4.1.1	Bcl-2 family protein	31
4.1.2	B-cell lymphoma-extra-large (Bcl-x _L)	32
4.1.3	Post-translational modifications (PTMs)	33
4.1.4	Deamidation of Bcl-x _L	34
4.2	Methodology	36
4.3	Results and Discussion	38
4.3.1	Stability of the wild type and deamidated Bcl-x _L systems	38
4.3.2	Intrinsically disordered region (IDR)	40
4.3.3	Cluster Analysis	46
4.3.4	Principal Components Analysis (PCA)	51
4.4	Conclusions	55
5	Impact of deamidation on structure and function of Bcl-x_L in membrane	57
5.1	Introduction	57
5.2	Methodology	61
5.2.1	Preparation of the C-tail and REMD simulation details	61
5.2.2	Simulation details in water systems	61
5.2.3	Generation of membrane-associated Bcl-x _L and simulation details . . .	62
5.3	Results and Discussion	62
5.3.1	Evaluation of the C-terminal tail	62
5.3.2	Stability of Bcl-x _L systems prior to and subsequent to deamidation . . .	63
5.3.3	Bcl-x _L and deamidated Bcl-x _L in water	64
5.3.4	Bcl-x _L and deamidated Bcl-x _L on membrane	71
5.3.5	Principal Components Analysis (PCA)	79
5.4	Conclusions	81
6	Investigation of Bcl-x_L-BH3-only peptide Complex	83
6.1	Introduction	83
6.2	Methodology	84
6.3	Results and Discussion	85
6.3.1	Stability of BH3-only peptides in water	85
6.3.2	Analysis of Complex systems	85
6.4	Conclusions	87

7	Keteniminium Chemistry	89
7.1	Introduction	89
7.1.1	Formation of Keteniminium Salt	89
7.1.2	[2+2] Cycloaddition Reaction	90
7.1.3	Intramolecular competition reactions	92
7.2	Methodology	94
7.2.1	Computational Methodology for KI Formation Study	94
7.2.2	Computational Methodology for [2+2] Cycloaddition Study	95
7.2.3	Computational Methodology for the Intramolecular Competition Reaction Studies	95
7.3	Results and Discussion	96
7.3.1	KI Formation Study	96
7.3.2	Results and Discussion of [2+2] cycloaddition Study	102
7.3.3	Intramolecular Competition Reactions between [2+2] Cycloaddition vs Electrocyclization	105
7.3.4	Intramolecular [2+2] Cycloaddition Competition Reactions	109
7.4	General Conclusions	110
8	Keteniminium Salts: Reactivity and Propensity toward Electrocyclization Reactions	111
8.1	Introduction	111
8.2	Methodology	112
8.3	Results and Discussion	114
8.3.1	Structure, Energetics and Reactivity of Keteniminium Ions in Electrocyclization Reactions	114
8.3.2	Energetic Analysis of Electrocyclization Reactions involving Keteniminium Ions	115
8.3.3	Population Analysis and Local Reactivity Descriptors	119
8.3.4	Nature of the Electrocyclization Reaction of Keteniminium Ions	121
8.3.5	Understanding Effect of Substituents on Keteniminium Reactivity	125
8.4	Conclusions	129
	Concluding Remarks	131

A	Supporting Information	153
A.1	Supporting Information for Bcl-x _L Study in Chapter 4.	153
A.1.1	Force field parameterization of non-standard iso-aspartate	153
A.1.2	Secondary Structure Analysis	154
A.1.3	B-factor coloring	154
A.1.4	Distance Analyses for the Combined Trajectories	154
A.1.5	Protein (Δ C terminal)-C terminal interactions (residues 196-209) for the Combined Trajectories	155
A.2	Supporting Information for Bcl-x _L Study in membrane in Chapter 5.	162
A.2.1	Area per lipid (APL)	162
A.3	Supporting Information for Electrocyclization Study in Chapter 8.	163
A.3.1	DFT Survey	163
A.3.2	Frontier Molecular Orbitals (FMO) Analysis	170
B	Publication List	173

Acknowledgments

I wish to express my deepest gratitude to my thesis supervisors Assoc. Prof. Saron Catak (Boğaziçi University) and Prof. Gérard Monard (Université de Lorraine) for their precious scientific guidance, endless attention, never-failing support and understanding. I am really proud of being the first student of Saron Catak and the last student of Gérard Monard. They supported and motivated me to be continue and reach my goals. I also wish to express my gratitude to Prof. Viktorya Aviyente for her support and encouragement to start my journey in computational chemistry.

I would also like to extend my appreciation to the members of the examining committee, Prof. F. Aylin Sungur (Istanbul Technical University), Prof. Nurcan Tüzün (Istanbul Technical University), Assoc. Prof. Başak Kayıtmazer (Boğaziçi University), Prof. Florent Barbault, (Université de Paris), and Prof. Mounir Tarek (Université de Lorraine) for their constructive comments and helpful suggestions for further studies. I also wish to express my gratitude to my "comite de suivi" Prof. Dr. Marco Cecchini and Prof. Dr. Bernard Maigret for their supporting remarks and their time.

Z. Pınar Haşlak, my office mate, Nancy is a beautiful place with your companion and I enjoyed ever moment with you. I would like to also thank Deniz Akgül for her endless support. I also want to thank Melin and Erdem from ITU for their friendship.

I would like to thank the former and current members of Computational Chemistry and Biochemistry Group (CCBG) and CCBU in Bogaziçi University. I am grateful of all of my lab mates; Pelin, Busenur, Beyza, Zeynep, Basak, Volkan, Aslıhan, Öyküm, Oğuzhan, Taylan, Özlem and Esmâ for the warm and friendly environment. I will miss our coffee time in Dunkin and our lunch time. I also want to thank all members of LPCT in Université de Lorraine for warm environment. I would like to thank Mrs Severine Bonenberger for spreading smiles and helping us. I would like to thank Alekos and Toni for their friendships. It is always a pleasure to work and have fun with you all.

I would like to thank the French Embassy in Ankara, Turkey for the ‘co-tutelle de thèse’ scholarship (Joint PhD scholarship) that enabled my residence in Nancy. This research was supported by TUBITAK 1001 (116Z513), Bogazici University Research Fund (BAP Grant numbers: 14260, 16863, and 15325), and TUBITAK 3001 (115Z738). GPU resources were allocated by the Mésocentre EXPLOR of the Université de Lorraine and the Centre de Calcul ROMEO of the Université de Reims Champagne-Ardenne as well as TUBITAK ULAKBIM High Performance and Grid Computing Center (TRUBA resources).

I would like to extend my gratitude to my friends, Seçil Soyutemiz, Gönül Mutlu, and Mehtap Karamanlı for their encouragement and invaluable support throughout these years. I would like to thank you my prep-class friends (INT-J) Gökçe and Emel. We laughed together,

cried together and stayed strong. I am really lucky to have you as my close friends. Additionally, I do not want to forget to thank my friends Selda, Eda and Neşe. We grew up together in Samsun. We shared really unforgettable moments and always support each other. Time flies. I really missed that times.

Additionally, I thank all lecturers and my classmates in the chemistry department of Ondokuz Mayıs University, particularly Prof. Ömer Andaç and Prof. Zerrin Heren for encouraging me in the beginning of Bogazici University journey.

Finally, my deepest thanks go to my family for their continuous support, encouragement, and never-ending love. I dedicate my dissertation to my family, particularly my mother and father İlvan and Yılmaz Tanriver. They dedicated their lives to support me and my sister to achieve our goals and to have a bright future. I would like to thank for Pelin and Erkan Sağlam for their support and assistance. We succeeded together. Lastly, Ece and Mete Han you make my life is happier than ever. I am really lucky to have you all.

See you on next journeys.

Abbreviations

3D	Three Dimensional
a.u.	Atomic unit
ACID	Anisotropy of the Induced Current Density Analysis
ADF	Amsterdam density functional
AIM	Atoms in molecules
AMBER	Assisted Model Building with Energy Refinement
approx.	approximately
Arg	Arginine
ASD	Atomic spin density
Asp	Aspartate
B3LYP	Becke-3-parameter Lee-Yang-Parr functional
BG	Binding groove
BLYP	Becke-Lee-Yang-Parr
BMK	Boese-Martin for kinetics
CDFT	Global reactivity descriptors
CPCM	Conductor-like screening model
DFT	Density Functional Theory
DM1	Aspartate deamidated Bcl-x _L
DM2	iso-Aspartate deamidated Bcl-x _L
DSSP	Definition of Secondary Structure Prediction
DZ	Double zeta (basis set)

DZP	Double zeta polarized (basis set)
EDG	Electron-donating group
EWG	Electron-withdrawing group
Exp.	Experimental
FMO	Frontier Molecular Orbital
GAFF	General AMBER Force Field
GGA	Generalized gradient approximation
GIAO	Gauge independent atomic orbital
Glu	glutamate
GTO	Gaussian type orbital
H-bond	Hydrogen bond
HF	Hartree-Fock theory
HMR	Hydrogen Mass Partitioning
HOMO	Highest occupied molecular orbital
IDR	Intrinsically disordered region
IEFPCM	Integral equation formalism polarizable continuum model
IRC	Intrinsic reaction coordinate
iso-Asp	iso-Aspartate
ITC	Isothermal titration calorimetry
KDE	Kernel density estimator
KI	Keteniminium salt
KS	Kohn-Sham
LCAO	Linear combination of atomic orbitals
LDA	Local density approximation
LIE	Linear interaction energy
LUMO	Lowest unoccupied molecular orbital
Lys	Lysine

M06-2X	Hybrid meta exchange-correlation functional
MD	Molecular Dynamics
MM	Molecular Mechanics
MM-GB/SA	Molecular Mechanics-Generalized Born/Surface Area
MM-PB/SA	Molecular Mechanics Poisson Boltzman Surface Area
MO	Molecular Orbitals
MOMP	Mitochondrial outer membrane permeabilization
MPW1K	Modified Perdew-Wang 1-parameter model (kinetic functional)
NBO	Natural bond orbital
NCI	Non-covalent interactions
NICS	Nucleus-Independent Chemical Shifts
NMR	Nuclear magnetic resonance
NPA	Natural population analysis
PBC	Periodic boundary conditions
PC	Principal components
PCA	Principal component analysis
PCM	Polarizable Continuum Method
PDB	Protein Data Bank
PES	Potential energy surface
PM3	Parameterization method 3
PM6	Parameterization method 6
PME	Particle-mesh Ewald
POPC	1-Palmitoyl-2-oleoylphosphatidylcholine
PRC	Pre-reactive complex or conformer
PTM	Post-translational modification
QM	Quantum Mechanics
QTAIM	Quantum theory of atoms in molecules

RDF	Radial distribution functions
Rg	Radius of gyration
RMSD	Root mean square deviation
RT	Room temperature
SCF	Self consistent field
SCRF	Self consistent reaction field
SE	Semi-empirical
SMD	Solvation model based on density
SS	Secondary structure
STO	Slater type orbital
TS	Transition state
TZ	Triple zeta (basis set)
TZP	Triple zeta polarized (basis set)
WT	Wild type

Résumé

Contexte

L'apoptose, connue sous le nom de mort cellulaire programmée, est un processus complexe et est initiée par trois voies, à savoir intrinsèque, également connue sous le nom de voie mitochondriale via divers stress intracellulaires, extrinsèque (voie médiée par les récepteurs de l'apoptose) via les récepteurs de l'apoptose, et les voies perforine/granzyme [1, 2, 3, 4]. Chaque voie est régulée par différents stimuli apoptotiques [4]. Les protéines de la famille Bcl-2 jouent principalement un rôle important sur la voie mitochondriale de l'apoptose en régulant la perméabilisation de la membrane externe mitochondriale et l'apoptose ultérieure [5, 6, 7, 8]. La famille Bcl-2 a été classée en trois sous-classes, à savoir les protéines anti-apoptotiques, les protéines pro-apoptotiques et les protéines BH3 uniquement (BOP ; BOP activatrices et sensibilisantes) (Figure 1) et médie la voie apoptotique mitochondriale (intrinsèque) en réponse à divers stimuli apoptotiques (stress cellulaire ou signaux de dommages) [9, 10].

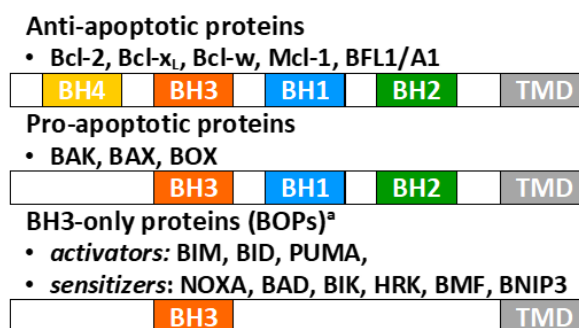


Figure 1: Présentation générale de la famille Bcl-2.^a Seuls BIK et HRK composent le domaine trans-membranaire.

La modification post-traductionnelle (PTM) est un mécanisme de régulation dans de nombreux processus biologiques. La déamidation est une réaction non enzymatique et l'une des principales modifications post-traductionnelles (PTM), qui est un mécanisme de régulation dans de nombreux processus biologiques. L'hypothèse des « horloges moléculaires » de Robinson et al. souligne l'importance de la déamidation de l'asparagine et de la glutamine et suggère que la déamidation est un mécanisme de synchronisation moléculaire biologique qui sert un contrôle génétique programmable à tout intervalle de temps souhaité et un contrôle des processus biologiques [11]. L'asparagine (Asn) et la glutamine (Gln), deux des 20 acides aminés naturels sont intrinsèquement instables dans des conditions physiologiques [12]. Gln et Asn sont connus

pour se déamider spontanément mais de manière non enzymatique en un mélange de glutamyl (Glu) et d'iso-glutamyl (iso-Glu) et un mélange de résidus d'aspartyl (Asp) et d'iso-aspartyl (iso-Asp), respectivement (Figure 2). Un exemple notable est la protéine transmembranaire mitochondriale, Bcl-x_L, [13, 14] qui fonctionne comme une protéine anti-apoptotique. Bcl-x_L appartient à la famille Bcl-2, [15] qui régule la voie mitochondriale de l'apoptose en réponse à divers stimuli apoptotiques [16].

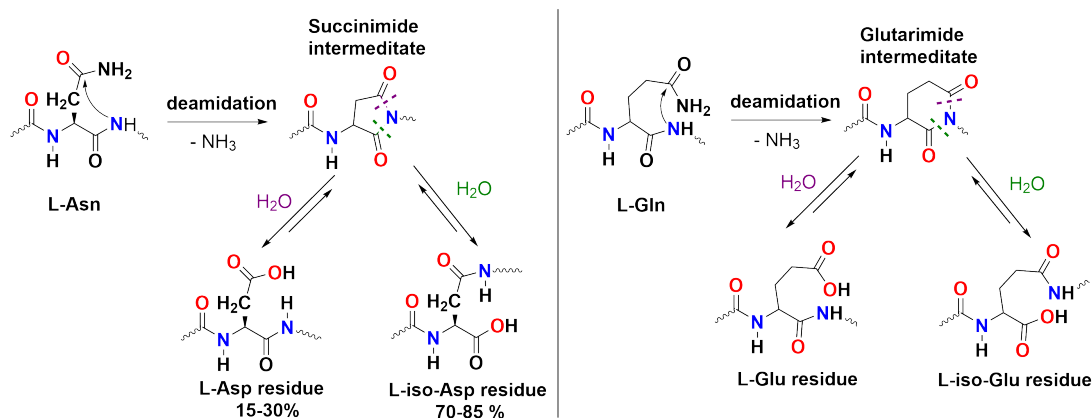


Figure 2: Mécanisme général des déamidations Asn et Gln.

Bcl-x_L est une protéine transmembranaire mitochondriale anti-apoptotique, connue pour jouer un rôle crucial dans la survie des cellules tumorales. Structuellement, Bcl-x_L se compose de deux hélices hydrophobes, six amphiphiles (Figure 3) et une queue C composée d'une α -hélice ($\alpha 9$), connu sous le nom de domaine transmembranaire (TMD) [13, 14, 17, 18]. La queue C, connue sous le nom de domaine transmembranaire (TMD) assure l'ancrage de Bcl-x_L à la membrane externe mitochondriale (MOM) (Figure 5.1) [13, 14, 17, 18]. Il est important de souligner que Bcl-x_L avec la queue C (c'est-à-dire Bcl-x_L pleine longueur) n'est pas résolu expérimentalement en raison de limitations expérimentales (solubilisation, de la protéine sous une forme repliée nativement, etc.) [18, 19]. Récemment, la queue C seule a été résolue expérimentalement à l'intérieur de nanodisques phospholipidiques (ID PDB : 6F46_{NMR} [19] et 6X7I_{NMR}). De plus, Bcl-x_L comprend une longue région intrinsèquement désordonnée (IDR), la boucle dite flexible entre $\alpha 1$ - $\alpha 2$. L'IDR a été omis dans la plupart des études précédentes, mais des études récentes ont montré l'importance de l'IDR puisque des modifications post-traductionnelles (PTM), qui peuvent affecter les fonctions, la stabilité et la localisation des protéines en réponse à divers stimuli apoptotiques se produisent dans cette région [20, 21, 22, 23, 24, 25].

La déamidation de Bcl-x_L est un commutateur pivot qui régule sa fonction biologique. L'impact potentiel de la déamidation sur la structure et la dynamique de Bcl-x_L est directement lié à la région intrinsèquement désordonnée (IDR), qui est le site principal des modifications post-traductionnelles (PTM). D'un point de vue informatique, l'identification des différences de conformation joue un rôle central dans la compréhension de l'impact de la déamidation dans l'IDR. Jusqu'à présent, il n'y a pas de connexion/explication structurelle claire sur la façon dont la déamidation induit la perte de l'activité Bcl-x_L. Dans cette étude, nous avons exploré les changements de conformation induits par la déamidation dans Bcl-x_L pour mieux comprendre sa perte de fonction en effectuant des simulations de dynamique moléculaire (MD) d'une microseconde.

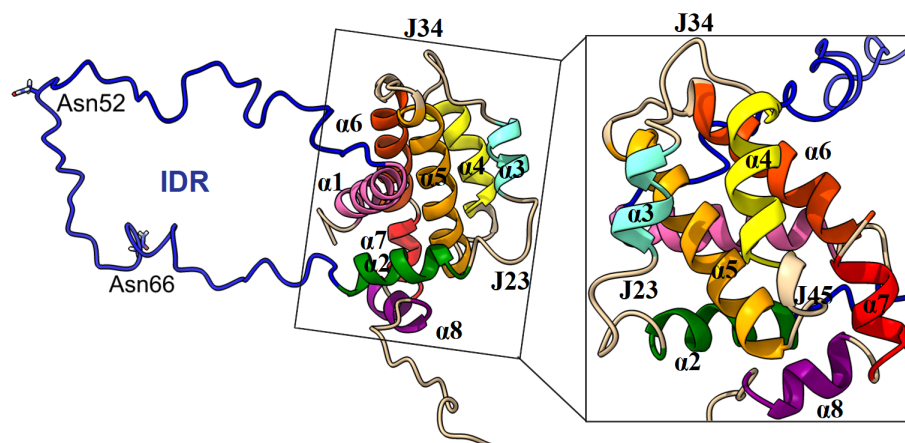


Figure 3: vues de face et de côté de Bcl-x_L (code PDB : 1LXL). (Le rectangle noir indique la vue de face de la rainure de reliure. La couleur bleue représente la région IDR (IDR), $\alpha 1$ en rose, $\alpha 2$ en vert, $\alpha 3$ en cyan, $\alpha 4$ en jaune, $\alpha 5$ en orange clair, $\alpha 6$ en orange, $\alpha 7$ en rouge et $\alpha 8$ en violet. "J" fait référence à la jonction entre deux hélices. J23 relie $\alpha 2$ et $\alpha 3$, J34 est la jonction de $\alpha 3$ et $\alpha 4$ et J45 relie $\alpha 4$ et $\alpha 5$.

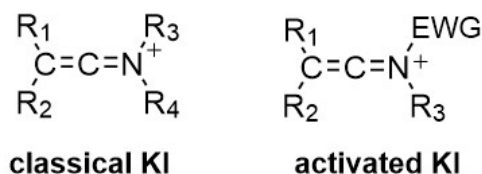


Figure 4: Structures générales des KI.

Le sel de céténiminium est l'intérêt principal de la deuxième partie de la thèse en combinant des études computationnelles et expérimentales. Ces dernières années, le sel de céténiminium (KI) a attiré l'attention et a fait l'objet de plus de 120 articles de recherche et revues. Les KI sont une alternative améliorée à leurs analogues cétones, en raison de leur réactivité plus élevée et de leur électrophilie élevée. Historiquement, les pionniers de l'utilisation et de la synthèse de KI sont Viehe et Ghosez[26, 27]. Diverses réactions de formation de KI, permettant une utilisation plus large de ces intermédiaires, ont été décrites, à savoir des réactions de α -haloénamines avec des acides de Lewis,[27, 28, 29] triflation d'amides,[30] méthylation des céténimines,[31] et protonation des ynamines[32, 33] et des ynamides[34, 35, 36] (Figure 6). Les KI sont principalement classés en deux groupes, à savoir les céténiminiumions classiques (aldo-KI et céto-KI) et activés comme le montre la figure 4. Les sels de céténiminium sont également des intermédiaires cationiques polyvalents et réactifs en chimie organique et ils sont utilisés dans un large éventail de réactions telles que la cycloaddition, les électrocyclisations $6\pi/10\pi$, la cyclisation Pictet-Spengler, et ainsi de suite (Figure 5). Dans la thèse, la chimie de KI a été couverte de la formation aux réactions dans lesquelles KI est impliqué. La chimie de KI a été divisée en deux chapitres. Le chapitre 7 a été divisé en trois sections, à savoir la formation de KI, les réactions de cycloaddition [2+2] et les réactions de compétition intramoléculaire. En bref, l'analyse structurale et énergétique et les différences de réactivité dans les dérivés d'amide et de céténiminium portant différents substituants ont été examinées au moyen de DFT. L'électrocyclisation est une

méthode puissante pour construire des motifs structuraux complexes. Le chapitre 8 couvre la réactivité et la propension des KI vers les réactions d'électrocyclisation. En outre, la véritable nature du mécanisme de cyclisation des sels de céténiminium est divulguée via une gamme techniques d'analyse. Les résultats informatiques ont été confirmés par des expériences.

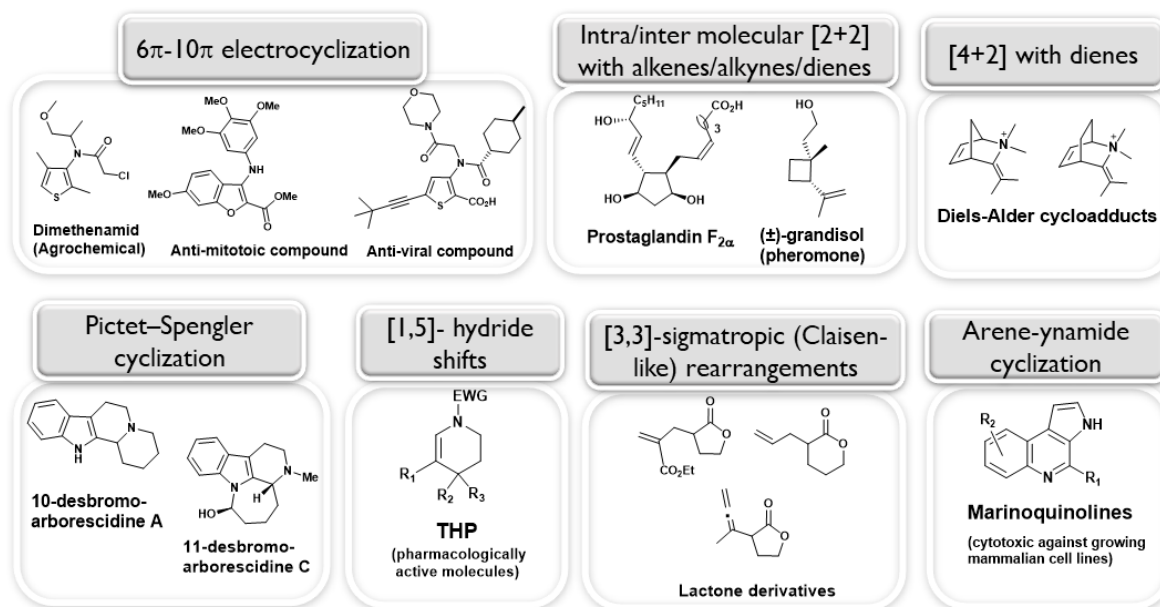


Figure 5: Résumé des réactions impliquant les KI.

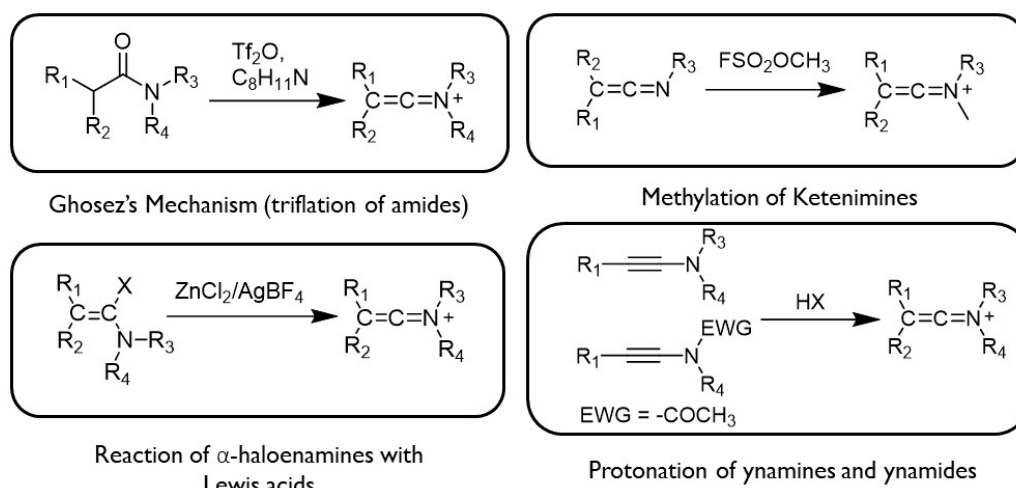


Figure 6: Diverses réactions de formation de KI.

Objectifs

Une brève introduction à nos sujets de recherche a été présentée au chapitre 1. Le chapitre 3 rappelle les principes de base des méthodes de mécanique moléculaire (MM) et de mécanique

quantique (QM).

Le premier sujet d'intérêt de cette thèse est l'étude de l'impact de la déamidation sur la structure et la fonction de Bcl-x_L anti-apoptotique pour mieux comprendre sa perte de fonction en effectuant des simulations de dynamique moléculaire (MD) d'une microseconde. Dans le chapitre 4, les conséquences structurales de la déamidation sur Bcl-x_L dans l'eau ont été mises en évidence au niveau atomique. Dans le chapitre 5, les impacts potentiels de la déamidation dans les changements conformationnels induits par l'IDR et l'association membranaire ont été étudiés en utilisant des simulations de dynamique moléculaire. Le chapitre 6 couvre l'étude du comportement structural du peptide BH3 uniquement pour comprendre les systèmes complexes entre la protéine anti-apoptotique et le peptide BH3 uniquement.

Dans la deuxième partie de la thèse, les sels de céténimine (KI) ont été étudiés depuis leur formation jusqu'à la réaction (chapitres 7 et 8). Ainsi, la compréhension de l'aspect mécanistique des réactions de formation de KI facilite les processus de conception et de développement de ces intermédiaires pour accéder à des structures complexes. Le chapitre 7 comprend trois sections. Premièrement, une vaste gamme de substituants et leurs effets sur la réactivité de l'amide de départ ont été examinés pour donner un aperçu de leurs contributions au mécanisme de formation de KI par activation d'un amide. Ensuite, les réactions de cycloaddition [2 +2] des KI avec alcène/alcyne ont été étudiées informatiquement et les résultats discutés au chapitre 7. Les réactions de compétition entre la cycloaddition intramoléculaire [2+2] et l'électrocyclisation 6 π de KI ont été examinées et les résultats expérimentaux ont été élucidés au moyen d'une étude DFT. Enfin, au chapitre 8, des dérivés de céténiminium portant différents substituants conduisant à six systèmes hétérocycliques différents ont été explorés via DFT et une gamme de techniques d'analyse différentes. Cette étude visait à donner un aperçu de la réactivité des dérivés de KI portant différents substituants et hétéroatomes vis-à-vis des réactions d'électrocyclisation.

Les conclusions générales de chaque chapitre et les travaux futurs ont été résumés au chapitre 9.

Résultats

Cette thèse présente les résultats de l'impact de la déamidation sur la structure et la fonction de Bcl-x_L et des sels de céténiminium depuis la formation du KI jusqu'à ses réactions.

Impact de la déamidation sur la structure et la fonction du Bcl-x_L anti-apoptotique dans l'eau

Afin d'examiner les comportements/différences conformationnels des systèmes de type sauvage (WT) et déamidés Bcl-x_L, des simulations MD d'une microseconde ont été effectuées en utilisant différentes vitesses de départ. La stabilité des systèmes et les interactions des liaisons H ont été explorées. L'analyse de clustering, les interactions de liaison H et l'analyse en composantes principales ont été combinées pour étudier les changements de conformation lors de la déamidation. À l'aide de l'ACP, nous nous sommes spécifiquement concentrés sur les changements de conformation dans le sillon de liaison (BG) lors de la déamidation des résidus IDR Asn52 et Asn66, en considérant à la fois les mutations Asp et iso-Asp. Des échantillonnages ont

été effectués à 300 K et un ensemble NVT utilisant le couplage de température Langevin[37] avec un gamma de $1,0 \text{ ps}^{-1}$.

Cette étude apporte une contribution significative à la connaissance des conséquences structurales de la déamidation sur Bcl-x_L. Les résultats de la simulation MD ont montré que les modèles de mouvement et d'interaction IDR ont considérablement changé lors de la déamidation. L'analyse en composantes principales (ACP) démontre des différences significatives entre le type sauvage et le Bcl-x_L déamidé et suggère que la déamidation affecte la structure et la dynamique de Bcl-x_L. Nos résultats suggèrent que la déamidation dans l'IDR modifie à la fois le nombre (%) et le type d'interactions non liées entre l'IDR et le noyau de Bcl-x_L. L'analyse de clustering souligne que le changement dans les interactions BG se produit principalement dans les sous-unités J23, $\alpha 3$, $\alpha 4$ et J45, et comprend cinq interactions spécifiques, auparavant inexistantes ou presque inexistantes, à savoir R102-D133 et R102-E129, E129-Y101 et E129-R103 et R103-Q111. La combinaison de l'analyse de clustering, de l'analyse de la liaison H et de l'ACP a révélé des changements conformationnels, d'interaction et dynamiques lors de la déamidation. Les différences dans les modèles de contact et la dynamique essentielle dans le sillon de liaison (BG) sont des indications claires des effets allostériques induits par la déamidation. Conformément aux études précédentes, nous montrons que la région intrinsèquement désordonnée joue un rôle très important dans la perte de la fonction apoptotique de Bcl-x_L, tout en offrant une perspective unique sur le mécanisme sous-jacent de mort cellulaire induite par la déamidation de Bcl-x_L. Cette étude est une première étape pour comprendre l'effet de la déamidation sur la structure et la fonction de Bcl-x_L en utilisant un modèle non tronqué et non modifié, soulignant également l'importance de simulations plus longues et multiples.

Impact de la déamidation sur la structure et la fonction de Bcl-x_L dans la membrane

Les informations structurales limitées sur la pleine longueur Bcl-x_L (FL) sont disponibles et l'impact de la déamidation dans la membrane associée Bcl-x_L ne sont pas bien compris. Cette étude a tenté d'élucider pour la première fois, la déamidation de Bcl-x_L dans un environnement membranaire pour évaluer les changements potentiels dans la structure et la dynamique des protéines et par conséquent comprendre sa perte de fonction (Figure 7). Les cycles de production ont été effectués à 300 K et un ensemble NVT utilisant le couplage de température Langevin[37] avec un gamma de $1,0 \text{ ps}^{-1}$. Nous nous sommes principalement concentrés sur les changements de conformation et la dynamique essentielle de Bcl-x_L lors de l'insertion de la membrane et de la déamidation. Alors que la queue C est plus flexible comme prévu dans l'eau et interagit avec la tête de la protéine, elle est plus stable dans la membrane grâce à l'interaction avec les lipides. Dans la membrane, les queues C ont été inclinées vers la membrane normale et $\alpha 2$, $\alpha 3$, et J23 dans le BG orienté vers la membrane et le BG interagit de manière lâche avec la membrane. Remarquablement, la déamidation de l'asparagine en aspartate/iso-aspartate dans les systèmes membranaires semble allostérie déclencher automatiquement les changements dans le sillon de reliure. L'analyse en composantes principales a illustré les transitions conformationnelles entre l'eau et les systèmes membranaires. L'analyse en composantes principales suggère que l'environnement de simulation affecte considérablement la dynamique essentielle impliquant les différences conformationnelles. Nos résultats suggèrent que le changement de

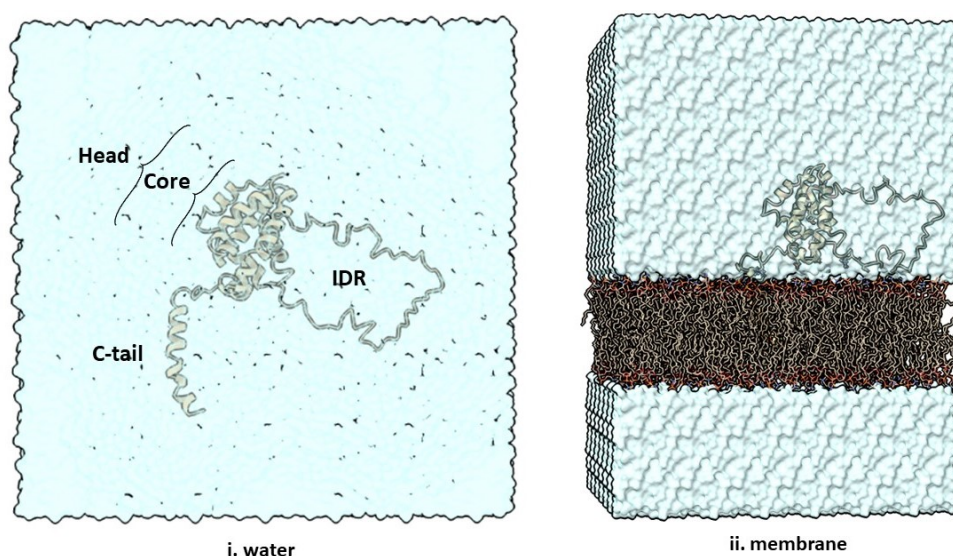


Figure 7: Représentation schématique de cette étude : Bcl-x_L et Bcl-x_L déamidé i.dans l'eau, et ii. en membrane. (La tête protéique fait référence au noyau et à l'IDR à l'exclusion de la queue C. La surface de l'eau est générée à l'aide de la présentation de surface ChimeraX[38].)

modèle d'interaction, la flexibilité du J89, l'orientation de la protéine vers la membrane et l'interaction protéine-membrane jouent un rôle central sur les différences structurales de la protéine lors de la déamidation. De plus, les différences fondamentales pourraient être des conséquences collectives/coopératives de l'association membranaire et de la déamidation. En d'autres termes, l'effet allostérique pourrait résulter à la fois de la déamidation dans l'IDR et dans l'environnement membranaire. De plus, contrairement aux résultats de Vasquez-Montes et al., nous n'avons pas observé de repliement de Bcl-x_L et de libération du domaine BH4 dans la membrane lors des simulations. L'analyse de cette étude est en cours. Les premiers résultats ont été partagés ici. Nous avons prévu d'effectuer une analyse plus approfondie pour une rationalisation et une clarification plus poussées des résultats des calculs. Nous pensons que cette étude apportera une contribution précieuse avec des implications potentielles pour le développement de thérapies anticancéreuses en présentant un aperçu des conséquences de la déamidation sur la structure et la fonction de Bcl-x_L. D'autres études se concentreront sur la compréhension des systèmes complexes (Bcl-x_L + BOPs/pro-apoptotics) afin de fournir un aperçu complet et une perspective complète sur l'impact de la déamidation Bcl-x_L.

Investigation du complexe peptidique Bcl-x_L-BH3-only

Dans cette étude, les comportements structuraux du peptide uniquement BH3 dans l'eau ont été étudiés et comparés aux systèmes complexes. Dans la deuxième partie de l'étude, nous nous sommes concentrés sur le complexe peptidique Bcl-x_L-BIM (Identifiant PDB : 4QVF_{X-RAY}) et le complexe peptidique Bcl-x_L-BID (Identifiant PDB : 4QVE_{X-RAY}). Notez que puisque Bcl-x_L dans ce complexe n'a pas l'IDR, nous avons modifié les modèles et le même protocole MD dans le chapitre précédent a été utilisé dans cette étude. L'IDR a été extrait d'un Bcl-x_L (1LXL_{NMR}) et ajouté aux modèles complexes. Les simulations MD ont confirmé que les

peptides non limités uniquement BH3 sont dynamiques dans l'eau par rapport aux systèmes complexes (état limité). Des perturbations de l'hélicité (hélices courtes) sont observées et les peptides sont instables dans l'eau conformément aux études précédentes. De plus, lorsque des peptides uniquement BH3 se sont liés à des protéines cibles, les peptides sont stables au contact de la protéine et ils forment des hélices. Cette étude est en cours. Dans un futur travail, nous étudierons des systèmes complexes dans un environnement membranaire avant et après déamidation. La compréhension des interactions dans les systèmes complexes ouvrira la voie à la conception d'inhibiteurs Bcl-x_L.

Chimie des sels de céténiminium

Cette section couvre les résultats et les discussions sur a) la formation de KI, b) la réaction de cycloaddition [2+2] et c) les réactions de compétition intramoléculaire.

Dans l'étude de la formation du KI, la réactivité des amides nucléophiles de départ vis-à-vis de l'anhydride triflique électrophile affecte directement la facilité de formation du KI. Les EDG sur les atomes C3 et N1 de l'amide de départ abaissent généralement les barrières d'activation du RDS. De plus, les résultats énergétiques ont été étayés par un modèle de distorsion/interaction, FMO et des descripteurs de réactivité. Enfin, une relation inverse a été observée entre les réactivités amide et KI. Alors que la nucléophilie des amides affecte la réactivité, l'électrophilie des KI joue un rôle central sur la réactivité du KI. Dans un prochain article/En tant que travail futur, cette relation sera étudiée plus en détail. Dans l'étude de cycloaddition [2+2], les calculs DFT rationalisent la différence de réactivité observée expérimentalement dans la cycloaddition [2+2] du céténiminium et des oléfines. La réaction s'effectue par étapes. Chaque réaction (mécanisme) implique un état de transition initial (TS1) conduisant à un intermédiaire qui suit un chemin bifurqué résultant en deux états de transition (TS2) et deux produits. Le produit principal est déterminé par le choc stérique des groupes substituants dans TS2. TS1 est l'étape de détermination de débit (RDS). Les données calculées ont également vérifié la compatibilité/l'utilisation de *N*-allyl KI dans [2 + 2] réactions de cycloaddition.

Dans les études de compétition intramoléculaire, des voies cinétiques et thermodynamiques favorables ont été déterminées et les données calculées ont montré l'effet de la longueur de chaîne sur la réaction de compétition entre les réactions d'électrocyclisation et de cycloaddition [2 + 2]. Les calculs DFT ont vérifié la facilité de formation du thiophène pour les réactions de compétition. On peut souligner que la facilité de formation du produit principal est la suivante: thiophène > [2+2]-cycloadduct > benzothiophène, respectivement. Enfin, dans l'étude de cycloaddition [2+2] intramoléculaire, les calculs DFT ont vérifié que l'étape de cycloaddition [2+2] est pilotée par des facteurs cinétiques et non thermodynamiques confirmant toutes les observations expérimentales.

Sels de céténiminium: réactivité et propension aux réactions d'électrocyclisation

Une étude de la théorie fonctionnelle de la densité prédictive (DFT) a été menée afin d'évaluer l'efficacité des réactions d'électrocyclisation des KI, dans le but de former une variété de systèmes hétérocycliques, à savoir les 3-amino(benzo)thiophènes, 3-amino(benzo) furanes, 3-aminopyrroles ainsi que 3-aminoindoles (Tableau 1). Une approche DFT a été utilisée et l'effet

des hétéroatomes (NMe, O, S) a été minutieusement étudié au moyen d’une analyse de population, QTAIM, NICS, ACID et de descripteurs de réactivité locale (fonctions de Parr et Fukui).

Table 1: Réactions d’électrocyclisation du KI conduisant à des systèmes (hétéro)cycliques [39].

Group I			Group II		
Keteniminium Salt			Target Compounds		
X	Groupe I		X		
N-Me	Enamine	1	N-Me	Pyrrole	9
O	Enol ether	2	O	Furan	10
S	Vinyl sulfide	3	S	Thiophene	11
C=C	Butadiene	4	C=C	Benzene	12
X	Groupe II		X		
N-Me	Aniline	5	N-Me	Indole	13
O	Phenyl ether	6	O	Benzofuran	14
S	Phenyl sulfide	7	S	Benzothiophene	15
C=C	Styrene	8	C=C	Naphthalene	16

L’électrocyclisation des énamines conduisant aux 3-aminopyrroles s’est avérée être à la fois cinétiquement et thermodynamiquement la plus favorable. Les céténiminiums substitués par l’aniline 5 conduisant aux 3-aminoindoles 13 ont l’énergie libre d’activation la plus faible dans le groupe II, par rapport aux céténiminiums substitués par l’éther phénylique et le sulfure de phényle fournissant les 3-aminobenzofuranes 14 et les 3-aminobenzothiophènes 15 correspondants, respectivement. La fraction aromatique du groupe II diminue la réactivité par rapport aux systèmes du groupe I, comme prévu en raison de la perturbation de l’aromaticité dans l’état de transition pour la cyclisation. De plus, la nature péricyclique des électrocyclisations a été confirmée à l’aide des méthodes FMO, QTAIM, NICS et ACID et la véritable nature du mécanisme de cyclisation des sels de céténiminium a été divulguée via une gamme de différentes techniques d’analyse, pointant vers une électrocyclisation de 10π pour le groupe II plutôt que l’électrocyclisation 6π observée dans le groupe I. De plus, les effets des substituants ont été étudiés afin de donner un meilleur aperçu de la réactivité des systèmes de céténiminium contenant des hétéroatomes vis-à-vis des réactions d’électrocyclisation. Dans l’ensemble, cette étude devrait contribuer à la compréhension des différences de réactivité des ions céténiminium et faciliter davantage les applications synthétiques.

Dans l’ensemble, cette thèse offre une perspective unique sur le mécanisme sous-jacent de la mort cellulaire induite par la déamidation Bcl-x_L. Les études sur le céténiminium contribueront également à la compréhension de la chimie du céténiminium (formation, différences de réactivité, etc.) et faciliteront davantage les applications de synthèse.

Chapter 1

Introduction

Bcl-x_L is the main focus in the first part of the thesis. Bcl-x_L is a mitochondrial trans-membrane protein that regulates apoptosis in response to various apoptotic stimuli. Bcl-x_L was characterized as an anti-apoptotic protein in 1993 [16]. In 1996, experimental structure of human Bcl-x_L was resolved by X-ray crystallography and nuclear magnetic resonance (NMR) [14]. In recent years (over 8400 research articles) Bcl-x_L has been subject to many experimental and computational articles, owing to its biological significance in cell survival and its potential for cancer therapy. Notably, Bcl-x_L undergoes post-translational modifications (PTMs) on its loop region (intrinsically disordered region-IDR), which is also the essential site for deamidation –a non-enzymatic reaction and regulatory mechanism in many biological processes. Deamidation on the IDR of Bcl-x_L induces loss of anti-apoptotic function. Hence, deamidation of Bcl-x_L is a pivotal switch that regulates its biological function. In recent studies, the importance of the IDR as well as hotspots on the IDR have been reported; nearly 20 experimental articles, reviews, and conference papers have been published with various aspects of deamidation in Bcl-x_L, but deamidation-induced structural changes and their effects on the anti-apoptotic function of Bcl-x_L are not yet completely understood. Understanding the dynamics of the IDR and the structural changes upon its deamidation plays a crucial role in elucidating potential impacts of deamidation on the structure and function of Bcl-x_L. This study aimed to computationally unravel the structural consequences of deamidation that lead to loss of Bcl-x_L anti-apoptotic function at the atomic level. The outcomes of this project are expected to pave the way for future experimental and computational studies.

Keteniminium salt is the main interest in the second part of the thesis by combining computational and experimental studies. In recent years keteniminium salt (KI) gains attention and has been subjected over 120 research articles and reviews. KIs are an improved alternative to their ketene analogues, due to their higher reactivity and high electrophilicity. Keteniminium salts are also versatile and reactive cationic intermediates in organic chemistry and they are used in a wide range of reactions such as cycloaddition, $6\pi/10\pi$ electrocyclizations, Pictet–Spengler cyclization, and so on. Historically, the pioneers of the use and synthesis of KI are Viehe and Ghosez [26, 27]. Various KI formation reactions, allowing a broader use of these intermediates, have been disclosed, namely reactions of α -haloenamines with Lewis acids,[27, 28, 29] triflation of amides,[30] methylation of ketenimines,[31] and protonation of ynamines [32, 33] and ynamides [34, 35, 36]. In the thesis, keteniminium salt was covered from formation to the reactions in which KI involves. KI chemistry was divided into two chapters. Chapter 7 was divided

into three topics, namely formation of KI, [2+2] cycloaddition reaction and intra-molecular competition reactions. Intramolecular and intermolecular [2 + 2] cycloaddition reactions of KIs with alkenes or alkynes are widely used methods to obtain cyclobutanone/cyclobutenone derivatives. Briefly, structural and energetic analysis and the reactivity differences in starting amides and keteniminium derivatives bearing different substituents were scrutinized by means of density functional theory (DFT). Electrocyclization is a powerful method to build complex structural motifs. Chapter 8 covers reactivity and propensity of KIs toward electrocyclization reactions. In addition, the true nature of the cyclization mechanism of keteniminium salts is disclosed via a range of different analysis techniques. Computational findings were in line with experiments.

Chapter 2

Objective and scope

Brief information about the research topics was presented in Chapter 1. Chapter 3 includes basic principles of Molecular Mechanics (MM) and Quantum Mechanics (QM) methods.

The first topic of interest in this thesis is the investigation of deamidation impact on the structure and function of anti-apoptotic Bcl-x_L to gain insight into its loss of function by performing microsecond-long molecular dynamics (MD) simulations. In Chapter 4 structural consequences of deamidation on Bcl-x_L in water is highlighted at the atomic level. In Chapter 5, the potential impacts of deamidation in the IDR and membrane association induced conformational changes is investigated by employing molecular dynamics simulations. Chapter 6 covers the investigation of the structural behavior of BH3-only peptide to understand complex systems between anti-apoptotic protein and BH3-only peptide.

In the second part of the thesis, keteniminium salts (KIs) are investigated from their formation to the reaction (Chapters 7 and 8). Thus, understanding the mechanistic aspect of the KI formation reactions eases the design and development processes of these intermediates to access complex structures. Chapter 7 includes three topics. Firstly, an extensive range of substituents and their effects on the reactivity of the starting amide is scrutinized to give insight on their contributions to the KI formation mechanism by activation of an amide. Then, [2+2] cycloaddition reactions of KIs with alkene/alkyne computationally is investigated and the outcomes is discussed. Competition reactions between intramolecular [2+2] cycloaddition and 6 π -electrocyclization of KI are examined and experimental findings are elucidated by means of DFT study. Lastly, in Chapter 8 keteniminium derivatives bearing different substituents leading to six different heterocyclic systems are explored via DFT and a range of different analysis techniques. This study aims to give insight on reactivity of KI derivatives bearing different substituents and heteroatoms towards electrocyclization reactions.

Chapter 3

Theoretical Background

This chapter summarizes Molecular Mechanics (MM), particularly Molecular Dynamics (MD) and Quantum Mechanics (QM) in order to provide the basic principles of the theoretical approaches used in the thesis.

3.1 Molecular Mechanics (MM)

Molecular Mechanics is a powerful method in order to calculate and predict properties of molecules and mostly used in molecular modeling. Molecular mechanics defines the total energy through a Force field (FF) which is a combination of a parameterized equation and its parameter value set. A typical force field consists of bonded and non-bonded terms as follows:

$$V = \sum_{bonds} V_{bond} + \sum_{angles} V_{bend} + \sum_{dihedrals} V_{tors} + \sum_{pairs} V_{vdW} + \sum_{pairs} V_{elec} \quad (3.1)$$

$$V = \sum_{bonds} K_{bond}(r - r_0)^2 + \sum_{angles} K_{bend}(\theta - \theta_0)^2 + \sum_{dihedrals} \frac{V_n}{2} [1 + \cos(n\phi - \gamma)] \quad (3.2)$$

$$+ \sum_{pairs} \frac{A_{ij}}{r_{ij}^{12}} - \frac{B_{ij}}{r_{ij}^6} + \sum_{pairs} \frac{q_i q_j}{\epsilon r_{ij}}$$

where K_{bond} is specific bond force constant, r is bond length and r_0 is equilibrium bond distance, K_{bend} is the angle bending force constant, θ is the bond angle, θ_0 is equilibrium bond angle, V_n is the amplitude, n is the number of minima on the potential energy surface (PES), ϕ is the torsion angle/dihedral angle and γ is the phase factor. For non-bonded terms: where van der Waals interaction between two atoms i and j separated by distance r_{ij} is described by the 12-6 Lennard Jones potential (LJ) with parameters A_{ij} and B_{ij} . LJ describes the repulsive and attractive forces between two particles as successively shown in the equation. Coulomb potential is described by electrostatic interaction between a pair of atoms i and j using the point charge q_i and q_j on atom, ϵ as the dielectric constant of medium and r as distance between charges.

Selection of force field (FF) depends on the system (the number of atoms, the research problem, details, and so on). Coarse grain (CG), united atoms (UA) and all atoms (AA) FFs are commonly used force fields. In this dissertation, we used a all atom model using Amber force fields.

3.1.1 Newton's equation of motion

MM is often used in conjunction with molecular dynamics (MD) using Newton's equations of motion:

$$F_i = m_i \mathbf{a}_i \quad (3.3)$$

The force is derived from the potential energy function with respect to the internal coordinates:

$$F_i = -\frac{\partial U(r)}{\partial r_i} \quad (3.4)$$

Equation 3.3 and Equation 3.4 define the Newton's second law of motion:

$$m_i \mathbf{a}_i = \mathbf{F}_i - \frac{\partial U(r)}{\partial r_i} \quad (3.5)$$

where F_i is force on an atom, m_i is mass of the atom along the coordinate r_i , \mathbf{a}_i is acceleration of the atom.

3.1.2 Integration of Newton's equations of motion

The equations of motion are integrated by using finite difference methods, such as leapfrog, Verlet algorithm, or velocity Verlet algorithm, which give approximate position and dynamic properties. The velocity Verlet algorithm calculates positions, accelerations, and velocity at the same time (Equations 3.7, 3.8, and 3.9).

$$v(t + \frac{1}{2}\Delta t) = v(t) + \frac{1}{2}a(t)\Delta t \quad (3.6)$$

$$x(t + \Delta t) = x(t) + v(t + \frac{1}{2}\Delta t)\Delta t \quad (3.7)$$

$$a(t + \Delta t) = f(x(t + \Delta t)) \quad (3.8)$$

$$v(t + \Delta t) = v(t + \frac{1}{2}\Delta t) + \frac{1}{2}a(t + \Delta t)\Delta t \quad (3.9)$$

Iterating those equations over time using molecular mechanics as a definition of the energy of a molecular system defines a molecular dynamics (MD) simulation.

3.1.3 Molecular dynamics simulations

MD simulation provides time-dependent behavior of a biomolecular system and changes in conformational properties by mimicking the biological environment conditions.

Historically, the first MD simulations were performed for a liquid hard sphere model by Alder and Wainwright in the late 1950's [40, 41]. In 1974, Rahman and Stillinger performed the first simulation in realistic environment, that is, in liquid water.[42] Then, the first MD simulation of proteins were studied by McCammon et al in 1977.[43] They studied the dynamics of a folded globular protein (bovine pancreatic trypsin inhibitor).

Periodic boundary conditions (PBC) are used to mimic the bulk effect and avoid boundary effects caused by finite size. PBC is the repetition of the simulation box (the unit cell) in all directions throughout space- so called images of the system in order to form an infinite lattice. When a molecule/particle moves and leaves the simulation box, one of its periodic images will enter from the opposite side with exactly the same way and direction. Thus, the number of molecules in the simulation box will conserve and the system feels as having no surface. Various periodic cell shapes, such as cubic, truncated octahedron, and rhombic dodecahedron (RHDO) are possible and the periodic cell is chosen corresponding to system size/shape and simulation program functionality.

There are two approaches for solvation model, namely implicit and explicit models. In PBC, the explicit solvent model is used. In explicit solvation, three types of water models are possible which are rigid point charges (i.e., fix atom positions), flexible point charges (i.e., atoms on spring) and polarizable (i.e., accounting for explicit polarization) models. The mostly used solvation model is the rigid TIP3P water model.

In PBC, direct summation, Ewald summation, and Particle-mesh Ewald (PME) are the most common approaches to calculate long-range interactions. Ewald Methods is computationally expensive. Particle Mesh Ewald (PME) is the most used method in MD to consider long-range electrostatic interactions.[44, 45] Compared to Ewald summation ($O(N^2)$), PME uses Fast-Fourier transform (FFT) to accelerate reciprocal space computations and scales as $O(N\log(N))$. Thus, it is a faster algorithm and reduce time for calculations.

Potential energy surface (PES) covers all possible conformations of a molecule/system. The ergodic hypothesis is that the ensemble averages utilized to compute expectation values can be substituted by time averages over the simulation. In other words, an average ensemble observable equals a time-averaged observable (Equations 3.10).

$$\langle A \rangle_{ensemble} = \langle A \rangle_{time} \quad (3.10)$$

In addition, MD simulations permit to find out the macroscopic properties of a system through microscopic simulations. A macroscopic state properties are calculated by using thermodynamic ensembles, which are a collection of microscopic states. The most common ensembles are:

- Microcanonical ensemble (NVE) ensemble; constant N, V, and E,
- Canonical ensemble (NVT); constant N, V, and T,
- Isothermal-isobaric ensemble (NTP); constant N, T, and P,
- Grand canonical ensemble (μVT); constant μ , V, and T.

where number of particles (N), volume (V), energy (E), temperature (T), pressure (P), and chemical potential (μ).

The most commonly used ensemble is NVT due to its computational efficiency. In this dissertation, NVT ensemble was used in all sampling simulations.

Various temperature algorithms are available in order to maintain a constant temperature during the simulations and to adjust the temperature to the desired value. Berendsen thermostat modifies/updates the velocity at an assigned time scale by using a weak-coupling algorithm

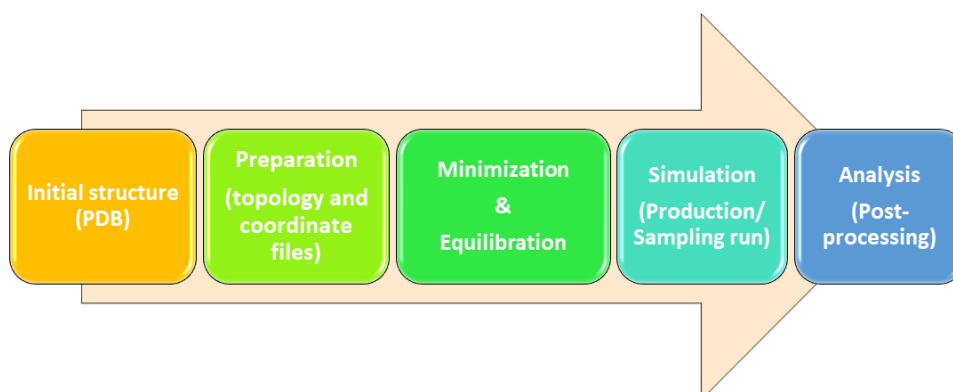


Figure 3.1: Representative MD simulation flow.

[46]. The drawback of the Berendsen thermostat is its weak velocity rescaling to ensure temperature distribution. In 1980, Andersen developed a stochastic collision model by having random (imaginary) collisions of molecules with an imaginary heat bath at the desired temperature.[47]. Langevin thermostat introduces the (random) collision frequency " γ " by imposing a frictional drag force on the motion of the solute in the solvent. This thermostat is widely used thermostat in production simulations. Nosé-Hoover, another frequently used thermostat, includes the heat bath explicitly as an additional degree of freedom. In order to maintain constant pressure Berendsen, Andersen, and Parrinello-Rahman barostats can be used in MD simulations.

The discrete time step, Δt is a limitation of MD. Longer time length can yield less efficient sampling. In order to increase the time steps and reach longer time length, constraints can be employed. H-bond vibration being the fastest motions in a simulation, the SHAKE algorithm can be carried out in order to constrain bonds involving all hydrogen bonds (i.e., by eliminating the fastest H bond vibrations).[48] The SHAKE algorithm allows an increase of the time step, usually 2 fs. Hydrogen Mass Repartitioning(HMR) can help increasing the time step to 4 fs by transferring a fraction of the mass of heavy elements (e.g., C, N, O, etc.) to their neighbouring hydrogen atoms, and in turn, slowing down the bond vibrations [49].

Taken together, MD simulation is an useful method to scrutinize protein, complex, and dynamic processes that occur in biological systems. MD parameters (temperature, length of run, and step size, etc.) and starting structure play crucial roles on MD simulation in order to sample representative conformations. In the end, typical MD flow are depicted in Figure 3.1.

3.1.4 Replica Exchange Molecular dynamics (REMD)

In classical/conventional MD, it is hard to scan/discover large areas of the energy landscape due to energy barriers between different local energy minima. To overcome the sampling problem in classical MD one of the mostly used methods is replica exchange molecular dynamics (REMD), also known as parallel tempering. REMD is an useful technique, which enhances the conformational sampling of proteins [50, 51]. Basically, REMD includes parallel multiple independent simulations at different temperatures which periodically attempt an exchange in temperature (Figure 3.2). Therefore, low temperature replicas can exchange temperature with higher temperatures and rapidly pass potential barriers by allowing enhanced sampling

of conformations. Besides temperature exchanges between replicas in temperature REMD (T-REMD), Hamiltonian REMD (H-REMD), pH-REMD, Reservoir REMD, constant Redox Potential REMD (E-REMD) are also the types of exchange attempts.

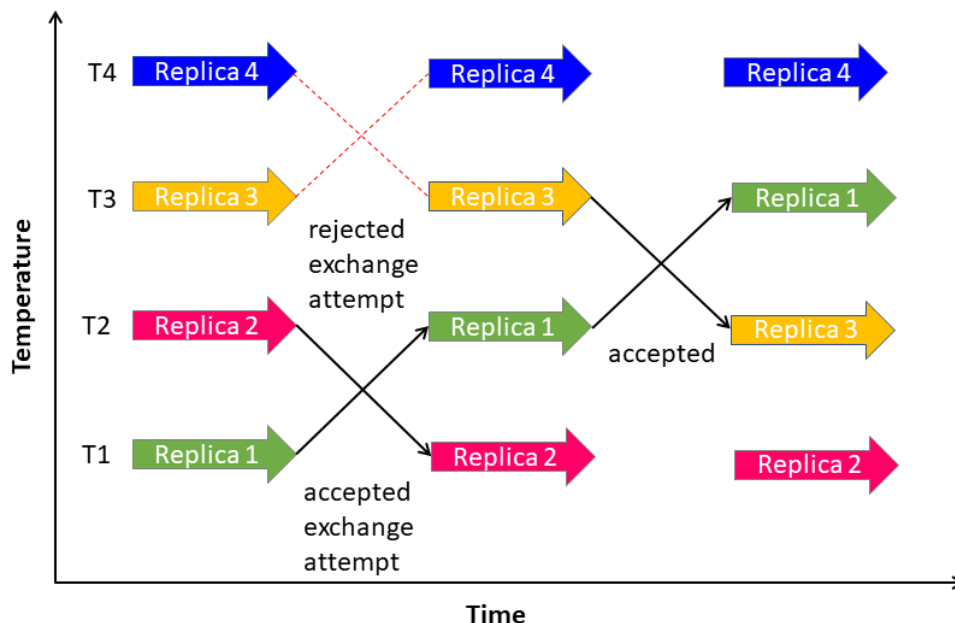


Figure 3.2: Schematic representation of REMD.

3.1.5 Principal components analysis (PCA)

Principal Components Analysis (PCA) provides insight into the dominant motions and the essential dynamics of the system.[52] Briefly, principal components analysis translates Cartesian coordinates (trajectories) into the dominant motions. Through PCA, the conformational differences between simulations are explored by investigating the distribution overlap. Visual inspections of principle componentd (PC) provide information on the similarity of the motions. PCs (Normal modes) can be visualized with Normal Mode Wizard (NMWiz)[53] in VMD (1.9.3)[54].

3.1.6 Clustering Analysis

Clustering is one of the popular techniques in order to group similar conformations into subsets (i.e., clusters) [55, 56]. Various clustering algorithms are available, such as dbscan, hierachical, k-means. Clustering algorithms detect and distinguish different clusters and group them based on conformational (dis)similarities. Clustering analysis gives insight into conformational changes/states during the simulations and help to understand structural and function relationships for a given system. In the thesis, HierAgglo algorithm (hierarchical agglomerative) with linkage and sieve was used by performing the combined clustering analysis.

3.2 Quantum Mechanics (QM)

3.2.1 The Schrödinger Equation

QM provides mathematical tools in order to describe the properties of microscopic systems. The behavior of electrons in molecules under the influence of the electromagnetic field exerted by nuclear charges can be described by the time-independent Schrödinger equation:

$$\hat{H}\psi = E\psi \quad (3.11)$$

where \hat{H} is the Hamiltonian operator and energy of the system E is the eigenvalue. ψ is the wave function which is the mathematical function that describes the spatial distribution of electrons and nuclei in the system. The Hamiltonian operator is the sum of kinetic energy operator and potential energy operator:

$$\hat{H} = \hat{T} + \hat{V} \quad (3.12)$$

For " m " is mass of a particle, the kinetic energy operator (\hat{T}) can be expressed in three dimensions as:

$$\hat{T} = -\frac{\hbar^2}{2m}\nabla^2 \quad (3.13)$$

where

$$\nabla^2 = \left[\frac{\partial^2}{\partial x^2} + \frac{\partial^2}{\partial y^2} + \frac{\partial^2}{\partial z^2} \right] \quad (3.14)$$

and

$$\hbar = \frac{h}{2\pi} \quad (3.15)$$

where \hbar is Planck's constant divided by 2π .

For a n particle system, the kinetic energy operator is represented as:

$$\hat{T} = -\frac{\hbar^2}{2m_i} \sum_{i=1}^n \nabla^2 \quad (3.16)$$

The potential energy operator for a system of charged nuclei i and j is as follows:

$$\hat{V}(\mathbf{r}) = \sum_{i>j} \frac{Z_i Z_j e^2}{4\pi\epsilon_0} \frac{1}{|\mathbf{r}_i - \mathbf{r}_j|} \quad (3.17)$$

where the atomic number of particle is represented as Z , the unit charge is e , ϵ_0 is the permittivity constant (value) and the distance between particles is r .

For a molecular system composed of electrons and nuclei, the potential energy operator in Equation 3.17 becomes:

$$\hat{V}(\mathbf{r}) = -\sum_{A,i} \frac{Z_A e^2}{4\pi\epsilon_0} \frac{1}{|\mathbf{r}_A - \mathbf{r}_i|} + \sum_{A>B} \frac{Z_A Z_B e^2}{4\pi\epsilon_0} \frac{1}{|\mathbf{r}_A - \mathbf{r}_B|} + \sum_{i>j} \frac{e^2}{4\pi\epsilon_0} \frac{1}{|\mathbf{r}_i - \mathbf{r}_j|} \quad (3.18)$$

In Equation 3.18, the electron-nuclei attraction is defined with the first term, nuclei-nuclei repulsion is accounted in the second term and the last term also presents electron-electron repulsion. Hence, Equation 3.12 can be written as:

$$\hat{H} = T_n + T_e + V_{e-n} + V_{n-n} + V_{e-e} \quad (3.19)$$

Two-particle systems can be solved accurately by the Schrödinger equation. However, the Schrödinger equation for multi-electron (many particle systems) is hard to solve and need some approximations. Hence, some approximations were proposed in order to solve the equation/problem, such as the Born-Oppenheimer Approximation, the Hartree-Fock (HF) theory, and the Density Functional Theory (DFT). The nuclei are much heavier than electrons therefore their motions are much slower than electron motions and the electronic wave function depends upon the nuclear positions but not upon their velocities. Born-Oppenheimer Approximation assumes that the positions of the nuclei can be considered to be fixed. This allows the separation of the Hamiltonian into nuclear $\hat{\mathcal{H}}_n$ and electronic $\hat{\mathcal{H}}_{el}$ parts. Equation 3.19 can be expressed as:

$$\hat{H} = T_n + V_{n-n} + \hat{\mathcal{H}}_{el} \quad (3.20)$$

The nuclear kinetic energy term in Equation 3.19 is therefore neglected, and nuclear-nuclear potential energy term is considered as a constant. Thus, the electronic structure of a molecule can be solved by the electronic Schrödinger equation:

$$\hat{\mathcal{H}}_{el}\Psi_{el} = E_{el}\Psi_{el} \quad (3.21)$$

And the total energy of the system is defined as:

$$E_{total} = E_{el} + V_{n-n} \quad (3.22)$$

One of the main approximation methods used in quantum mechanics in order to solve Equation 3.21 is the variational method which allows us to estimate the energy of the ground state of a many particle system. Variational principle states that the expectation value of the Hamiltonian which is computed with any trial wave function (Φ) is always higher than or equal to the energy of the ground state (ϵ_0).

$$\frac{\int \Phi^* \hat{H} \Phi}{\int \Phi^* \Phi} \geq \epsilon_0 \quad (3.23)$$

An approximation to the ground state can be found by varying Φ inside a given set of functions and looking for the function that minimizes the expectation value of the Hamiltonian. Hartree-Fock Theory and Density Functional Theory are based on this variational principle.

3.2.2 The Hartree-Fock (HF) Theory

The Hartree-Fock (HF) theory is one of the approximate theories in order to solve the many-body Hamiltonian. In the Hartree-Fock method, the electrons are considered as occupying single-particle orbitals making up the many-electron wave function. By an effective potential each electron experiences the presence of electrons in other orbitals. The overall electronic wave function of a system composed of N number of electrons is defined as a Slater determinant which is constructed by antisymmetrized product of one-electron wave functions, satisfying the Pauli Exclusion Principle.

$$\Psi^{SD}(\vec{x}_1, \vec{x}_2, \dots, \vec{x}_N) = \frac{1}{\sqrt{N!}} \begin{vmatrix} \chi_1(\vec{x}_1) & \chi_2(\vec{x}_1) & \dots & \chi_N(\vec{x}_1) \\ \chi_1(\vec{x}_2) & \chi_2(\vec{x}_2) & \dots & \chi_N(\vec{x}_2) \\ \vdots & \vdots & & \vdots \\ \chi_1(\vec{x}_N) & \chi_2(\vec{x}_N) & \dots & \chi_N(\vec{x}_N) \end{vmatrix} \quad (3.24)$$

A spin orbital (χ) is simply the product of a spatial orbital (φ) and the spin function (g) in a given coordinate r . The value of $g(m_s)$ can be either α or β depending on the value of the quantum number m_s .

$$\chi_i(r) = \varphi(r)g(m_s) \quad (3.25)$$

Molecular orbital coefficients are varied according to the variational principle and the overall wave function is optimized in an iterative manner until no further changes occur. This procedure is called the Self-Consistent Field (SCF). Hartree-Fock equation is used for the minimum energy calculations of the corresponding orbital of energy ϵ_i :

$$\hat{F} = \epsilon_i \chi_i \quad (3.26)$$

The Fock operator for each electron i (\hat{F}_i) is expressed by:

$$\hat{F}_i = -\frac{1}{2}\nabla_i^2 \sum_k^{nuclei} \frac{Z_k}{r_{ik}} + V_{HF(i)} \quad (3.27)$$

where $V_{HF(i)}$ is the Hartree-Fock potential which accounts for the average repulsive potential experienced by each electron due to the other electrons.

The SCF strategy uses some guess wave functions to construct the Fock operator, and then solve the Schrödinger equation. The procedure is then iterated by using the output functions as new input functions or with more sophisticated methods until the input and output functions are the same. If the convergence fails, the trial functions are varied and the process is iterated upon till self-consistency is attained to yield numerical solutions to the Hartree-Fock potential.

Electrons as charged particles expose Coulomb repulsion and the motion of one electron has an impact on the motion of the others. Hartree-Fock theory stems from the description of the dynamic electron correlation as induced by their instantaneous mutual repulsion. The methods, which are based on the wave function calculation, such as Configuration Interaction (CI), Møller-Plesset Perturbation Theory and Coupled Cluster are computationally very expensive. Density functional methods potentially offer as accurate results but with a lower computational cost.

3.2.3 Semi-Empirical Methods

Semi-empirical (SE) methods use of parameters derived from experimental (empirical) data and theoretical approximations in order to simplify the Hartree-Fock (HF) method. Semi-empirical methods proposed distinct approximations to the Hamiltonian by neglecting many integrals (particularly two electron integrals) in order to speed up/simplify the calculations and reduce the computational cost. Additionally, SE methods consider only the valence shell electrons and a minimal basis set is used. Several semi-empirical methods have been developed and parameterized with different approximations. SE are commonly based on the Zero Differential Overlap approximation (ZDO) which neglects the overlap between different basis functions centered on different atoms:

$$\phi_\mu^A(i)\phi_\mu^B(i) = 0 \quad \text{if } A \neq B \quad (3.28)$$

The various ZDO models can be grouped according to their approximations for the one and two electron integrals. When complete neglect of differential overlap (CNDO) [57] uses zero-differential overlap (ZDO) for the two-electron integrals, intermediate neglect of differential

overlap model (INDO) [58] covers the integrals that are over orbitals centred on the same atom (one-center two electron integrals).

Mostly used modern semi-empirical methods are neglect of diatomic differential overlap model (NDDO) based,[59] such as MNDO, AM1, PM3, PM6, and PM7. In the MNDO method (modified neglect of diatomic overlap) introduced by Dewar and Thiel [60], the repulsions between atoms which are separated by their van der Waals distances are overestimated. AM1 (Austin Model 1) [61] treats the hydrogen bondings better than MNDO but the misrepresentation of the hydrogen bonds is still a problem. PM3 (parametrized model number 3) [62] method uses the same equations and formalism as the AM1 method but the number of parameters for each element is different. PM6 (Parameterized Model 6) includes improved parameters (esp. transition metal systems) and core-core interaction[63]. PM7 (Parameterized Model 7) is an improved version of PM6 which adds explicit terms to describe non-covalent interactions (NCIs).

3.2.4 Density Functional Theory

Density Functional Theory (DFT) is one of the extensively used the method for the quantum mechanical calculations of many-body systems [64, 65]. Contrary to Hartree-Fock Theory which deals directly with the wave function, DFT is based on the electron density. In 1964, DFT was introduced with the Hohenburg-Kohn that proposed that the density of a system determines all its ground-state properties. Calculation of the kinetic energy of the system is the main difficulty in the Hohenburg-Kohn approach. The Kohn-Sham (KS) density functional theory provides a workaround by dividing the kinetic energy (KE) functional of a system into two parts: a) one that considers electrons as non-interacting particles and b) a small correction term accounting for electron-electron interaction as follows:

$$E[\rho(r)] = E_{KE}[\rho(r)] + E_H[\rho(r)] + E_{XC}[\rho(r)] \quad (3.29)$$

where $\rho(r)$ refers to the total electron density at a particular point "r". $E_{KE}[\rho(r)]$ is the kinetic energy of the non-interacting electrons:

$$E_{KE}[\rho(r)] = \sum_i^N \int \psi_i(r) - \frac{\nabla^2}{2} \psi_i(r) dr \quad (3.30)$$

where $\psi_i(r)$ is the Kohn-Sham molecular orbitals.

$E_H[\rho(r)]$ is the electron-electron Coulombic energy which does not consider the correlation between motions of electrons (Equation 3.31)

$$E_H[\rho(r)] = \frac{1}{2} \int \int \frac{\rho(r_1)\rho(r_2)}{|r_1 - r_2|} dr_1 dr_2 \quad (3.31)$$

The last term, the exchange-correlation (XC) energy ($E_{XC}[\rho(r)]$) corresponds to the correction to the kinetic energy appearing from the interacting nature of electrons of opposite spin (correlation term) and non-classical corrections to the electron-electron repulsion energy between electrons of the same spin (exchange term) given by:

$$E_{XC}[\rho(r)] = \int \rho(r)\epsilon_X[\rho(r)]dr + \int \rho(r)\epsilon_C[\rho(r)]dr \quad (3.32)$$

The wave function of this system with N number of electrons can be shown as a Slater determinant of one-electron functions χ_i . Hence, the electron density can be written as:

$$\rho(r) = \sum_i^N \langle \chi_i | \chi_i \rangle \quad (3.33)$$

Therefore, the hamiltonian h_i^{KS} of the Kohn-Sham equations:

$$h_i^{KS} \chi_i = \varepsilon_i \chi_i \quad (3.34)$$

where h_i^{KS} is the Kohn-Sham Hamiltonian and ε_i is the KS orbital energy. The KS Hamiltonian can be expressed as:

$$h_i^{KS} = -\frac{\nabla^2}{2} - \sum_k^{nucleus} \frac{Z_k^2}{|r_i - r_k|} + \int \frac{\rho(r)}{|r_i - r_j|} dr + V_{XC} \quad (3.35)$$

The exchange correlation potential V_{XC} is the functional derivative of the XC in Equation 3.32.

$$V_{XC}[\rho(r)] = \varepsilon_X[\rho(r)] + \varepsilon_C[\rho(r)] + \frac{\partial \varepsilon_X(r)}{\partial \rho} + \frac{\partial \varepsilon_C(r)}{\partial \rho} \quad (3.36)$$

The exchange-correlation energy (EXC) is separated into two terms, namely an exchange term "E_X", which is related to the interactions between electrons of the same spin and a correlation term "E_C", which is associated with the interactions between electrons of opposite spin. These terms also denote the electron density functionals.

$$E_{XC}[\rho(r)] = E_X[\rho(r)] + E_C[\rho(r)] \quad (3.37)$$

Most common DFT functionals were summarized herein. The local density approximation (LDA) includes the exchange-correlation functional together and assumes that the electron density is uniform everywhere given by:

$$E_{XC}^{LDA}[\rho(r)] = E_X^{LDA}[\rho(r)] + E_C^{LDA}[\rho(r)] = \int \rho(r) \varepsilon_X^{LDA} \rho(r) dr + \int \rho(r) \varepsilon_C^{LDA} \rho(r) dr \quad (3.38)$$

where Thomas- Fermi-Dirac method (approx. to the exchange energy):

$$E_X^{LDA}[\rho(r)] = C_X \int \rho(r)^{4/3} dr \quad (3.39)$$

and ε_X^{LDA} referring the exchange energy per electron:

$$\varepsilon_X^{LDA} = C_X \rho^{1/3} \quad (3.40)$$

with C_X a constant, which is equal to 0.7386. The correlation energy $E_C[\rho(r)]$ is based on Monte Carlo (MC) calculations for a homogeneous electron gas of different densities [66, 67, 68].

Local Spin Density Approximation (LSDA) accounts for spin dependence into the functionals and allows different orbitals for electrons with different spins for the spin polarized systems. $E_{XC}^{LSDA}[\rho(r)]$ is expressed as:

$$E_{XC}^{LSDA}[\rho(r)] = E_{XC}^{LSDA}[\rho_\alpha(r), \rho_\beta(r)] = E_X^{LSDA}[\rho_\alpha(r), \rho_\beta(r)] + E_C^{LSDA}[\rho_\alpha(r), \rho_\beta(r)] \quad (3.41)$$

where α and β refers to spin up and spin down densities, respectively. $E_X^{LSDA}[\rho_\alpha(r), \rho_\beta(r)]$ is:

$$E_X^{LSDA}[\rho_\alpha(r), \rho_\beta(r)] = -2^{1/3} C_X \int [\rho_\alpha^{4/3}(r) + \rho_\beta^{4/3}(r)] dr \quad (3.42)$$

and exchange energy per electron ϵ_X^{LSDA} is described as:

$$\epsilon_X^{LSDA} = -2^{1/3} C_X [\rho_\alpha^{1/3} + \rho_\beta^{1/3}] \quad (3.43)$$

Generalized gradient approximation (GGA) is the second generation of density functionals. In contrast to LDA methods, GGA method assumes that the electron density is inhomogeneous and includes both the density and gradients ($\Delta\rho(r)$) for the variation of ρ with position.

$$E_{XC}^{GGA}[\rho_\alpha(r), \rho_\beta(r)] = \int f(\rho_\alpha(r), \rho_\beta(r), \Delta\rho_\alpha, \Delta\rho_\beta) \quad (3.44)$$

where f is a function of ρ_α and ρ_β , and their gradients. E_{XC}^{GGA} is divided into exchange and correlation parts and each part is modelled independently.

The commonly used E_X functionals are B88, PW86, PW91, PBE[69]. The frequently used the E_C functionals are LYP, PW91, PBE, P86 [70] and any exchange functional can be used with any correlation functional; BLYP functional [71, 72] is also an combination of B88 exchange functional and Lee-Yang-Parr correlation functional [71, 73].

Meta-GGA (M-GGA) depend on the kinetic energy density or higher order density gradients. Hybrid density functional (H-GGA) methods join non-local Hartree-Fock exchange (HFX) with local/semi-local conventional GGA exchange in the E_{XC} term obtained from KS orbitals.

$$E_{XC}[\rho(r)] = a_0 E_X^{HFX}[\{\psi_i\}] + (1 - a_0) E_X^{DFT}[\rho(r)] + E_C^{DFT}[\rho(r)] \quad (3.45)$$

where a_0 coefficient refers to the fraction of HFX [74]. B3LYP, MPW1K, and O3LYP are some of the popular examples of HGGA functionals.

Hybrid-meta GGA (HM-GGA) functionals depend on the HF exchange, the electron density and its gradient, and the kinetic energy density. Examples of HM-GGA are BMK, MPWB1K, M06-2X and so on. Range-separated (RS) functionals (CAM-B3LYP, ω B97X, M11 and son on.) account for long-range and short-range interactions. Double-hybrid DFT (DH-DFT) functionals (B2-PLYP, DSD-BLYP, DSD-PBEP86, etc.) includes Møller–Plesset perturbation theory methods and show considerably better performance. However, computational cost is high compared to the methods mentioned above.

Lastly, the functionals used in this thesis are B3LYP,[71, 75], M06-2X, [65, 76], hybrid-GGA MPW1K,[77] range-separated ω B97XD and double hybrid B2PLYP functionals[78] to establish hierarchy in the “Jacob’s Ladder”.

Basis Sets

Basis set is the mathematical expression to define the orbitals within a system and is based on linear combination of atomic orbitals (LCAO-MO) approximation, expressed as:

$$\psi_i = \sum_{\mu=1}^n \phi_{\mu} c_{\mu i} \quad (3.46)$$

where ψ is the i^{th} molecular orbital, ϕ_{μ} denotes the μ^{th} atomic orbital, $c_{\mu i}$ molecular orbital coefficients, and n is the number of atomic orbitals.

There are three types of basis sets, namely Slater-Type Orbitals (STO's), Gaussian-Type Orbitals (GTO's), and Contracted Gaussian-Type Orbitals (CGTO's). The STO's are useful for hydrogen-like species and have higher accuracy but they fail to describe non-spherical orbitals and computational cost is high. Therefore, GTO's were proposed to overcome these pitfalls. They are much easier to compute and are widely used in DFT calculations. There are several different types of basis sets, such as minimal, double zeta (DZ), triple zeta (TZ), quadruple-zeta (QZ), and so on.

Various basis sets have been developed over the years. Split-valence basis was introduced by Pople *et al.* to split and treat valence and core orbitals separately. It uses only one basis function for each core atomic orbital (AO), and a larger basis for the valence AO's, thus decreasing the computational cost. The mostly used Pople basis sets are 3-21G, 6-21G, 6-31G*, 6-311G** and 6-31++G**. The former notation at left hand-side of the dash denotes the number of primitive Gaussian functions used to calculate core atomic orbitals and right hand-side of the dash presents the valence shell orbitals, which are composed of a linear combination of many Gaussian functions.

Polarization and diffuse functions are used to improve the basis sets to get more reliable/accurate results for electronic energy. In Pople basis sets, one asterisk (*) or (d) implies that polarization functions added to heavy atoms. Two asterisks (**) or (d,p) is used to consider both heavy atoms and hydrogens. In diffuse function, when a plus sign (+) refers to addition of diffuse functions to heavy atoms, two plus signs (++) show the diffuse function addition to light atoms.

Solvation Models

Solvation models account for solvent environments of molecular systems and mimic biological environment/experimental environment to obtain more accurate and realistic outcomes. The solvent models are divided into two groups, namely as explicit and implicit solvent models. In the explicit solvent models, all solvent molecules are included and free energy of solvation was calculated by considering solvent-solute interactions. Explicit models enable more realistic approach, yet are computationally expensive. Implicit solvent model, also known as continuum solvation model presents the solvent as a continuous medium and provides uniform polarizability by employing static dielectric constant (ϵ). The solute molecule is placed inside a cavity embedded in an uniform polarizable medium. The main advantages of implicit solvent models is to reduce computational cost. In general, total free energy of solvation is given by:

$$\Delta G_{\text{solvation}} = \Delta G_{\text{cavity}} + \Delta G_{\text{dispersion}} + \Delta G_{\text{electrostatic}} + \Delta G_{\text{repulsion}} \quad (3.47)$$

where ΔG_{cavity} denotes that free energy required to form the solute cavity. Dispersion interactions between solute and solvent is represented as $\Delta G_{dispersion}$. The third term, $\Delta G_{electrostatic}$, is the electrostatic energy and $\Delta G_{repulsion}$ is the energy caused by the exchange solute-solvent interactions, which is not included in the cavitation energy term.

Various implicit solvation models are available, namely conductor-like polarizable continuum model (CPCM),[79] integral equation formalism polarizable continuum model (IEF-PCM),[80] solute model based on density (SMD),[81] and COSMO,[82] etc. Polarizable Continuum Model (PCM) is one of the widely used implicit solvent models introduced by Tomassi and coworkers [83, 84]. This model defines the cavity surface through spheres defined by Van der Waals (vdW) radii centered at each atom. Conductor-like PCM (CPCM) treats the conductor-like screening solvation boundary condition. Another widely used continuum solvation model is IEFPCM, formulated by Cancés and Menucci [80, 85]. It uses connected spheres (a set of overlapping spheres) to model the solute, with radii of the spheres similar to solute atoms. Integral Equation Formalism of PCM was conducted for DFT solvent calculations in this thesis. SMD is based on the QM charge density of a solute molecule interacting with a continuum description of the solvent [81].

Population Analysis (Atomic Charge Models)

Since partial atomic charges are not physical observables, several charge models have been developed. Atomic charges are mainly calculated by using the Mulliken population analysis, the natural population analysis (NPA), or the Hirshfeld population analysis. The atomic charges basically gives insight into the charge distribution in a structure/molecule, which, in turn, can help picturing structural and reactivity differences. While Mulliken, Löwdin, and NPA charge schemes are based on wave functions, Hirschfeld analysis is based on electron density. If the electron density of each atom is known, the atomic partial charge can be determined by using Equation 3.48 [86]. The partial charge of an atom A is equals to nuclear charge Z_A minus to electron density in r as follows:

$$q_A = Z_A - \int \rho_A(r) dr \quad (3.48)$$

In QM calculations, the total number of electrons (N) can be defined as:

$$N = \sum_{\mu}^{AO} (PS)_{\mu\mu} \quad (3.49)$$

where \mathbf{P} is the electron density and \mathbf{S} is the overlap population summed over all atomic orbitals.

The Mulliken population is one of the well known methods for atomic charge analysis and is expressed as:

$$q_A = Z_A - \sum_{\mu \in A}^{AO} (PS)_{\mu\mu} \quad (3.50)$$

in which for the atom A, the atomic charge and the atomic number is denoted by q_A and Z_A , respectively. Sum of $\mu \in A$ indicates that consideration of atomic orbitals, which is centered on the A_{th} atom. Of note, even if Mulliken population analysis is a simple and computationally attractive method, it highly sensitive to basis set choice and fail to give realistic results in ionic species.

Natural population analysis (NPA) based on Natural Bond Orbitals (NBO) is a frequently used method developed by Weinhold and co-workers [87]. Natural bond orbitals are an orthonormal set of localized orbitals that describe possible Lewis structures of bonding electrons and lone pairs. Advantages of this method over Mulliken population are that NPA displays less basis set sensitivity/dependent and more rational electron distribution in ionic compounds.

Charges from electrostatic potentials (CHELP), charges from electrostatic potentials using a grid (CHELPG), and the Merz-Kollman-Singh (MKS) are also broadly used charge models and depends on the reproduction of the molecular electrostatic potential, that is, electrostatic potential fitting. Atom in molecules (AIM) and Hirshfield are density related charge, that is, based on the electron density.

3.2.5 Non-covalent Interaction Analysis (NCIs)

Non-covalent Interactions (i.e., H-bond, cation- π , π - π interactions, electrostatic interactions and van der Waals interactions, and so on) are known to contribute to the stability of molecules, such as proteins. Non-covalent interactions can be determined *via* NCI index based on the electron density ($\rho(r)$) and the reduced density gradient(s)[88] as follows:

$$s = \frac{1}{2(3\pi^2)^{1/3}} \frac{|\nabla\rho(r)|}{\rho(r)^{4/3}} \quad (3.51)$$

in which, s is the reduced density gradient and ρ is the electron density. " s " dramatically changes in the presence of a weak interaction producing density critical points on 2D plot of s and ρ . Additionally, NCIs are visualized by using NCIPLOT program [88].

3.2.6 Conceptual Density Functional Theory (CDFT)

Conceptual DFT involving global and local reactivity descriptors is a powerful tool in order to and understand chemical reactivity and regioselectivities [89, 90, 91]. Parr and coworkers are the pioneers of Conceptual DFT. [89] In CDFT, the electron density plays a crucial role on the description of atomic and molecular ground states in quantum mechanics. CDFT is based on the Hohenberg-Kohn theorem, where the ground state energy of a system with N electrons and external potential $V(r)$ are defined as a function of electron density depicted in Equation 3.52.

$$E[\rho(r)] = E[N; v(r)] \quad (3.52)$$

Global reactivity descriptors

Global reactivity descriptors -chemical potential " μ ", hardness " η ", electronegativity " χ ", softness " S ", electrophilicity index " ω ", nucleophilicity index " N " and so on- were introduced to calculate and predict chemical concepts, such as reactivity, chemoselectivity, and regioselectivity.

Chemical potential " μ " is introduced by Parr et al.[92]:

$$\mu = \left(\frac{\partial E}{\partial N} \right)_{v(r)} \quad (3.53)$$

where E is total energy, N is the number of electrons, and $v(r)$ is the external potential of the system.

Hardness " η " is the second derivative of energy " E " and based on the HSAB principles defined by Domingo et al.[93]:

$$\eta = \left(\frac{\partial^2 E}{\partial N^2} \right)_{v(r)} \quad (3.54)$$

Softness S is expressed as the inverse of hardness " η ". Hardness " η " is the second derivative of energy " E " defined by Domingo et al.[94]

$$S = \frac{1}{\eta} \quad (3.55)$$

The electrophilicity index " ω ", combines electronic chemical potential " μ " and absolute chemical hardness " η " to measure the reactivity of an electrophilic reagent. The electrophilicity index ω was defined by Parr et al.[95] as follow:

$$\omega = \frac{\mu^2}{2\eta} \quad (3.56)$$

Nucleophilicity index " N_u " was developed by Domingo and co-worker. The relative nucleophilicity index N is the HOMO energies with respect to HOMO energy of tetracyanoethylene (TCE). Tetracyanoethylene is taken as a reference since it has lowest HOMO energy in which the value of $N_u(\text{TCE})$ and provide nucleophilicity scale of positive values in Equation 3.57 shown as:

$$N_u = E_{HOMO(Nu)} - E_{HOMO(TCE)} \quad (3.57)$$

Local Reactivity Descriptors

Local Reactivity Descriptors also provide several ways to predict and give insight into the activity of a specific atomic site (r) within a molecule. Electron density play a crucial role on the fundamental local reactivity descriptors. The Fukui function $f(r)$ was proposed by Parr and Yang [95] based on Fukui's frontier orbital theory, assuming a reagent approaches others from the reactive side which has the highest value of $f(r)$, defined as:

$$f(r) = \left(\frac{\partial \rho(r)}{\partial N} \right)_{v(r)} \quad (3.58)$$

They assumed a frozen core [96], in which;

$$\partial \rho = \partial \rho_{valence}$$

and defined $f^-(r)$ for electrophilic and $f^+(r)$ for nucleophilic attacks as:

$$f^-(r) \approx \rho_{HOMO}(r) \quad (3.59)$$

$$f^+(r) \approx \rho_{LUMO}(r) \quad (3.60)$$

The condensed Fukui functions based on Mulliken charges proposed by Yang and Mortier [97] and Fukui functions are used to determine the most favored electrophilic, nucleophilic, and radical attack sites as follows:

$$f^- = q_k(N) - q_k(N-1) \quad (3.61)$$

$$f^+ = q_k(N+1) - q_k(N) \quad (3.62)$$

$$f^0 = 1/2[q_k(N+1) - q_k(N-1)] \quad (3.63)$$

where, N is the number of total electrons and $q_k(N)$, $q_k(N+1)$, $q_k(N-1)$ are the atomic charges in the original, anionic radical and cationic radical species, respectively corresponding to the site k.

Domingo and coworkers [96] introduced Parr functions $P(r)$ based on atomic spin density (ASD) for the radical of the original reagent. Local electrophilic P_k^+ and nucleophilic P_k^- Parr functions are used to predict nucleophilic and electrophilic attacks, respectively. The Parr functions $P(r)$ (Equation 3.64 and Equation 3.65) are given by:

$$P^-(r) = \rho_s^{rc}(r) \quad (3.64)$$

$$P^+(r) = \rho_s^{ra}(r) \quad (3.65)$$

where $\rho_s^{rc}(r)$ and $\rho_s^{ra}(r)$ are the ASD of the radical cation and anion, respectively.

Furthermore, the local electrophilicity ω_k and nucleophilicity N_k indices of a site k also permit to detect to predict the most favored nucleophilic-electrophilic attack sites. They are calculated using the Fukui functions and the Parr functions defined as:

$$\omega_k = \omega f_k^+ \quad (3.66)$$

$$N_k = N f_k^- \quad (3.67)$$

$$\omega_k = \omega P_k^+ \quad (3.68)$$

$$N_k = N P_k^- \quad (3.69)$$

Chapter 4

Impact of deamidation on the structure and function of anti-apoptotic Bcl-x_L in water

4.1 Introduction

Apoptosis, known as programmed cell death, is a complex process and is initiated by three pathways, namely intrinsic, also known as mitochondrial pathway via diverse intracellular stresses, extrinsic (death receptor-mediated pathway) via death receptors, and perforin/granzyme pathways [1, 2, 3, 4]. Each pathway is regulated by different apoptotic stimuli [4]. The Bcl-2 family proteins mainly play an important role on the mitochondrial pathway of apoptosis by regulating mitochondrial outer membrane permeabilization and subsequent apoptosis [5, 6, 7, 8].

4.1.1 Bcl-2 family protein

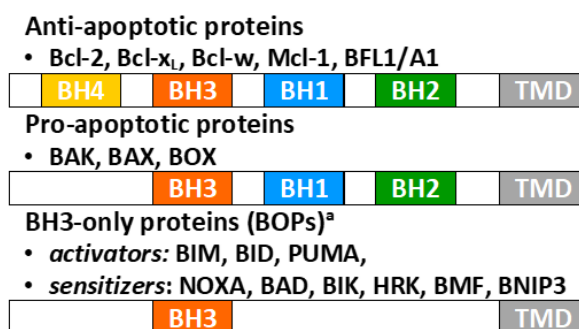


Figure 4.1: General presentation of Bcl-2 family.^a Only BIK and HRX comprise the TMD.

The Bcl-2 family was classified into three sub-classes, namely anti-apoptotic proteins, pro-apoptotic proteins, and BH3-only proteins (BOPs; activator and sensitizer BOPs) (Figure 4.1) and mediates the mitochondrial (intrinsic) apoptotic pathway in response to various apoptotic stimuli (cellular stress or damage signals) [9, 10]. Bcl-2 family proteins maintain/preserve

balance in healthy cells. When this balance is disrupted, elevated numbers of anti-apoptotic proteins are observed in various cancer cells, such as chronic myelogenous leukemia (CML), pancreatic cancer, ovarian and small-cell lung cancer [76, 98, 99].

4.1.2 B-cell lymphoma-extra-large (Bcl-x_L)

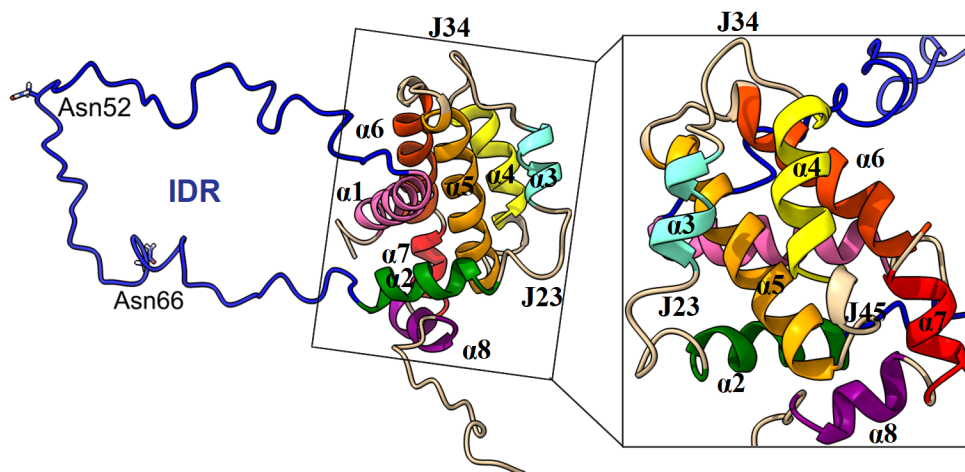


Figure 4.2: Front and side views of Bcl-x_L (PDB code: 1LXL). (The black rectangle indicates the front view of the binding groove. Blue color represents the IDR region (IDR), $\alpha 1$ in pink, $\alpha 2$ in green, $\alpha 3$ in cyan, $\alpha 4$ in yellow, $\alpha 5$ in light orange, $\alpha 6$ in orange, $\alpha 7$ in red, and $\alpha 8$ in purple. “J” refers to the junction between two helices. J23 connects $\alpha 2$ and $\alpha 3$, J34 is the junction of $\alpha 3$ and $\alpha 4$ and J45 connects $\alpha 4$ and $\alpha 5$.

Structurally, Bcl-x_L consists of two hydrophobic, six amphiphilic helices (Figure 4.2) and a C-tail composed of an α -helix ($\alpha 9$), known as the transmembrane domain (TMD)[13, 14, 17, 18]. Note that to date, the C-tail ($\alpha 9$ helix) had not been resolved in any of the available PDB structures of Bcl-x_L, but more recently the C-tail alone was experimentally resolved in phospholipid nanodiscs (PDB ID: 6F46_{NMR}[19] and PDB ID: 6X7I_{NMR}). Bcl-x_L also comprises four Bcl-2 homology domains (BH1-4) and a hydrophobic “binding groove” between $\alpha 2$ - $\alpha 5$ helices capped by a short C-terminal ($\alpha 8$ helix). The binding groove (BG) of Bcl-x_L accommodates the BH3 domain of the BOP and pro-apoptotic proteins. Furthermore, Bcl-x_L has an intrinsically disordered region (IDR) (residues 21-84), the so-called “loop region” between $\alpha 1$ - $\alpha 2$. Specific residues within the IDR of Bcl-x_L are post-translationally modified in response to diverse stimuli. Most of the previous studies lacked/omitted the IDR,[100, 101, 102, 103] however, the deletion of IDR increases the anti-apoptotic activity of Bcl-x_L (hyper-function),[104] hence, Bcl-x_L without IDR fails to give full insight into the structure and function of the protein. Analysis of the intrinsically disordered region is essential since the IDR is the main site for post-translational modifications (PTMs)[21, 22, 23, 24]. The importance of the IDR as well as hotspots on the IDR have been reported in recent studies[20, 25, 105, 106, 107]. Two asparagine residues (Asn52 and Asn66)[25] on the IDR are well documented to deamidate and this, in turn, is known to play a pivotal role on reduction/loss of anti-apoptotic activity of Bcl-x_L [25, 105, 106]. The impact of PTMs on Bcl-x_L are not yet completely understood, however,

apoptotic stimuli (DNA damage, UV, nutrient deprivation, chemotherapy, etc.) is known to induce PTMs in Bcl-x_L that lead to a) the release of BOP and the subsequent activation of pro-apoptotic proteins, and b) the inhibition of its binding to pro-apoptotic and BH3-only proteins, leading to apoptotic cell death[4, 108]. One of the goals of this study is to elucidate the impact of PTMs that take place on the IDR, specifically deamidation, on the general structure of Bcl-x_L, which may eventually lead to the release of BOPs or an inefficiency of sequestering BOPs.

4.1.3 Post-translational modifications (PTMs)

Post-translational modification (PTM) is a regulatory mechanism in many biological processes. Most common modifications are acetylation, acylation, amidation, deamidation, phosphorylation, glycosylation, ubiquitination, nitrosylation and SUMOylation [109, 110, 111]. Influence of post-translational modifications within the IDR are important to understand regulation and downregulation of Bcl-x_L [25, 105, 106, 112]. Specific residues within the IDR of Bcl-x_L are post-translationally modified in response to diverse stimuli. However, the effects of PTM on Bcl-x_L are not completely understood. Figure 4.3 presents known PTM sites on the IDR region,[25, 106] namely deamidation (Asn52 and Asn 66) [13, 113, 114, 115], phosphorylation (Thr47, Ser49, Ser62, and Ser 73) [21, 116], and cleavage (Asp61 and Asp76) [23, 24, 117]. Notably, the modifications increase negatively charged residues on the IDR and these can change the interactions between IDR and core of Bcl-x_L and hence structural behaviour. Among PTMs, deamidation is of particular interest to this study.

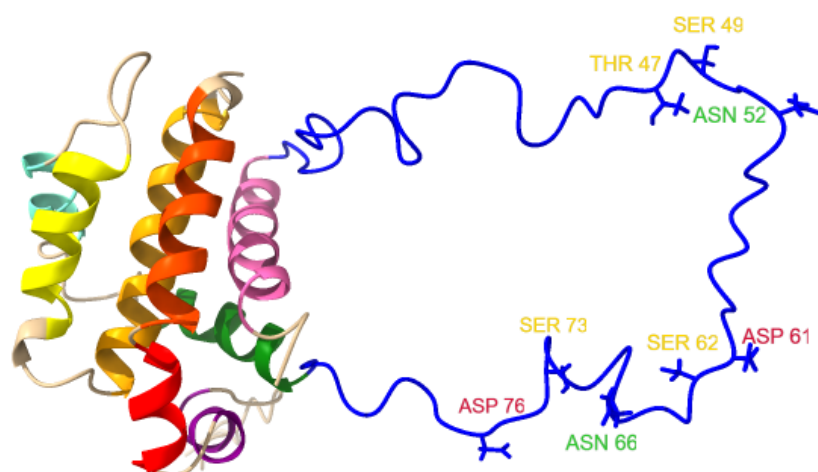


Figure 4.3: Representation of Bcl-x_L (PDB ID:1LXL) with known PTM residues/sites on the IDR region. (Blue color denotes the IDR regions, α 1 in pink, α 2 in green, α 3 in cyan, α 4 in yellow, α 5 in light orange, α 6 in orange, α 7 in red, and α 8 in purple.)

4.1.4 Deamidation of Bcl-x_L

Deamidation is a non-enzymatic reaction and one of the pivotal post-translational modifications (PTMs), which is a regulatory mechanism in many biological processes. ‘Molecular clocks’ hypothesis by Robinson et al. emphasizes the importance of asparagine and glutamine deamidation and suggests that deamidation is a biological molecular timing mechanism that serves a programmable genetic control to any desired time interval and control of biological processes [11]. Deamidation rate is determined by protein structure and environment; deamidation half times of proteins are shown to vary from a few hours to more than 100 years [118]. Asparagine (Asn) and glutamine (Gln), two of the 20 naturally occurring amino acids, are inherently unstable under physiological conditions [12]. Gln and Asn are known to spontaneously yet non-enzymatically deamidate into a mixture of glutamyl (Glu) and iso-glutamyl (iso-Glu) and a mixture of aspartyl (Asp) and iso-aspartyl (iso-Asp) residues, respectively (Figure 4.4) [11, 119]. This, in turn, replaces a neutral residue with a negatively charged one and has the potential to cause severe electrostatic clashes leading to structural deformations, which may eventually have dramatic biological consequences. Gln deamidation is usually substantially slower than Asn deamidation, hence asparagine deamidation has more biologically relevant consequences. PIMT/PCMT repair mechanism converted iso-Asp to the mixture of Asp and iso-Asp over succinimide intermediate and does not fully goes back to Asn [11, 12, 25, 114, 118]. It important to mention that contrary to reversible PTMs, such as phosphorylation which is a fast process, [25] deamidation is a slower reaction and an irreversible PTM. The only way, which can mitigate its effects is the neosynthesis of natural protein, in this case, Bcl-x_L. Hence, deamidation is different from other PTMs and drew our attention to understand its impacts on proteins with time.

A notable example is the mitochondrial trans-membrane protein, Bcl-x_L, [13, 14] which functions as an anti-apoptotic protein. Bcl-x_L belongs to the Bcl-2 family, [15] which regulates the mitochondrial pathway of apoptosis in response to various apoptotic stimuli [16]. Bcl-x_L indirectly binds to BH3-only proteins and prevents them from activating pro-apoptotic proteins or directly binds to pro-apoptotic proteins and inhibits their pro-apoptotic activities, which lead to cell death [108, 120, 121]. Additionally, Bcl-x_L also indirectly plays a major role in autophagy [18, 122] and senescence [123, 124] pathways. Since Bcl-x_L is known to play a pivotal role in the survival of tumor cells, understanding the inter-relations among apoptosis, autophagy and senescence is pertinent in determining how Bcl-x_L regulates cell survival or cell death [125].

Only three asparagine residues (Asn52, Asn66 and Asn185) with an (n+1) glycine residue (Asn-Gly) exist in structure of Bcl-x_L. However, Asn185, being embedded in the core region, is not prone to deamidation due to less water-exposure; as a result, it has a much longer deamidation half-life when compared to Asn52 and Asn66. Both asparagine residues, Asn52 and Asn66, are located in the IDR and undergo deamidation leading to a complete loss of protein function [13, 76, 98, 113, 115]. While Bcl-x_L deamidation leads to apoptosis in normal cells, tumor cells are known to have acquired resistance to apoptosis and a clear survival advantage by suppressing Bcl-x_L deamidation and its biological consequences [98]. In 1997, Aritomi et al. published the first report on Bcl-x_L’s susceptibility to deamidation, when defining the crystal structure of rat Bcl-x_L (PDB ID: 1AF3X-Ray) [13]. They defined the deamidation sites of rat Bcl-x_L by high performance liquid chromatography (HPLC) and iso-Asp was only de-

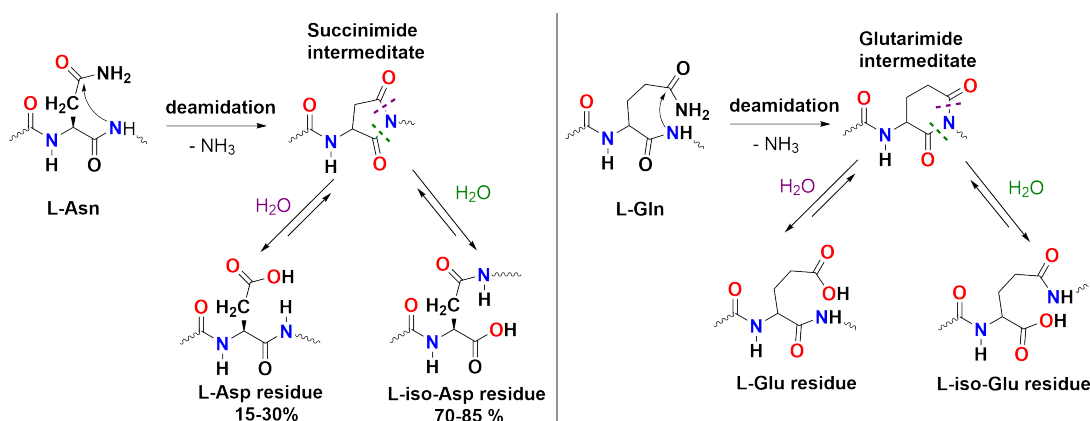


Figure 4.4: General mechanism of Asn and Gln deamidations.

tected in Asn52 and Asn66 showing the susceptibility of both residues. Similarly, Takehara and Takahashi reported that Asn52 and Asn66 residues of human Bcl-x_L are prone to deamidation [98]. In general, Bcl-x_L deamidation is accelerated by DNA-damage inducing agents used in cancer treatment [76, 115, 126]. Notably, unlike the rest of the Bcl-2 family, asparagine-glycine (Asn-Gly) sequences in the IDR of Bcl-x_L are evolutionarily conserved, showing their biological significance.

Previously, Deverman et al. (Weintraub lab) reported that the deamidation of Bcl-x_L down-regulates the anti-apoptotic activity of Bcl-x_L [113]. However, in 2003 they published an erratum indicating that an undetected mutation was observed and Bcl-x_L-BIM binding was recovered, that is, Bcl-x_L does not lose its ability to bind to the BH3-only proteins upon deamidation [127]. However, they had failed to consider the possibility of iso-Asp conversion in their study. Later, Alexander and coworkers confirmed the initial results of Deverman et al. by showing the loss of Bcl-x_L's anti-apoptotic function when deamidated, and reported that iso-Asp52/iso-Asp66 residues in the IDR region prevent the sequestering of BH3-only proteins [115]. Therefore, it is imperative to further investigate the structural changes in Bcl-x_L upon deamidation of Asn52 and Asn66 in order to clarify these seemingly controversial experimental results. The current study is the first step towards this goal, where we computationally explore the structural and biological consequences of Bcl-x_L deamidation at the atomic level. More recently, in 2018, Follis et al. reported a new NMR structure of a Bcl-x_L phosphomimetic mutant (S62E-Bcl-x_L, PDB ID: 6BF2_{NMR}, 20 conformers) and experimentally investigated the effect of PTMs in the intrinsically disordered region (phosphorylation and deamidation in IDR) on the regulation of apoptosis [105]. They proposed that phosphorylation (S62E) and deamidation (N52D and N66D) in the IDR induce allosteric interactions in the binding groove leading to the release of pro-apoptotic proteins, which in turn trigger apoptosis.

Previous experimental studies, mentioned earlier, indicated the significant impact of deamidations in the IDR on the function of Bcl-x_L [25, 105, 106, 128, 129, 130]. On the other hand, there is only a limited number of computational studies performed on Bcl-x_L that includes the IDR. In 2013, Maity et al. reported significant differences between the conformational dynamics of Bcl-x_L in water and in membrane (total 1.6 μs , implicit models) [102]. In water, the C-tail covered the binding groove and acted as a lid. In water and membrane environments, principal components of the motions were significantly different implying conformational transitions of

Bcl-x_L in the membrane. However, the model used by Maity et al. was truncated by removing the Bak peptide from its complex with Bcl-x_L (PDB ID: 1BXL_{NMR}), moreover, the IDR was not present. In 2017 Priya et al.[131] investigated the influence of the IDR on the function of Bcl-x_L by comparing Bcl-x_L with and without the IDR (total 800 ns, NPT simulations). They showed that the IDR allosterically modulates the structural dynamics of Bcl-x_L and they validated this finding through testing the effect of phosphorylation of S49 and S62 in the IDR. Phosphorylation in the IDR induced changes in electrostatic interactions in the BG, showing allosteric regulation. In Priya's study, deamidation in the IDR was not explored and the complete experimental (NMR) structure (PDB ID: 1LXL (residues 2–196)) of Bcl-x_L was not utilized. More recently, in 2020, Marassi and coworkers described and investigated the conformation of full-length Bcl-x_L in both its soluble and membrane-anchored states using NMR spectroscopy, isothermal titration calorimetry (ITC) and molecular dynamics (1 μ s \times 5 MD simulations) [132]. The study mostly focused on the tail-groove interaction in solution. Their model was modified Bcl-x_L/Bak-BH3 complex (PDB: 1BXL_{NMR}) by adding a loopIDR section from 1LXL_{NMR} and by replacing the C-terminal His-tag with the C-tail (residues 210–233) from 6X7I_{NMR}. The Bak-BH3 peptide was removed, and the C-tail was docked into the binding groove. The MD simulations in their study was somewhat limited and did not offer any insight on deamidation in the IDR. Taken together, the computational studies, in general, had short simulation times (maximum 1 μ s) causing limited sampling; moreover, these studies used truncated or modified models of Bcl-x_L, where the IDR was subsequently added. To date, the mechanism by which Bcl-x_L deamidation induces apoptosis remains unclear. In the current study, we used a non-modified, non-truncated experimentally available form of Bcl-x_L, unlike previous studies. This study is the first attempt to investigate the structural and biological consequences of Bcl-x_L deamidation at atomic resolution through microsecond long MD simulations. In this context, clustering, principal component analysis (essential dynamics) and H-bond interactions were particularly scrutinized.

4.2 Methodology

Initial structure “1LXL” was retrieved from the Protein Data Bank (Homo sapiens); cloning artifacts and histidine tags were removed. Deamidated structures (DM1 and DM2) were built by replacing Asn to Asp and iso-Asp, respectively. MD simulations were performed by using the Amber18 program package [133]. All MD simulations were performed using the Amberff14SB [134] force field implemented in the Amber18 program package [133] and solvation was carried out using the TIP3P [135] explicit water model forming cubic boxes. Counter ions (sodium or chloride) were added into each system to neutralize charges. Amber force field for L-iso-Asp, which is a non-standard amino acid, was parameterized with the antechamber and tleap modules as implemented in the Amber simulation package (see details in Appendix A: Figure A.1 and Table S1). After the preparation step, all systems (WT, DM1 and DM2) were minimized using the steepest descent method with harmonic restraints on all heavy atoms. In the minimization step, NVT ensemble with Andersen temperature coupling [47] was employed and the velocities were randomly updated every 10 steps. Long range interactions were calculated using the particle mesh Ewald (PME)[45] method with the default 8 Å cutoff distance. SHAKE algorithm was carried out in order to constrain bonds involving hydrogen atoms [48]. Equilibration runs

were performed using the NPT ensemble with a Monte Carlo barostat. Time step for the equilibration runs was set to 2 fs. A five-step equilibration protocol was conducted as follows: 1) all heavy atoms were restrained with a harmonic potential of $50 \text{ kcal mol}^{-1} \text{ \AA}^{-2}$ for 0.1 ns at 10 K, to provide a proper geometry for the H atoms. 2) restraints on the oxygen atoms of water molecules were removed to optimize the positions of water molecules with respect to the protein environment using the same restraining potential for 0.1 ns at 10 K. 3) the harmonic potential was decreased to $5 \text{ kcal mol}^{-1} \text{ \AA}^{-2}$ by repeating the 2nd step. 4) the entire system was equilibrated without restraints for 0.1 ns at 10 K. Under the Andersen thermostat [47] the velocities were randomly updated every 10 steps throughout equilibration steps 1-4. 5) The systems were gradually heated to 300 K for 2 ns using the Berendsen thermostat [46] with a coupling time of 1.0 ps. Production runs were performed at 300 K and an NVT ensemble utilizing Langevin temperature coupling [37] with a gamma of 1.0 ps^{-1} . The time step for production runs was set to 4 fs, using hydrogen mass repartitioning (HMR), [49] to accelerate MD simulations.

All analyses were performed with the cpptraj [136] module of Amber18. The backbone root mean-square deviation (RMSD) analysis was performed using the backbone atoms of Bcl-x_L's core region defined by residues 85-96, 120-131, 137-156, 162-176 in line with the core region definition (residues 85-98, 123-127, 140-156, and 162-175) of Liu et al [100, 101]. Reference structure for wild-type (WT) simulations are NMR structure of Bcl-x_L (PDB ID: 1LXL). In deamidated systems initial/built structure was used as a reference. Secondary structure contents were calculated using the Definition of Secondary Structure Prediction (DSSP) algorithm [137]. For hydrogen bond (H-bond) calculations, the distance criteria was defined as $\geq 3.2 \text{ \AA}$ based on heavy atom distances (acceptor to donor heavy atom) and angle cutoff is 135° . Contact percentage (%) in H-bond analysis is defined as the percentage of total contacts during simulations. Linear Interaction Energy (LIE) analysis was performed to evaluate non-bonded long-range interactions. The results were visualized by B-factor coloring to effortlessly pinpoint the hotspots between IDR and protein (excluding IDR, ΔIDR).

Combined clustering analysis was performed by using HierAgglo algorithm (10 clusters, linkage, based on the RMSD of C α of protein residues (ΔIDR) (1-20,85-209@CA)) to explore the major conformational changes among wild-type and deamidated systems (Table 4.2). Each system includes equal number of frames (625000 frames/each). The last 5 μs were used in the calculations of longer simulations to keep the same number of frames for each system. Sieve (100, random) was also employed [55]. Clustering findings were also combined with Principal component analysis (PCA). The clusters from 1 to 9 of each system were also used in the calculation of principal component analysis.

Principal component analysis (PCA) was performed with the cpptraj module and principal components (PCs) were visualized with the Normal Mode Wizard (NMWiz) [53] in VMD (1.9.3). Firstly, the combined trajectories were RMS-fitted to an overall averaged structure using the backbone atoms of the binding groove (residues 85-156) to remove global translational and rotational motions. The coordinate covariance matrices (288 atoms total, 864 coordinates) were calculated using the same mask, namely the binding groove (residues 85-156). Then, the coordinate covariance matrices were diagonalized to obtain the first 10 PCs (i.e., eigenvectors) and their eigenvalues. All histograms in PCA were calculated using a Gaussian kernel density estimator (KDE). Graphics were plotted by Gnuplot (version 4.6) (<http://www.gnuplot.info/>) and Xmgrace (version 4.0) (<http://plasma-gate.weizmann.ac.il/Grace/>). Chimera [138] (version 1.14), ChimeraX, [38] and VMD [54] (version 1.9.3) were used for the visualization and illus-

tration of the studied models.

4.3 Results and Discussion

From a computational viewpoint, the identification of conformational differences plays a pivotal role in understanding the impact of deamidation in IDR. Up to now, there is no clear structural connection/explanation on how deamidation induces the loss of Bcl-x_L activity. In order to scrutinize conformational behaviors/differences of wild-type (WT) and deamidated Bcl-x_L systems, microsecond-long MD simulations were performed using different starting velocities. The stability of the systems and H-bond interactions were explored. Clustering analysis, H-bond interactions, and PCA analysis were combined to investigate the conformational changes upon deamidation. Using PCA, we specifically focused on the conformational changes in the binding groove (BG) upon deamidation of IDR residues Asn52 and Asn66, by considering both Asp and iso-Asp mutations. The terms “DM1” and “DM2” refer to Asp and iso-Asp deamidated Bcl-x_L, respectively. An overview of all the systems studied is shown in Table 4.1. Overall, the total amount of MD simulation time is 90 μ s.

Table 4.1: Summary of the Initial Set up.

Initial Structure	Water	Na ⁺	Total atoms	Simulation time
1LXL _{NMR} (Bcl-x _L , WT)	44408	14	136431	5 μ s \times , 9 μ s \times 1
DM1-1LXL (DM1)	44406	16	136423	5 μ s \times 4, 10 μ s \times 1
DM2-1LXL (DM2)	44406	16	136423	5 μ s \times 3, 8 μ s \times 2
			Total	90 μ s
Initial simulation box size = 111.757 \times 111.757 \times 111.757 \AA^3				

4.3.1 Stability of the wild type and deamidated Bcl-x_L systems

A backbone root mean-square deviation (RMSD) analysis was performed for wild type and deamidated Bcl-x_L’s core region and their binding grooves (residues 85-156) as well as the IDRs (residues 21-84) to evaluate the stabilities of the systems during the simulations. RMSD plots in Figure 4.5 illustrate that the core regions of WT, DM1, and DM2-Bcl-x_L are stable (< 3.0 \AA) during the simulations. Figure 4.5 shows that the IDR is highly flexible with very large range of RMSD for each system during the simulations. The RMSD fluctuations are, on average, the same for each system in the range of 10 to 15 \AA , indicating that the large and similar mobility of the IDR in comparison to initial structure. Per-residue RMSD analysis was also performed to see which helices in the core and the BG are responsible for the increase in RMSD (Figures 4.6). Average per-residue RMSD analysis illustrates that $\alpha 2$ shows higher fluctuations in DM1. Additionally, regarding all simulations (WT, DM1, and DM2), the J23 junction connecting $\alpha 2$ and $\alpha 3$ displays larger deviation with higher per residue RMSD (Figure 4.6). We also evaluated the stability of the helices during the MD simulations through secondary structure analysis (Figures A.2-A.4). We saw that $\alpha 1$ - $\alpha 8$ helices were generally preserved in

all simulations. Interestingly, persistent (long-lived) and/or ‘transient but re-occurring’ helical formations in the IDR were observed.

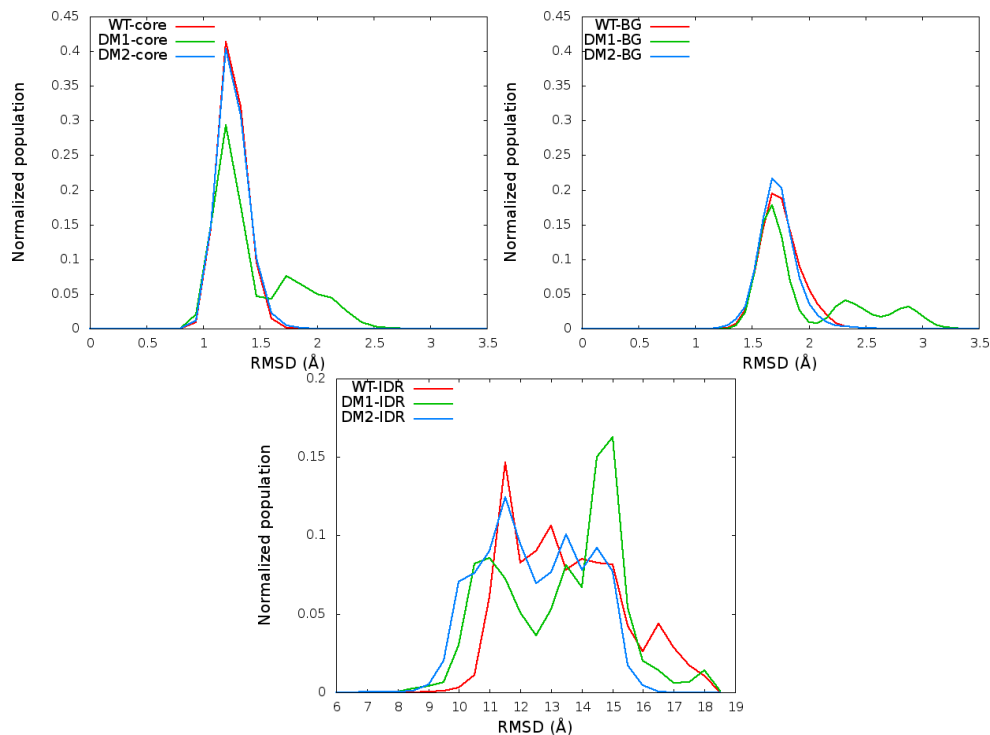


Figure 4.5: RMSD histogram for the core, the BG, and the IDR of WT, DM1 and DM2 simulations with respect to initial/starting structures before MD simulations.

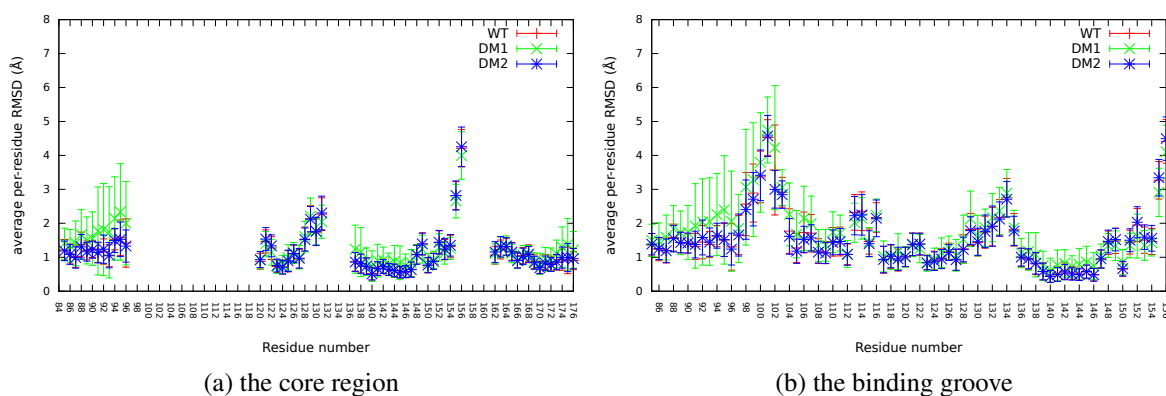


Figure 4.6: Backbone per-residue RMSD plots for a) core helices and b) the binding groove of all WT, DM1, and DM2 simulations with respect to initial/built structure.

4.3.2 Intrinsically disordered region (IDR)

Literature studies have shown that understanding the influence of post-translational modifications, i.e., deamidation on the IDR will lead to better insight into regulation and downregulation of Bcl-x_L [25, 105, 106, 112]. Structurally, the initial extended form of the IDR was not preserved throughout the simulations. Instead, simulations show that the interactions between the IDR and the protein core region are transient (short-lived) and consistently re-occurring, and the IDR approaches the core region in various ways. Particularly to verify this observation we performed several simulations, and in each case the IDR did not stay extended and approached the protein core even though the simulation boxes were large enough to accommodate extended forms. Hence, it is safe to say that the 1LXL PDB structure does not constitute a representative structure of the IDR. The IDR generally approaches/moves towards the core regions and mostly interacts with $\alpha 1$, $\alpha 2$ and $\alpha 6$ throughout the simulations. Despite the large flexibility of the IDR, transient (short-lived) but consistently re-occurring interactions, exist between the IDR and protein core.

Non-covalent interactions (NCI), such as salt-bridges, H-bonds, and cation- π interactions are known to contribute to the stability of proteins. Among the NCI, H-bond interactions in particular were explored. H-bond interactions between protein (Δ IDR)-IDR in Figures 4.7 and 4.8 depicted transient interactions and the changes in interaction pattern up-on deamidation. While the IDR in WT transiently interact with $\alpha 1$, $\alpha 2$ and C-terminal part, deamidated Bcl-x_L, particularly DM2 transiently interacts with the residues between $\alpha 6$ and the C-terminal part. These outcomes imply that increase in negative charge and backbone changes can affect interaction pattern and movements of the IDR.

H-bond interactions of IDR residues 52 (N52, D52, iso-D52) and 66 (N66, D66, iso-D66) with the protein core (excluding the IDR) were also examined before and after deamidation to check for disruption of pre-existing or formation of new interactions. Representative snapshots of WT, DM1, and DM2-Bcl-x_L involving H-bond interactions between residue 52, residue 66 in the IDR and core are shown in Figure 4.9. In wild type simulations, N52 transiently interacts with the core residues of the protein such as N52-R91, N52-R6, N52-S164, N52-E202, N52-R204 (Figures 4.7, 4.8, and 4.9a).

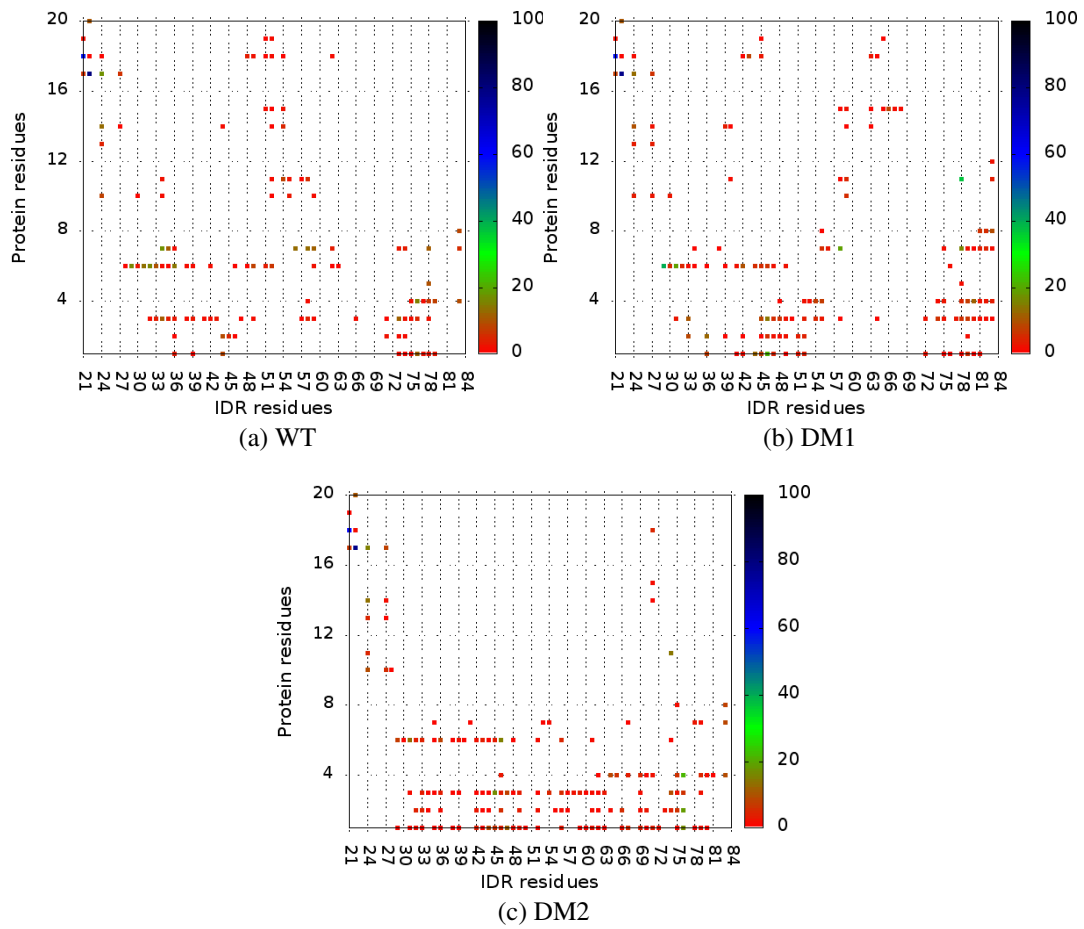


Figure 4.7: H-bond interactions plots for $\alpha 1$ residues of the protein-IDR residues of WT, DM1, and DM2 simulations. The color bar shows overall contact percentage during the simulations.

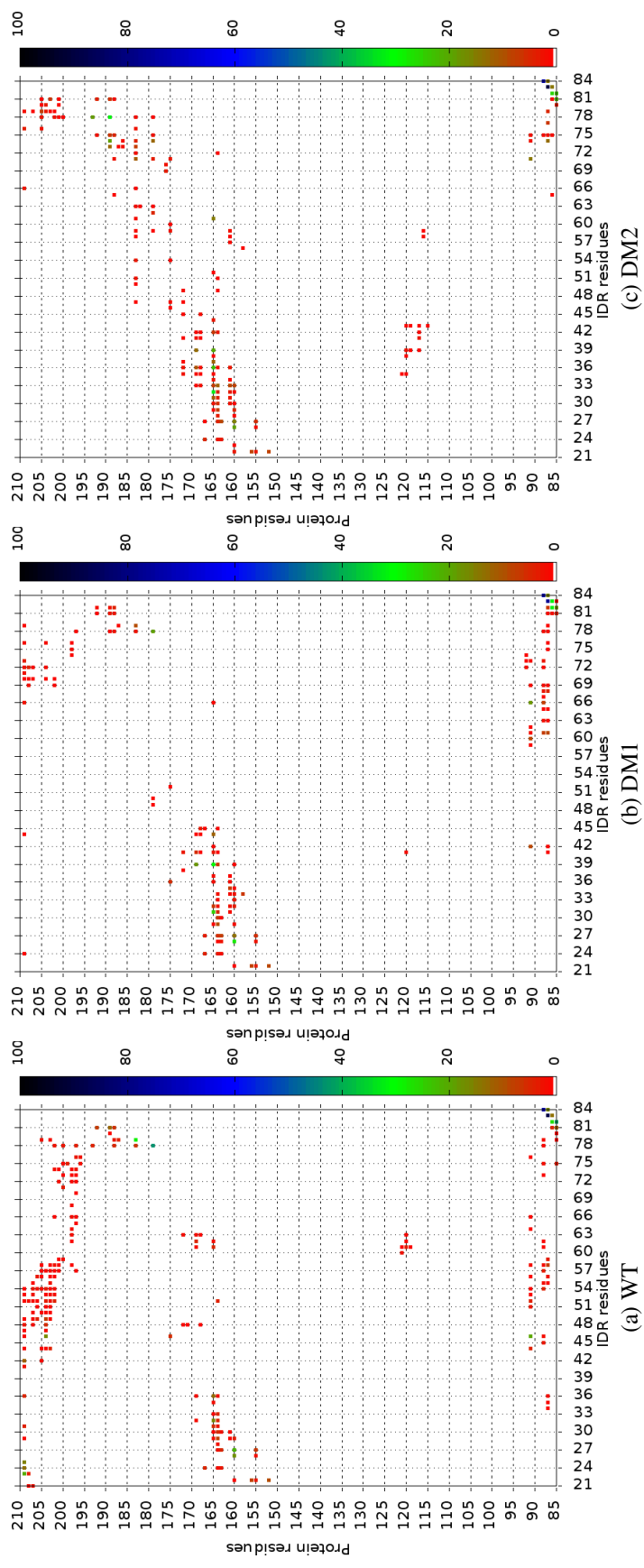


Figure 4.8: H-bond interactions plots for the protein (α 2-C-terminal residues)-IDR residues of WT, DM1, and DM2 simulations. The color bar shows overall contact percentage during the simulations.

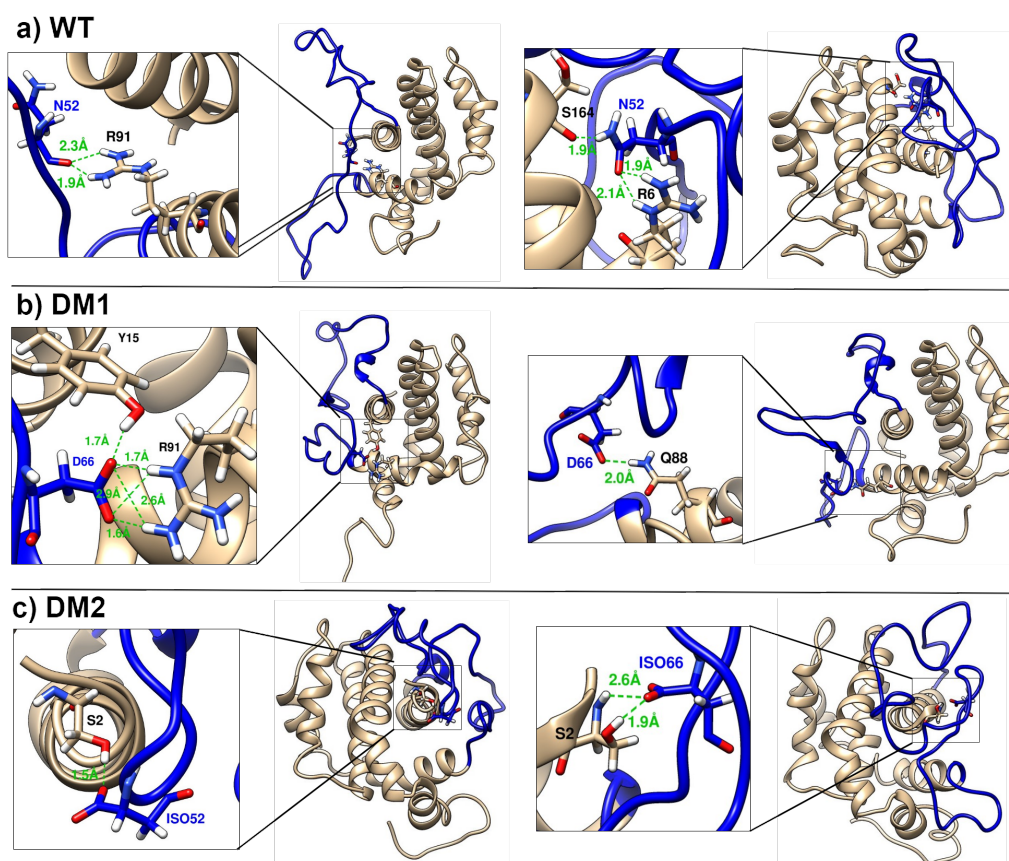


Figure 4.9: H-bond interactions between residue 52, residue 66, and protein core in representative a) WT, b) DM1, and c) DM2. Blue color denotes IDR region. ISO52 and ISO66 refer to iso-Asp52 and iso-Asp66, respectively.

More interestingly, once deamidated (simulation DM1), mostly D66 instead of D52, interacts with the core residues. D66 transiently interacts with R91, Y15, Q88 and R209 in DM1, while N66 in wild type did not interact with neither Tyr15, Gln88 nor R209 (Figures 4.7, 4.8 and 4.9a). D52 also transiently interacts with the first three residues (M1, S2, and Q3) in DM1. Compared to wild type and DM1, in DM2 (iso-Asp) simulations, S2 in $\alpha 1$ has transient interactions with iso-D52 and iso-D66 (Figure 4.7). As a result of the structural changes that iso-Asp deamidation introduces in the IDR backbone, the number of interactions between residues iso-D52 and iso-D66 and the protein core were considerably less. Linear Interaction Energy (LIE) analysis was also performed to evaluate long-range interactions between the protein core and the IDR. Bfactor coloring based on Average LIE analysis results (Figure A.5) illustrated that only N52 in WT, both D52 and D66 in DM1, and only iso-D66 in DM2 display stabilizing interactions with the protein core. Additionally, Figure A.5c demonstrated stabilizing interactions between $\alpha 8$ and the IDR in DM2.

Interestingly, R78 in the IDR interactions considerably altered upon deamidation. While R78-E179 interaction (42.8 %) stands out in WT, this interaction dramatically decreases in DM1 (19.3%) or nearly non-exists in DM2 (1.1%) (Figure 4.8). Instead, R78-D11 (37.1 %) in DM1 and R78-D189 (31.8%) in DM2 interactions were observed and these interactions are

nearly non-existent in WT. Although non-existent in WT simulations, transient but consistently recurring H-bond interactions between IDR residue S74 and a multitude of residues (D189, D11, K87, E179) in the protein core were observed in DM2. Moreover, the H-bond interaction profile of core residue R91 changed significantly. R91-N52 and R91-E46 interactions were originally observed in WT. However, consequent to deamidation, transient R91-D66, R91-E42, and R91-A60 in DM1 and R91-H71 in DM2 were detected. These findings indicate that the IDR behavior has changed significantly upon deamidation; this will be further analyzed in the following sections.

Additionally, the IDR transiently interacts with itself (intra-IDR regions) and hinge formations were observed. Different interaction patterns were clearly observed in each system (Figure 4.10). This outcome supports the flexibility of the IDR. Taken together, these results highlight the diversity of the IDR-protein core interactions. The extra negative charge introduced via deamidation understandably induces changes in the H-bond interaction patterns between the IDR and the protein core. These interactions could allosterically affect the dynamics of Bcl-x_L. Accordingly, clustering analysis and essential dynamics of WT and deamidated systems will be comparatively explored in the following section.

Priya et al.[131] in their computational study (100 ns \times 2 in total for Bcl-x_L with IDR) had reported transient interactions between the IDR and the core region of the Bcl-x_L. In line with the findings of Priya et al., most of our simulations for WT show that the IDR residues E31, E32, E39 and R78 temporarily interact with core residues R165, R6, R91, and E7, respectively. All interactions mentioned above are also observed in DM1 and DM2 simulations, except for the E39-R91 interaction. On the other hand, the increased/improved interactions between E31-R165 in DM1 and DM2 and between R78-E7 in DM1 are observed. Additionally, compared to WT, improved or new R165 interactions in deamidated systems, particularly in DM2 stand out. Our simulations verified the transient but re-occurring nature of these interactions. This, once again, is an indication that the contact patterns in the reported NMR structure are different than the simulated ones.

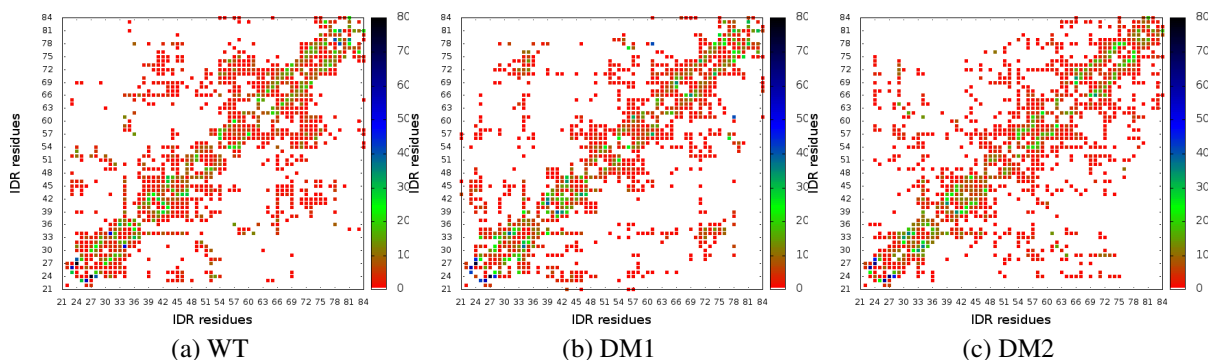


Figure 4.10: H-bond interactions plots (expressed in overall contact percentage) for the IDR-IDR residues of WT, DM1, and DM2 simulations. The color bars show the contact percentage during the simulations

In DM2 simulations, conversion of Asn to β -aminoacid iso-Asp, which disrupts the IDR backbone by the additional carbon atom is expected to cause substantially larger conformational

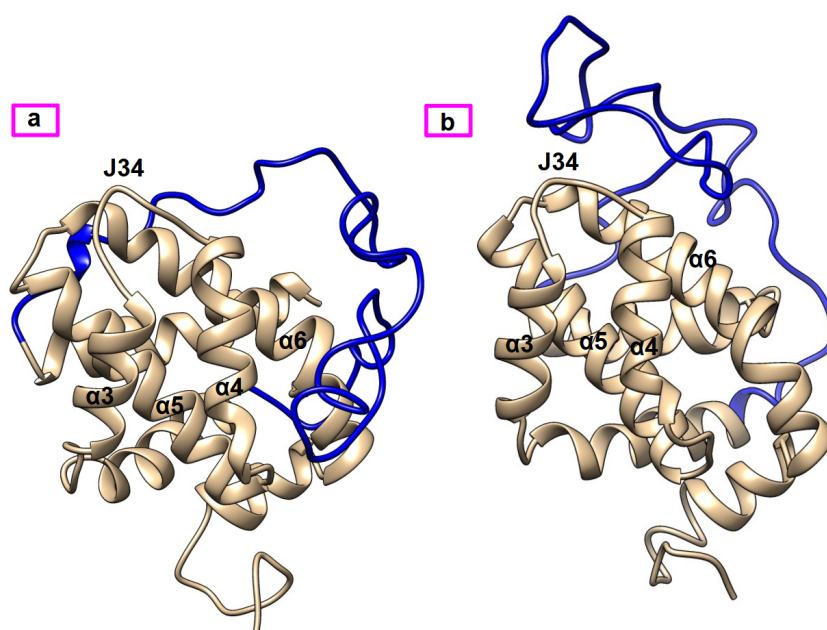


Figure 4.11: Representative positions of the IDR for a) DM2-SIM4 and b) DM2-SIM5. (Blue color denotes the IDR.)

changes compared to those caused by conversion to Asp. Intriguingly, IDR movements in DM2-SIM4 and DM2-SIM5 were considerably different than all other simulations. Figures 4.11a and 4.11b depict mid-IDR residues approaching the binding groove (BG), more specifically, $\alpha 4$ and the junction of $\alpha 4$ and $\alpha 5$ (J45) in DM2-SIM4 and the junction of $\alpha 3$ and $\alpha 4$ (J34) in DM2-SIM5. DM2 simulations suggest that the extra carbons in the backbone, caused by Asn conversion to iso-D52 and iso-D66, change the conformational behavior of the IDR, as seen by the IDR's approach to the BG; this may prevent/affect binding ability of BOP or pro-apoptotic proteins to the binding groove of Bcl-x_L.

Furthermore, in the experimental work of Follis et al. in 2018, negatively charged D61, E62, D52, and D66 in the IDR region were positioned near and electrostatically inter-acted with the positively charged arginines (R100, R102, R103; known as the 'Arginine cluster') on the J23 of the BG. However, in the experimental NMR model reported by Muchmore et al.[14] (PDB ID: 1LXL), neither S62 and D61 nor N52 and N66 interacted with the Arginine cluster in J23. In the current study, we monitored interactions between deamidation residues 52 (N52, D52, and iso-D52) and 66 (N66, D66, and iso-D66) and the Arginine cluster in all systems (WT, DM1, and DM2). Radial distribution functions (RDF) between the Arginine cluster's guanidinium hydrogens and the side chain oxygen atoms of residues 52 and 66 were calculated to monitor these interactions. The RDF plots show no interaction in the range of 0-10 Å in 13 out of 15 simulations (Figure 4.12). However, in two simulations (WT-SIM4 and D1-SIM4), RDF showed interactions in the range of 3.0-6.0 Å. To check the viability of these interactions, distance analysis was performed on simulations WT-SIM4 and D1-SIM4. Distance plots depict that these interactions are not persistent during the simulations (Figures 4.13a and 4.13b). More importantly, Follis et al. claimed that PTMs (phosphorylation and deamidation) that lead to these interactions induce a structural rearrangement at the distal binding groove (BG), which could

lower Bcl-x_L's affinity for BOP. Therefore, we focused on possible structural rearrangements in the binding groove, which stem from deamidation, and affect the dynamics of the distal BG. To do so we have performed thorough clustering analysis and Principal Component Analysis as shown in following sections.

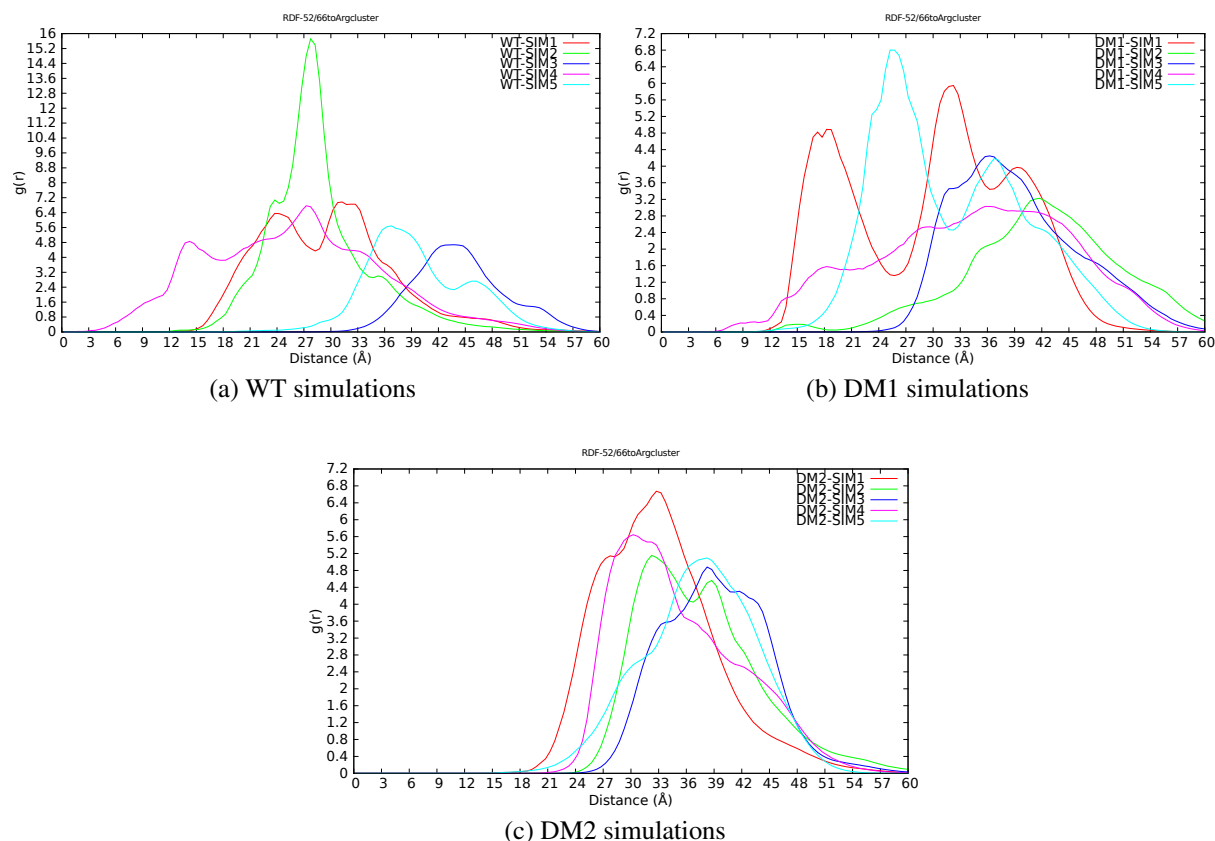


Figure 4.12: a-c) Radial distribution function, $g(r)$, vs the distance between side chain oxygen atoms of residues 52 and 66 and H atoms of the guanidinium moieties in Arg cluster.

4.3.3 Cluster Analysis

Clustering analysis was performed to group (dis)similar conformations into subsets and gives insight into conformational changes/states upon deamidation. The representative clusters of each system (WT, DM1, and DM2) were chosen/selected with respect to their contributions (Table 4.2) to each cluster for further analysis. “C” refers to cluster.

10 clusters were investigated, and the first five clusters were detected as mostly populated clusters, accounting for more than 92% of the conformations (Table 4.2). The cluster zero (C0) is the largest cluster comprising more than 70 % for each system and includes the main conformation of the protein, that is common for three systems. Then, the next four clusters were explored, and representative clusters were identified for each system with respect to their contributions to the clusters. Notably, the clusters are well separated in each system (WT, DM1, and DM2). WT is mostly populated in the first (C1) and second clusters (C2). The

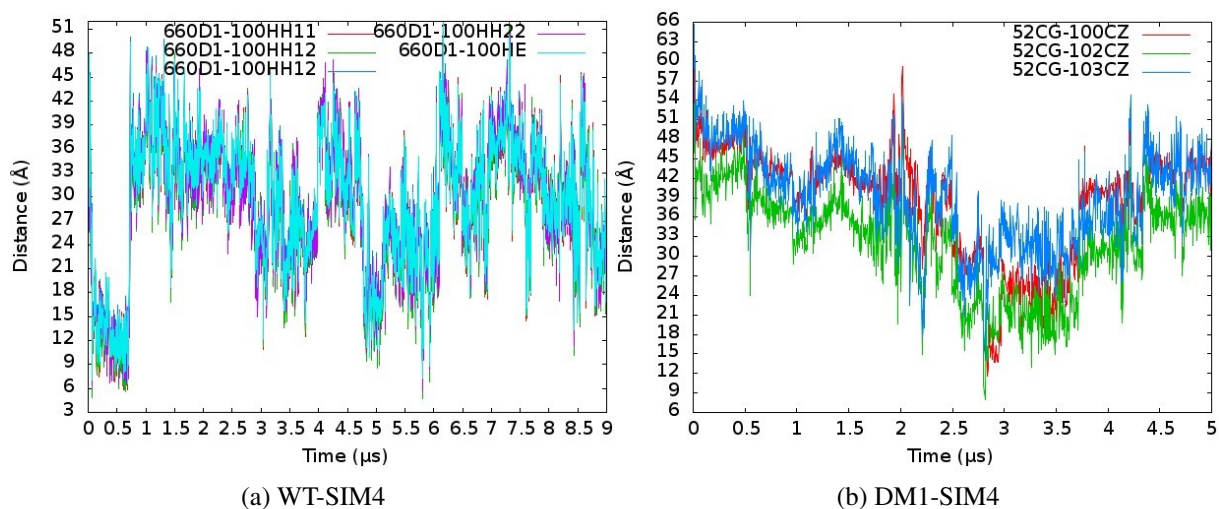


Figure 4.13: Distance plot between a) N66@OD1 and guanidinium H atoms of R100. b) D52@CG and R100,102,103@CZ.

Table 4.2: Combined clustering summary for WT, DM1, and DM2.

#Cluster	Total	Frac	# of WT frames	# of DM1 frames	# of DM2 frames	%Frac1	%Frac2	%Frac3	WT%	DM1%	DM2%
0	1371061	0.7312	442023	479201	449837	70.72	76.67	71.97	32.2	35.0	32.8
1	125061	0.0667	84785	17478	22798	13.57	2.80	3.65	67.8	14.0	18.2
2	113336	0.0604	91033	9597	12706	14.57	1.54	2.03	80.3	8.5	11.2
3	105247	0.0561	218	85876	19153	0.03	13.74	3.06	0.2	81.6	18.2
4	83539	0.0446	1526	7239	74774	0.24	1.16	11.96	1.8	8.7	89.5
5	26706	0.0142	627	4191	21888	0.10	0.67	3.50	2.3	15.7	82.0
6	19804	0.0106	822	1233	17749	0.13	0.20	2.84	4.2	6.2	89.6
7	14211	0.0076	1699	11400	1112	0.27	1.82	0.18	12.0	80.2	7.8
8	10451	0.0056	2038	4946	3467	0.33	0.79	0.55	19.5	47.3	33.2
9	5584	0.003	229	3839	1516	0.04	0.61	0.24	4.1	68.8	27.1

third cluster is a representative cluster for DM1 and the fourth cluster, even the fifth cluster is mostly populated with DM2. We further investigated the first five clusters in order to understand the differences among them. Firstly, the structures of the representative clusters (C0-C4) were examined. Structural representatives of these five clusters (C0-C4) were depicted in Figure A.6. Remarkably, main differences in cluster 3 (C3), which is the representative cluster for DM1 are shifts in helices $\alpha 1$ - $\alpha 3$ and $\alpha 8$ (Figure 4.14) and the narrowing of the J23 towards J45 (Figure 4.15). Radius of gyration (Rg) of the back-bone atoms of Y101-A104 in J23 and L130-D133 in J45 were analyzed to follow the narrowing of the bottom side of the BG (Figure 4.15). Rg in C3, which is a representative cluster of DM1, is lower than the others indicating the narrowing bottom side of the BG. Figure 4.16 displayed that the RMSD of cluster 3 (C3) is higher than the rest. These outcomes suggest that DM1 induces considerable conformational changes in the BG.

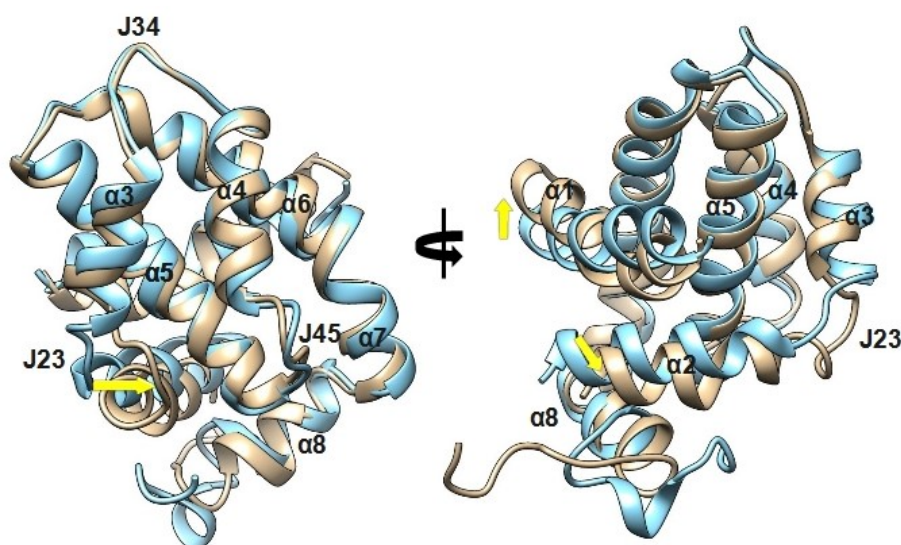


Figure 4.14: Front and side superimposition of the representative structures for clusters 0 and 3. Blue and tan color refer to C0 and C3 representative structures, respectively.

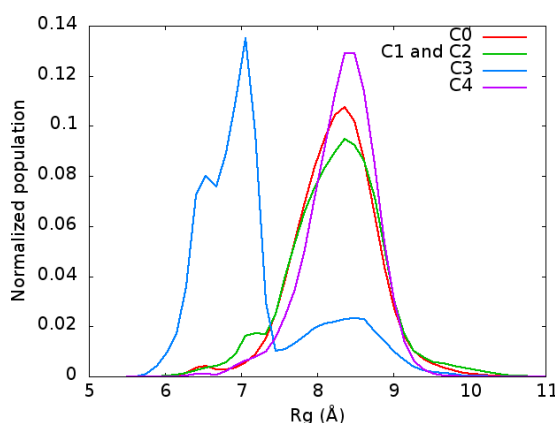


Figure 4.15: Radius of gyration (Rg) of the backbone atoms of Y101-A104 in J23 and L130-D133 in J45 of the most populated clusters (C0-C4).

Secondly, significant differences in the clusters encouraged us to further explore the impact of deamidation on the binding groove (BG) by studying more closely the interaction patterns, specifically H-bonding. In order to pinpoint the residues that contribute to the narrowing of the binding groove (Figures 4.14 and 4.15), hydrogen bonds (H-bond) between residues lying on either side of the BG were explored.

Most prominently, in cluster 3, which is the representative cluster for DM1, R102 interactions are primarily responsible for the narrowing of the binding groove (Figures 4.17 and 4.18). Indeed, R102 on J23 interacts with D133 (J45) and E129 (α 4) indicating the importance of the R102 residue. However, these interactions are nearly absent in other clusters. Instead, R102 mostly interacts with E98 in other clusters (C1, C2 and C4) and this interaction moves R102 away from the groove and causes the bottom side (J23 and J45) of the BG to stay open (Figure 4.18). Another important residue involved in the narrowing of the bottom side of the groove

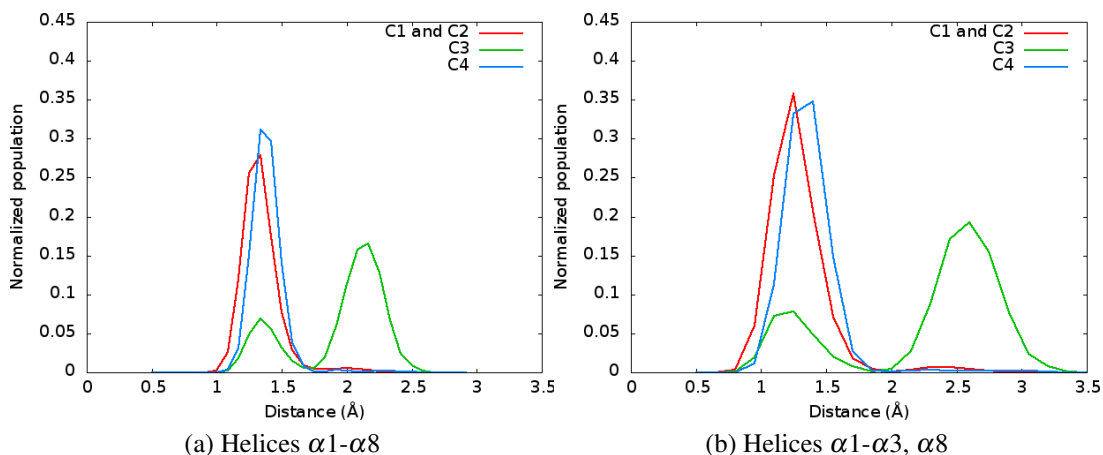


Figure 4.16: Backbone RMSD histogram for the helices of clusters 1-4 with respect to NMR structure.

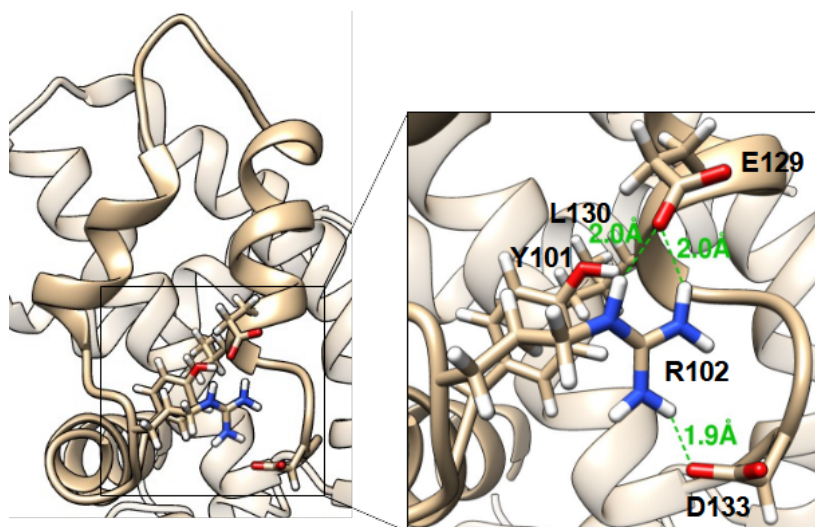


Figure 4.17: Representation of key H-bond interactions between the BG residues in DM1 (C3).

(J23-J45) is E129 ($\alpha 4$), which interacts with Y101 (J23) and R103 (J23) (Figure 4.18). Besides H-bond interaction, CH- π interaction between Y101-R102 and Y101-L130 was detected in cluster 3 by facilitating/supporting R102-D133 interaction, in turn narrowing of the BG (Figure 4.17). Moreover, in DM1 H-bond interactions between R103 (J23) and Q111 ($\alpha 3$), and between E98 (J23), and F105 ($\alpha 3$) were observed, which result in the covering of the top of the groove (Figures 4.18 and A.9b). The distance plots for the combined trajectories are also given in Figure A.8.

Additionally, the C-terminal part (residues 196-209) movements and interactions are generally different among the clusters. In DM2, the differences arise from the C-terminal part- $\alpha 8$ interactions, which are nearly non-existent in C1 and C2 (WT). Distance plots in Figure 4.19 display key interactions in the C-terminal. The distance plots for the combined trajectories are given in Figure A.10. Moreover, the IDR in C4 (DM2) is mostly oriented to $\alpha 6$ - $\alpha 8$ side and

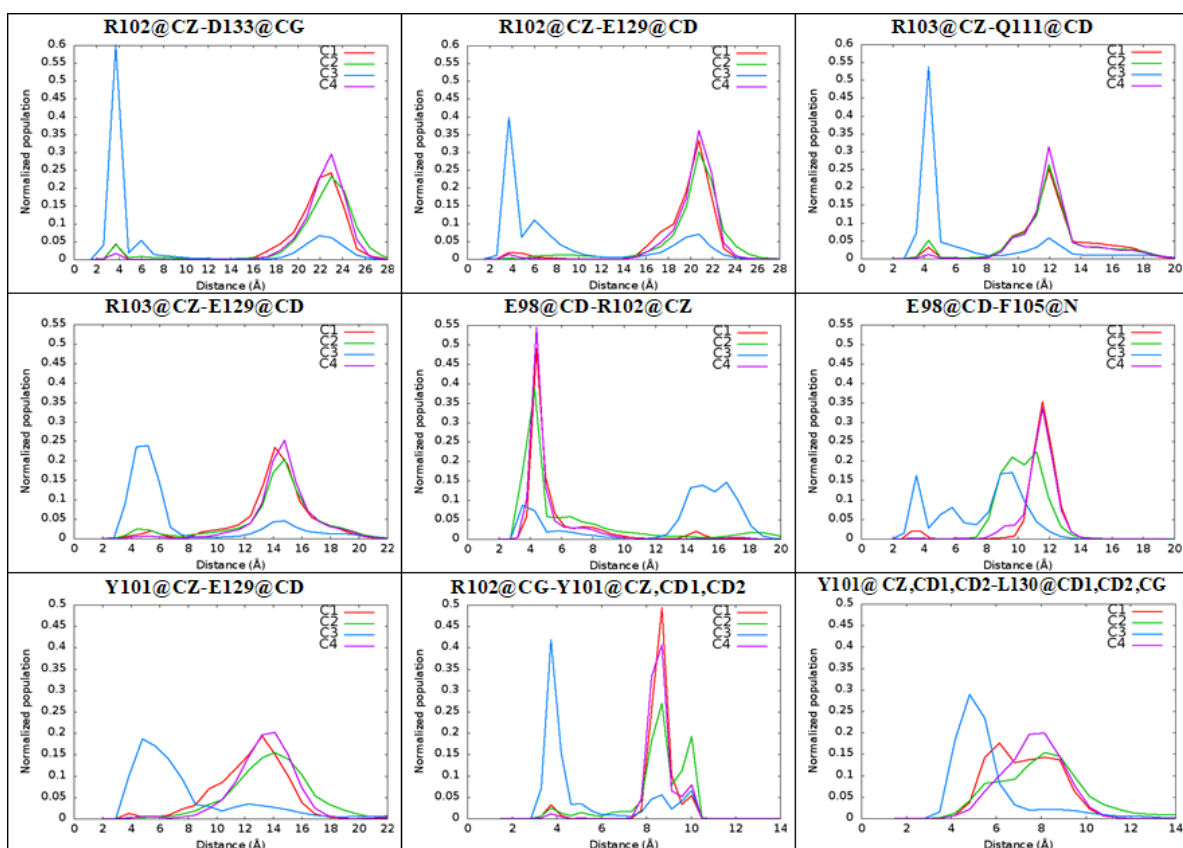


Figure 4.18: Distance histograms for the key interactions in the binding groove of the representative clusters (WT:C1, C2, DM1:C3, DM2:C4).

approach $\alpha 4$ in BG (Figure A.7). This could prevent access of the pro-apoptotics and BOPs to the BG and may impair its function.

Priya et al. also reported that R103 (J23) and R139 ($\alpha 5$) of wild-type Bcl-x_L behave like a gate by covering the bottom side of the binding groove compared to that of Bcl-x_L without IDR [131]. We observed this type of behavior in DM1, alas, between different residues (R102, D133, E129). Lastly, in 2019, Lee and Fairlie pointed out notable differences in the orientation of Phe105 ($\alpha 3$) and Tyr101 (J23) among Bcl-x_L complex structures depending on the identity of the BOP[139] and pro-apoptotic peptides it engaged [140]. It should be noted that these two residues play a pivotal role in binding to BOPs and pro-apoptotics [139, 141]. Remarkably, we observed that the Tyr101-Phe105 interaction decreases in DM1 simulations, indicating that deamidation has led to the disruption of a significant interaction enabling Bcl-x_L's binding to pro-apoptotic peptides. This in turn leads to its loss of anti-apoptotic function. Taken together, asparagine deamidation to aspartate in the IDR seems to allosterically induce the binding groove from an “open” to a “narrow” state. More specifically, the rotations and interactions of J23 and $\alpha 3$ residues, particularly R102 and R103 have a significant effect on the rearrangement of the binding groove (Figures 4.17 and 4.18).

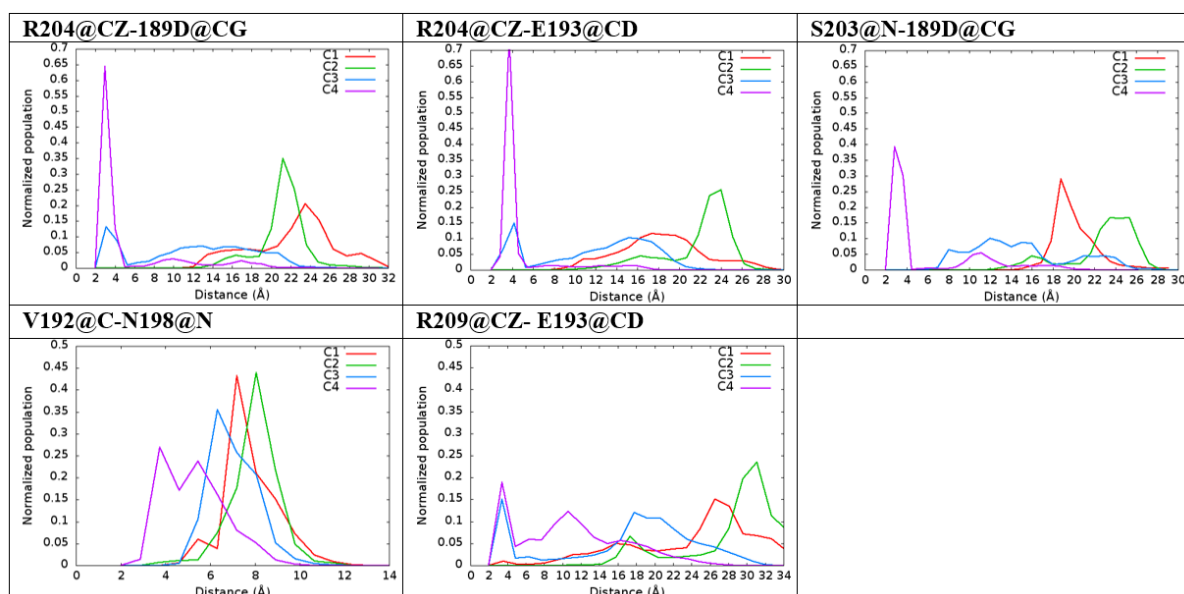


Figure 4.19: Distance histograms for the selected H-bonded residues between the C-terminal and $\alpha 8$ of the representative clusters (WT:C1, C2, DM1:C3, DM2:C4).

4.3.4 Principal Components Analysis (PCA)

PCA provides insight into the dominant motions and the essential dynamics of the system[52]. Briefly, PCA translates Cartesian coordinates (trajectories) into the dominant motions. Through PCA, the conformational differences between simulations are explored by investigating the distribution overlap; visual inspection provides information on the similarity of the motions. Since the binding groove which accommodates the BOPs and pro-apoptotic proteins is the main/crucial site for the execution of the anti-apoptotic function of Bcl-x_L, we focused on the evaluation of the BG dynamics. The structural differences induced by deamidation were further investigated by comparing the essential dynamics of the systems studied. PCA computations were performed in two steps: a) combining the trajectories, which were obtained from the cluster analysis (from C1 to C9) for each system and projected separately onto each system (WT, DM1, and DM2) and then identifying the differences among them b) visually comparing the PC modes of each system.

Since we are interested in the differences between these systems, we have chosen to exclude the C0, which is common for three of them. First, all trajectories from C1 to C9 were combined and each system (WT, DM1 and DM2) was separately projected. We limited our analysis to the first four PCs, since approximately 80 % of the cumulative variance was covered by them (Figure 4.20b). PC projection histograms in Figure 4.21 illustrate that PC1 and PC2 show significant differences among the systems (WT, DM1 and DM2), particularly for DM1 indicating considerable conformational changes. These results also imply the difference in overall motions among the systems. PC projections shown in heatmap plots (Figure 4.22) show distribution of conformations along the first three PCs. PCs of deamidated Bcl-x_L illustrate notable differences compared to WT. Remarkably, DM1 scans a different and larger conformational spaces as depicted in Figure 4.22. Large conformational sampling in DM1 refers to notable conformational

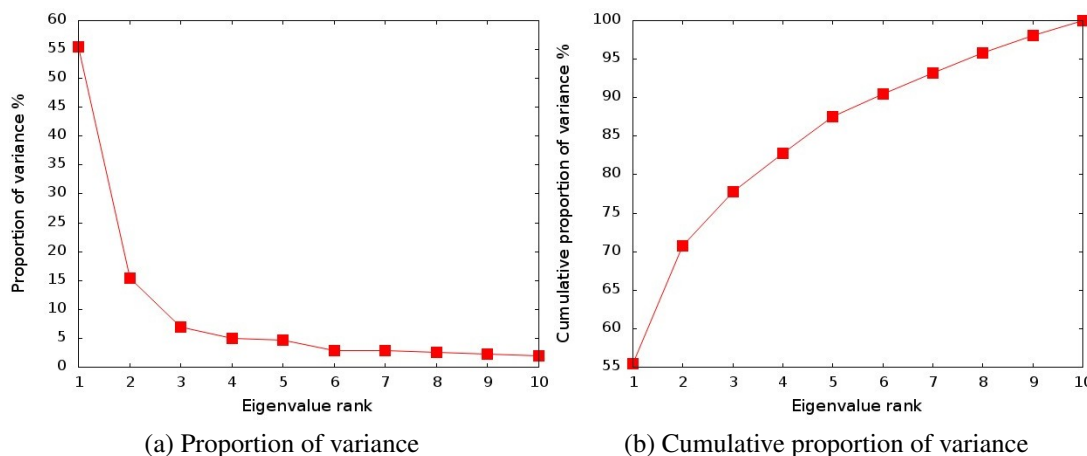


Figure 4.20: a) Proportion of variance b) Cumulative sum of total variance captured by the first 10 PCs for the combined clusters (From C1 to C9 for WT, DM1, and DM2).

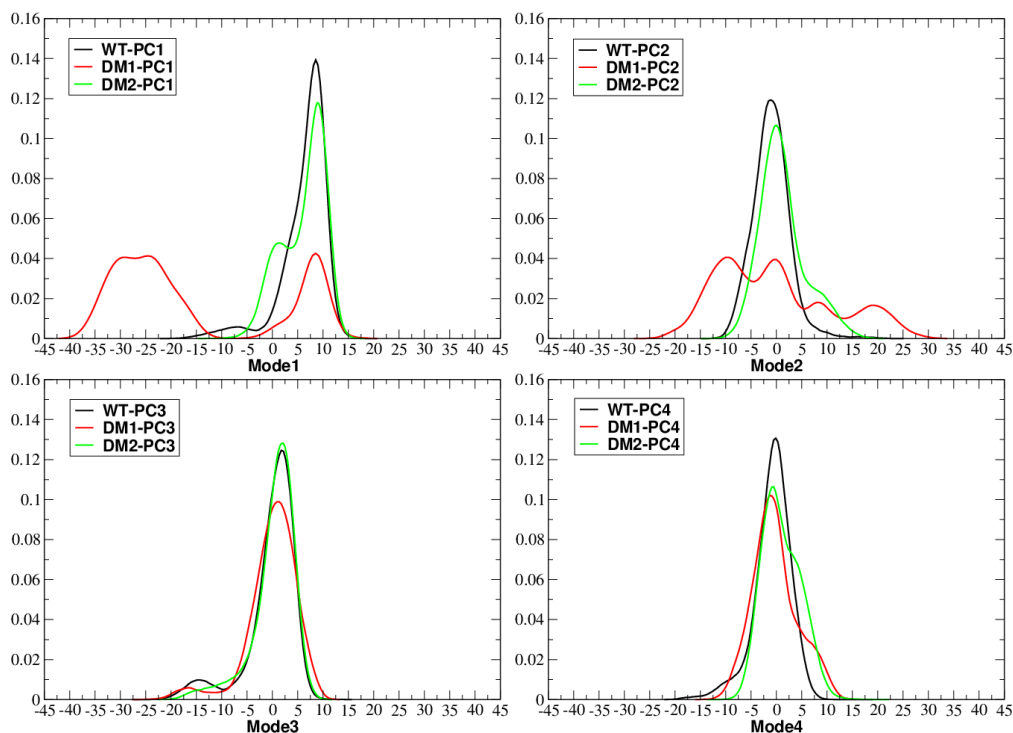


Figure 4.21: Top four PC projections (modes) for each system (WT, DM1, and DM2). (Zero (0) indicates the average structure.)

changes. Pertaining to DM2, the PCs in Figure 4.22 also depict considerable difference with respect to WT indicating that different types of motions and conformations were sampled.

Secondly, the three normal modes of deamidated systems were compared visually against WT system. Since the first three PCs generally cover the overall motion as verified earlier with PC plots, the first three PC motions (modes) were compared by using NMWiz[53] in VMD (1.9.3)[54] (Figure 4.23). The most prominent motion in the PCs of DM1 is the mobility of the

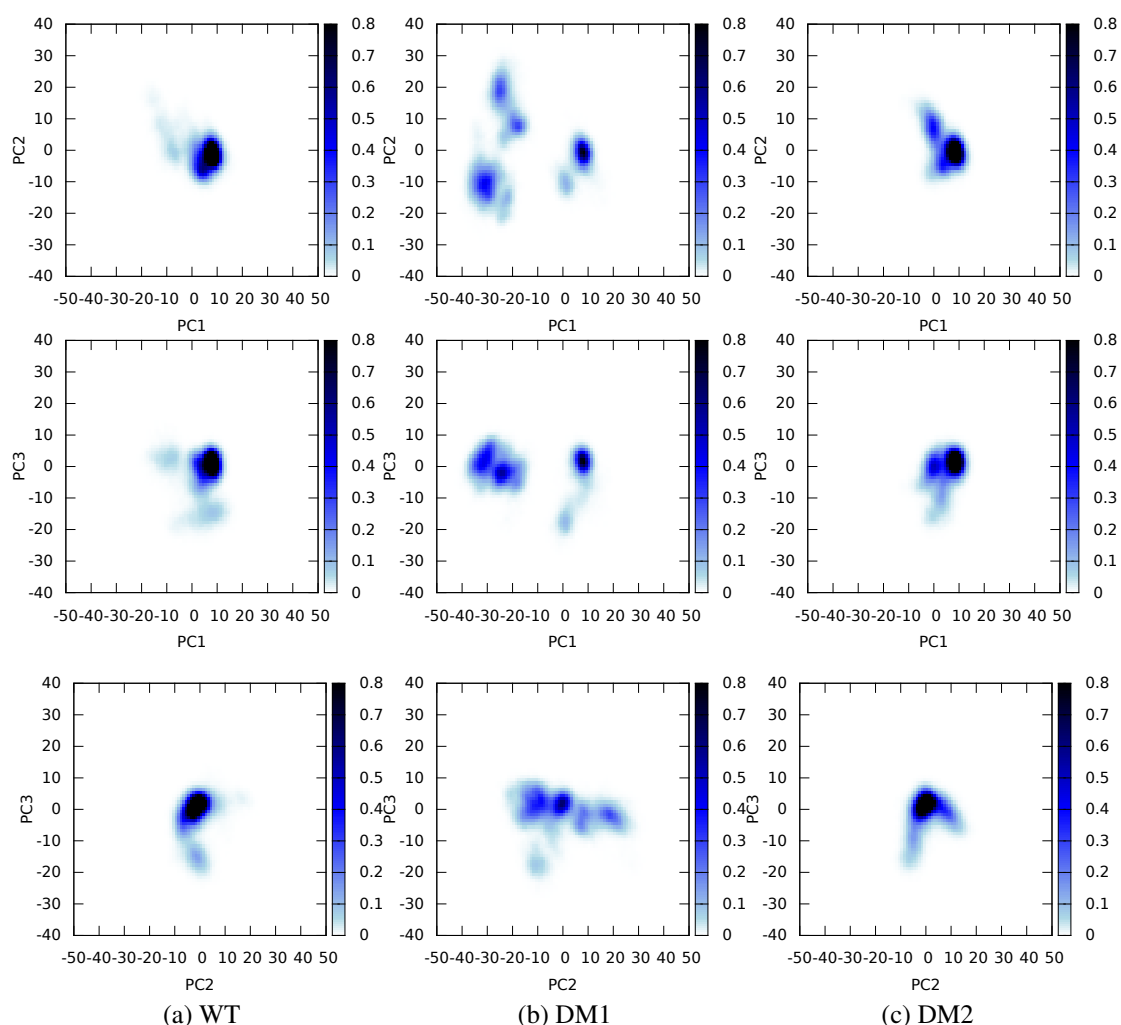


Figure 4.22: Projection of top three PC modes onto the combined MD runs (WT+DM1+DM2) shown in heatmaps.

$\alpha 2$ helix (Figure 4.23b). These results are also in line with the fluctuations of $\alpha 2$ in the per residue RMSD analysis of DM1 (Figure 4.6). Additionally, the proximal side of the junction 23 (J23) connecting $\alpha 2$ and $\alpha 3$ is highly mobile in DM1. In DM2 simulations, movement of J45 connecting $\alpha 4$ and $\alpha 5$ (junction of $\alpha 4$ - $\alpha 5$) was observed (Figure 4.23, Mode 3).

In general, DM1 displays remarkably higher fluctuations and scans different conformational spaces. DM2 simulations also behave different from the wild-type, implying change in structure and essential dynamics of the binding groove upon deamidation. In the deamidated systems, particularly DM1, the binding groove motions are significantly different from the rest, suggesting prominent impact of IDR deamidation on the distal BG. It should be noted that some motions in the binding groove (helices or junctions) seem partly similar for all systems (WT, DM1, and DM2), but overall motions of corresponding PCs do not overlap among different systems. The results suggest that PC motions are complex, regardless of the identity of the system.

Previously, in their computational study, Priya et al. reported that while Bcl-x_L without IDR

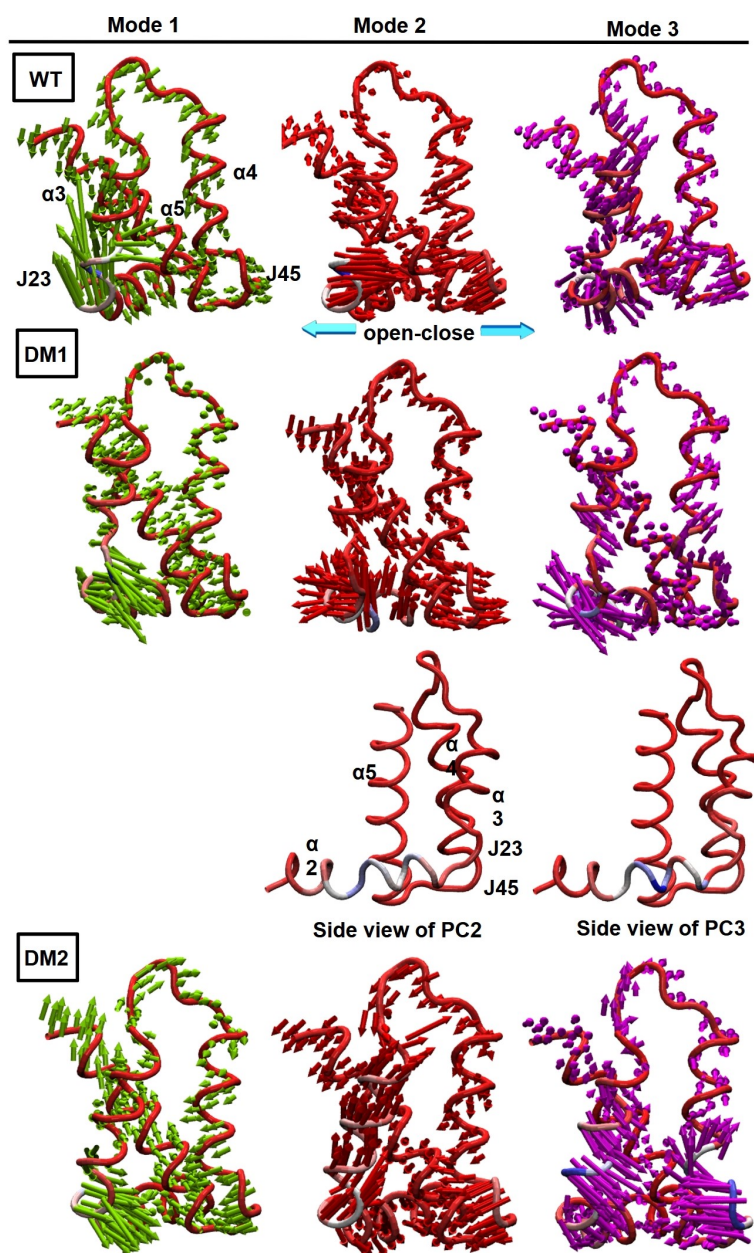


Figure 4.23: The first three PC modes for a) the BG of WT b) DM1 (front and side views) and c) DM2 simulations. (Blue color indicates higher residue mobility. Arrows display the direction and magnitude of the motion.)

displayed open-close motions (PDB: 1R2D_{X-Ray}, residues 2–29, 83–196), Bcl-x_L with IDR (PDB:1LX_{NMR}, residues 2-196) showed swinging motions, correlating with the longitudinal motions of $\alpha 2$ and $\alpha 3$ during 100 ns \times 2 MD simulations [131]. Contrary to Priya's results, we observed open-close motions in all systems that bear the IDR (Figure 4.23). This result emphasizes the importance of performing multiple and long simulations to observe the full spectrum of possible motions and more importantly, the necessity to use of the complete protein structure, which includes the IDR.

Taken together, PCA findings revealed that PC motions of DM1 and DM2 considerably differ from WT and suggest that deamidation impacts the structure and motion of Bcl-x_L, in particular, the dynamics surrounding the BG. This, in turn, may lead to loss of ability to bind BOP/pro-apoptotics, rendering Bcl-x_L unfit for its anti-apoptotic function. Particularly, DM1 deamidation in the IDR causes remarkable changes in the essential motions of the Bcl-x_L binding groove. Based on these outcomes, it could be concluded that deamidation of IDR allosterically influences the binding groove by changing the dynamics of the protein. This finding conforms with Follis's [105] suggestion that PTMs on the IDR may allosterically remodel the binding groove to trigger apoptosis. Furthermore, MD results also show the pivotal role of performing multiple simulation to understand the impact of deamidations and to explore the behavior of the studied systems more efficiently.

4.4 Conclusions

This study entails a significant contribution to the knowledge on structural consequences of deamidation on Bcl-x_L. The increase in negatively charged residues on the IDR, as a result of deamidation, was shown to change the essential dynamics of the binding groove of Bcl-x_L and hence, to alter its structural behavior and conceivably impair its function. One of the most important findings of this study is that the change in IDR motions upon deamidation may significantly affect accessibility of the binding groove. Indeed, the IDR allosterically influences the BG of the protein and induces conformational modifications that lead to changes in the interaction network. Our findings suggest that deamidation in the IDR changes both the number (%) and type of non-bonded interactions between the IDR and Bcl-x_L's core. The clustering analysis points out that the change in BG interactions occur mainly in subunits J23, α 3, α 4, and J45, and include five specific, previously non-existent or nearly non-existent, interactions, namely, R102-D133 and R102-E129, E129-Y101 and E129-R103, and R103-Q111. These allosterically induced interactions are shown to be responsible for the narrowing and covering of the groove upon deamidation. Moreover, PCA analysis along the first three principal components show remarkable differences in essential motions of the binding groove's of wild type and deamidated Bcl-x_L. The combination of clustering, H-bond and PCA analysis outcomes suggest that deamidation on the IDR not only impacts the structure by causing remarkable changes in the essential motions of the binding groove but alters its structural behavior, interaction patterns, and expectedly impairs its function. These findings will bring a unique perspective to the underlying mechanism of Bcl-x_L deamidation-induced cell death by bringing forward the structural knowledge necessary to develop anti-cancer therapeutics. Additionally, a concerted effort is required and underway to fully explore the structural changes that full-length Bcl-x_L (including both IDR and C-tail) undergoes upon PTMs and the consequences on its complex biological environment, including the dynamics of the mitochondrial outer membrane and its specific protein-protein interactions. This study is a first step in understanding the effect of deamidation on the structure and function of Bcl-x_L by using a non-truncated and unmodified model, also highlighting the importance of longer and multiple simulations.

Chapter 5

Impact of deamidation on structure and function of Bcl-x_L in membrane

5.1 Introduction

The Bcl-2 family proteins mainly play an important role on the mitochondrial pathway of apoptosis by regulating mitochondrial outer membrane permeabilization (MOMP) and subsequent apoptosis as discussed in the previous chapter [5, 6, 7, 8]. MOMP as usually considered as the ‘point of no return’ causes the release of pro-apoptogenic factors (cytochrome c and apoptosis inducing factors (AIF) etc.) from intermembrane space (IMS) into the cytosol to promote caspase activation and apoptosis [7, 8, 20, 142]. The exact mechanism of action of Bcl-2 family is still not well-defined/understood. However, direct activation,[143] displacement,[144] embedded together,[145] and unified [146] models [147, 148, 149] are the mainly proposed models to give insight into this process.

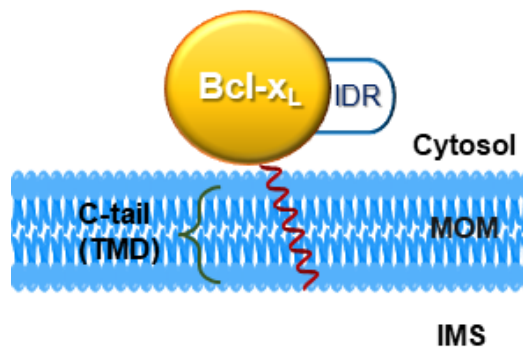


Figure 5.1: Schematic representation of membrane-anchored Bcl-x_L

Briefly, BH3-only proteins (BOPs) are divided into two groups, namely activator and sensitizer in the direct activation model. Anti-apoptotic proteins (Bcl-x_L, Bcl-2, etc.) inhibit the activator BOPs, such as BIM and BID but not pro-apoptotic proteins (Bax and Bak) to suppress apoptosis. Sensitizer BH3-only proteins (BAD, NOXA, etc.) replace the activator BOPs from the anti-apoptotic proteins to promote apoptosis. Note that Bax and Bak are activated by activator BOPs. The displacement model, also known as the de-repression model, proposes that

pro-apoptotic Bax and Bak are active in cells and must be sequestered by anti-apoptotic proteins for cell survival. BOPs only play the sensitizer role and inhibit their respective anti-apoptotic proteins to promote apoptosis. Note that direct activation and the displacement models do not account for a role for the membrane. Embedded together model proposes an active role for the membrane and joins the key aspects of the direct activation and the displacement models. Bcl-2 family proteins are inserted into membrane and change their conformations that dictate their functions. Cytoplasmic anti-apoptotic proteins are recruited to membranes upon apoptotic stimuli. At the membrane, anti-apoptotic proteins inhibit the activator BOPs and pro-apoptotic proteins to prevent MOMP. Sensitizer BOPs displace the activator BOPs and pro-apoptotics from anti-apoptotic proteins to stimulate/initiate apoptosis. Activator BOPs recruit Bax to the membrane to induce MOMP and apoptosis. These interactions are reversible and are governed by equilibrium constants that are altered by the concentrations and interactions of the proteins with each other and with membranes. Lastly, unified model develops the embedded together model by offering that the anti-apoptotic proteins sequester the activator BOPs (mode 1) and sequester pro-apoptotic Bax and Bak (mode 2). However, the unified model postulates that inhibition of apoptosis through mode 1 is less efficient and therefore easier to overcome by sensitizer BOPs. In addition, the unified model extends the role of Bcl-2 family proteins and the regulation of MOMP to mitochondria dynamics. In this chapter, we accounted for the role of the membrane.

As mentioned in the previous section, Bcl-x_L, consisting of 233 amino acids, is an α -helical transmembrane protein and possesses four Bcl-2 homology (BH1-4) regions and eight helices with a C-tail (residues 210–233) composed of an α helix (α 9). The C-tail, known as a transmembrane domain (TMD) provides anchoring of Bcl-x_L to the mitochondrial outer membrane (MOM) (Figure 5.1) [13, 14, 17, 18]. It is important to stress that Bcl-x_L with the C-tail (i.e., full-length Bcl-x_L) is not experimentally resolved due to the experimental limitations (solubilization, low yields, production of the protein in a natively folded form etc.) [18, 19]. Recently, the C-tail alone was experimentally resolved inside phospholipid nanodiscs (PDB ID: 6F46_{NMR}[19] and 6X7I_{NMR}). Additionally, Bcl-x_L includes a long intrinsically disordered region (IDR), the so-called flexible loop between α 1- α 2. The IDR was omitted in most of the previous studies, yet recent studies exhibited the importance of the IDR since post-translational modifications (PTMs), which can affect functions, stability and localization of the proteins in response to various apoptotic stimuli occur in this region [20, 21, 22, 23, 24, 25].

Bcl-x_L is mostly found on mitochondrial outer membrane (MOM) and is in a dynamic equilibrium between cytosol and membrane in healthy cells [150, 151, 152, 153, 154]. Upon apoptotic induction, such as DNA damage and oxidative stress, Bcl-x_L translocated to the MOM and localized/anchored to the MOM by its C-tail (Figure 5.1) [151, 155].

In the previous studies the use of truncated Bcl-x_L or Bcl-x_L in the presence of detergents provided initial but limited insights on the structure and consequent impact on the function of the protein. In 2013, Todt et al experimentally reported that Bcl-x_L retro-translocated BAX from the MOM to cytoplasm and substitution or removal of the C-tail of Bcl-x_L decreases BAX retro-translocation, by increasing mitochondrial BAX level and cell death [151]. In 2013, Maity et al. investigated dynamics of Bcl-x_L (Δ 45-84 in the IDR) and Bcl-x_L-BH3 complex (PDB ID: 1BXL_{NMR}, Δ 45-84) in water and membrane by means of MD simulations (1.6 μ s in total) [102]. Simulation results showed that the conformational dynamics between water and membrane are considerably different, indicating the conformational transitions in membrane

environment. Noted that they fully inserted Bcl-x_L inside the membrane instead of anchoring from the C-tail and the loop is missing. In water the C-tail (residues 197-217) was docked to the BG before MD as well. In 2015, Yao et al. reported structural information for Bcl-x_L (Δ 45-84) in water and membrane including a complete C-tail using NMR and ITC [107]. They observed that the C-tail behaved as a pseudo-inhibitor in water system and provided integration on membrane/lipid nanodiscs. The C-tail formed a transmembrane α -helix inside the membrane by adopting an approximately 25° tilt. They also developed methods to isolate and characterize the membrane-embedded C tail to prepare protein suitable for structural and biochemical studies.[17] In 2016, Maity et al. comparatively modelled the C-tail of Bcl-x_L with respect to the known C tail of Bax (PDB ID: 1F16 [156]) using Modeller [157]. They presented the insertion modes (from association to insertion) of the C-tail into the DOPC bilayer (80 lipid per layer) using PMF calculations [158]. Calculations showed that electrostatic interactions, especially R232 and K233 drive the membrane insertion and the C-tail adopts a tilt angle of approximately 30°. More recently, the same group showed the significance of the charged and polar residues at the terminal ends of C-tail by performing Adaptive Biasing Force based MD simulations (for a total of 2.67 μ s) [159]. While double mutated C-terminal residues (R232A and K233A) destabilized the membrane-associated states and the membrane-embedded states, N terminal (N211A and R212A) only reduced the stability of the fully inserted state. In 2018, Follis et al. experimentally demonstrated that PTMs in the IDR (phosphorylation on S62 or deamidation of N52 and N66) cause a structural rearrangement in the distal BG that reduce the anti-apoptotic activity of Bcl-x_L [105]. Additionally they experimentally demonstrated that in membrane environment the IDR did not change the global conformation of the core region and the C-tail anchoring behavior. In 2018 Raltchev et al. described an experimental method to generate natively folded membrane-anchored proteins using SortaseA-based ligation approach and resolved the C-tail structure of Bcl-x_L using NMR (PDB ID: 6F46) [19]. They suggested that the BG of Bcl-x_L loosely interacted with the membrane. Intriguingly, Vasquez-Montes et al. hypothesized a membrane-inserted non-canonical mode of Bcl-x_L, and experimentally characterized membrane-inserted conformations of Bcl-x_L by modulating lipid composition [160, 161]. They reported that the α 6 helix was inserted into the membrane leading to the disruption of Bcl-x_L packing and the release of BH4 domain (α 1), and that the presence of the C-tail is not required. They showed conformational switching between the anchored (canonical) and the inserted conformations of Bcl-x_L (non-canonical). Recently, Ryzhov et al presented the preparation and conformations of Bcl-x_L both in water and membrane with combination of experimental and computational studies (1 μ s \times 5 NPT MD simulations per environment) [162]. In water system, they used modified Bcl-x_L by removing Bax peptide from the complex (PDB ID: 1BXL_{NMR}) and adding a loop from 1LXL_{NMR} and the C-tail from 6X7I_{NMR}. Their membrane systems include 156 DMPC, 39 DMPG and Bcl-x_L was formed using 1LXL_{NMR} and 6X7I_{NMR}. They investigated full-length Bcl-x_L both in water and membrane, yet they did not offer any insight into deamidation-induced conformational changes in Bcl-x_L. For these reasons, the contribution and impact of deamidation on Bcl-x_L function in membrane is still open for further investigation. In the current study, we will explore impact of membrane (protein-membrane interactions (PMI)) and to give deeper insight into the loss of Bcl-x_L function upon deamidation.

From structural point of view, since most of previous studies lack the membrane environment and the IDR or use Bcl-x_L in the presence of detergents, the conformational changes

between water and the membrane inserted state are poorly understood. However, while the detergents solubilize the C-tail, they also usually destabilize the soluble domain and change the interaction pattern. It may even lead to the distortion of the protein structure and function [149]. Thus, the C-tail was eliminated in the previous studies. Moreover, structural information about Bcl-x_L prior and subsequent to deamidation are limited. Recent studies give insight into the structure of the membrane-inserted conformation of Bcl-x_L but little is still known about the molecular details nor any deamidation impacts [105, 107, 160, 161]. Therefore, these findings provide only a glimpse to understand the structural reasons of the loss of Bcl-x_L function and interaction with membrane. In this context, the consideration of the membrane role is crucial to provide a broader perspective on conformational changes of full-length Bcl-x_L in the membrane environment and to elaborate on the localization of the protein in the membrane. More importantly, deamidated Bcl-x_L (Asp and iso-Asp deamidated versions) has not been elucidated both in water and membrane environments. Membrane insertion could also contribute to an allosteric change in the BG of the protein by promoting conformational and functional changes in combination with deamidation. Hence, a concerted effort is required to explore the structural changes in full-length Bcl-x_L upon deamidation and its consequences on the complex biological environment, focusing on the dynamics and possible collective effects of the protein head, the C-tail and protein-membrane interactions (PMIs). Therefore, the ultimate goal of this study is to fully understand deamidation-induced conformational changes both in water and in membrane in order to scrutinize conceivable reasons of loss of its function (Figure 5.2). The impact of Bcl-x_L deamidation in water and in membrane is explored by monitoring the structural changes, particularly the BG during microsecond long MD studies. This study attempts to elucidate for the first time, deamidation of Bcl-x_L in membrane environment to evaluate potential changes in the protein structure and dynamics and consequently understand its loss of function.

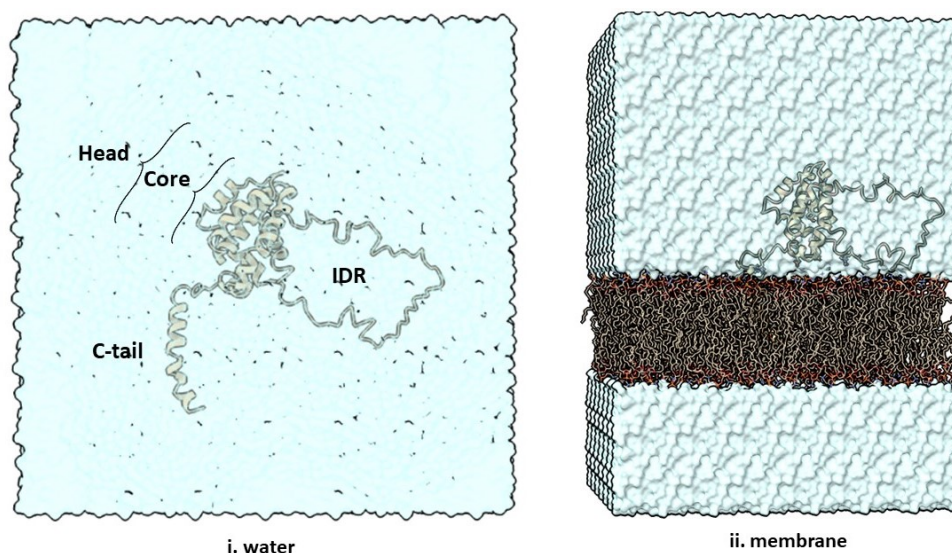


Figure 5.2: Schematic representation of this study: Bcl-x_L and deamidated Bcl-x_L *i.* in water, and *ii.* in membrane. (Protein head refers to the core and the IDR excluding the C-tail. The water surface is generated using the ChimeraX[38] surface presentation.)

5.2 Methodology

5.2.1 Preparation of the C-tail and REMD simulation details

The initial structure of the C-tail (24 residues, F210-K233 residues) including acetyl (ACE) group cap was modelled by tleap implemented in the Amber18 program package[133]. Generalized Born model (GB-Neck2) was performed in combination with mbondi3 intrinsic radii, and ff14SBonlysc. An alpha helix shape was given by cpptraj[136] using the `make structure` command afterwards. The C-tail system was minimized and equilibrated without restraints in three steps as follows: 1) the system was gradually heated from 10K to 300K using Andersen thermostat[47] with random velocity update every 10 steps for 12 ns. 2) The microcanonical (NVE) ensemble was applied at 300 K for 0.1 ns. 3) Langevin temperature coupling[37] with a gamma of 1.0 ps^{-1} was applied at 300 K for 1 μs . The SHAKE algorithm was carried out in order to constrain bonds involving hydrogen bonds. Time step for the third step of the equilibration and Replica-Exchange Molecular Dynamics (REMD) were carried out for 4 fs, using hydrogen mass repartitioning (HMR),[49] to accelerate REMD simulations. REMD[50] technique, which enhances the conformational sampling of proteins was used to sample representative C-tails. Eight replicas with temperature range between 270-468.7 K were used for REMD simulations with an acceptance ratio of ≈ 0.2 [163]. 20 μs long REMD simulations were performed for each replica. The Langevin thermostat[37] with a gamma of 1.0 ps^{-1} was employed, and exchange attempts were tried every 5 fs.

5.2.2 Simulation details in water systems

The initial structure of Bcl-x_L (ΔC) “1LXL_{NMR}” was extracted from the Protein Data Bank (Homo sapiens); extra residues were removed from the PDB file. Bcl-x_L and the C-tail candidates were joined using Chimera (version 1.14) to obtain full-length Bcl-x_L [138]. Deamidated structures (DM1 and DM2) were built by replacing Asn to Asp and iso-Asp, respectively. MD simulations were performed using the Amberff14SB82 force field implemented in the Amber18 program package[133]. Cubic boxes were built using the TIP3P [135] explicit water model and the boxes were designed large enough to accommodate extended forms for all systems. Counter sodium or chloride ions were added to neutralize each system. The Particle Mesh Ewald (PME) method with a default 8 Å cutoff distance was employed to account for long-range electrostatic interactions [44, 45]. All systems (FL, DM1 and DM2) in Table 5.1 were minimized using the NVT ensemble with the Andersen temperature coupling [47] with randomly updated velocities every 10 steps after a short steepest descent minimization using harmonic restraints on all heavy atoms. A five-step equilibration protocol was performed using the NPT ensemble with a Monte Carlo barostat as follows: 1) all heavy atoms are restrained with a harmonic potential of $50 \text{ kcal mol}^{-1} \text{ \AA}^{-2}$ for 0.1 ns at 10 K. 2) only the oxygen atoms of the water molecules are restrained using the same restraining potential for 0.1 ns at 10 K. 3) the harmonic potential is decreased to $5 \text{ kcal mol}^{-1} \text{ \AA}^{-2}$ while repeating the 2nd step. 4) the entire system is equilibrated without restraints for 0.1 ns at 10 K. 5) the system is gradually heated to 300 K for 2 ns using the Berendsen thermostat [46] with a coupling time of 1.0 ps. For the equilibration steps 1 to 4, velocities were randomly updated every 10 steps under the Andersen thermostat. Sampling simulations were performed at 300K and NVT ensemble with Langevin temperature coupling

[37] with a gamma of 1.0 ps^{-1} . The time step for sampling runs was 4 fs via hydrogen mass repartitioning (HMR) [49].

5.2.3 Generation of membrane-associated Bcl-x_L and simulation details

1-Palmitoyl-2-oleoylphosphatidylcholine (POPC) is the most abundant lipid in MOM and is used as a representative model for MOM [164, 165, 166, 167]. Therefore, in the study POPC lipid was used to mimic the MOM. All protein associated membrane systems were generated by CHARMM-GUI Membrane Builder [168, 169] and each layer included 240 POPC lipids. Prepared systems (Bcl-x_L and deamidated Bcl-x_L) were oriented with respect to the membrane (if needed) to avoid the IDR insertion into the membrane. A 50 Å water thickness was added on both top and bottom of each system. 0.15 M KCl was added into the system in order to mimic physiological conditions. In all simulations Amberff14SB [134] and Lipid14 [170] force fields were used for protein and membrane, respectively. Moreover, the TIP3P [135] explicit water model was used. A minimization followed by a six-step equilibration protocol was conducted/applied for all initial systems. The minimization and the first five steps in the equilibrium runs were repeated using the same protocols as in the water system simulations. A sixth stage was added and consisted in letting the systems equilibrate without restraints for 4 ns at 300 K using the Berendsen thermostat86 with a coupling time of 1.0 ps. The area per lipid (APL) was calculated in order to check membrane equilibration and its compliance with known experimental APL (Figure A.11). Finally, microsecond long MD simulations with Langevin thermostat with a gamma of 1.0 ps^{-1} were performed for each system at 300K (above phase transition temperature of POPC). Additionally, the cpptraj [136] module of Amber18 was used for the analyses of the MD trajectories.

5.3 Results and Discussion

Limited structural information about full-length Bcl-x_L (FL) is available and the impact of the deamidation in the membrane associated Bcl-x_L is not well understood. Relations/interactions between the IDR, the C-tail, and the membrane need to be unraveled to understand their roles on the structure and function of Bcl-x_L. In this context, full-length Bcl-x_L was explored in water and membrane prior to and after deamidation by considering both Asp and iso-Asp mutations (DM1 and DM2, respectively). The studied systems were tabulated in Table 5.1. We primarily focused on the conformational and dynamic changes in the binding groove upon deamidation in the IDR, as well as their environmental impacts. The findings are discussed under water and membrane environments. Mainly, the stability of each system, hydrogen bond interactions and principal component analysis are investigated to identify/detect conformational differences during simulations.

5.3.1 Evaluation of the C-terminal tail

Subsequent to 20 μs long REMD simulation between 270 K and 468.7 K, the frames at 293.6K were extracted from REMD trajectories. Energy of each frame in Table 5.2 was calculated by esander in the cpptraj [136] module of Amber18. Secondary structure analysis was performed

Table 5.1: Summary of the initial system setup.

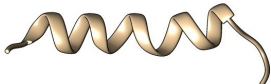
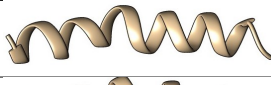
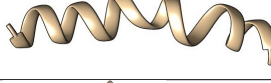

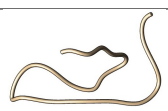
Water system	Water	Na+	Total atoms	Simulation box (\AA^3)	Simulation time
Bcl-x _L (FL-wat)	71146	11	217032	130.383 × 130.383 × 130.383	1 μ s × 4, 2 μ s × 1
DM1-Bcl-x _L (DM1-wat)	71144	13	217024	130.383 × 130.383 × 130.383	1 μ s × 2, 2 μ s × 3
DM2-Bcl-x _L (DM2-wat)	71144	13	217024	130.383 × 130.383 × 130.383	1 μ s × 2, 2 μ s × 3
Membrane system	Water	K+/Cl-	Total atoms	Simulation box (\AA^3)	Simulation time
FL-memb					
FL-C1-memb	84338	245/234	321396	129.445 × 129.439 × 207.818	1.5 μ s
FL-C2-memb	72640	209/198	286230	129.445 × 129.349 × 184.544	1.5 μ s
FL-C3-memb	73052	211/200	287470	129.445 × 129.349 × 185.787	1 μ s
DM1-memb					
DM1-C1-memb	84414	246/233	321620	129.445 × 129.439 × 207.818	1 μ s
DM1-C2-memb	72585	212/199	286065	129.445 × 129.349 × 184.544	1 μ s
DM1-C3-memb	72998	213/200	287306	129.445 × 129.349 × 185.787	1 μ s
DM2-memb					
DM2-C1-memb	84414	246/233	321620	129.445 × 129.439 × 207.818	1 μ s
DM2-C2-memb	72585	212/199	286065	129.445 × 129.349 × 184.544	1 μ s
DM2-C3-memb	72998	213/200	287306	129.445 × 129.349 × 185.787	1 μ s
Water thickness in membrane systems is 50 \AA .					
Wat and memb refer to water and membrane systems, respectively.					

using the Definition of Secondary Structure Prediction (DSSP) algorithm,[137] and successive helix residues were identified. In the scope of this study, the C-tail candidates were selected in the aspect of minimum energy, secondary structure, and helix content criteria to better represent the C-tail behavior in full-length systems (Table 5.2). The tail candidates were evaluated under three groups, namely helix (three helical tails), min energy structure (hairpin) and random coil with min. energy. In the first group, the C-tail having the helix (criteria $h > 16$) with minimum energy was selected as the first candidate. Two candidates were available for maximum helix content ($h = 22$) and were selected as second and third candidates. Then, the C-tail with minimum energy was used as a 4th candidate. Lastly, minimum energy random coil was used 5th candidate in the study. For the sake of completeness, we continued with five tails. Additionally, some recent studies showed that the C-tail formed a transmembrane α -helix inside the lipid membrane with various helix content/long (h_{18} to h_{22}) [19, 107]. Thus, helical models were used in membrane systems.

5.3.2 Stability of Bcl-x_L systems prior to and subsequent to deamidation

Prior to comprehensive investigation of all systems (FL, DM1, DM2) in water and membrane, stability of each system was initially analyzed using the backbone root mean-square deviation (RMSD) analysis with respect to the initial/built structure. The core helices (< 3.0) are stable during the simulations (Figure 5.3). The IDR is highly flexible in all systems (Figure A.12). Figure 5.4 depicts that the C-tails inside the membrane considerably lower RMSD values than the C-tail in water and are not flexible as expected due to the surrounding lipids. Additionally,

Table 5.2: Representative C-tail candidates used in the study.

C-tail candidates	Tail structure	Criteria	Energies of C-tail (kcal/mol)	Full-Length ID
C1 (h17)		min. energy successive helix 16	-496.8658	FL-C1
C2 (h22-m1)		max successive helix	-484.9407	FL-C2
C3 (h22-m2)		max successive helix	-464.8594	FL-C3
C4 (min)		min. energy	-559.3848	FL-C4
C5 (coil)		min energy random coil	-487.6524	FL-C5

the stability of the helical contents and structural behavior of the studied systems were also evaluated using the Definition of Secondary Structure Prediction analysis [137] (Figure A.13). In general, $\alpha 1$ - $\alpha 8$ were preserved their helical structures. Partial unfolding in the helical tails were observed in all water systems, especially deamidated systems. In membrane, helical tails preserved during the simulations. Furthermore, helical tendency was seen in the IDR in line with previous studies [19, 171].

5.3.3 Bcl-x_L and deamidated Bcl-x_L in water

Structural behaviors of Bcl-x_L bearing the C-tail (FL) in water were evaluated before and after deamidation to identify the changes during simulations and to understand the structural consequences. Moreover, water system was considered as a reference to assess the outcomes of membrane systems. Structurally, the C-tails did not preserve their initial extended forms, which do not make contact with the protein head before the simulations. The C-tails approached the protein head during the simulations. Additionally, the C-tails are highly dynamic in water and the flexible junction connecting $\alpha 8$ and $\alpha 9$ (J89) contributes the C-tail to move according to various orientations. Notably, as depicted in Figure 5.5 the C-tails of deamidated models aligned/positioned towards different region of the protein core/head. This observation pertains to almost all C-tails (except the systems bearing C2 tail). The C-tails in native form positioned differently with respect to deamidated ones (for all snapshots see: Figure A.14).

H-bond interactions were examined during the simulations in order to detect persistent (long-lived) and transient (short-lived) but consistently re-occurring interactions. Temporary (short-lived) interactions among the C-tail-protein head (C-tail-loop and C-tail-BG (mostly $\alpha 2$ and J23)), and tail-junction of $\alpha 8$ and $\alpha 9$ (J89) were observed during the simulations. In general, the terminal residues, that is, N211, R212, W213, R232 and K233 residues in the C-tail drive the H-bond interactions with the protein head.

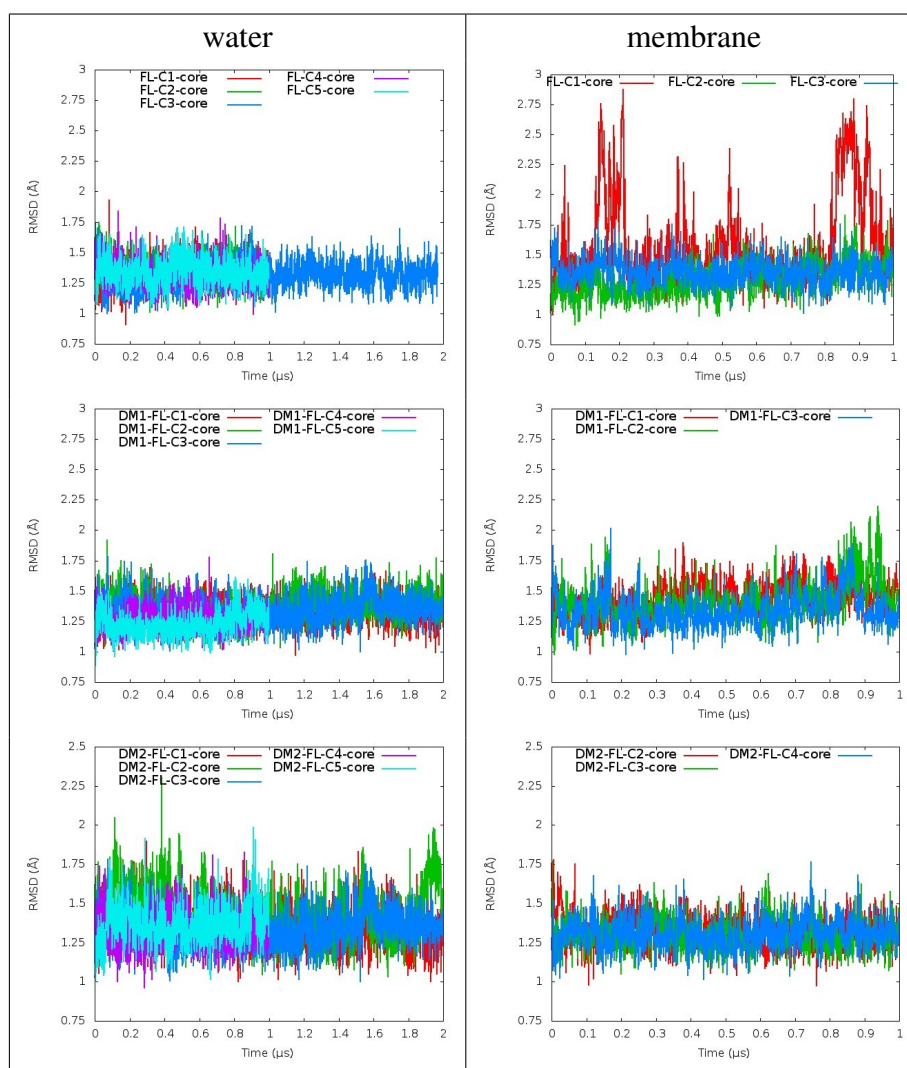


Figure 5.3: Backbone RMSD plots for core helices of FL, DM1 and DM2-Bcl-x_L simulations with respect to initial/built structures. (Every 20 frames)

Yao et al mentioned that the C-tail interactions with G94 in $\alpha 2$, G138 in $\alpha 5$ and G196 in J78 in the BG indicate close conformation of the BG with the C-tail [107]. When we checked these interactions for all water systems, we observed transient interactions (short-lived) with the C-tail residues and the BG residues (G138 in $\alpha 5$ and/or G196 in J78). We also examine the adjacent residues of G94, G138 and G196 to check possibility to shift the interactions. In the adjacent residues we detected persistent and/or transient (short-lived) interactions with the C-tail, but the C-tails did not fully cover the BG (Figure 5.6). Instead, the C-tail interacts with outer side residues in the BG or approaches to the bottom side of the BG. Additionally, in DM1 simulations, the C-tail mostly interacts more with the loop than with the BG. We suggest that these interactions could be an indicator of a C-tail approach to the BG (not only on the inner side but also on outer residues of the BG). This may cause/trigger the pseudo-inhibitor activity in water by inhibiting/preventing the binding affinity of pro-apoptotics and BOPs.

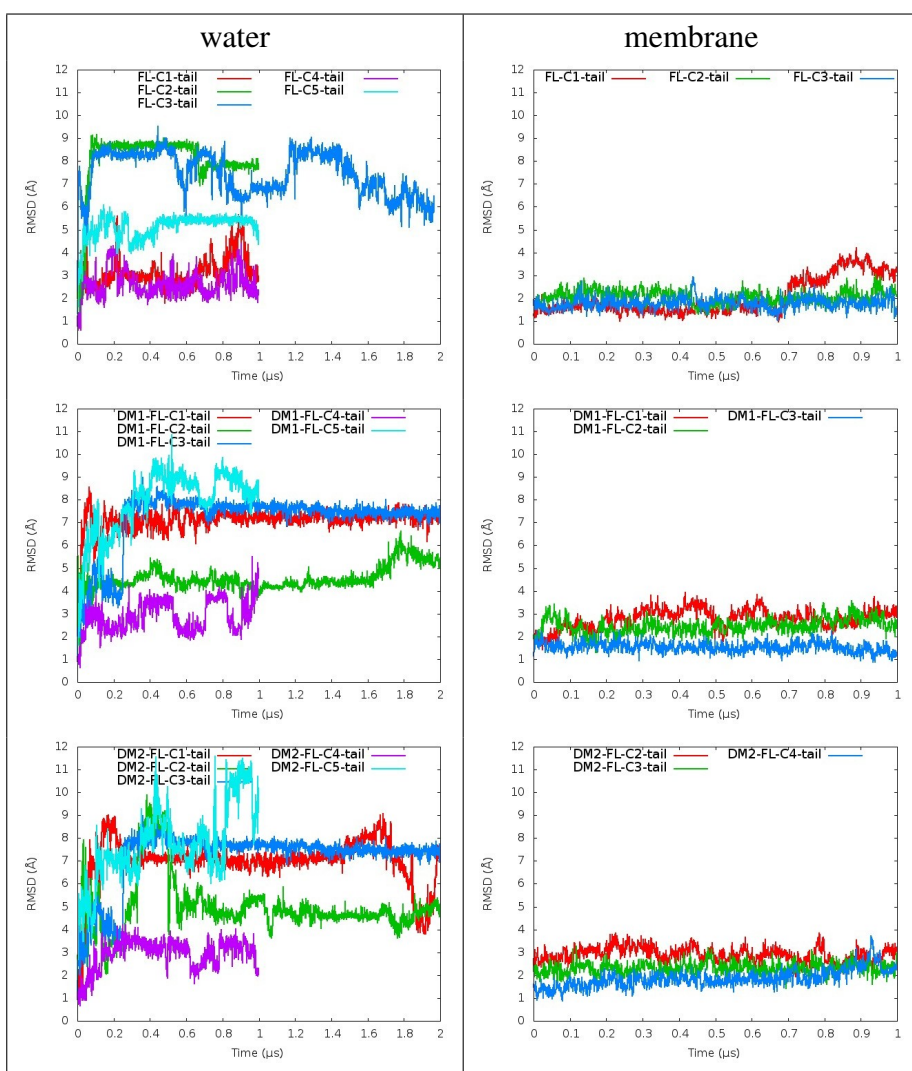


Figure 5.4: Backbone RMSD plots for the C-tails of FL, DM1 and DM2-Bcl-x_L simulations with respect to initial/built structures (Every 20 frame).

Intrinsically disordered region (IDR, loop)

The loop behavior was also investigated throughout the simulations. The initial extended structure of the loop was not preserved during the simulations. In water systems, the loop transiently interacts with the protein core (protein excluding the loop and the C-tail) and the C-tail. In general, the loop approaches $\alpha 1$, $\alpha 2$, $\alpha 6$, $\alpha 7$, and J89. H-bond interactions between protein (Δ IDR)-IDR in Figures 5.7 and 5.8 showed the transient interaction between the IDR and protein and depicted that deamidation altered the interaction pattern between protein and the IDR and conformational behavior of the IDR. Remarkably, the C-tail of Bcl-x_L was less interacted with the IDR compared to the deamidated ones (Figure 5.8). Deamidated IDR transiently interact with the C-tail. In deamidated systems, the increase in negative charge residues in the IDR could facilitate the C-tail-loop interaction and mediate the position of the C-tail (residues

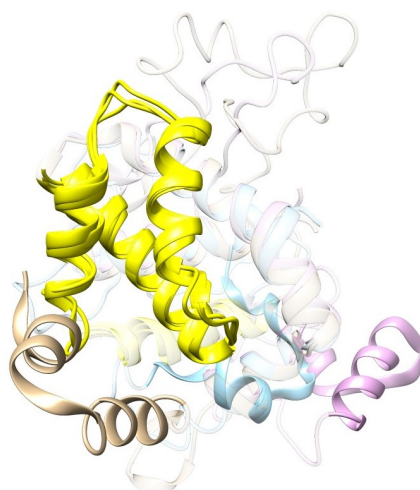


Figure 5.5: Representative positions of the C-tails among Bcl-x_L and deamidated Bcl-x_L in water. (Yellow color presents the binding groove. Tan, blue, and pink colors denote the C-tails of FL-C3, DM1-C3, and DM2-C3, respectively. Water was not shown for clarity.

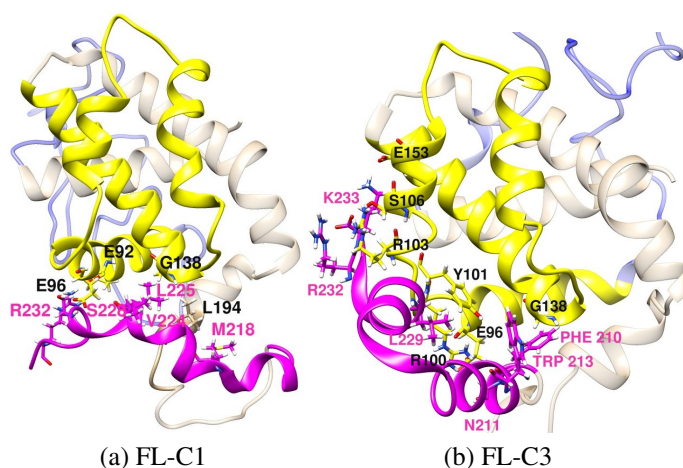


Figure 5.6: Representative orientations of the BG and the C-tail residues in water. (Blue color denotes loop region (IDR). Magenta and yellow colors present the C-tail and the BG, respectively.)

210-233). These observations suggest that the differences in the C-tail and the loop movements can affect membrane localization behavior/affinity and can alter the accessibility of the BG for pro-apoptotic proteins or BOPs.

Additionally, in the FL simulation, N52 and N66 did not interact with the C-tail residues, both D52 and D66 in DM1 and only iso-D66 in DM2 interact with the C-tail (Figure 5.8). R232 and R209 transiently interacted with D52 and D66 in DM1. In DM2 simulations, isoD66-R232 and isoD66-K233 transient interactions were detected. This could indicate that deamidation may invoke the loop-C-tail interactions.

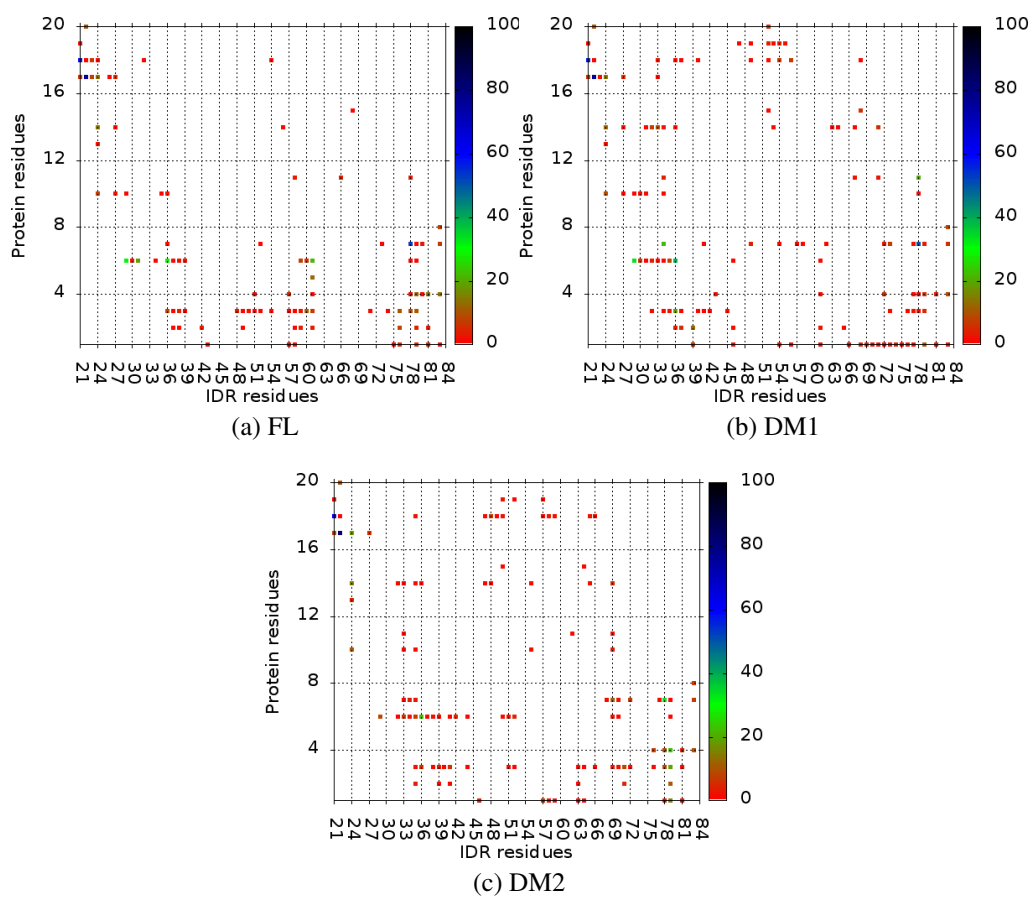


Figure 5.7: H-bond interactions plots for $\alpha 1$ residues of the protein-IDR residues of FL, DM1, and DM2 simulations. The color bar shows overall contact percentage during the simulations.

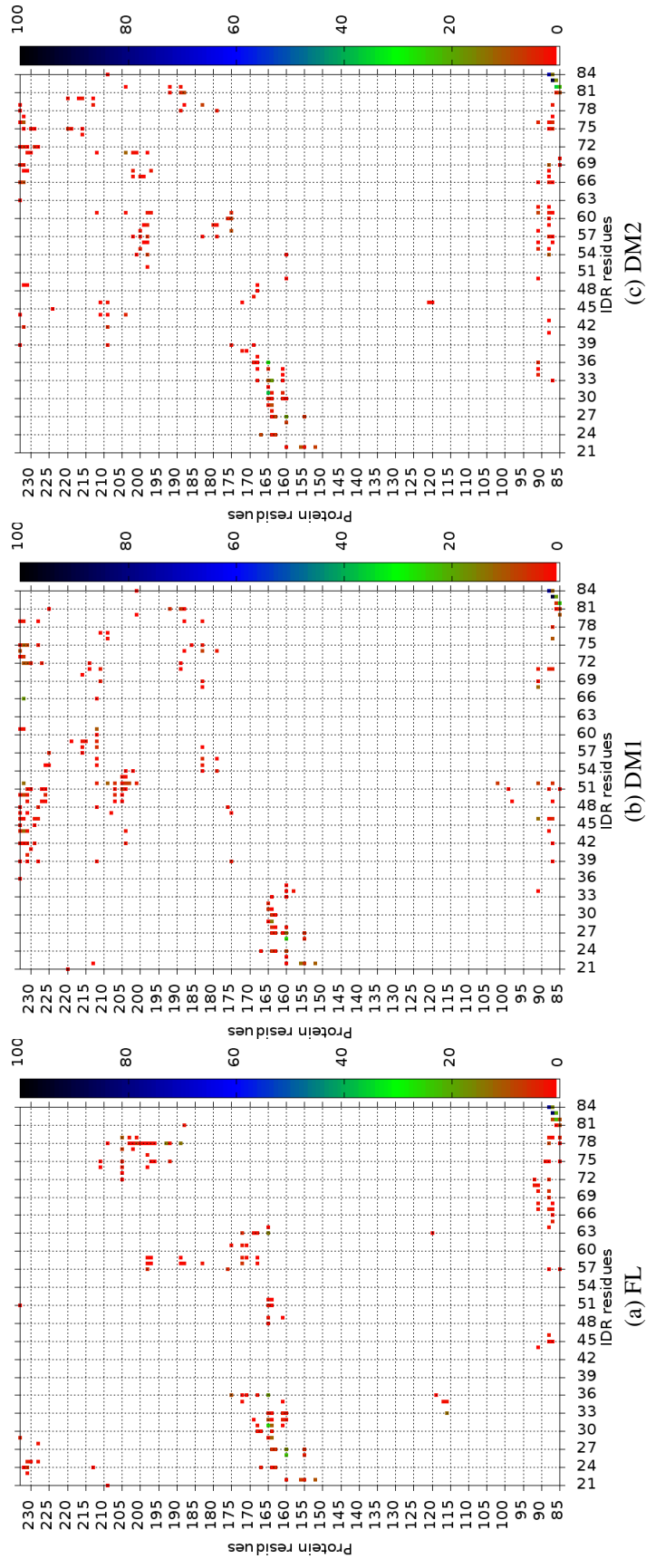


Figure 5.8: H-bond interactions plots for the protein ($\alpha 2$ -C-terminal residues)-IDR residues of FL, DM1, and DM2 simulations. The color bar shows overall contact percentage during the simulations.

Notably, transient D52-R102 interaction in the DM1 simulation urged us to re-visit the experimental work of Follis et al [105]. They displayed that negatively charged residues (D61, E62, D52 and D66) interacted with positively charged arginines (R100, R102, R103; known as Arg cluster.) in junction 23 connecting $\alpha 2$ and $\alpha 3$ (J23). In order to follow this interaction, radial distribution functions (RDF) were computed between side chain oxygen atoms of residues 52 and 66 and the hydrogen atoms of the guanidinium moieties in the Arg cluster (Figure 5.9) both in water and membrane systems. This interaction was only detected in DM1-C3 in water in the range of 1.0-3.0 Å. Through the distance analysis the frequency/stability of this interaction was also followed (Figure 5.10) and approximately after 1.5 μ s transient but consistently re-occurring R102-D52 interaction was inspected on DM1-C3.

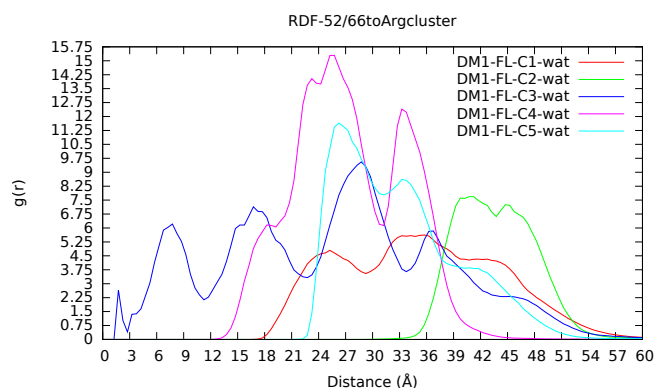


Figure 5.9: Radial distribution function, $g(r)$, vs the distance between side chain oxygen atoms of residues 52 and 66 and H atoms of the guanidinium moieties in Arg cluster in DM1-wat simulations.

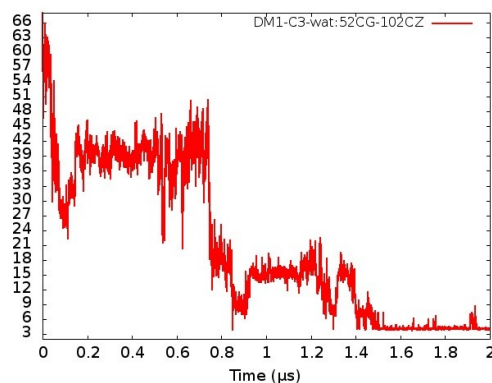


Figure 5.10: Distance plot between Asn52@CG and CZ atoms of guanidinium moieties of R102 in the simulation of DM1-C3) in water. (Every 15 frames)

Deamidation Impact on the Binding Groove (BG)

Deamidation impact on the BG were examined more closely through the H-bond analysis in order to detect key H-bond interactions before and after deamidation. Remarkably, R103-

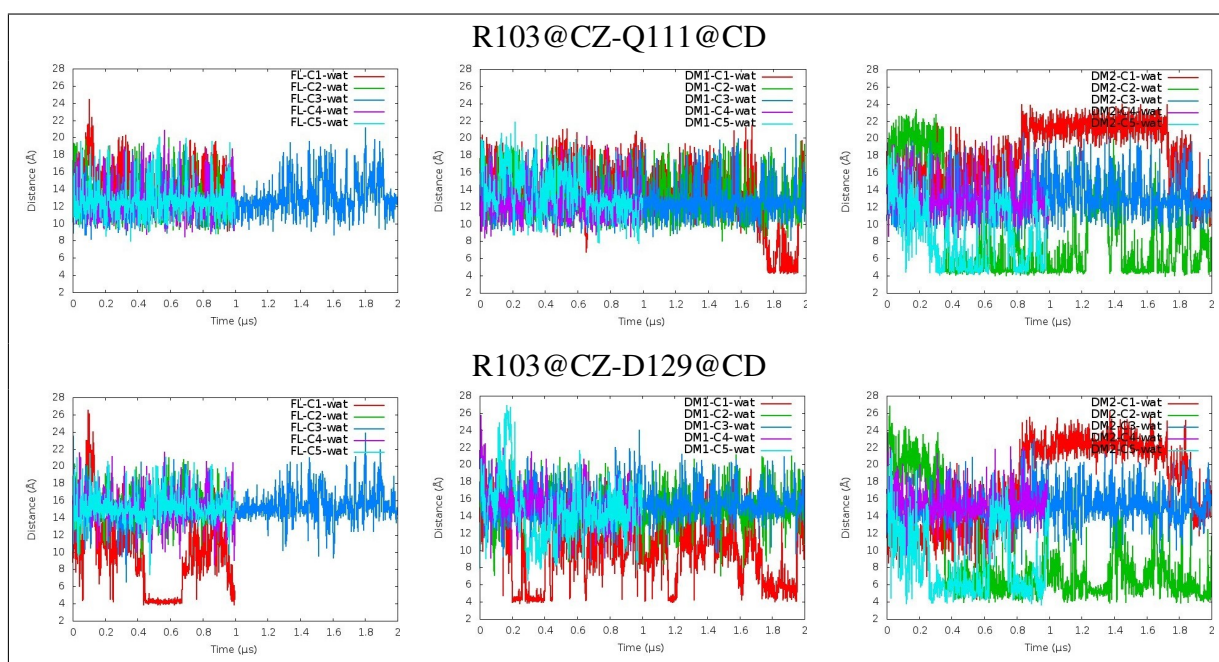


Figure 5.11: Distance evolution plots for key H-bonded residues in the BG of FL-wat, DM1-wat and DM2-wat in water. (Every 30 frames.)

Q111 (42.9 % in DM2-C2 and 25.6 % in DM2-C5) and R103-E129 (21.6 % in DM2-C2) were detected in two out of five iso-Asp mutated (DM2-wat) simulations. These interactions provide to cover the top side of the BG. Distance analysis in Figure 5.11 also showed that while R103@CZ-Q111@CD interaction was seen in DM2-wat, this interaction was not available in FL-wat simulations. Additionally, in the models bearing the C1 tail, particularly (FL-C1 and DM1-C1) R103-D133 (43.7% - 25.2%) and R103-E129 (30.6% - 15.8%) interactions were detected. However, the R103-D133 and R103-E129 interactions decreased in DM1-C1 in half. Transient (short-lived) R103-D133 interaction was observed in DM2 (three out of five) as well.

Taken together, considerable/subtle differences were observed in the behavior of the IDR and the C-tail upon deamidation. The BG is not fully closed with the C-tail. Instead, the dynamic C-tail approaches the bottom and side of the BG. Intriguingly, the C-tail mostly prefer to interact with the IDR in DM1 simulations. In general, R103 interactions with Q111 and D129 in the binding groove are the key interactions as particularly detected in DM2 simulations. Conformational changes upon deamidation will be further investigated by means of PCA in the following section.

5.3.4 Bcl-x_L and deamidated Bcl-x_L on membrane

Membrane insertion related conformational changes in protein and protein-membrane interactions (PMI) gain importance in order to fully understand the structure and function relationship of Bcl-x_L upon deamidation. As discussed earlier, deamidation and membrane mediated impacts on the protein head still remain unclear. In this section, we focused to detect the deamidation-induced conformational changes on the protein, particularly the BG. Since pre-

vious studies showed that the C-tail forms an α -helix inside the membrane, Bcl-x_L with three helical models (C1-C3) were investigated in this section [17, 19, 107].

In line with the experimental study of Yao et al [17, 107], the head of Bcl-x_L preserved its fold during the simulations. The head of deamidated systems also maintained their folds. In addition, we also examined the possible behavior of the membrane-inserted non-canonical model of Bcl-x_L suggested by Vasquez-Montes et al [160, 161]. In all simulations α 6 did not enter the membrane while α 1 stayed intact with the protein head.

Structural behavior and interactions of the C-tail in membrane

As mentioned above, Bcl-x_L anchored to the membrane through its C-tail. After association of the C-tails of Bcl-x_L and deamidated Bcl-x_L to the POPC membrane, we observed that all C-tails stayed/remained inside the membrane during the simulations. The tails have smoother/ordered α -helices inside the membrane through the interaction with POPC side chains. N-terminal (N211, R212, W213: upper leaflet) and C-terminal (S231, R232, and K233: lower leaflet) tail residues also transiently and/or persistently interact with the phosphatidylcholine head (PC head) during the simulations. These interactions/residues confirm that the C-tails stay inside the membrane and help to sustain the secondary structure by stabilizing the C-tail helices in the membrane in a good agreement with the computational study of Maity et al [159]. Additionally, R232 and K233 also protrude from membrane in most of the simulations (Figure 5.12).

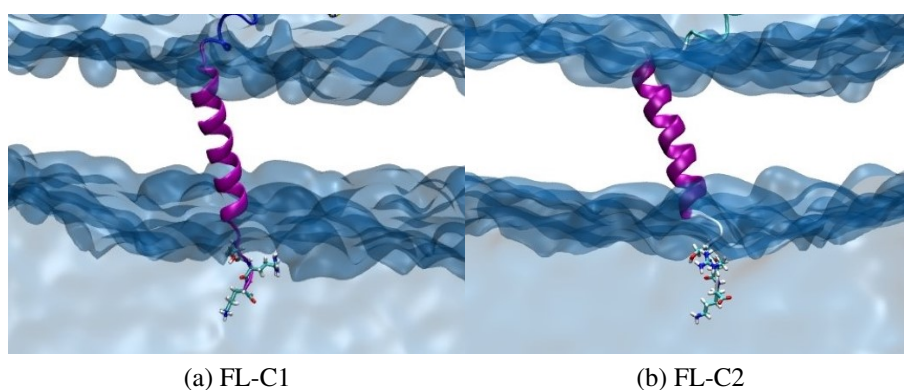


Figure 5.12: The representative snapshots of membrane-embedded C-tails and its water interactions (POPC bilayer was not shown for clarity. Snapshots taken at 1.5 μ s. The water surface was generated using the VMD[54] quicksurf presentation.)

The tilt angle of the C-tail is also one of the important factors that affect the protein position and movement above the membrane. Tilt angle calculations of Yao et al.[107] and Ryzhov et al.[162] displayed that the C-tail helix (α 9) spanning 213-233 and 207-230 (after 1 μ s MD simulations) tilted approximately by 25° and 36° relative to the membrane, respectively. The C-tails before and after deamidation were inspected through the simulations in order to detect helix tilt in the lipid bilayer/membrane (Figure 5.13). In general, average tilt angle is 21° and the C-tail helix spans around residues 210-231. DM1 models are slightly more tilted compared to the FL and DM2 simulations/models.

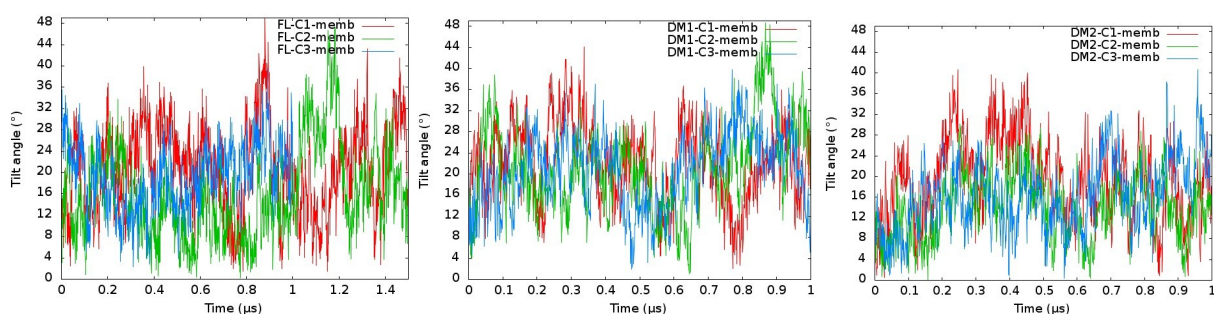


Figure 5.13: The tilt angle evolution plots for the C-tails of FL, DM1, and DM2 simulations with respect to the membrane plane simulations in membrane during simulations. (Every 5 frame)

More importantly, the junction 89 connecting $\alpha 8$ and $\alpha 9$ (J89) facilitates the flexible orientation/movement of the protein head during the simulations in line with the experimental results of Ryzhov et al., which observed higher NMR peak intensity at residues 199-205 [162]. The flexibility of J89 triggers the protein head to lean towards to the membrane leading to interaction with phosphatidylcholine head (PC head).

Intrinsically disordered region

The role of an IDR in the loss of apoptotic function of Bcl-x_L was investigated in membrane systems. Membrane association of the C-tails resulted in a limited movement/approach of the IDR towards the protein head due to the orientation of the BG towards membrane. The IDR above the membrane has a less accessible area to move compared to the water systems. The IDRs approach the side of $\alpha 6$ (right side) and $\alpha 8$ due to the lean/approach of BG from $\alpha 3$ and J23 sides to the membrane. Direction of the IDR mostly shifted to $\alpha 1$, $\alpha 6$ - $\alpha 8$, and J67. Figures 5.14 and 5.8 illustrated that interaction pattern was changed upon deamidation. Notably, deamidated systems transiently interact with the residues in J89. However, no IDR-J89 interaction was observed in Bcl-x_L (Figure 5.8). Furthermore, the IDR also transiently interacts with PC head of the POPC membrane. Remarkably, the deamidated IDR interacts with the PC head more than Bcl-x_L. The increase in negative charge affects both membrane interaction and in turn the BG movement/direction.

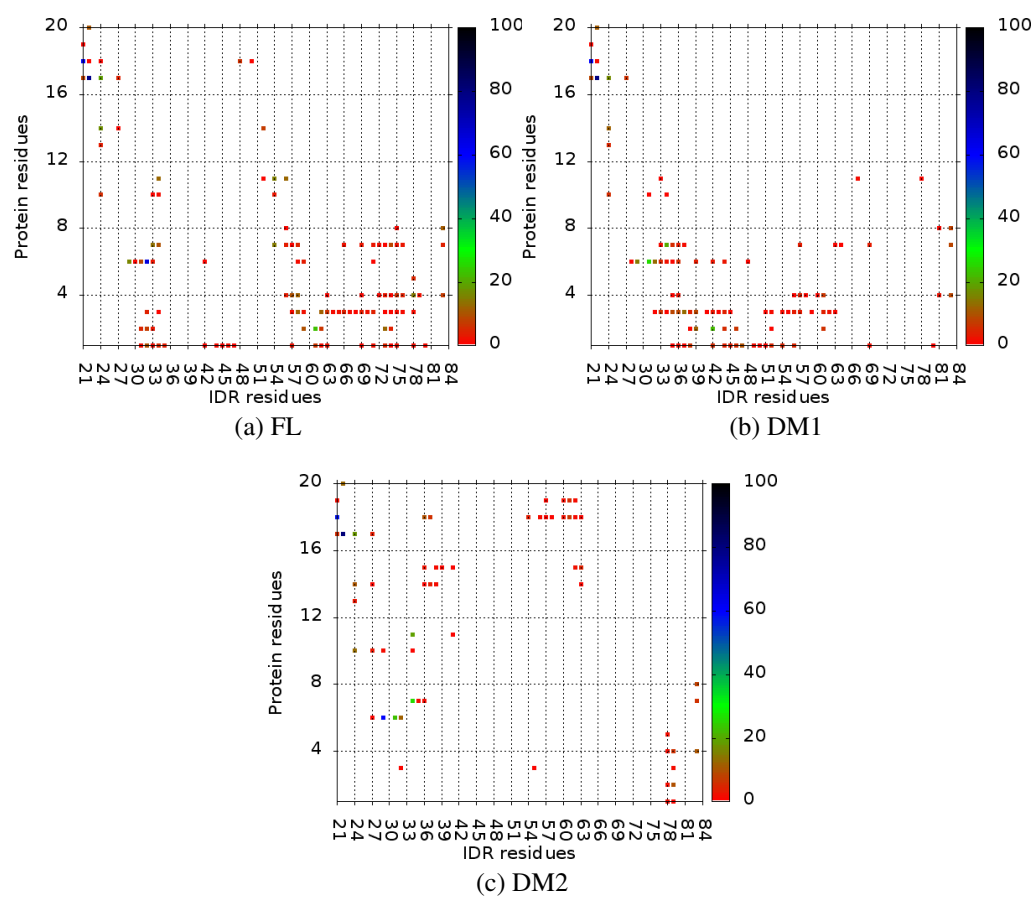


Figure 5.14: H-bond interactions plots for $\alpha 1$ residues of the protein-IDR residues of FL, DM1, and DM2 simulations in membrane. The color bar shows overall contact percentage during the simulations.

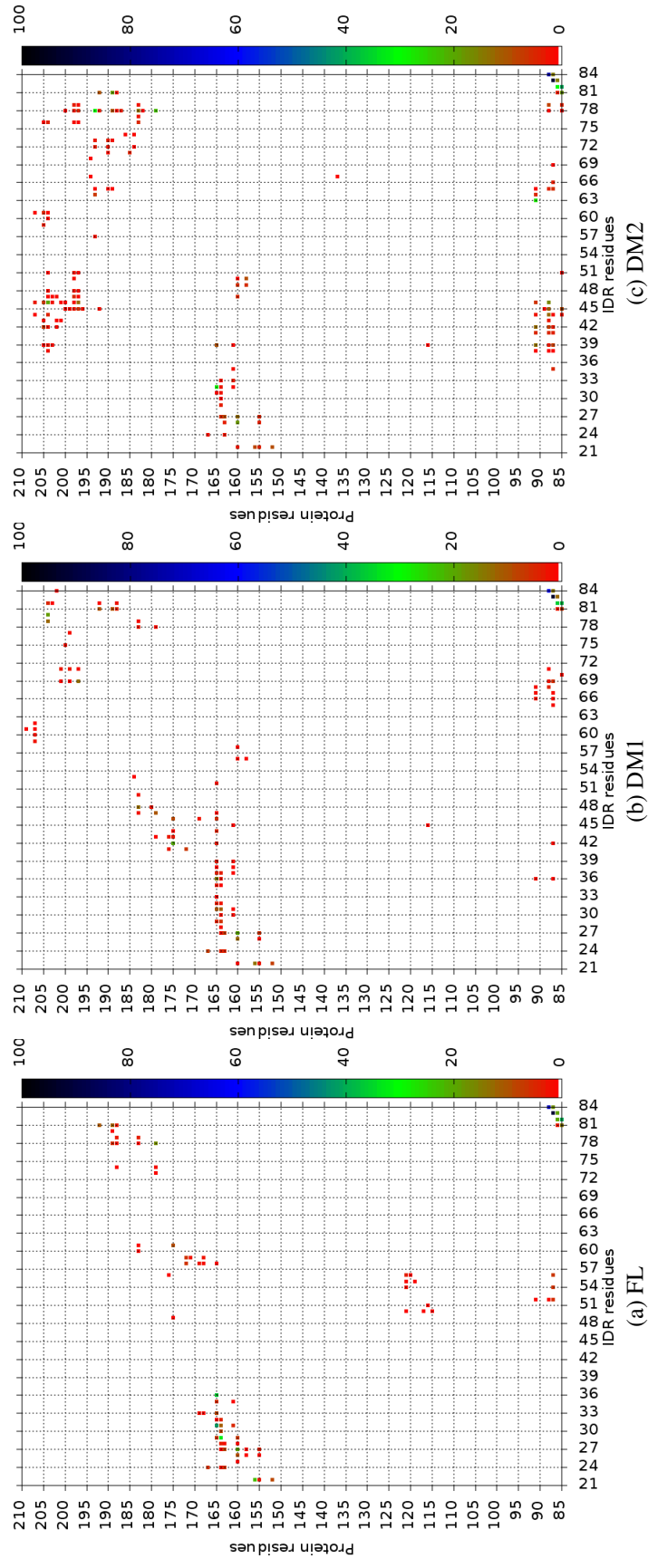


Figure 5.15: H-bond interactions plots for the protein (α 2-C-terminal residues)-IDR residues of FL, DM1, and DM2 simulations. The color bar shows overall contact percentage during the simulations in membrane.

Deamidation Impact on the Binding Groove (BG)

Influences of the IDR and the membrane insertion on the binding groove were also scrutinized in order to understand their potential roles on the BG. Previously, in the experimental study of Raltchev et al. they reported that the binding groove is in close proximity to the membrane suggesting that the BG loosely interacts with the membrane and await binding partners [19]. In line with the experimental studies,[17, 19, 107] we also observed that the BG loosely interacts with the membrane and mostly stays open. The protein head, particularly the BG is highly dynamic during the simulations. Initially the BG is perpendicular to the membrane, and the BG is open (Figure 5.16). After short a while the BG specifically leans towards the membrane from $\alpha 2$, $\alpha 3$, and J23 sites in most of the simulations (Figure 5.17). Transient interactions of the BG, particularly J23, $\alpha 2$, and $\alpha 3$ with the PC polar heads of the membrane were detected (Figures 5.17 and 5.18). Ryzhov also confirmed the BG and lipids interaction and observed mostly $\alpha 2$ - $\alpha 4$ reflecting the BG is less in contact with cytosol [162]. We also observed short-lived interactions between the bottom side of the BG ($\alpha 2$ - $\alpha 4$) and the PC head in Bcl-x_L (FL) simulations. During the simulations the bottom of the BG closes too much to the membrane from time to time by preventing the possible bindings partners, namely pro-apoptotic proteins and BOPs, particularly in Bcl-x_L simulations. Intriguingly, unlike the BG of Bcl-x_L, the BG in DM1 simulations moves above the membrane and minimally/rarely gets contact with the membrane. Due to increase in negative charge in the IDR, in two out of three DM1 simulations the IDR interacts with the membrane and may push up the BG above (Figure 5.18). The fact that BG has less contact with the membrane may contribute the change in the BG-BG residue interactions.

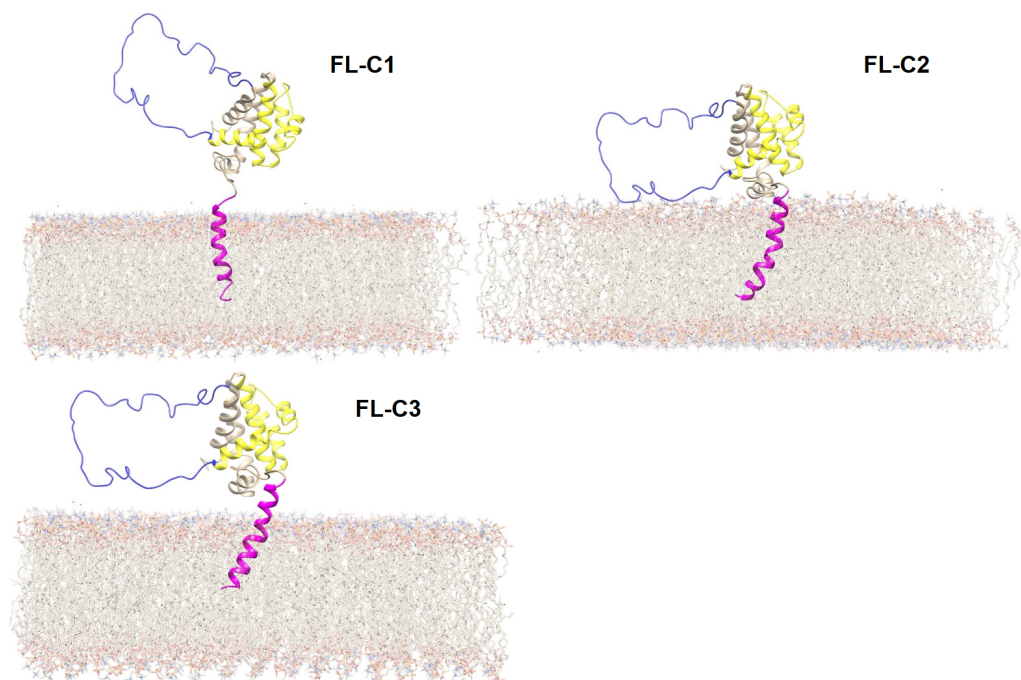


Figure 5.16: Initial structures of FL models in membrane. (Blue color denotes the IDR. Magenta and yellow colors present the C-tail and the BG, respectively. Water was not shown for clarity.)

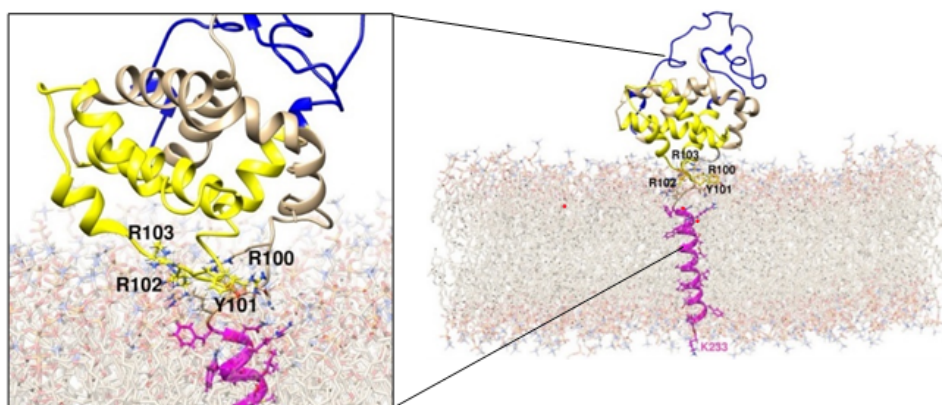


Figure 5.17: Representative orientation of the BG of FL-C3 toward the membrane.

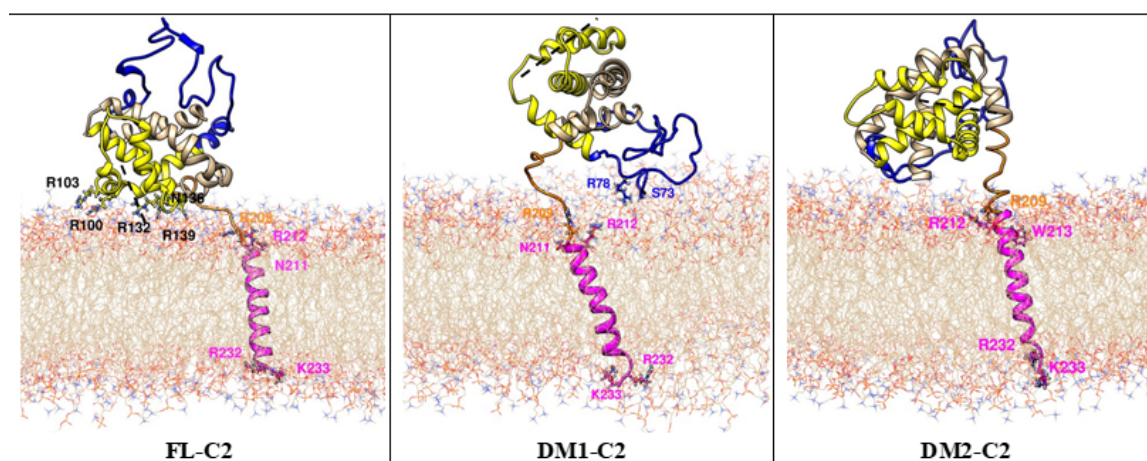


Figure 5.18: Representative protein head-membrane interactions in the simulations. (Blue color denotes the IDR and orange for J89. Magenta and yellow colors present C-tail and the BG, respectively. The black dashed line presents the position of the BG.)

Remarkably, transient J23 residues (R100-R103)-C-tail interactions in Bcl-x_L are considerably higher than the deamidated ones. H-bond interactions among the J23 residues, particularly the Arg cluster (R100, R102, and R103) and the PC heads reach maximum up to 38.7 %. In deamidated simulations Arg cluster tends to interact with α 3, α 4, and J45 in order to narrow the BG instead of interacting with the membrane. This outcome suggests that the PC head interactions with the Arg cluster could prevent the narrowing of the BG and render the BG open.

Key H-bond interactions in the BG were also detected and followed during the simulations (Figure 5.19). Remarkably, in all simulations of DM1s on membrane, R103-D133 (in the range 27.4-55.8%), R103-E129 (in the range of 10.6-65.3 %) interactions were detected. Particularly, the R103-D133 interaction in DM1 contributes to the narrowing of the bottom side of the binding groove. Distance analysis also depicted larger R102-D133 distances in Bcl-x_L (2 out of 5) and DM2 compared to DM1 simulations (Figure 5.19). Taken together, R103-D133 and R103-E129 are the key interactions, leading to the narrowing and the covering of the BG. These

outcomes also stress that deamidation in the IDR allosterically affect the BG groove and alters the interaction pattern. Consequently, it may impair its function.

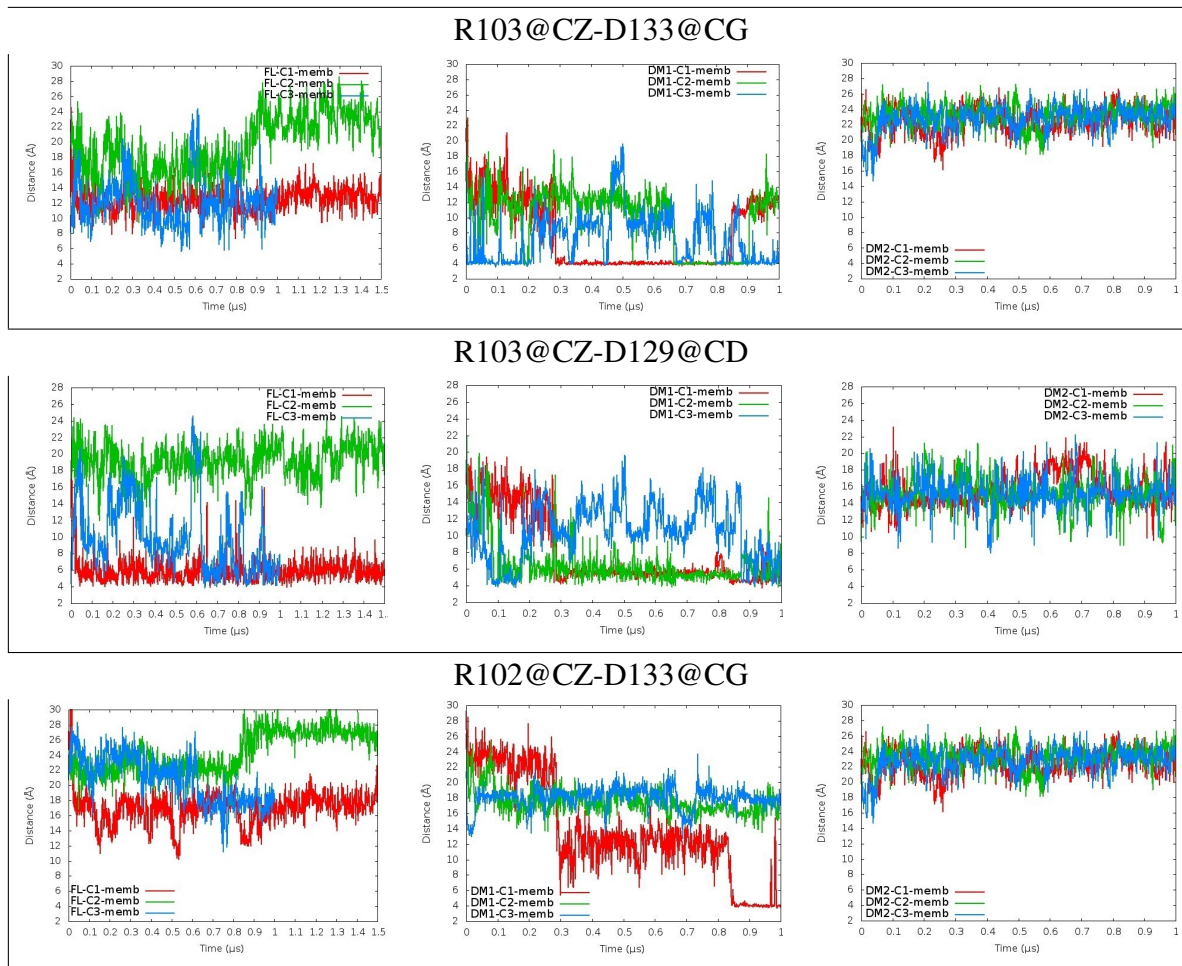


Figure 5.19: Distance evolution plots for key H-bonded residues in the BG of FL-memb, DM1-memb and DM2-memb in membrane. (Every 30 frames.)

Radius of gyration (R_g) analysis was also performed to further monitor time evolution of the narrowing of the bottom side of the BG using the backbone atoms of J23 and J45 residues during the simulations. Figure 5.20 shows that FL-memb R_g 's generally fluctuate in the range of 6.0-11.5 Å. Compared to FL-memb, the R_g seems to reach a stable trend in DM1-memb and DM2-memb. In DM1 simulations, the R_g is lower than with the others indicating a narrowing of J23 and J45. The R_g 's of the DM2 simulations are also slightly lower (in general range of 5.5-10.0 Å) than with Bcl- x_L . The R_g outcomes also confirm the allosteric effect of deamidation.

In 2017, Priya et al claimed that R103 and R139 cover the bottom part of the BG by behaving like a gate [131]. In our study, we suggest that R103 interactions play major role to cover the inner side of the BG, especially for the deamidated systems. Taken together, deamidation in IDR indicates that R103-D133, R103-E129 and R103-Q111 interactions collectively provide/contribute closure and narrowing of the BG in membrane systems. These results also may indicate that deamidation in membrane environment allosterically affects the BG of Bcl-

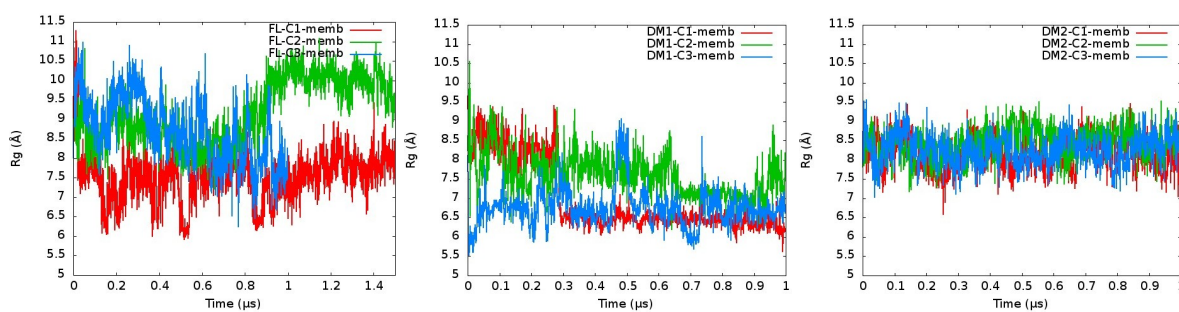


Figure 5.20: Rg as a function of time for the backbone atoms of J23 and J45 of FL, DM1 and DM2 simulations in membrane. (Every 20 frames)

x_L in terms of the change in the interaction pattern (i.e., protein-membrane interactions and the IDR interaction) and narrowing of the BG. Notably, compared to water environment, Bcl- x_L shows crucial differences in the BG upon deamidation. This could indicate that the increase in negative charges in the IDR and membrane association collectively impacts on the structure of the protein.

Overall, the BG is mostly oriented towards the membrane from the $\alpha 3$ and J23 sites, but in DM1 simulations it is oriented to the opposite direction and is in less contact with the membrane. The Arginine cluster in J23, particularly R103 interactions, plays an essential role on the narrowing of the BG. During DM1 simulations, the narrowing of the bottom side of the BG was observed and these results suggest that deamidation allosterically affects the BG and this may imply the loss of Bcl- x_L function upon deamidation.

5.3.5 Principal Components Analysis (PCA)

The essential dynamics and the dominant motions of the BG in the water and in membrane systems were scrutinized using principle component analysis (PCA) in order to get insights into the structural/conformational differences in both environments [52]. Basically, PCA converts cartesian coordinates into dominant motions. The changes in their conformations and the dominant motions of Bcl- x_L prior to and subsequent to deamidation were investigated by examining the overlaps of the distributions. PCA was comparatively investigated in three groups by combining all independent simulations (24 in total (15 in water and 9 in membrane systems)). The combined 24 independent simulations were separately projected for each system (WT, DM1 and DM2 in water and membrane). Since approximately 80 % of the cumulative variance was reached by the first four PCs, only the first four PCs were depicted herein (Figure 5.21).

PC scatter plots in Figure 5.22 illustrate that the water and membrane models overlap less with each other and cover different conformational spaces. This outcome indicates that the simulation environment considerably affects the essential dynamics, which results in unsimilar motions and conformational differences. Moreover, the finding also indicates that the conformational transitions from water to the membrane environment. In addition, DM2-wat explores/scans larger area than DM2-memb. Conformational distributions in membrane environment are considerably reduced in DM2-memb implying a rigidity and less flexibility of the iso-Asp deamidated Bcl- x_L in membrane.

In water, deamidated and FL simulations display notable differences (Figure 5.23). Deami-

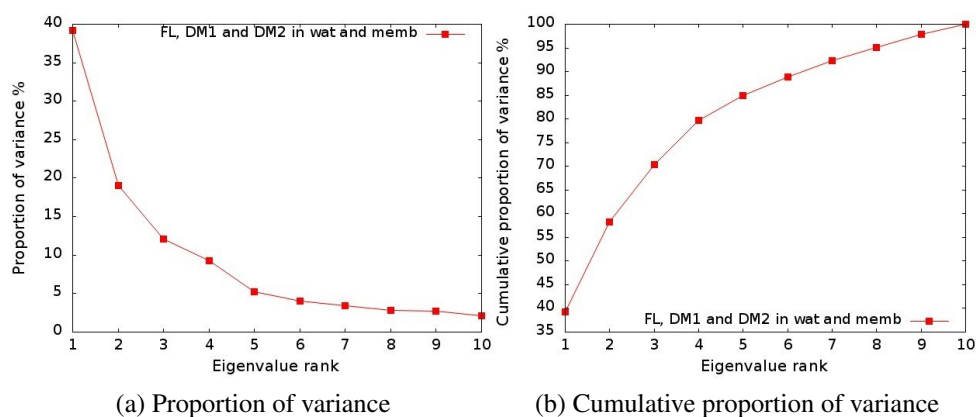


Figure 5.21: a) Proportion of variance b) Cumulative sum of total variance captured by the first 10 PCs for the combined clusters (FL, DM1, and DM2.)

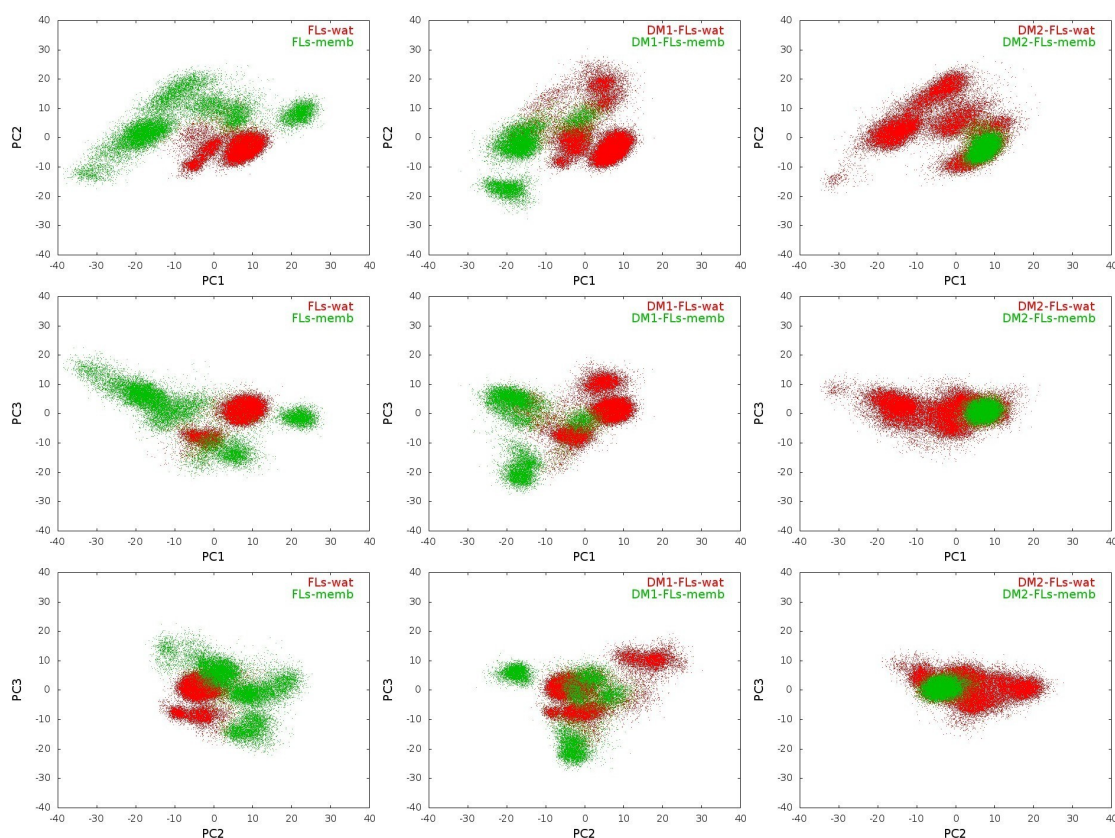


Figure 5.22: PC scatter plots for top three PC modes of all MD runs onto all MD runs. (Every 5 points were plotted.)

dated proteins explore larger and distinct areas than FL-wat. Particularly, DM2-wat simulations scan considerably different and larger areas indicating considerable changes in conformations and overall motions. In membrane, larger differences were observed between Bcl-x_L and deamidated Bcl-x_L systems. FL-memb, DM1-memb, and DM2-memb explore distinct areas and the

deamidated systems are less flexible and overlap less compared to FL-memb (Figure 5.23). FL-memb scans larger conformational area/distributions. Deamidated systems cover limited areas, particularly D2-membs, which indicate a less flexible BG. These findings suggest that deamidation and membrane integration allosterically effects the dynamics of the BG leading to conformational differences. Moreover, the essential dynamics of the systems are also environment dependent and show different behaviors.

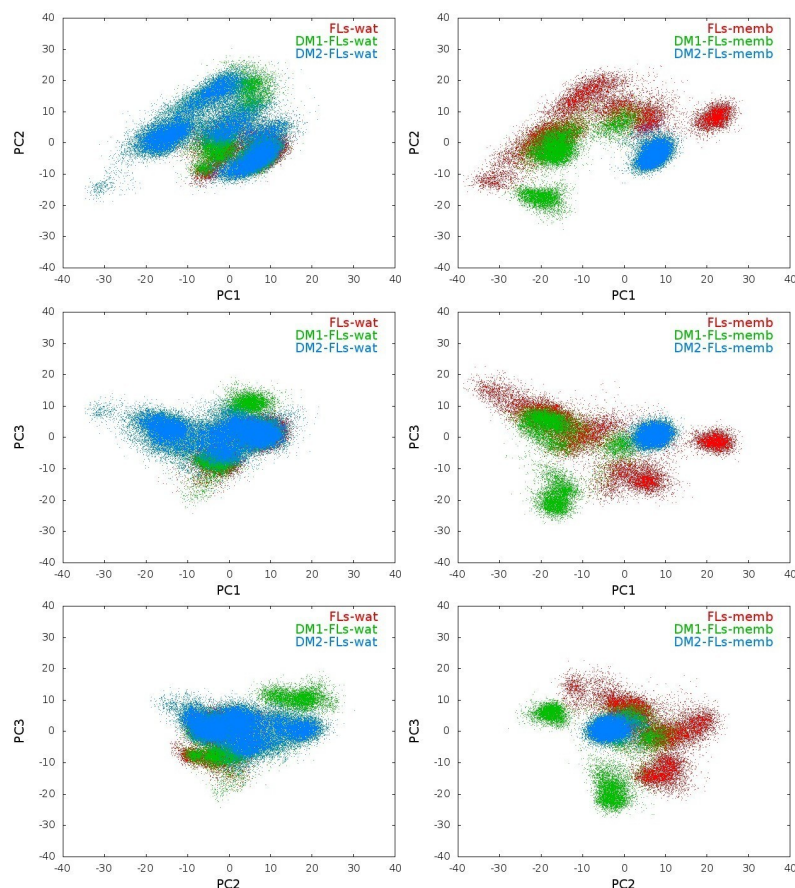


Figure 5.23: PC scatter plots for top three PC modes of water (left) and membrane systems (right) onto all MD runs. (Every 5 points were plotted.)

Taken together, considerable differences in PC distributions between the water and membrane environments highlight the structural differences/transition upon membrane integration.

5.4 Conclusions

In recent years full-length Bcl-x_L was experimentally evaluated but structural understanding of full-length Bcl-x_L before and after deamidation in the membrane has been missing. In this study, the conformational/structural role of deamidation on the tertiary structure of membrane-anchored Bcl-x_L was deciphered using MD simulations by considering both in water and membrane environments. We mainly focused on the conformational changes and essential dynamics

of Bcl-x_L upon membrane insertion and deamidation. While the C-tail is more flexible as expected in water and interacts with the head of the protein, it is more stable in membrane through the interaction with the lipids. In membrane, the C-tails were tilted to the membrane normal and $\alpha 2$, $\alpha 3$, and J23 in the BG were oriented towards the membrane while the BG interacted loosely with membrane. Remarkably, asparagine deamidation to aspartate/iso-aspartate in membrane systems seems to allosterically trigger the changes in the binding groove. PCA illustrated the conformational transitions between water and membrane systems. PCA suggests that the simulation environment considerably affects the essential dynamics implying conformational differences. Our findings suggest that interaction pattern change, flexibility of the J89, protein orientation towards membrane and protein-membrane interaction play a pivotal role on the structural differences of the protein upon deamidation. Furthermore, the pivotal differences could be collective/cooperative consequences of membrane association and deamidation. In other words, allosteric effect could arise from both the deamidation in the IDR and the membrane environment. In addition, unlike the outcome of Vasquez-Montes et al., we did not observe Bcl-x_L refolding and the release of BH4 domain in membrane during the simulations. Analysis of this study is still in progress. Initial results were shared herein. We have planned to perform further analysis for further rationalization and clarification of the computational findings. We believe that this study will provide a valuable contribution with potential implications towards developing anticancer therapeutics by presenting insights into the consequences of deamidation on the structure and function of Bcl-x_L. Further studies will focus on understanding complex systems (Bcl-x_L + BOPs/pro-apoptotics) in order to provide comprehensive insight and full perspective on the impact of Bcl-x_L deamidation.

Chapter 6

Investigation of Bcl-x_L-BH3-only peptide Complex

6.1 Introduction

BH3-only proteins (BOPs) are divided into two groups, namely activator and sensitizer (Figure 6.1). Andrews and coworkers described BOPs as orchestrators of apoptosis in their review.[147] While activator BH3-only proteins (BIM, BID and PUMA) directly induce apoptosis, sensitizers (BAD, NOXA, etc.) indirectly induce it. BOPs only consist of a BH3 domain and this domain plays a pivotal role for the interactions with the BCL2 family proteins and regulation of MOMP. Since full-length of BH3-only proteins are not available except BID, BH3 peptides derived from each of the BH3-only proteins were used in the literature. Literature results showed that BH3 peptides mimic the corresponding full length protein and induce BAX and BAK oligomerization and MOMP [143, 144, 172]. BH3 domains of activator BH3-only proteins/peptides interact with the binding groove of Bcl-x_L and lose their functions. In addition, they directly promote MOMP by activating Bak and Bax.[173] As mentioned in the previous chapter, the binding groove of Bcl-x_L accommodates BH3-only peptides. Rajan et al reported crystal structures of Bcl-x_L in complex with BID and BIM peptides (4QVE and 4QVF, respectively) and showed that BH3-only peptides bind the binding groove of Bcl-x_L and formed alpha helical conformations. Furthermore, owing to their sequence variations of the peptides, different interaction modes and conformational changes were observed.[139] Additionally, Bcl-x_L is a potential target for Bcl-x_L inhibitors design, known as BH3-mimetics. For instance, Navitoclax targeting BCL-2, Bcl-W and Bcl-x_L and Venetoclax (Venclexta and Venclyxto) for BCL-2 are already in the market [174].

In 2013, Maity et al. investigated dynamics of Bcl-x_L (PDB ID: 1BXL_{NMR}, Δ45-84) in water and the pre-equilibrated DOPC membrane by means of MD simulations (1.6 μs in total) [102]. Simulation results showed that the C-tail covered the binding groove in water after 60 ns of simulation. When BAK peptide was also included in the water system, the C-tail was displaced with BH3-only peptide. In membrane, BAK reduced its binding affinity due to conformational changes in the binding groove. Contrary to Maity et al, In 2015 Yao et al showed that membrane-anchored Bcl-x_L has a higher affinity to the BID peptide when compared to Bcl-x_L in water.[107] Due to the competition between the C-tail and the BID peptide in water, the

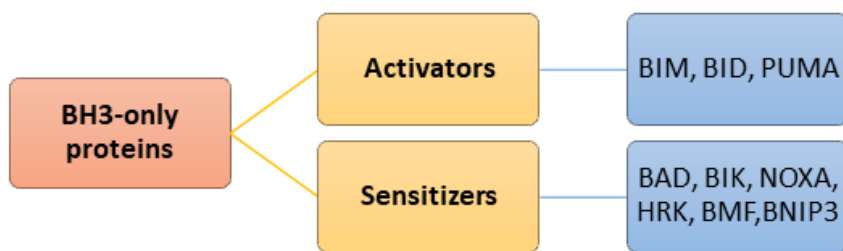


Figure 6.1: The BOP family.

C-tail behaved as a pseudo-inhibitor by binding to the binding groove of Bcl-x_L and showed cytoprotective activity. Moreover, Pécot et al.[175] reported that the BH3 binding affinity of membrane-associated Bcl-x_L was enhanced compared to its counterpart in water since there was no competition between C-tail of membrane-anchored Bcl-x_L and the BH3 peptides to interact with the binding groove of Bcl-x_L. There is an obvious contradiction between the results of Maity et al., Yao et al., and Pécot et al. in the binding affinity of the peptide to the membrane-bound Bcl-x_L. The reason for the contradiction could be that Maity et al. used modified Bcl-x_L structure, which lacks a real C-tail. The C-tail they use in their study is histidine tagged in order to facilitate purification. In this context, further investigation is needed to clarify the reason of binding affinity variations when Bcl-x_L is bounded to the membrane. Additionally, in previous studies, the Bcl-x_L structures in complex systems did not include the IDR. Yet recent studies emphasized the importance of the IDR as mentioned in the previous chapter. For these reason, in order to give further insights on these complex systems, we considered the impact of the IDR.

In this study, the structural behaviors of BH3-only peptide in water was investigated and compared with some complex systems. In the second part of the study, we focused on the Bcl-x_L-BIM peptide complex (PDB ID: 4QVF_{X-RAY}) and the Bcl-x_L-BID peptide complex (PDB ID: 4QVE_{X-RAY}). In this context, since Bcl-x_L in the experimental complexes does not have the IDR we modified the models. The IDR was extracted from a Bcl-x_L (PDB ID: 1LXL_{NMR}) structure and added to the complex models.

6.2 Methodology

Initial structures (4QVF,[139] 4QVE,[139] and 1LXL [14]) were provided from the Protein Data Bank (Homo sapiens). The Bcl-x_L ΔC+BIM peptide complex I and Bcl-x_L ΔC+BID peptide complex II systems were prepared as follows: 4QVF and 1LXL were used to prepare complex system I (Bcl-x_L ΔC+BIM peptide). To prepare the complex system II, 4QVE and 1LXL were used (Bcl-x_L ΔC+BID peptide). Missing residues and loop sections were provided from 1LXL. For proper addition of the residues, 1LXL were fitted and added to 4QVF and 4QVE using Profit (Version 3.1) [176] and the tleap module from Amber, respectively. All MD simulations were performed using the Amberff14SB [134] force field implemented in the Amber18 program package[133] and solvation was carried out using the TIP3P [135] explicit water model forming cubic boxes. Counter ions (sodium or chloride) were added into each system to neutralize charges. The same MD protocol as the one described in chapter 4 was used in this study.

6.3 Results and Discussion

First, we concentrated on the understanding of the structural behavior of the BID and BIM peptides in water (unbounded state). Then, initial analysis results of the complex systems (bounded state) were discussed herein. The studied systems were tabulated in Table 6.1. As mentioned above, our complex systems include Bcl-x_L with the IDR and a BH3-only peptide.

Table 6.1: Initial structure set up.

Initial Structure	Water	Na ⁺	Total atoms	Simulation time
BH3-only peptide (Simulation box = 74.505x74.505x74.505 Å ³)				
BIM	13372	2	40547	1 μs
BID	13403	2	40563	1 μs
Bcl-x _L -BH3-peptide complex (Simulation box = 111.757x111.757x111.757 Å ³)				
Bcl-x _L -BIM complex	44265	15	136360	1 μs
Bcl-x _L -BID complex	44234	15	136344	1 μs

6.3.1 Stability of BH3-only peptides in water

Figure 6.2 displays that BH3-only peptides show higher RMSD values indicating instability of the peptides in water. Additionally, secondary structure analysis results also displayed reduction of helix length (partial unfolding) (Figure 6.3). Literature data demonstrated that hydrophobic residues tend to cluster in order to minimize solvent exposure and this lead to the reduction of helix length and partial to complete loss of helical character[144, 177, 178, 179].

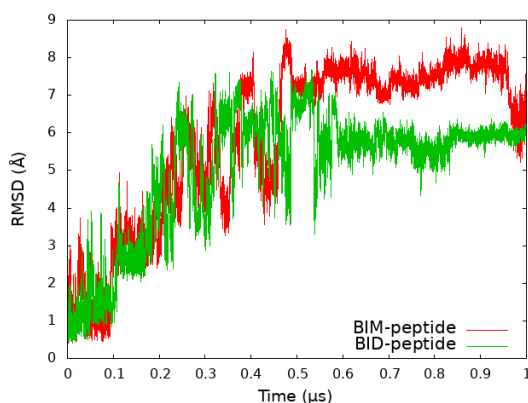


Figure 6.2: Backbone RMSD plot for BH3-only peptides with respect to X-Ray structures.

6.3.2 Analysis of Complex systems

As seen in Figure 6.4 when peptides are bounded to target proteins, they formed helices. Figure 6.5 shows that the core helices are stable and that the loop regions display a higher RMSD for

complex systems. Secondary structure analysis in Figure 6.6 also demonstrates that the BH3 peptide is considerably stable in contact with Bcl-x_L.

Investigation of the Bcl-x_L-BOP complexes both prior to and following deamidation is an upcoming study in order to give insight interactions between anti-apoptotic protein and BH3-only peptides.

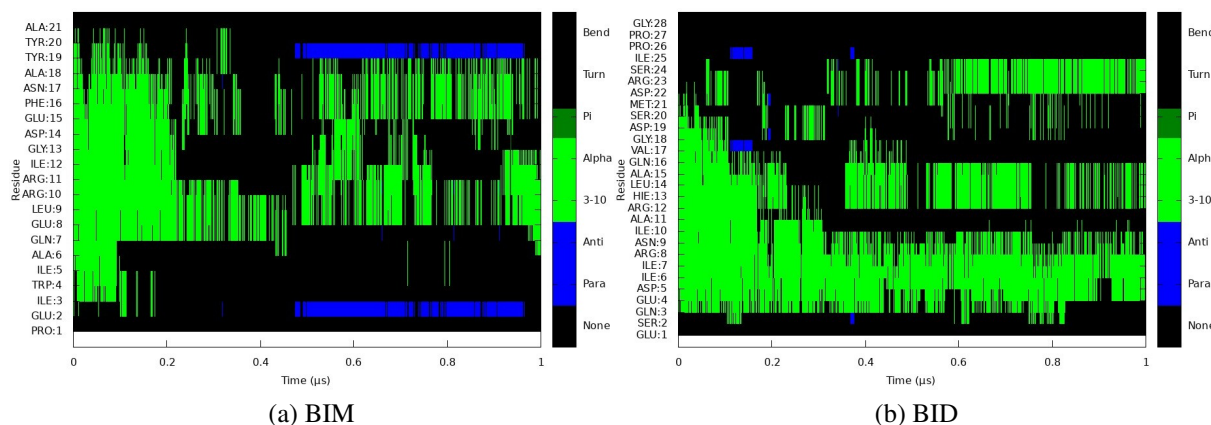


Figure 6.3: Secondary structure plots of a) BIM b) BID peptides.

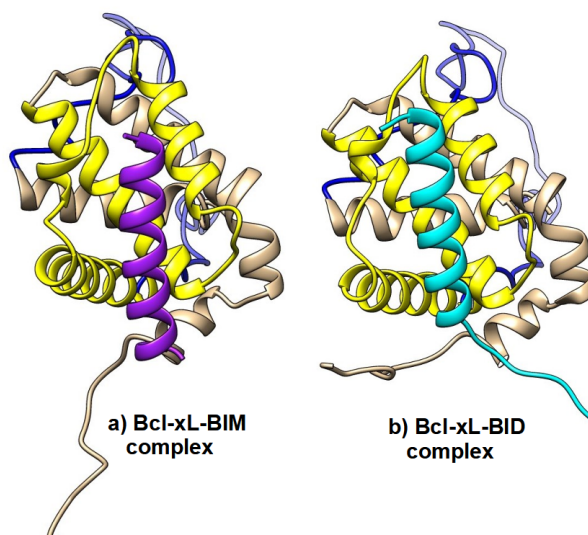


Figure 6.4: Representative structure of a) Bcl-x_L-BIM complex b) Bcl-x_L-BID complex. (Blue and yellow colors refer to the IDR and the the binding groove. BIM peptide in purple, BID peptide in cyan.)

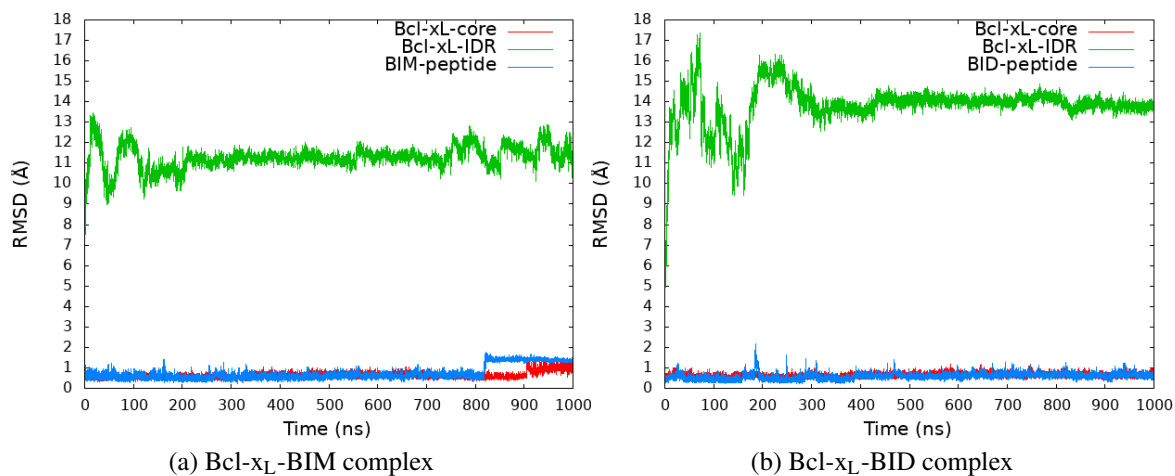


Figure 6.5: Backbone RMSD plots of a) Bcl-x_L-BIM complex b) Bcl-x_L-BID complex with respect to the built structures.

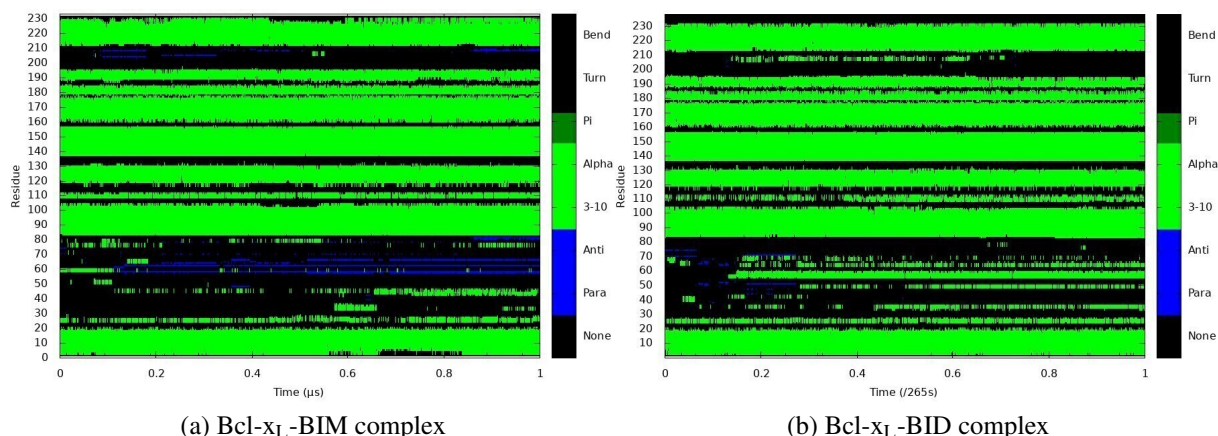


Figure 6.6: Secondary structure plots of a) Bcl-x_L-BIM complex b) Bcl-x_L-BID complex.

6.4 Conclusions

MD simulations confirmed that unbounded BH3-only peptides are dynamic in water compared to their corresponding complex systems (bounded state). Disruption of helicity (short helices) are observed and the peptides are unstable in water in line with previous studies. They are significantly more stable in contact with Bcl-x_L. Analysis results of complex systems showed that BH3 peptides preserved their helical shapes, yet loop regions were highly flexible. This study is in progress. As a future work we will investigate complex systems in membrane environment before and after deamidation. Understanding of the interactions in complex systems will pave the way to design future Bcl-x_L inhibitors.

Chapter 7

Keteniminium Chemistry

7.1 Introduction

Keteniminium salts (KIs) are versatile and reactive intermediates in organic chemistry[32, 180]. Historically, the pioneers of the use and synthesis of KI are Viehe and Ghosez[26, 27]. KIs are an improved alternative to their ketene analogues, due to their higher reactivity and high electrophilicity. Furthermore, KIs do not undergo undesired side reactions, such as dimerization or polymerization, as readily as ketenes [28, 30, 180, 181, 182, 183]. KIs are mainly categorized in two groups, namely classical (aldo-KI and keto-KI) and activated keteniminium ions as depicted in Figure 7.1.

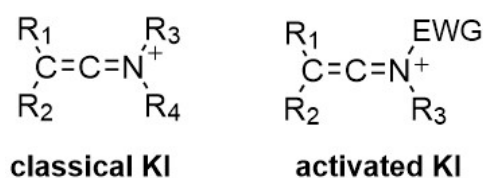


Figure 7.1: General structures of KIs.

Keteniminium salts have a wide range of synthetic applications [32, 180]. They are mostly used as key intermediates in electrocycloaddition reactions,[184, 185] intermolecular and intramolecular cycloaddition reactions,[181, 186, 187] [1,5]-sigmatropic hydrogen shifts,[188, 189] and Claisen rearrangements[190] (Figure 7.2). KIs were shown to undergo [2+2] cycloadditions with alkynes and are also used as dienophiles in Diels-Alder reactions [186, 191, 192]. [2+2] cycloaddition products of KI and alkenes can also undergo nucleophilic addition on the cyclobutyliminium ion to produce highly stereoselective quaternary centers [193].

7.1.1 Formation of Keteniminium Salt

As mentioned above, the formation reaction of KI was first mentioned by Viehe and coworkers in 1967 [33]. However, some drawbacks limit the use of this procedure, such as the initial formation of a highly reactive and sensitive ynamine and a side reaction of the KI formed

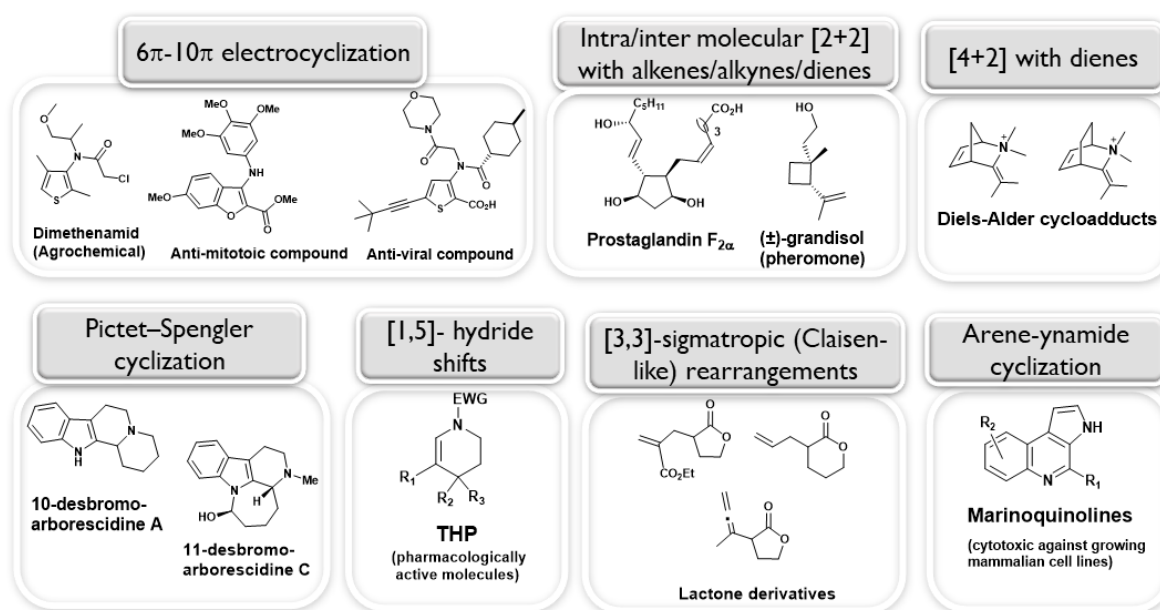


Figure 7.2: Summary of the reactions involving KIs.

with its precursor. In the following years, various alternative formation reactions of KIs, allowing a broader use of these intermediates, have been disclosed in Figure 7.3, namely reactions of α -haloenamines with Lewis acids,[27, 28, 29] triflation of amides,[30] methylation of ketenimines,[31] and protonation of ynamines [32, 33] and ynamides [34, 35, 36]. Particularly, in 1981, Ghosez and coworkers [30] reported the synthetically most useful and commonly used formation method by activation of amides with triflic anhydride. In context of this study, we focused on the KI formation reaction from the reaction of tertiary amides (Ghosez's KI formation) since it requires milder conditions and is the synthetically most used KI formation method. The effect of substituents on starting amide reactivity was investigated by considering the mechanism of amide triflation. A broad range of substituents were selected, and energetic analysis was performed to assess relative reactivities and their effect on the ease of KI formation. Furthermore, reactivity of experimentally available starting amides with different substituents was computationally investigated with various aspects, namely FMO, and reactivity descriptors.

7.1.2 [2+2] Cycloaddition Reaction

Due to limited general methods to attain substituted aminocyclobutanes and aminocyclobutenes, a straightforward general access from the corresponding iminium salts has gained considerable attention. Inter and intramolecular [2 + 2] cycloaddition reactions of KI with alkenes or alkynes are extensively used methods to access cyclobutanones/cyclobutenones and various complex compounds in organic synthesis that can be derived from the them. In this context, a DFT study was performed in order to investigate the experimentally observed reactivity differences in the [2+2] cycloaddition reactions.

N-allyl groups are known to be easily cleaved under mild conditions to provide free amines [194]. Although the allylic double bond in keteniminium salt is expected to be deactivated by the electron withdrawing effect of the iminium cation, the compatibility of *N*-allylic groups

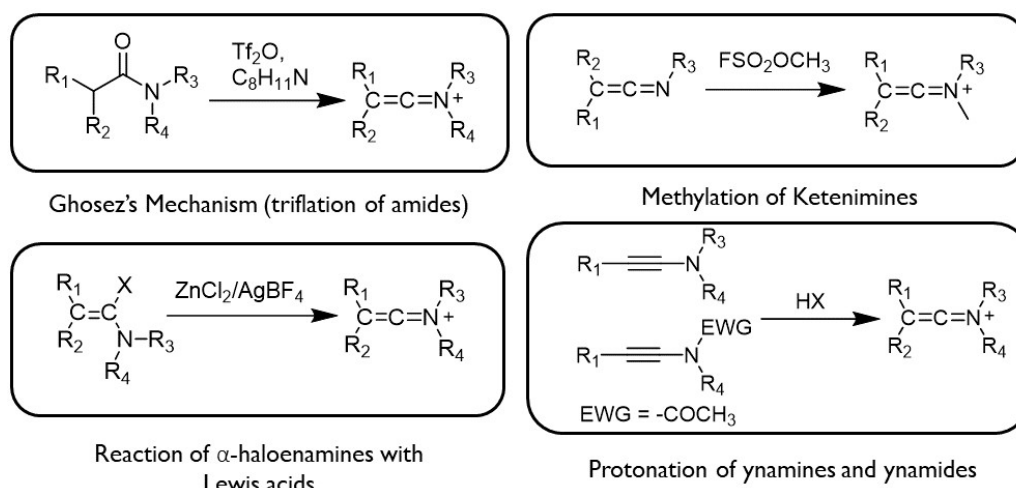


Figure 7.3: Various formation reactions of KI.

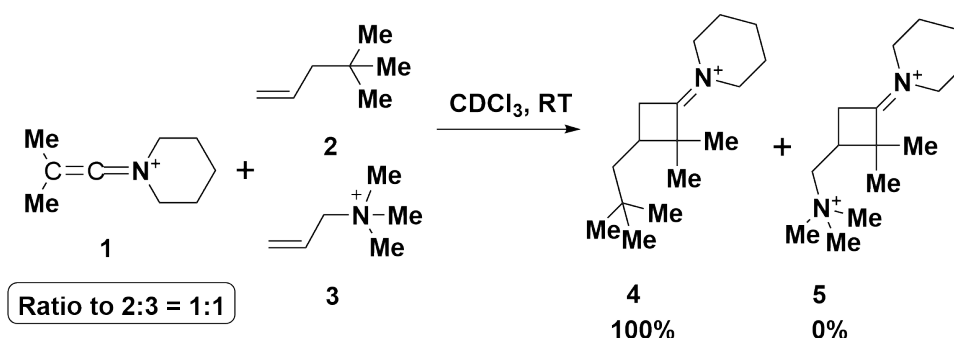


Figure 7.4: Competition reaction between allylammonium 3 and corresponding alkene 2 in a [2 + 2] cycloaddition with KI 1.

in the [2 + 2] cycloadditions of keteniminium salts was initially assessed to rule out the possibility of an intermolecular competitive reaction. Preliminary experimental results based on a competition reaction highlighted the lower reactivity of the allylammonium salt 3, which is used to mimic the keteniminium *N*-allyl group (Figure 7.4). When KI 1 was added to a 1:1 mixture of alkene 2 and 3, cyclobutaniminium 4 resulting from the [2 + 2] cycloaddition of 1 and 2, was exclusively observed and no trace of 5 was detected confirming our suggestions that the positively charged nitrogen atom in the keteniminium salts would considerably decrease the reactivity of the adjacent *N*-allyl groups toward electrophiles (Figure 7.4).

This study aimed to elucidate the reaction mechanism for [2+2] cycloaddition reaction of KI and olefins and rationalize the experimental data by means of DFT calculations. Two alkene (olefin) derivatives in Figure 7.4 were studied in order to determine the substituent effect on the cycloaddition reactions [195].

Secondly, alkynes are usually much more reactive species than the corresponding alkenes toward electrophiles as verified in the competition reaction depicted in Figure 7.5. When keteniminium 1 was added to a 1:1:1 mixture of 10, 11, and 12, the [2 + 2] cycloaddition occurred, in 15 minutes, exclusively with alkyne 10. However, upon mixing keteniminium salt 1 with

alkenes 11 and 12 (1:1 ratio), the [2 + 2] cycloaddition was completed in 1 h giving 14:15 in a 80:20 ratio, also evidencing that cis-alkenes react faster than trans-alkenes [195]. We aimed to validate and rationalize the experimental data by means DFT calculations.

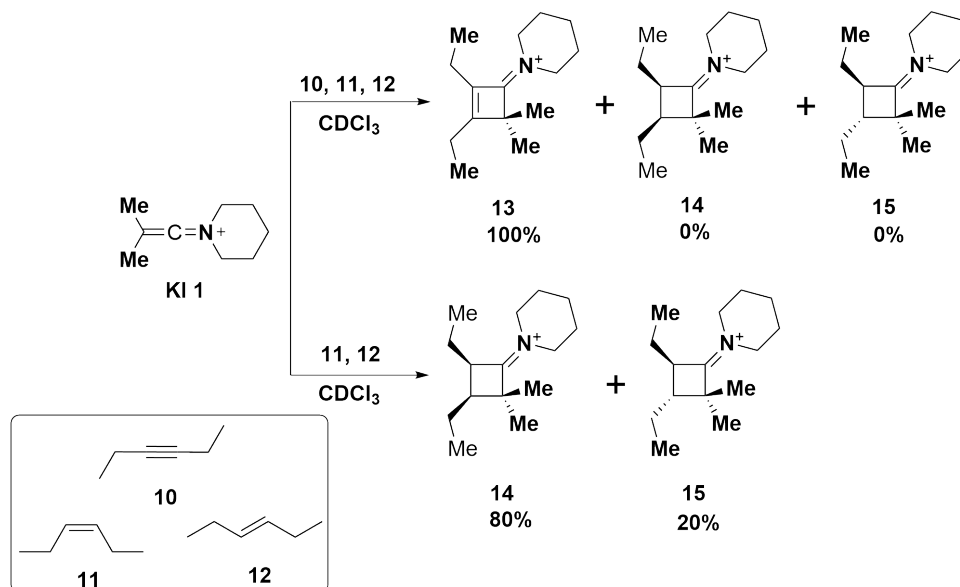


Figure 7.5: Competition reaction experiment between 10, 11, and 12 in a [2 + 2] cycloaddition with KI 1.

7.1.3 Intramolecular competition reactions

This section includes computational rationalization of the experimental competition studies, which were given below.

Firstly, intramolecular competition reactions were performed to investigate which type of reactivity involving a KI is favored between a [2+2] cycloaddition on a C=C double bond and a 6π -electrocyclization. Hence, three amides bearing different terminal olefins and a S-Ph moiety were synthesized by our experimental collaborators. Indeed, once the KI E is formed, it can either evolve through a [2+2] cycloaddition giving the cyclobutaniminium F or through a 6π -electrocyclization giving the benzothiophene G. Interestingly, the experimental results were highly dependent on the length of the chain (Table 7.1). When $n=3$, the [2+2] intramolecular cycloaddition was favored and gave exclusively product Fn=3 with a 4-5 bicyclic system. For $n=4$, crude NMR revealed a 9:1 ratio of products F/G where the 4-6 bicyclic system Fn=4 was the major compound underlining the preference of the [2+2] intramolecular cycloaddition. This trend was then reversed with longer chain ($n=5$) and the formation of the 7-membered ring was not observed. Only the formation of the benzothiophene Gn=5 was detected in the crude NMR. These interesting results experimentally proved that the kinetics of both reactions are very close and they can be switched from one mechanism to another only by modification of the length of the side chain containing the C=C double bond. In order to rationalize and validate the experimental outcomes, intramolecular competition reactions between 6π -electrocyclization and

Table 7.1: Intramolecular competition reaction between a 6π electrocyclization and [2+2] cycloaddition [196].

n	F	G	Conversion (%)
3			100:0
5			0:100

[2+2] cycloaddition reactions bearing the various carbon chain lengths were computationally investigated (Table 7.1) [196].

Secondly, competition reactions proved that the formation of thiophene 9 was the fastest pathway in all cases, with an isolation yield ranging from 77% to 84%. No benzothiophenes 15 or [2+2] cycloaddition adducts 14 were detected in the crude mixture. Such a difference of reactivity between a vinyl sulfide and a phenyl sulfide is not surprising, as the latter would require a higher energy to break the aromaticity of the phenyl ring during the cyclization step. A DFT study was performed in order to elucidate the favorable formation of the thiophene in Figure 7.6 [197]. Note that, electrocyclization reaction of KI was further discussed in the following chapter.

Lastly, the effect of alkyl chain length (addition of one more methylene group (-CH₂-) in intramolecular [2+2] reaction were experimentally exined in order to discern which cycle (five or six) was easier to form in 16. Internal competition reaction was performed and cyclobutane iminium 17 was the only intermediate formed and no trace of 18 was detected (confirmation by ROESY correlations on the product resulting from the reduction of the iminium). In order to explore and rationalize the reactivity differences in the intramolecular [2+2] cycloaddition reaction a computational study was performed at the M06-2X/6-31+G(d,p) in CHCl₃ (Figure 7.7) [187].

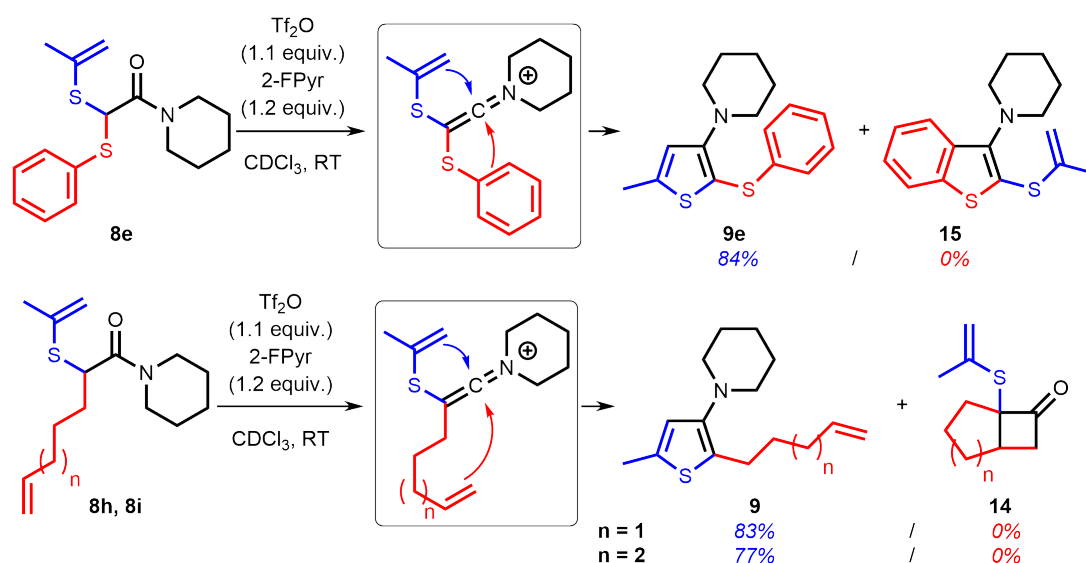


Figure 7.6: Intramolecular competition reactions between formation of thiophene, benzothio-phenene, and [2+2]-cycloadduct.

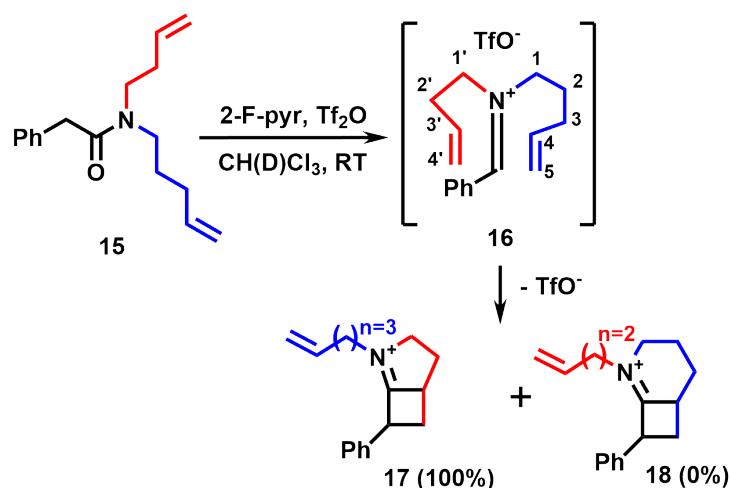


Figure 7.7: Intramolecular competition reaction to access five vs six membered rings [187].

7.2 Methodology

7.2.1 Computational Methodology for KI Formation Study

A density functional theory (DFT) study was performed where KI formation reactions were modeled using a hybrid meta-generalized gradient-approximation (HM-GGA) via the M06-2X functional [65, 76]. M06-2X was selected for its well-known performance in functional organic systems and its inclusion of dispersion effects [198, 199]. The 6-31+G(d,p) basis set was employed for all atoms, except sulfur for which the 6-311++G(3df,3pd) extra basis set was used for higher accuracy [200, 201]. The effect of the solvent environment was modelled by means of the self-consistent reaction field (SCRF) theory [84] using the IEF-PCM approach

[85, 202] as implemented in the Gaussian 16 (G16, Revision A.03) program package [203]. Geometry optimizations were performed in chloroform (CHCl_3 , $\epsilon=4.7113$) and dichloromethane (CH_2Cl_2 , DCM, $\epsilon=8.93$) taking into account the experimental conditions for each reaction. All free energy values are relative to the corresponding separate reactants and are reported at 298 K and 1 atm. Free energy of reactions (ΔG_{rxn}) was calculated using product complex (PC). Intrinsic reaction coordinate [204, 205, 206, 207, 208] (IRC) calculations were performed for all systems in order to verify and track each transition state (TS) leading to its corresponding reactant, intermediate and product. Distortion/interaction energy [209, 210, 211] was conducted for further investigation of substituent effects using the M06-2X/6-31+G(d,p) in CHCl_3 . Frontier molecular orbitals (FMO)[212, 213] and reactivity descriptors[90, 91] were performed using the 6-311++G(d,p) basis set and the 6-311++G(3df,3pd) extra basis set was used for sulfur atoms. FMO and the descriptors were analyzed and calculated using Multiwfn (version 3.7)[214]. HOMO and LUMO orbitals were visualized using Chemissian (version 4.60) developed by Skripnikov[215]. CYLview (version 1.0b) was used for the illustration of the studied structures[216].

7.2.2 Computational Methodology for [2+2] Cycloaddition Study

Density functional theory (DFT) calculations utilizing the meta-hybrid GGA M06-2X were performed. M06-2X was chosen for its well-known performance in organic systems with dispersion effects. The effect of the solvent environment was taken into account by means of the self-consistent reaction field (SCRF) theory. Geometry optimizations were employed in chloroform (CHCl_3 , $\epsilon=4.7113$) within the integral equation formalism-polarizable continuum (IEF-PCM) model as implemented in the Gaussian 09 (G09) program package [217]. Intrinsic reaction coordinate (IRC) calculations were performed to trace each transition state (TS) to its corresponding reactant, intermediate or product. All free energies are reported at 298K and 1 atm. CYLview software[216] was used for visualization of the computed structures.

7.2.3 Computational Methodology for the Intramolecular Competition Reaction Studies

All optimizations were carried out the widely used hybrid meta-GGA functional, at the M06-2X/6-31+G(d,p) level of theory using IEF-PCM [85, 202] with the Gaussian software package (G09 [217] for the first and third study). The meta-GGA M06-2X was utilized due to its well-known effectiveness in organic systems with dispersive effects [65, 76, 218].

In the first study, 6-311++G(3df,3pd) extra basis was used for the sulfur atom in order to provide more accurate results [200, 201]. For each transition state (TS), corresponding reactant and products were verified through intrinsic reaction coordinate (IRC) calculations [204, 205, 206, 207, 208]. Additionally, BMK [219] and MPW1K [77] kinetic functionals were employed for energy refinements to provide accurate evaluation of the activation barriers [200, 220].

In the second study, all optimizations were performed using in Gaussian 16 (G16, Revision A.03) [203]. 6-311++G(3df,3pd) extra basis set was used for the sulfur atoms to attain more accurate results [200, 201]. In order to evaluate the activation barriers accurately energy refinements were performed with hybrid-GGA MPW1K, range-separated CAM-B3LYP[221]

and double hybrid B2PLYP[78] functionals.

7.3 Results and Discussion

This section covers the results and discussions of a) KI formation, b) [2+2] cycloaddition reaction and c) intramolecular competition reactions.

7.3.1 KI Formation Study

As discussed above, KI formation from the reaction of tertiary amides with triflic anhydride and collidine was mostly used method [30]. The reaction mechanism consists of three consecutive steps as depicted in Figure 7.8. The first step is the electrophilic activation of the amide with triflic anhydride, providing a transient O-triflyliminium triflate, which at the second step, upon reaction with collidine, gives the corresponding α -trifloylenamine. Then the enamine undergoes elimination to access the desired keteniminium salt in the final step. Computed data shows that the first step, which is the electrophilic activation of the starting amide, is the rate-determining step (RDS) (Figure 7.8). This indicates that the reactivity of the amide towards Tf_2O directly affects the overall KI formation process. Therefore, substituent effects on the C3 and N1 atoms of the amide leading to the corresponding KI were further investigated in this section.

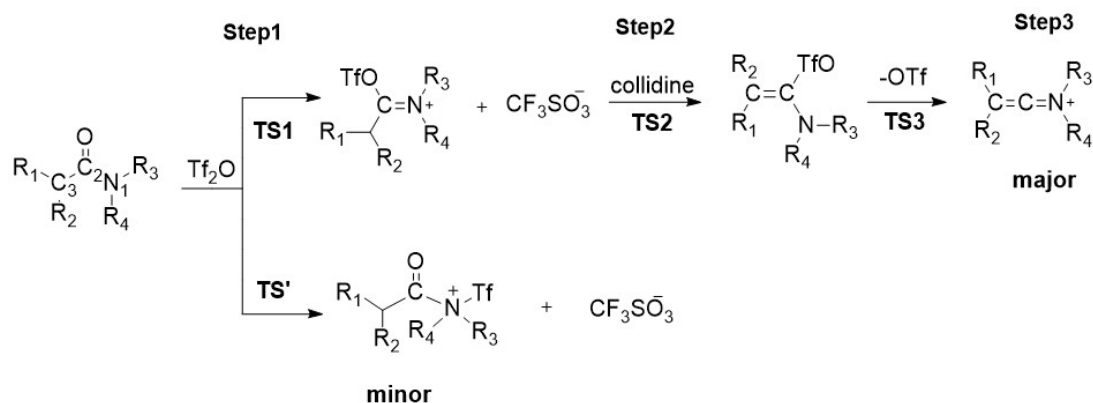


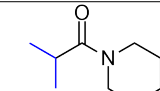
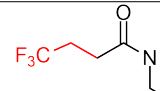
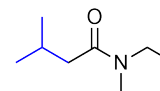
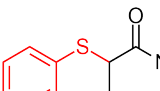
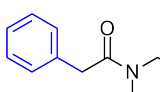
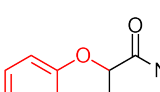
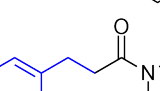
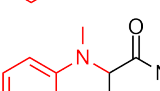
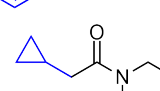
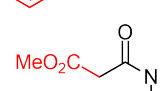
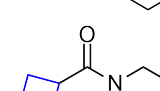
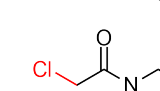
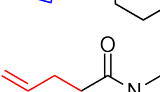
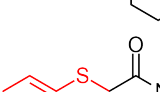
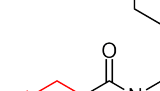
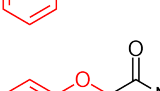
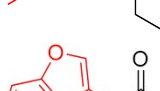
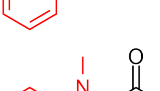
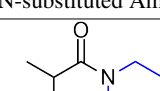
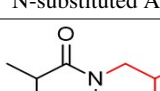
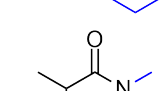
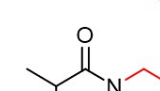
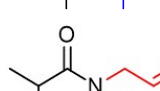
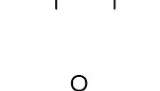
Figure 7.8: Ghosez's KI formation reaction from amides with triflic anhydride.

Various amides, leading to experimentally accessible KIs, were selected. The effects of substituents on the reactivity of the starting amides and KI were inspected under three subsections by means of energetic, frontier molecular orbitals (FMO), and reactivity descriptors.

Energetics Analysis of KI formation

The energetic cost of the formation reactions of KIs with various substituents and their relative reactivities were examined in two groups according to the substituent placement, namely C3 and N1 substituents (Figure 7.8) as mentioned previously. In general, EDGs were shown to decrease activation barrier when compared to EWG substituted amides, regardless of the position of the substituent. Blue colored substituents in Table 7.2 represent EDG while red colored substituents represent EWG groups. The reported barriers herein belong to the RDS.

Table 7.2: Gibbs free energies of activation (ΔG^\ddagger) and reaction (ΔG_{rxn}) for the RDS of Ghosez's reaction with C3 and N substituted amides.

Entry	C3-substituted Amide	ΔG^\ddagger	ΔG_{rxn}	Entry	C3-substituted Amide	ΔG^\ddagger	ΔG_{rxn}
1a		29.8	9.2	10a		31.3	4.8
2a		27.9	7.5	11a		30.1	13.1
3a		28.0	8.9	12a		30.9	11.7
4a		28.6	8.5	13a		30.5	9.2
5a		27.7	5.5	14a		28.5	12.5
6a		27.9	6.7	15a		29.7	14.9
7a		29.6	1.2	16a		28.8	7.7
8a		30.5	11.1	17a		30.1	12.3
9a		28.1	10.7	18a		29.5	7.8
Entry	N-substituted Amide	ΔG^\ddagger	ΔG_{rxn}	Entry	N-substituted Amide	ΔG^\ddagger	ΔG_{rxn}
1a		29.8	9.2	3b		30.6	11.4
1b		30.1	9.9	4b		33.5	22.6
2b		32.6	11.1	5b		33.7	18.7

Amide Reactivity

In the pursuit of energetic analysis of the substituted starting amides and their contribution to formation reactions of KI, the substituent effects on amide reactivity were examined by means of several analysis techniques, namely, Frontier Molecular Orbitals (FMO) and Reactivity Descriptors.

The highest occupied molecular orbitals (HOMOs) and reactivity indices of the amides under study were inspected to rationalize the calculated order of activation barriers by using Multiwfn (version 3.7) [214]. Table 7.3 reveals that while EDGs raise the HOMO energy levels by enriching carbonyl oxygen with electrons, EWGs lower the HOMO energy level in line with the activation barriers (Table 7.2). Intriguingly, the amides bearing heteroatoms (9a, 11a-13a and 16a-17a) also increase the HOMO level due to the electron-donating ability of lone pairs on the heteroatoms. Figure 7.9 depicted that lone pairs of the heteroatoms provide remarkable contributions to the HOMO level and raise the HOMO level. However, smaller HOMO lobes of carbonyl oxygen in the amides (9a and 11a-13a) clarify the higher barriers in the range of 30.5-32.2 kcal/mol compared to larger HOMO lobes of 1a and 5a ($\Delta G^\ddagger = 29.8$ and 27.7 kcal/mol, respectively).

Table 7.3: Calculated HOMO energy (eV), nucleophilicity index (eV), and local nucleophilicity indices for the substituted amides for the substituted amides.(M06-2X/6-311++G(d,p)//M06-2X/6-31+G(d,p) in CHCl₃.)

C3 substituted amides									
		O (C=O)					N1		
Amide	HOMO	Nu	Nu _k	Nu _k	Amide	HOMO	Nu	Nu _k	Nu _k
1a	-8.095	2.509	0.4811	0.4685	10a	-8.291	2.314	0.4463	0.4280
2a	-8.081	2.524	0.4715	0.4751	11a	-7.890	2.715	0.0880	0.0299
3a	-8.123	2.482	0.4713	0.4658	12a	-7.804	2.801	0.0591	0.0143
4a	-8.136	2.469	0.4753	0.4506	13a	-6.784	3.821	0.0604	0.0355
5a	-8.120	2.485	0.4938	0.4597	14a	-8.357	2.248	0.4627	0.4240
6a	-8.091	2.514	0.4779	0.4709	15a	-8.380	2.225	0.4536	0.4009
7a	-8.132	2.473	0.4745	0.4634	16a	-8.031	2.574	0.0886	0.0250
8a	-8.202	2.403	0.4577	0.4474	17a	-7.780	2.824	0.0757	0.0082
9a	-7.587	3.018	0.0715	0.0296	18a	-6.827	3.778	0.1137	0.0181
N substituted amides									
1b	-8.279	2.326	0.4811	0.4685					
1a	-8.095	2.509	0.4865	0.4811					
2b	-8.363	2.242	0.4392	0.4260					
3b	-8.361	2.244	0.4497	0.4369					
4b	-8.944	1.661	0.3628	0.3352					
5b	-8.779	1.826	0.3701	0.3749					

Conceptual DFT is a powerful tool to predict chemical reactivity by way of employing global and local reactivity descriptors [89, 90, 91]. In line with the HOMO energy levels, EDGs

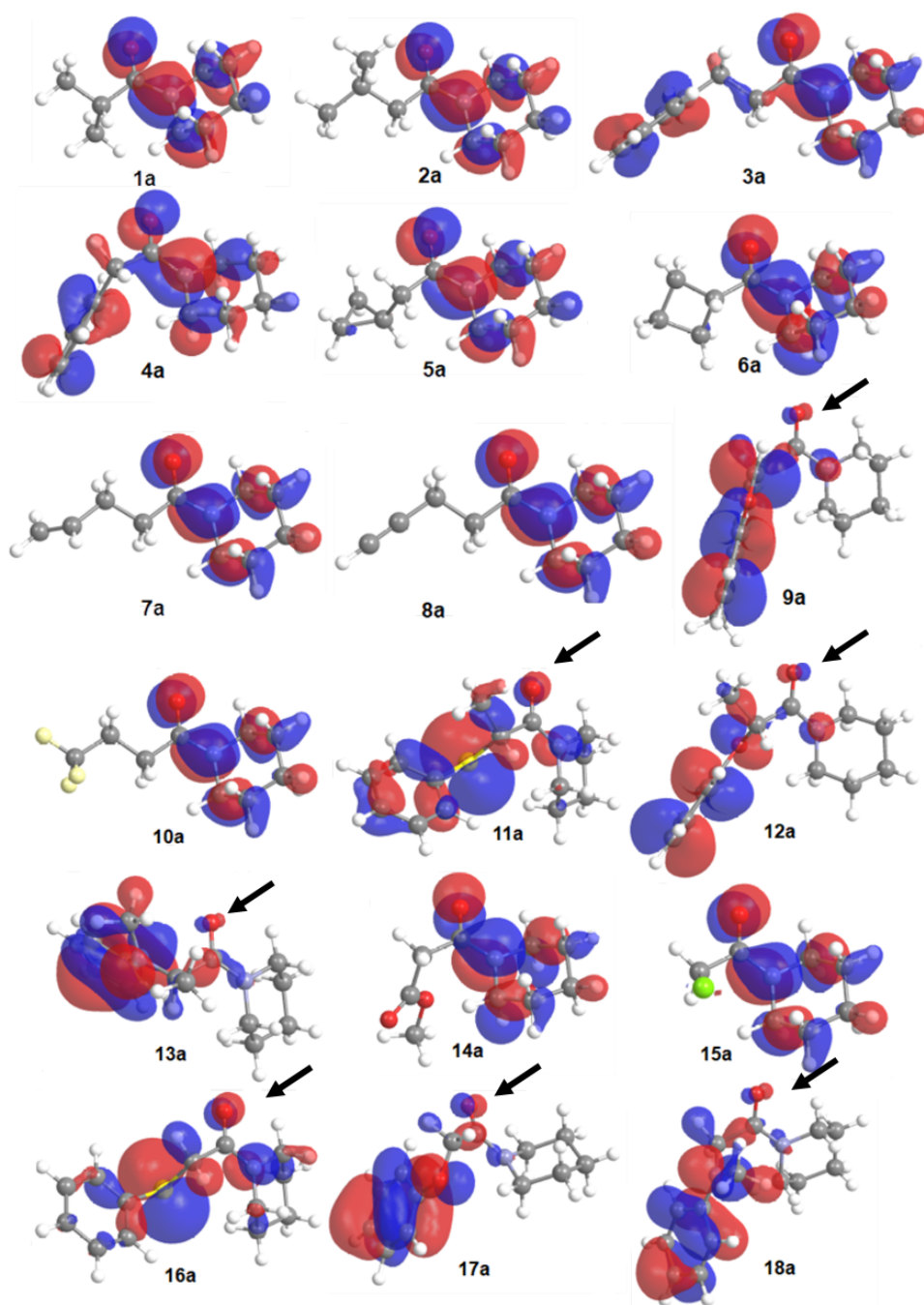


Figure 7.9: HOMO orbitals of C₃-substituted amides. (M06-2X/6-311++G(d,p)//M06-2X/6-31+G(d,p) in CHCl₃, extra basis set for S atom; iso-surface value = 0.03 au)

also enhances the nucleophilicity index (Nu), which is a measure of the nucleophilicity of the starting amides. The nucleophilicity of the amides bearing EDGs are higher than those having EWGs with both C₃ and N substituted amides. EDGs increase the nucleophilicity of the amides and improves the ease for KI formation reaction. Notably, EWGs on nitrogen (4b and 5b) dramatically decrease both HOMO energy levels and nucleophilicity indices in line with higher

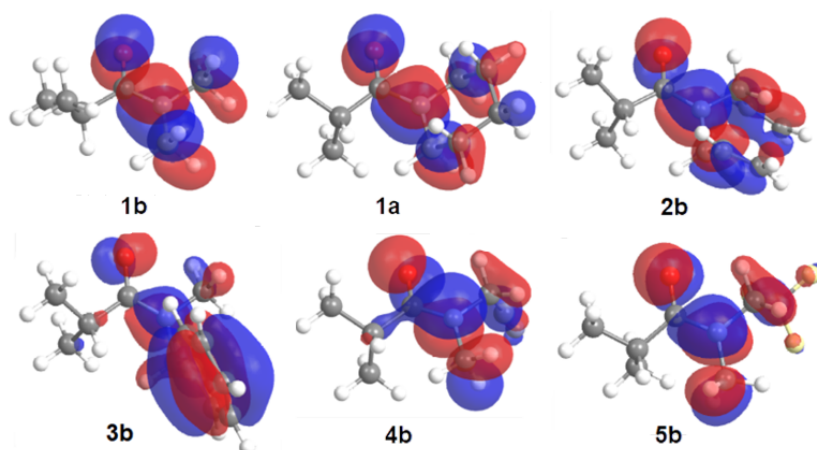


Figure 7.10: HOMO orbitals of N-substituted amides. (M06-2X/6-311++G(d,p)//M06-2X/6-31+G(d,p) in CHCl_3 ; iso-surface value = 0.03 au)

activation barriers ($\Delta G^\ddagger \approx 33.6$ kcal/mol). Moreover, Fukui, local nucleophilicity indices and dual descriptors were analyzed for the amides with heteroatoms, the descriptors are higher on hetero atoms than the carbonyl oxygen, showing the reason of decrease in nucleophilicity and increase in HOMO levels for these systems (Table 7.4). Taken together, the outcomes of HOMO levels and nucleophilicity indices are in line with the energetic results.

Higher Fukui indices (f^-) and local nucleophilicity index (Nu_k) on carbonyl oxygen of the amides in Tables 7.3 and 7.4 indicates higher nucleophilicity of this oxygen, in turn, higher reactivity of the carbonyl oxygen leading to KIs. More importantly, the differences in local reactivity descriptor values between carbonyl oxygen and nitrogen results encourage us to investigate the side reaction barriers of the amides with selected substituents. The amides with smaller (1a, 2a, 10a, and 1b) and larger (5a, 9a, 15a and 4b) Nu_k were selected to get insight into the effect of the substituents on the side reaction. Table 7.5 depicted the activation barriers differences between the main and the side reaction for the selected amides. Free energy of activation differences shows the amides bearing EWGs tend to decrease the activation barriers of the amides leading to KIs (major product). Intriguingly, the TSs (TS-15a and TS-4b) of Ghosez reaction with 15a and 4b leading to KIs (KI-15a and KI-4b) are kinetically favored over those of their side reactions by 2.8 and 2.6 kcal/mol, respectively. The differences in activation barriers may indicate that kinetic product can be changed by using the suitable substituents. Additionally, contrary to 1a and 1b, which lead to keto-KI, the use of the amide leading to aldo-KI may increase the activation barrier of the side reaction and, thus, decrease the formation of N-sulfonylated minor product.

KI Reactivity

Finally, we evaluated how reactivity of the amides correlates to the reactivity of the resulting KIs. Therefore, FMO and reactivity descriptor analysis on all KI's studied was performed.

The substituent effects on the lowest unoccupied molecular orbital (LUMO) energies and electrophilicity of the KIs were analyzed to investigate the relationship with amide reactivity and predict electrophilic behaviors of resulting KIs (Table 7.6). Notably, KI reactivity is in-

versely correlated to the activation barriers for the formation of KI. Unlike amide reactivity, electrophilicity of KI impacts on KI reactivity. EWGs lower the LUMO level leading to decrease in the HOMO-LUMO gap and increases the reactivity of the KIs leading to lower energy barrier. In line with the LUMO energy level, electrophilicity index (ω) of the KIs with EWG is higher than KI with EDGs due to rendering central carbon of KI more electrophilic and increasing reactivity of KIs. This intriguing reverse connection will be further investigated in an upcoming paper to give comprehensive insight on the KI reactivity.

Table 7.4: Calculated condensed fukui (f-) and condensed dual descriptors (CDD) for the heteroatom substituted amides.

C-subst. amide	X=S,O,N			O (carbonyl oxygen)		N ₁ atom	
	f-	CDD	Nu _k	f-	CDD	f-	CDD
1a	-	-	-	0.1917	-0.1742	0.1867	-0.1844
2a	-	-	-	0.1868	-0.1726	0.1882	-0.1858
3a	-	-	-	0.1899	-0.1818	0.1877	-0.1844
4a	-	-	-	0.1925	-0.1750	0.1825	-0.1783
5a	-	-	-	0.1987	-0.1808	0.1850	-0.1839
6a	-	-	-	0.1901	-0.1724	0.1873	-0.1853
7a	-	-	-	0.1919	-0.1819	0.1874	-0.1833
8a	-	-	-	0.1905	-0.1713	0.1862	-0.1816
9a	0.0515	-0.0093	0.1554	0.0237	-0.0085	0.0098	-0.0069
10a	-	-	-	0.1929	-0.1758	0.1850	-0.1798
11a	0.4378	-0.3318	1.1885	0.0324	-0.0071	0.0110	-0.0045
12a	0.1122	-0.0956	0.3142	0.0211	-0.0085	0.0051	-0.0037
13a	0.1469	-0.1453	0.5612	0.0158	-0.0056	0.0093	-0.0080
14a	-	-	-	0.2058	-0.1713	0.1886	-0.1842
15a	-	-	-	0.2039	-0.0996	0.1802	-0.1490
16a	0.4956	-0.3821	1.2759	0.0344	-0.0089	0.0097	-0.0033
17a	0.1104	-0.0921	0.3118	0.0268	-0.0100	0.0029	0.0002
18a	0.1430	-0.1330	0.5402	0.0301	-0.0141	0.0048	-0.0034
N-subst. amide	O (carbonyl oxygen)		N1 atom				
	f-	CDD	f-	CDD			
1a	0.1917	-0.1742	0.1867	-0.1844			
1b	0.2091	-0.1918	0.2068	-0.1998			
2b	0.1959	-0.1832	0.1900	-0.1899			
3b	0.2004	-0.1809	0.1947	-0.1955			
4b	0.2184	-0.2006	0.2018	-0.1917			
5b	0.2027	-0.1642	0.2053	-0.1898			

Table 7.5: Calculated activation barrier differences between main reaction leading to KI major product and side reaction leading N-sulfonylated minor product. (Prime sign (') refers to TS of side reaction.)

	ΔG^\ddagger	$\Delta\Delta G^\ddagger$		ΔG^\ddagger	$\Delta\Delta G^\ddagger$
TS-1a	29.8	1.8	TS-12a	30.9	-0.2
TS-1a'	28.0		TS-12a'	31.1	
TS-2a	27.9	0.7	TS-15a	29.7	-2.8
TS-2a'	27.2		TS-15a'	32.5	
TS-5a	27.7	0.1	TS-1b	30.1	2.6
TS-5a'	27.6		TS-1b'	27.5	
TS-9a	28.1	-0.3	TS-4b	33.5	-2.5
TS-9a'	28.4		TS-4b'	36.0	
TS-10a	31.3	-0.5	TS-5b	33.7	-4.2
TS-10a'	31.8		TS-5b'	37.9	

7.3.2 Results and Discussion of [2+2] cycloaddition Study

A computational study was performed to rationalize the experimentally observed reactivity difference in the [2+2] cycloaddition of keteniminium 1 with olefins 2 and 3 (Figure 7.4) [195]. All possible reaction pathways for the [2+2] cycloaddition of keteniminium 1 with alkenes 2 and 3 were computationally explored (Figure 7.11). The conformational space, including spatial orientations within pre-reactive complexes (PRCs), were thoroughly investigated. Calculations verified a stepwise reaction mechanism, where the initial transition state TS1 leads to a highly strained cyclopropane-like intermediate INT; this is incidentally the rate-determining step (Figure 7.12). Figure 7.12 depicts transition state geometries for the rate-determining step and the corresponding intermediates. The reaction path subsequently bifurcates, resulting in two transition states TS2, which lead to two cyclobutaniminiums. The major product is determined by the steric clash of substituent groups in TS2 (Figure 7.11). In line with the experiment, cyclobutaniminium 4, which results from the [2+2] cycloaddition of 1 and 2, is both the kinetic and the thermodynamic product in the competition reaction between allylammonium 3 and corresponding alkene 2 (Figure 7.12). The free energy of activation for the cycloaddition of 1 and 3 ($\Delta G^\ddagger = 42.5$ kcal/mol) is significantly high, validating the assumption that alkylammonium 3 is unreactive towards cycloaddition with 1 due to the electron withdrawing nature of the cationic quaternary amine.

Frontier Molecular Orbital (FMO) analysis [212, 213] and Natural Population Analysis (NPA) [87] were carried out at the same level of theory. FMO was investigated in order to evaluate the reactivity difference between 2 and 3 (Figure 7.12). The HOMO-LUMO gap between HOMO of 2 and LUMO of 1 (4.01 eV) is considerably smaller than the corresponding gap for 3 and 1 (8.81 eV) (Figure 7.13). The small gap between 1 and 2 implies high reactivity and larger orbital interaction and is consistent with experimental data. Moreover, FMO analysis

Table 7.6: Calculated LUMO energy and electrophilicity index for the substituted KIs. M06-2X/6-311++G(d,p)//M06-2X/6-31+G(d,p) in CHCl₃. Units in eV.

Entry	KI	LUMO	ω	Entry	KI	LUMO	ω
C3 substitution							
KI-1a		-1.547	2.437	KI-10a		-2.012	2.818
KI-2a		-1.681	2.552	KI-11a		-2.009	2.795
KI-3a		-1.822	2.495	KI-12a		-1.999	2.798
KI-4a		-1.691	2.488	KI-13a		-1.759	2.591
KI-5a		-1.712	2.544	KI-14a		-2.176	2.964
KI-6a		-1.864	2.685	KI-15a		-2.637	3.376
KI-7a		-1.727	2.526	KI-16a		-2.107	2.890
KI-8a		-1.926	2.720	KI-17a		-2.246	3.022
KI-9a		-1.821	2.668	KI-18a		-1.717	2.520
N substitution							
KI-1b		-1.620	2.504	KI-3b		-1.512	1.782
KI-1a		-1.547	2.437	KI-4b		-2.070	2.894
KI-2b		-1.719	2.549	KI-5b		-2.045	2.860

shows that the cationic center has significantly lowered the HOMO of 3, rendering it unreactive.

Similarly, NPA results reveal, as expected, a considerably larger negative charge on carbon C3 of 2 (-0.456), compared to that of 3 (-0.362), indicating higher reactivity in the former alkene (Table 7.7). Note that electron density distributions on carbons C3 and C4 are approximately

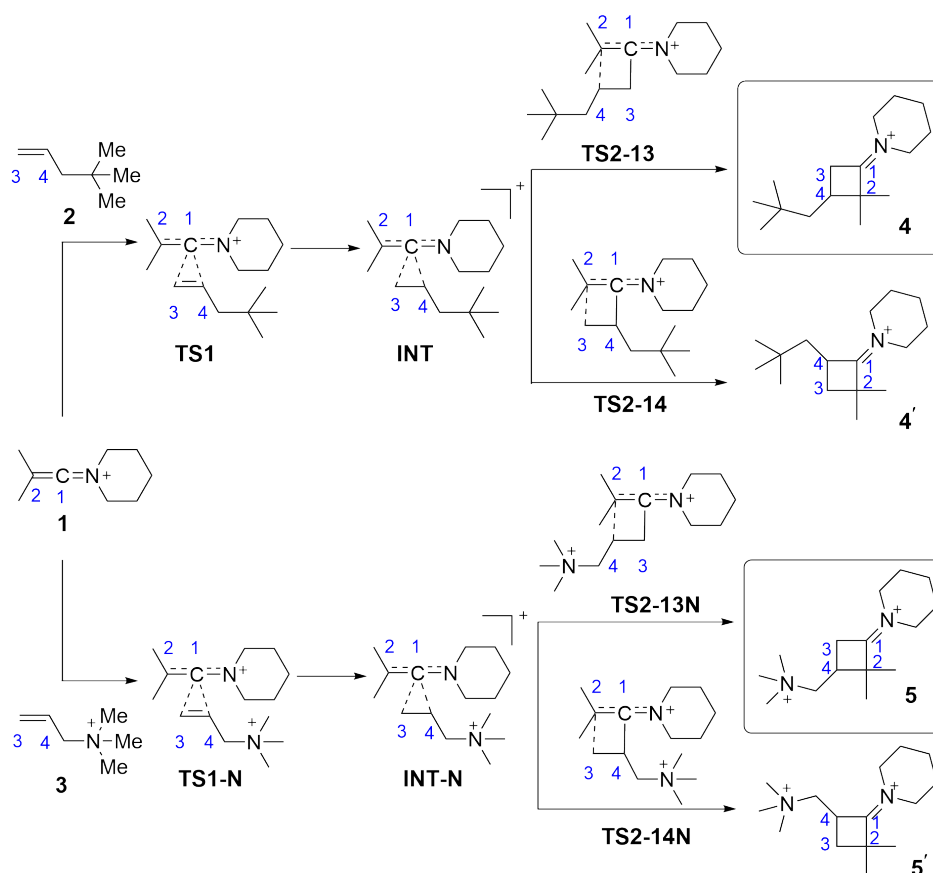


Figure 7.11: Possible reaction mechanisms for the [2 + 2] cycloaddition of keteniminium 1 with olefins 2 and 3.

equal in allylammonium 3, whereas C3 has a significantly higher negative charge than C4 in 2. The difference in the charge distributions is reflected in the critical distances in Figure 7.12, where INT and INT-N bond lengths are shown to be significantly different. Moreover, NPA charges on the allylic double bond of *N,N*-diallyl-ket closely resemble those of allylammonium 3 (Table 7.7), which was specifically chosen to mimic the reactivity of *N*-allyl substituents. Thus keteniminium *N*-allyl substituents are predicted to be similarly unreactive toward cycloaddition.

The competition reaction depicted in Figure 7.5 was modeled at the same level of theory to understand the difference in reactivity of alkyne 10, alkenes 11 and 12 toward cycloaddition with KI 1 [195]. Reaction barriers were compared to identify the most feasible reaction, revealing alkyne 10 as the most reactive reaction partner and cyclobuteniminium 13, the major product of the competition reaction, as both the kinetic and the thermodynamic product (Table 7.8), with highly exergonic reaction energies. Both the reaction mechanisms and the energetic results are in good agreement with a recent study by Domingo et. al.[222] which investigated the reaction mechanism for the [2+2] cycloaddition of keteniminiums with acetylene and propyne at the MPWB1K/6-311G(d,p) level of theory [223]. Note that unlike the cycloaddition of allylammonium 3, which is predicted to have a very high activation barrier ($\Delta G^\ddagger = 42.5$ kcal/mol, Figure 7.12) and therefore, deemed unlikely, alkenes 11 and 12 (Table 7.8) have comparable activation barriers with alkene 2 and are experimentally reported to react with keteniminium 1

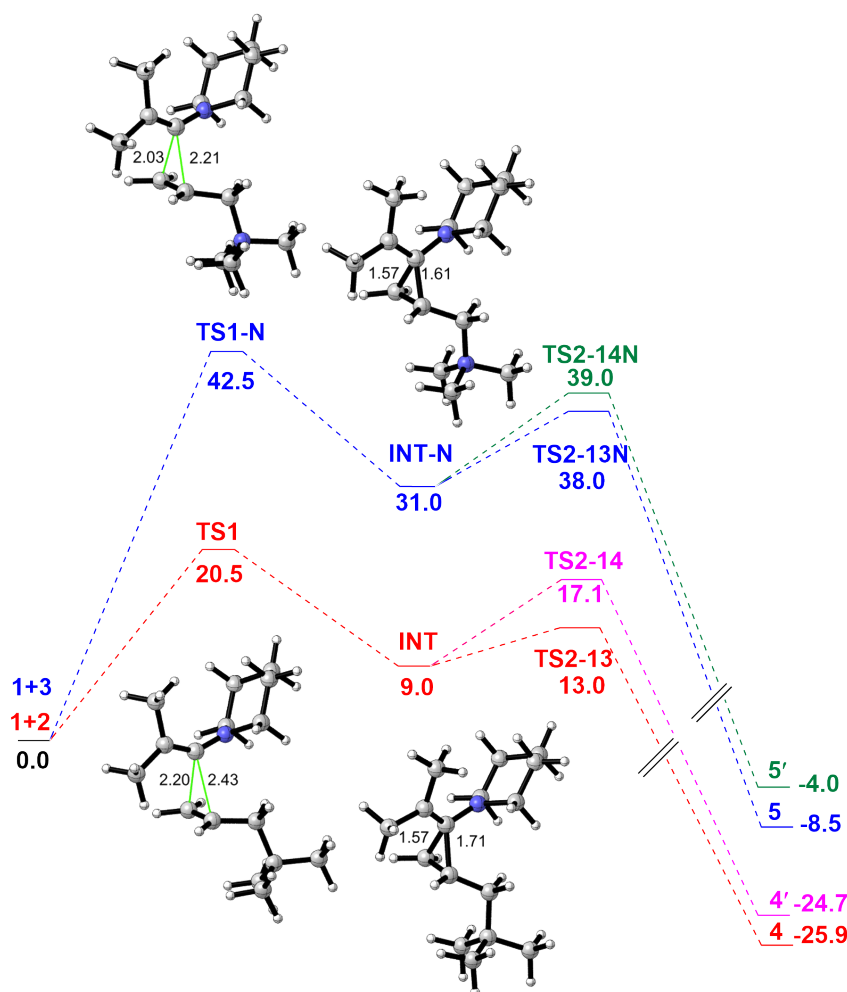


Figure 7.12: Free energy profile for the [2+2] cycloaddition reaction of KI 1 with alkenes 2 and 3. Optimized transition states TS1 and intermediates. M06-2X/6-31+G(d,p) with IEF-PCM in CHCl_3 ; free energies in kcal/mol.

at different reaction rates that are fully consistent with the computed relative barriers, depicting cis-alkene 11 to be slightly more reactive than trans-alkene 12. Note that 11 leads to one product due to symmetry.

7.3.3 Intramolecular Competition Reactions between [2+2] Cycloaddition vs Electrocyclization

In the first competition reaction, a DFT study was performed to investigate the intramolecular competition reaction between 6π -electrocyclization and [2 + 2] cycloaddition reactions bearing the various carbon chain lengths ($n = 3$ and 5) in Table 7.1 [196]. Previous computational studies revealed that the [2 + 2] cycloaddition is a stepwise reaction, where the rate-determining step (RDS) is the initial addition of the central carbon atom of the KI onto the π -system, corresponding to TS-i.[187, 193, 222] Therefore, TS-i was used for comparison in the competition

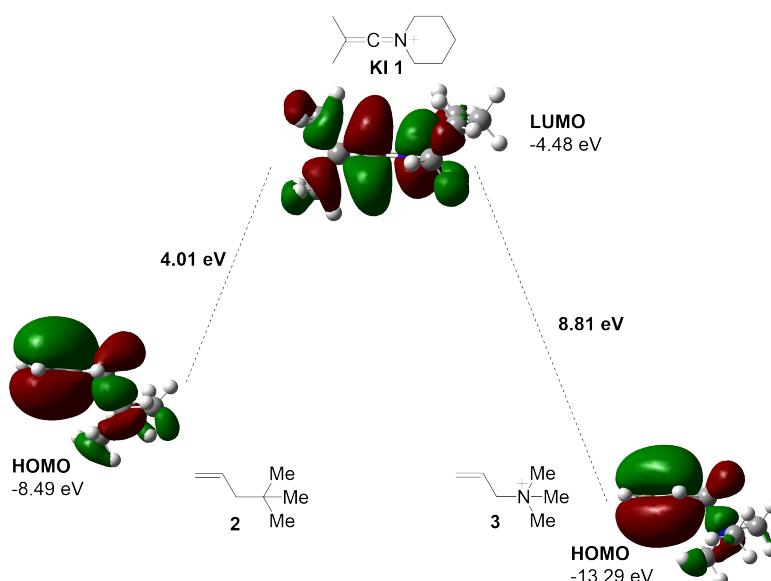
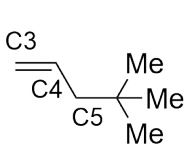
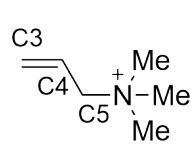
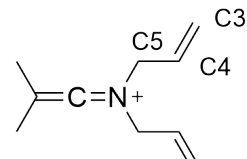


Figure 7.13: HOMO-LUMO gaps between KI 1 and alkenes 2 and 3. M06-2X/6-31+G(d,p); iso-surface value = 0.02 au.

Table 7.7: Natural Population Analysis (NPA) of alkenes 2, 3, and *N,N*-diallyl keteniminium. M06-2X/6-31+G(d,p).

			
2	3	<i>N,N</i>-diallyl-ket	
	C3	C4	C5
2	-0.456	-0.223	-0.498
3	-0.362	-0.319	-0.291
<i>N,N</i>-diallyl-ket	-0.376	-0.298	-0.295

reactions. The computed data showed that the activation barrier for the [2 + 2] cycloaddition reaction of E ($n = 3$) ($\Delta G^\ddagger = 10.8$ kcal/mol) is significantly lower than the electrocyclization reaction ($\Delta G^\ddagger = 21.4$ kcal/mol) reflecting the higher conversion of Fn=3 (100%). Moreover, the [2 + 2] cycloaddition reaction of E ($n = 3$) is also highly exergonic ($\Delta G_{\text{rxn}} = -34.5$ kcal/mol) compared to electrocyclization of En=3 ($\Delta G_{\text{rxn}} = 8.2$ kcal/mol). Hence, the cycloaddition reaction of En=3 is favored both kinetically and thermodynamically, validating the experimentally observed outcome. BMK and MPW1K results ($\Delta G^\ddagger = 10.3$ kcal/mol and 8.4, respectively) are consistent with the M06-2X results (Figure 7.14 and Table 7.9). In the case of En=5, BMK and MPW1K considerably lowered the activation barrier of electrocyclization reaction ($\Delta G^\ddagger = 16.1$ kcal/mol and 14.0, respectively) and the computational data is in agreement with the ex-

Table 7.8: Free energies of activation (ΔG^\ddagger) and reaction (ΔG_{rxn}) (kcal/mol) for the [2 + 2] cycloaddition reaction of KI 1 with alkyne 10, alkenes 11 and 12. M06-2X/6-31+G(d,p) with IEF-PCM in CHCl_3 .

Reaction	ΔG^\ddagger_1	ΔG^\ddagger_2		ΔG_{rxn}	
		i	ii	i	ii
KI 1 + alkyne 10	17.0	11.4	12.2	-41.4	-39.7
KI 1 + <i>cis</i> -alkene	19.8	15.7		-23.2	
KI 1+ <i>trans</i> -alkene	21.2	17.8	19.3	-25.5	-25.6

perimental observations. Figure 7.14 shows that even if the [2 + 2] cycloaddition reaction of E ($n = 5$) leads to thermodynamically more stable product, due to the higher difference in Gibbs free energy of activation ($\Delta\Delta G^\ddagger = 5.5$ kcal/mol) the electrocyclization reaction is kinetically favored over the cycloaddition reaction in line with the experimental results. $E_{n=5}$ affords the kinetic product $G_{n=5}$ (100%) as the major product of the competition reaction. Figure 7.15 demonstrates transition state structures for the studied systems. Consequently, computational findings allowed us to determine favorable kinetic and thermodynamic pathways and investigate the effect of chain length on the competition reaction.

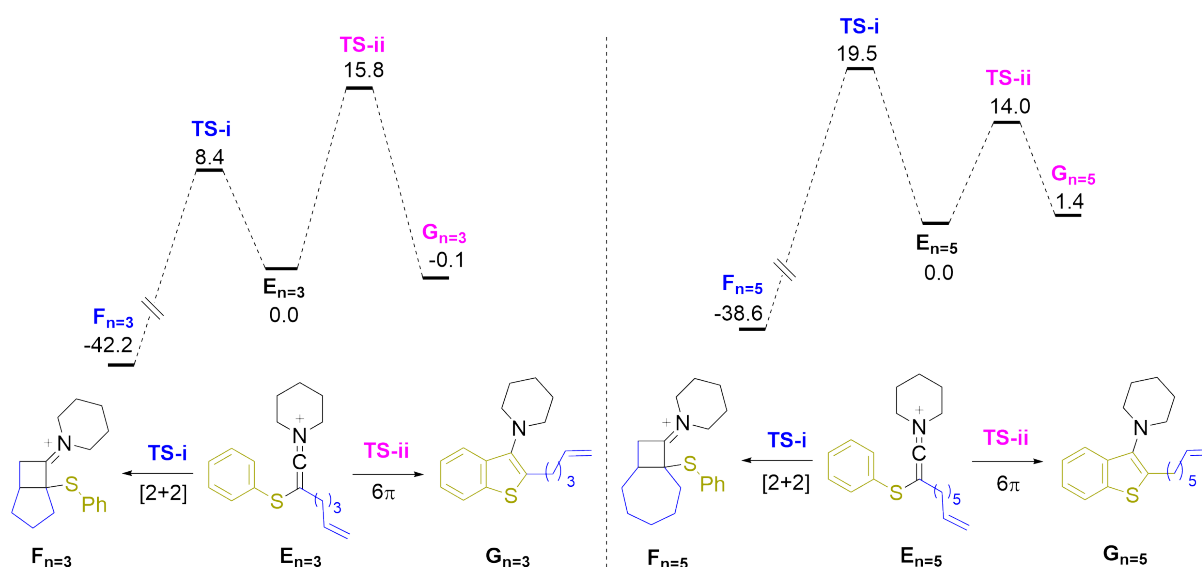


Figure 7.14: Free energy profiles for the competition reactions. MPW1K/6-31+G(d,p)//M06-2X/6-31+G(d,p) with IEF-PCM in CHCl_3 ; 298 K and 1 atm; free energies in kcal/mol; 6-311++G(3df,3pd) extra basis set for sulfur atom.

In the second competition reaction, a DFT study was performed to investigate the reactivity differences of the intramolecular competition reactions between formation of thiophene, benzothiophene and [2+2]-cycloadduct, and rationalize the favorable formation of the thiophene in Figure 7.6 [197]. Table 7.10 displays Gibbs free energies of activation (ΔG^\ddagger) and

Table 7.9: Gibbs free energies of activation (ΔG^\ddagger) and reaction (ΔG_{rxn}) (kcal/mol) for the competition reaction.

	BMK/6-31+G(d,p)				MPW1K/6-31+G(d,p)				Exp.
	Path i	Path ii	Path i	Path ii	Path i	Path ii	Path i	Path ii	
	ΔG^\ddagger		ΔG_{rxn}		ΔG^\ddagger		ΔG_{rxn}		
n=3	10.3	18.3	-42.0	3.9	8.4	15.8	-42.2	-0.1	100:0
n=5	19.4	16.1	-39.8	4.8	19.5	14.0	-38.6	1.4	0:100

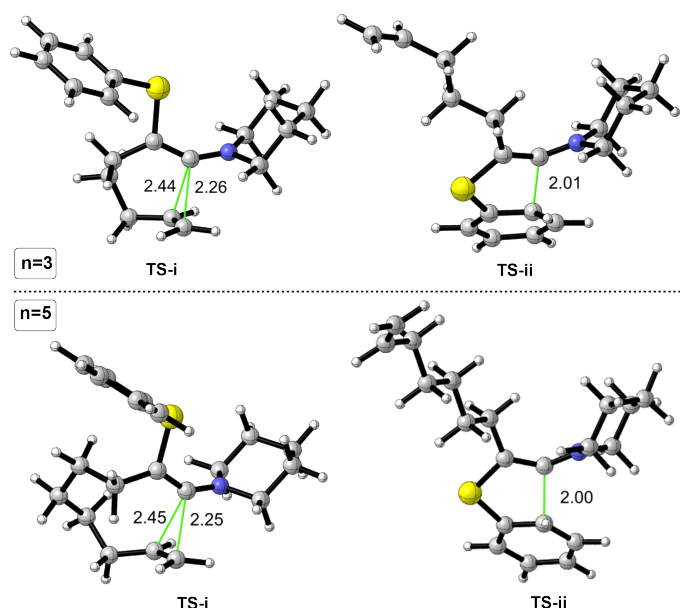
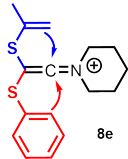
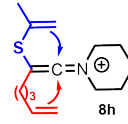


Figure 7.15: Optimized TSs for the intramolecular [2+2] cycloaddition and 6π electrocyclization of En=3 and En=5. M06-2X/6-31+G(d,p) with IEF-PCM in CHCl_3 ; 298 K, 1 atm; critical distances in Å. 6-311++G(3df,3pd) basis set for sulfur atom.

reaction (ΔG_{rxn}), respectively. Energies in kcal/mol at 298 K and 1 atm. Regardless of the level of theory similar barrier trends were observed. In the cycloaddition reaction of 8h, only the first transition state (TS1) results were presented, since previous studies disclosed that the rate-determining step of the stepwise [2+2] cycloaddition reaction is the initial addition of the central carbon atom of the KI onto the π -system of pentenyl [187, 193, 196, 222, 224]. In the competition reaction of 8e, due to the disruption of the aromaticity, the activation barrier for the formation of benzothiophene ($\Delta G^\ddagger = 16.4$ kcal/mol) is significantly higher than the barrier of the formation of thiophene ($\Delta G^\ddagger = 8.3$ kcal/mol). The formation of thiophene is both kinetically and thermodynamically favored in line with the experimentally observed findings (100%) (Figure 7.6 and Table 7.10). Similarly, in the case of 8h, energetic analysis showed that 8h undergoes 6π -electrocyclization reaction rather than the cycloaddition reaction. The activation barrier for the electrocyclization is considerably lower than the cycloaddition reaction validating the experimental outcome. Major product of the competition reaction for 8h is the kinetic product 9h

(100%). Consistent with the experimental studies, the formation of thiophene (9e and 9h) is preferred over both the formations of the benzothiophene 15e and [2+2]-cycloadduct 14h. Additionally, in our previous study, competition reaction between 6 π -electrocyclization reaction to give benzothiophene and [2+ 2] cycloaddition reaction to give the cyclobutaniminium were investigated at the same level of theory (MPW1K/6-31+G(d,p)//M06-2X/6-31+G(d,p)) [196]. In that study, due to the significantly lower activation barrier, the cycloaddition reaction ($\Delta G^\ddagger = 8.4$ kcal/mol) was favored both kinetically and thermodynamically over 6 π -electrocyclization leading to the formation of benzothiophene ($\Delta G^\ddagger = 15.8$ kcal/mol). Taken together, in the light of both experimental and computational studies, it can be deduced that the ease of formation of the major product is follows: thiophene > [2+2]-cycloadduct > benzothiophene, respectively.

Table 7.10: Gibbs free energies of activation (ΔG^\ddagger) and reaction (ΔG_{rxn}) for the competition reactions.

		MPW1K/6-31+G(d,p)	CAM-B3LYP/6-31+G(d,p)	B2PLYP/6-31+G(d,p)	Exp.
 8e	ΔG^\ddagger	8.3	10.0	13.4	100
	ΔG_{rxn}	-30.8	-25.4	-20.6	
	ΔG^\ddagger	16.4	19.2	23.7	0
	ΔG_{rxn}	2.5	7.2	11.4	
 8h	ΔG^\ddagger	9.3	10.8	13.9	100
	ΔG_{rxn}	-27.3	-22.5	-18.0	
	ΔG^\ddagger	11.0	13.5	16.7	0
	ΔG_{rxn}	-39.5	-30.7	-26.7	

7.3.4 Intramolecular [2+2] Cycloaddition Competition Reactions

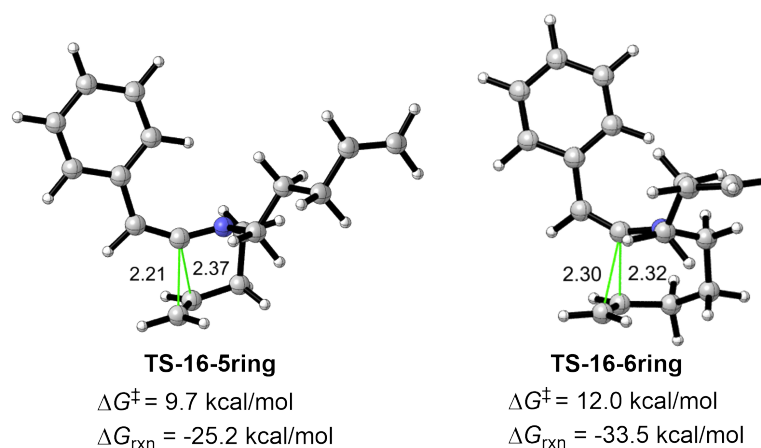


Figure 7.16: Optimized TS structures for the intramolecular cycloaddition of 16. M06-2X/6-31+G(d,p) with IEF-PCM in CHCl_3 ($\epsilon=4.7113$); critical distances in Å.

In order to explore the intramolecular competition reaction of keteniminium 16 (Figure 7.7), a computational study was performed at the M06-2X/6-31+G(d,p) level of theory in CHCl_3

[187]. Previous computational works[195, 222] revealed the first step (binding of the central carbon of the KI to the olefin) in intermolecular [2+2] cycloadditions of keteniminiums to be rate determining. Herein, the reaction profile for the intramolecular [2+2] reaction was re-examined to verify the step that will determine the ultimate outcome. It was shown that the first step of the reaction is still rate-determining. Moreover, computed data revealed that first transition state 16-5ring leading to 17 is favored over that of its counterpart, 16-6ring leading to 18, by 2.3 kcal/mol, while product stabilities favored 18 by 8.3 kcal/mol. Optimized transition state geometries for the first TSs leading to 17 and 18 are depicted in Figure 7.16. In line with the experimental findings, the difference in activation barriers for the first step indicate 17 is the kinetic product and the competition reaction is dictated by kinetic rather than thermodynamic factors.

7.4 General Conclusions

In KI formation study, the reactivity of the starting nucleophilic amides towards the electrophilic triflic anhydride directly affects the ease of formation of the KI. EDGs on both C3 and N1 atoms of the starting amide generally lowers the activation barriers of the RDS. Additionally, the energetic findings were supported with distortion/interaction model, FMO, and reactivity descriptors. Lastly, reverse relationship was observed between amide and KI reactivities. While nucleophilicity of the amides affect the reactivity, electrophilicity of the KIs plays a pivotal role on KI reactivity. In an upcoming paper/As a future work, this relationship will be further investigated.

In [2+2] cycloaddition study, DFT calculations rationalize the experimentally observed reactivity difference in the [2+2] cycloaddition of keteniminium and olefins. The reaction takes place with stepwise fashion. Each reaction (mechanism) involves an initial transition state (TS1) leading to an intermediate which follows a bifurcated path resulting in two transition states (TS2), and two products. The major product is determined by the steric clash of substituent groups in TS2. TS1 is the rate determining step (RDS). Computed data also verified the compatibility/use of *N*-allyl KI in [2 + 2] cycloaddition reactions.

In the intramolecular competition studies, favorable kinetic and thermodynamic pathways were determined and the computed data displayed the effect of chain length on the competition reaction between [2 + 2] cycloaddition and electrocyclization reactions. DFT calculations have verified the ease of the formation of thiophene for the competition reactions. This can be emphasized that the ease of formation of the major product is follows: thiophene > [2+2]-cycloadduct > benzothiophene, respectively. Lastly, in intramolecular [2+2] cycloaddition study, computed data have verified that the [2+2] cycloaddition step is driven by kinetic and not thermodynamic factors confirming all experimental observations.

Chapter 8

Keteniminium Salts: Reactivity and Propensity toward Electrocyclization Reactions

8.1 Introduction

Electrocyclization is a powerful method to build complex structural motifs. Recently we reported an efficient access to naphthylamines using intramolecular $6\pi/10\pi$ electrocyclization of keteniminium salts,[184] where the electrocyclizations of KIs were compared with ketenes, allenes, and trienes (Figure 8.1a). The computed data showed that keteniminium salts -both kinetically and thermodynamically- undergo electrocyclization more readily than ketenes, allenes, and trienes. Besides, naphthylamines, (benzo)thiophenes, (benzo)furans and indoles are also core scaffolds for several bioactive compounds used in various areas, such as agrochemicals, [225] pharmaceuticals,[226] antimitotic agents,[227] inhibitors of tubulin polymerization,[228] tumor growth,[229, 230] and anti-viral [231, 232] compounds (Figure 8.2).

Our previous study has described an efficient access to 3-aminobenzothiophene derivatives through the 6π -electrocyclization of the corresponding KI (Figure 8.1b) [185]. These derivatives were obtained with the use of various N-substituents, particularly *N*-allyl and *N*-diallyl protecting groups under mild conditions. In addition, several plausible pathways for the cyclization of KI were computationally examined, namely a 6π -electrocyclization, a stepwise cationic cyclization involving a KI and a ‘direct’ cationic cyclization without formation of a keteniminium salt [185]. 6π -electrocyclization was suggested as the prevailing mechanism due to the higher activation barrier of the cationic ring closure proceeding without the formation of a keteniminium salt ($\Delta\Delta G^\ddagger \approx 8.0$ kcal/mol, M06-2X/6-31+G(d,p)). Accordingly, 6π -electrocyclization initially leads to an intermediate (Int) bearing a H atom. Upon deprotonation, aromaticity is established and the end product is obtained (Figure 8.1a). The present study aims to extend this knowledge to assess the ease of formation of a variety of heterocyclic systems, by means of computationally analyzing the relative barriers of 6π -electrocyclizations of keteniminiums, leading to pyrroles 9, furans 10, thiophenes 11 as well as indoles 13, benzo-furans 14, and benzothiophenes 15 (Table 8.1) [39]. Moreover, the true nature of the cyclization mechanism of KIs will be thoroughly scrutinized via a range of different analysis techniques.

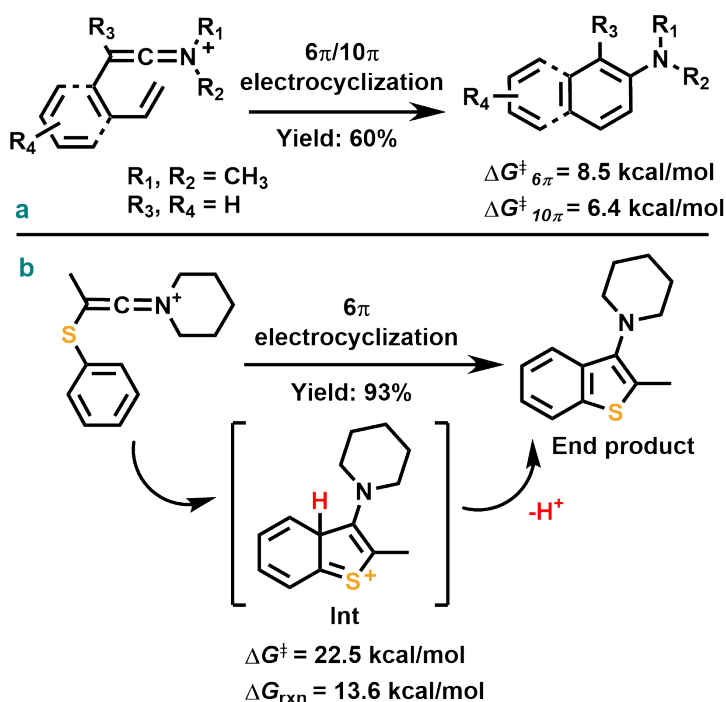


Figure 8.1: Access to (hetero)cyclic compounds using KI intermediates (M06-2X/6-31+G(d,p) in gas phase).

Furthermore, we focus on reactivity differences among keteniminium derivatives bearing different substituents and heteroatoms. This knowledge will allow substituent modifications to obtain more reactive/activated KI to access the desired heterocyclic compounds. We aim to examine a plethora of substituents including electron donating group (EDG) and electron withdrawing group (EWG). The molecular systems under investigation in this study were divided into two groups, namely Group I and Group II as tabulated in Table 8.1.

8.2 Methodology

A density functional theory (DFT) study has been conducted in order to explore and compare the ease of formation of different heterocyclic systems via electrocyclization reactions of keteniminium ions. All reactions were modeled using M06-2X, a hybrid meta-GGA known for its good performance in organic systems with dispersion effects [65, 76, 218]. The 6-31+G(d,p) basis set was employed for all calculations. Ultrafine grid was applied for highly accurate integral evaluation (see Appendix, Table S1 for a DFT survey) [233]. For systems bearing sulfur atoms, namely vinyl sulfide and phenyl sulfide substituted KIs leading to thiophenes 11 and benzothiophenes 15, respectively, the 6-311++G(3df,3pd) basis set was employed on sulfur atoms for more accurate results [201, 234]. All geometry optimizations and frequency calculations were performed in chloroform (CHCl_3 , $\epsilon = 4.7113$) using IEF-PCM [85, 202] with the Gaussian 09 (G09) program package [217]. All free energies are reported at 1 atm and 298 K. Furthermore, energy refinements were conducted with hybrid-GGA MPW1K,[77] range-separated ω B97XD and double hybrid B2PLYP [78] functionals to establish hierarchy in the “Jacob’s Ladder” to

accurately evaluate the barriers. Frequency calculations were utilized to define stationary points as minima (ground states) or first order saddle points (transition states). Intrinsic reaction coordinate (IRC) calculations were conducted to verify that each transition state (TS) leads to its corresponding reactant and product [204, 205, 206, 207, 208]. Additionally, Frontier Molecular Orbital (FMO)[212, 213] analysis, as well as nucleus-independent chemical shift (NICS) [144, 235] analysis were performed using the 6-311++G(d,p) basis set. The NICS values were computed using ghost atoms (Bq) at the center and 1 Å below and above the ring critical points (RCP) by the GIAO [236, 237] (gauge-independent atomic orbital) method. The (3,+1) ring critical points were defined using the XAIM program developed by Bader [238]. ACID calculations (anisotropy of the current-induced density) were performed with the code provided by Herges and coworkers [239, 240]. Natural Bond Orbital (NBO 6.0)[241] and the quantum theory of atoms in molecules (QTAIM) calculations were performed at the M06-2X/ATZ2P in CHCl₃ with no frozen core and good numerical quality with the Amsterdam Density Functional package (ADF) [242, 243].

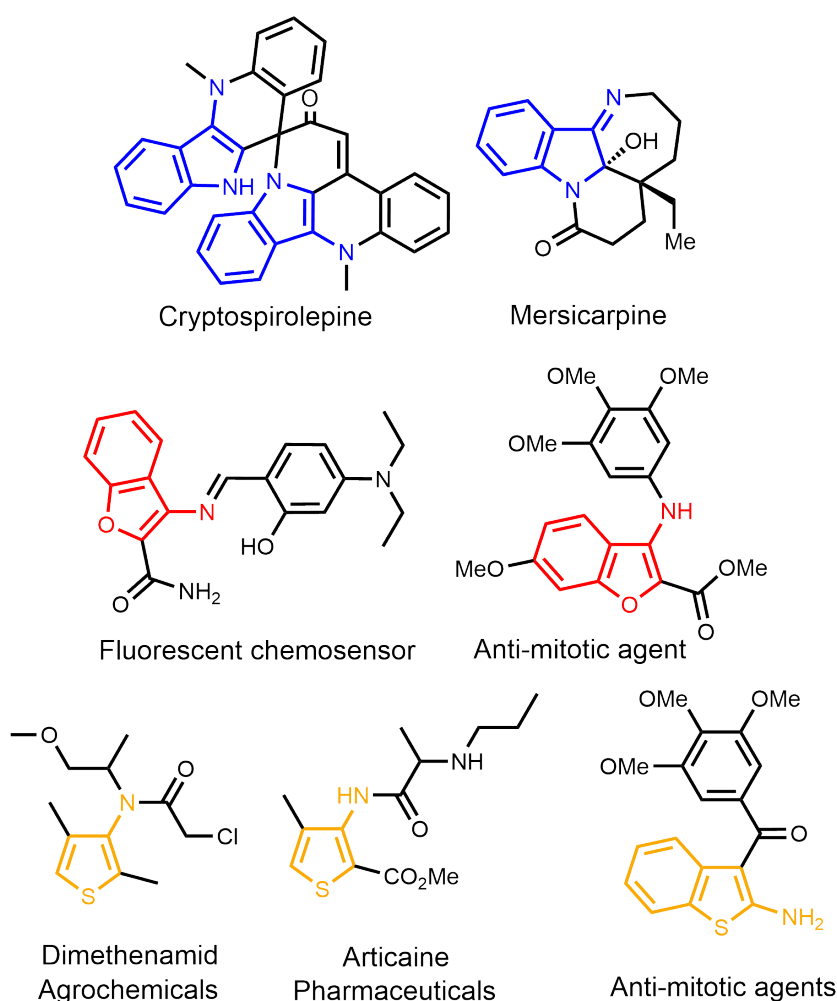


Figure 8.2: Illustration of bioactive heterocyclic compounds.

Table 8.1: Electrocyclization reactions of KI leading to (hetero)cyclic systems [39].

Keteniminium Salt			Target Compounds		
X	Group I		X	Group II	
N-Me	Enamine	1	N-Me	Pyrrole	9
O	Enol ether	2	O	Furan	10
S	Vinyl sulfide	3	S	Thiophene	11
C=C	Butadiene	4	C=C	Benzene	12
X	Group II		X		
N-Me	Aniline	5	N-Me	Indole	13
O	Phenyl ether	6	O	Benzofuran	14
S	Phenyl sulfide	7	S	Benzothiophene	15
C=C	Styrene	8	C=C	Naphthalene	16

8.3 Results and Discussion

In an effort to assess and compare the ease of electrocyclization reactions of keteniminium ions depicted in Table 8.1, a thorough DFT study was executed [39]. Firstly, a detailed structural and energetic analysis comparatively assessing relative reactivities of keteniminiums was performed. Secondly, the true nature of the reaction mechanism was explored by means of several analysis techniques. Thirdly, the effect of various substituents on the reactivity of keteniminium ions towards 6π -electrocyclization reactions was elucidated. Finally, computational predictions were experimentally confirmed for a selection of KI.

8.3.1 Structure, Energetics and Reactivity of Keteniminium Ions in Electrocyclization Reactions

Structural features of keteniminium ions (Table 8.1), comparative energetics and relative reactivities in electrocyclization reactions are detailed in this section.

Structural Features of Keteniminium Ions

Conformational spaces were scanned for each KI depicted in Table 8.1 and surprisingly, minimum energy conformers of enamine 1 and aniline 5 showed a non-linear orientation for $C3=C2=N1$ atoms (KI-1:134.2° and KI-4:132.6°, respectively) when compared to systems containing O and

S heteroatoms (Figure 8.3). Linear conformers ($C3=C2=N1$ bond angles 180°) of enamine 1 and aniline 5 were found to be considerably higher in energy ($\Delta G_{rel} = 7.8$ and 9.5 kcal/mol, respectively, M06-2X/6-31+G(d,p) in $CHCl_3$) (Figures 8.4a and 8.5a). Upon closer inspection of the $C4-X-C3$ angles of the non-linear conformers of KI-1 and KI-4, it was revealed that when $X=N$, the nitrogen atom (N_x) bears sp^2 character and has trigonal planar geometry. Whereas, $C4-X-C3$ angles for linear conformers (Figures 8.4a and 8.5a) illustrate that the nitrogen atom (N_x) exhibits trigonal pyramidal geometry and sp^3 character. This points to a $N_x=C3-C2=N1$ type conjugated structure that competes with the expected $N_x-C3=C2=N1$ form of the keteniminium, for KI-1 and KI-4. As expected, the $C4-X-C3$ angles of keteniminiums with $X=O$, S atoms (KI-2, KI-3, KI-5, and KI-6) are bent and the $C3=C2=N1$ structure is linear (Figure 8.3).

Additionally, non-covalent interactions,[88] more particularly $CH-\pi$ and cation- π interactions, were also considered for Group II keteniminium ions (Figure 8.3 and Figure A.15). $CH-\pi$ interactions were shown to contribute to the stabilities of KI-4 ($CH\cdots\pi$ distance = 3.41 Å and 3.67 Å) and KI-6 ($CH\cdots\pi$ distance = 3.43 Å and 3.51 Å). However, directionality plays an important role in $CH-\pi$ interactions,[244] and the ring orientation must allow the interaction of the CH with the aromatic quadrupole moment, as such, even a $CH\cdots\pi$ distance of 3.48 Å (in KI-4) may not constitute a $CH-\pi$ interaction (see NCIPLOT in Figure A.15). Moreover, large $CH\cdots\pi$ distances (as in KI-5) have much less stabilizing effects and do not qualify as $CH-\pi$ interactions.

Effect of N_x -substituents on enamine and aniline bearing keteniminium ions

The linearity of the KI is clearly affected by the substituents on the aniline and enamine nitrogen (N_x). In order to elucidate the effect of the N_x -substituent, the N-methyl group in enamine 1 and aniline 5 were replaced by electron withdrawing fluorocarbons ($-CF_3$ and $-CH_2CF_3$) and a tosyl group ($-Ts$). Structural features are illustrated in Figures (Figures 8.4 and 8.5, and indicate that for both enamine and aniline systems, electron withdrawing groups (EWG) increase linearity in the reactant conformers and lower $\Delta\Delta G_{rel}$, albeit still favoring the non-linear conformation. The computed data reveals that linearity can be somewhat restored in keteniminiums bearing aniline and enamine moieties by reducing the electron density on the N_x nitrogen atom via electron-withdrawing substituents. This verifies that the loss of linearity in these KI's originates from the willingness of the N_x lone pair to compete for a double bond, forming the conjugated structure $N_x=C3-C2=N1$, where the $C3-C2$ bond is no longer a double bond and the $C3-C2-N1$ moiety is no longer linear.

8.3.2 Energetic Analysis of Electrocyclization Reactions involving Ketiminium Ions

A level of theory study was performed to assess the energetic cost of electrocyclization reactions involving keteniminium ions illustrated in Table 8.1. The effect of the heteroatom (X) was further scrutinized by adding a non-hetero 'ethylene' group as X to fully assess the ease of formation of (hetero)cyclic systems. Evolution of bond distances (Table A.3) were examined throughout the electrocyclization reaction coordinate for all hetero-systems. $C3-C2$ and N_x-C3 bond lengths of non-linear enamine 1 and aniline 5 show partial double bond character and closely resemble bond lengths of the TS, whereas $C3-C2$ bonds of the linear conformers in

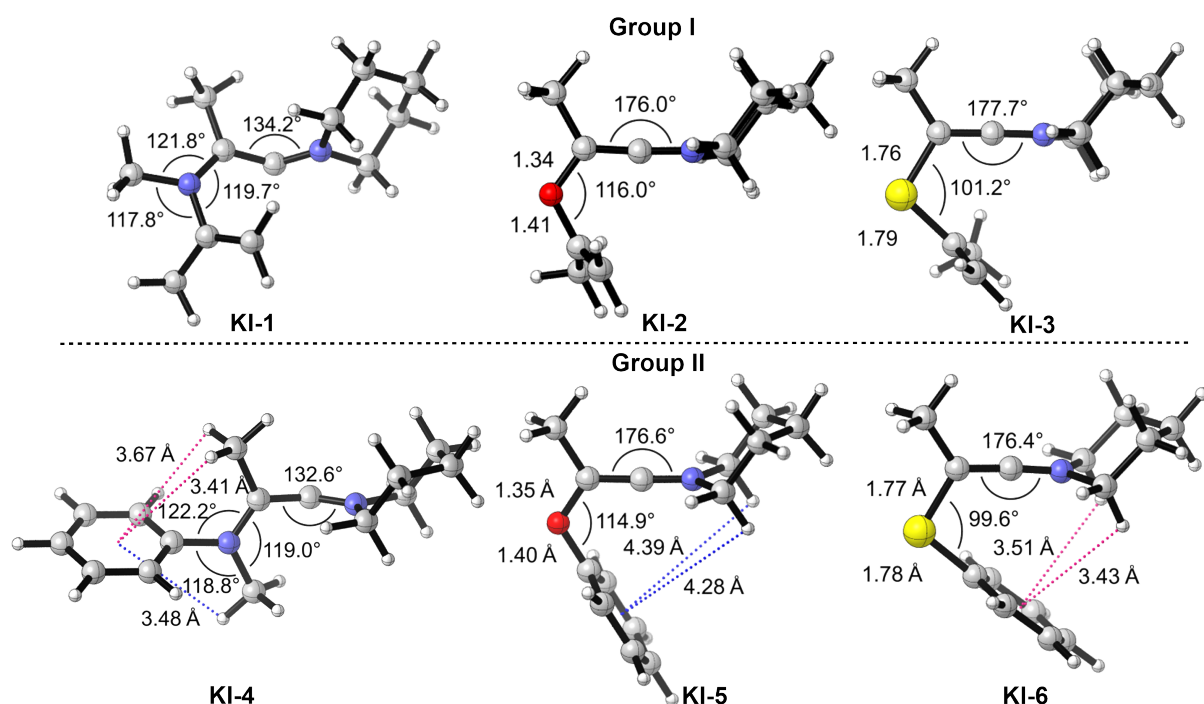


Figure 8.3: Optimized structures of KIs (M06-2X/6-31+G(d,p) in CHCl_3 , extra basis set for sulfur atoms; pink and blues colors denote $\text{CH}-\pi$ interaction, non- $\text{CH}-\pi$ interaction, respectively).

question are double bonds and N_x-C_3 bond lengths display single bond character (Table A.3). This validates that the electrocyclization reactions leading to pyrrole 9 and indole 13 proceed from a non-linear pre-reactive conformer (PRC), as such all Gibbs free energies of activation and reaction for these system were calculated from the PRC. Computed free energies of activation (ΔG^\ddagger) and reaction (ΔG_{rxn}) are presented in Table 8.2. All energies for the formation of pyrrole (entry 1) and indole (entry 5) are relative to the pre-reactive conformer (PRC). Electrocyclization reactions involving vinylic double bonds (Group I) were shown to have significantly lower activation barriers in the range of 4.8–15.5 kcal/mol (B2PLYP/6-31+G(d,p)/M06-2X/6-31+G(d,p)) compared to their phenylic counterparts (Group II), which have barriers varying between 16.4 and 25.5 kcal/mol, due to the disruption of aromaticity in the latter. It should be noted that similar barrier trends were observed regardless of the level of theory.

Among Group I molecules, formation of the pyrrole derivative 9 has the lowest activation barrier (TS1, $\Delta G^\ddagger = 3.0$ kcal/mol, M06-2X/6-31+G(d,p) in CHCl_3) and is, therefore, predicted to undergo electrocyclization most readily. Similarly, in the second group, the indole derivative 13 has the lowest free energy barrier (10.8 kcal/mol, M06-2X/6-31+G(d,p) in CHCl_3), predicting a higher ease of formation when compared to benzofuran 14 and benzothiophene 15. The same reactivity pattern is observed in both groups; thiophene 11 (benzothiophene 15) being the least reactive, followed by furan 10 (benzofuran 14).

Structural features of transition states disclose further information on the extent of the reaction (Figure 4). Critical distances in the range of 2.19–2.42 Å reveal the reactant-like nature of the transition states for Group I resulting in more exothermic reactions and lower free ener-

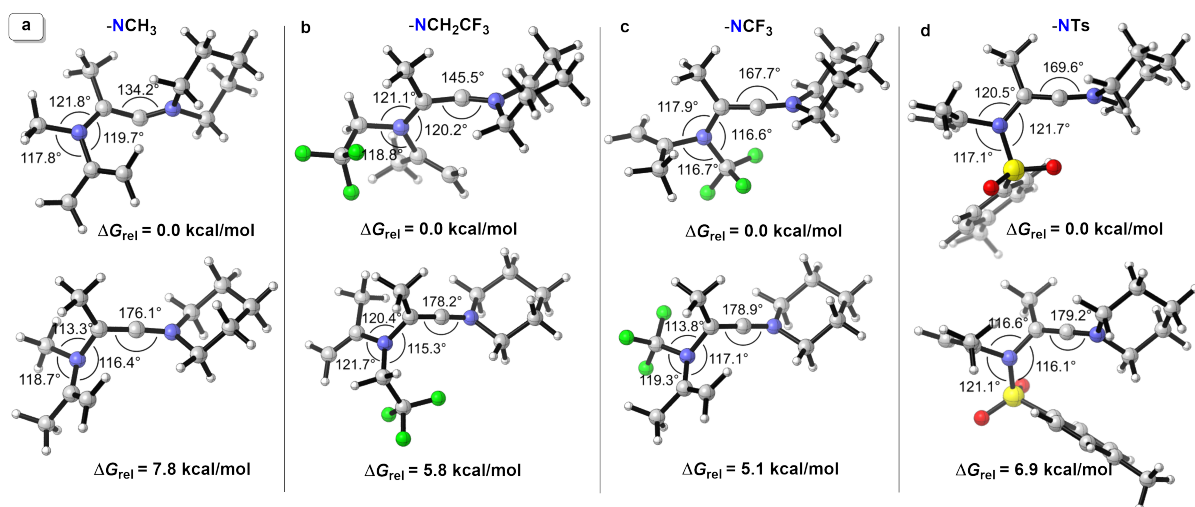


Figure 8.4: Optimized structures for KIs of Nx-substituted enamine derivatives in Group I (M06-2X/6-31+G(d,p) in CHCl_3 , extra basis set for S atom).

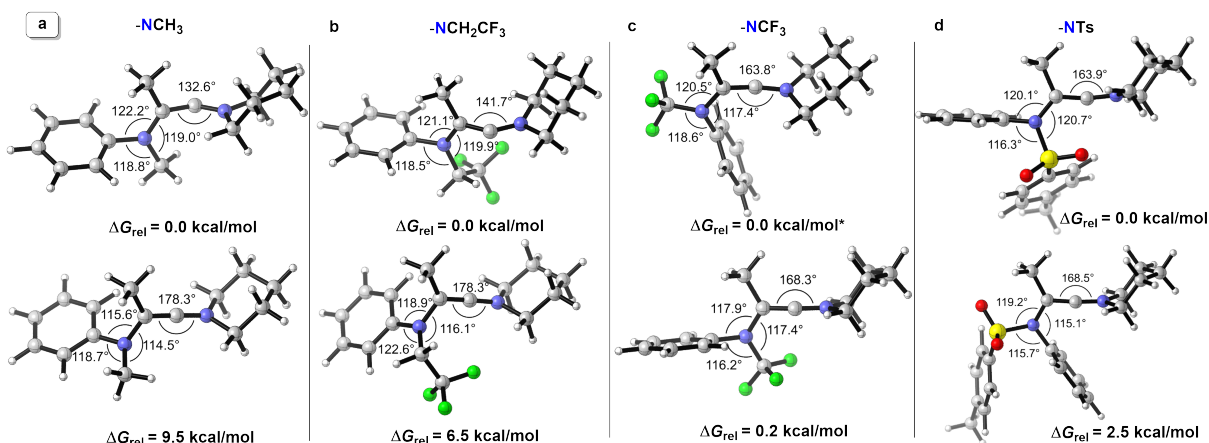
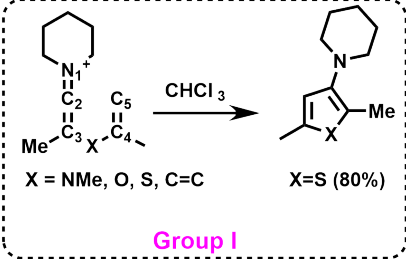
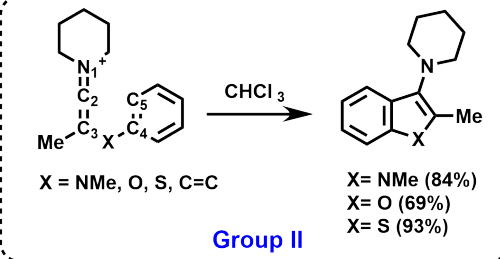


Figure 8.5: Optimized structures for KIs of Nx-substituted aniline derivatives in Group II. (M06-2X/6-31+G(d,p) in CHCl_3 , extra basis set for S atom.) *M06-2X/6-31+G(d,p)//B3LYP/6-31+G(d,p) in CHCl_3 to overcome imaginary frequency.

gies of activation. Whereas, for Group II, much shorter C–C critical distances (in the range of 1.98–2.10 Å) highlight the product-like nature of the transition states (TSs), leading to significantly higher free energies of activation and endothermic reactions. Only aniline substituted KI leading to indole 13 results in a slightly exothermic reaction ($\Delta G_{\text{rxn}} = -4.9$ kcal/mol, M06-2X/6-31+G(d,p)) in Group II. Hence, early TS characteristics verify higher reactivity of Group I. Additionally, the C3=C2=N1 bond angle is significantly smaller for enamine and aniline containing systems (134.5° and 133.5° for TS1 and TS4, respectively) compared to others.

In our recent work, an efficient access to 3-aminobenzothiophene with various substituents was reported (Figure 8.2b) [185]. In that study, benzothiophene 15 (entry 7) was successfully synthesized at room temperature (RT) and computationally optimized at the same level of theory (M06-2X/6-31+G(d,p)) in gas phase ($\Delta G_{\text{gas}}^\ddagger = 22.5$ kcal/mol).[185] Current data ($\Delta G_{\text{solvent}}^\ddagger =$

Table 8.2: Free energy barriers (ΔG^\ddagger), and reaction free energies (ΔG_{rxn}) for electrocyclization reactions of KIs. Free energies in kcal/mol.

<div style="display: flex; justify-content: space-around; align-items: center;"> <div style="text-align: center;">  <p>Group I</p> </div> <div style="text-align: center;">  <p>Group II</p> </div> </div>									
		M06-2X		MPW1K		ω B97XD		B2PLYP	
Entry	Group	ΔG^\ddagger	ΔG_{rxn}	ΔG^\ddagger	ΔG_{rxn}	ΔG^\ddagger	ΔG_{rxn}	ΔG^\ddagger	ΔG_{rxn}
1	pyrrole	3.0	-37.8	1.9	-42.4	2.9	-39.3	4.8	-34.3
2	furan	6.0	-23.8	4.8	-27.8	5.5	-26.6	10.1	-19.1
3	thiophene	11.4	-22.2	9.9	-27.4	10.9	-25	15.5	-16.9
4	benzene	9.2	-34.8	10.4	-38	8.0	-37.6	14.5	-29.3
	Group II	ΔG^\ddagger	ΔG_{rxn}	ΔG^\ddagger	ΔG_{rxn}	ΔG^\ddagger	ΔG_{rxn}	ΔG^\ddagger	ΔG_{rxn}
5	indole	10.8	-4.9	10.1	-8.3	11.6	-5.8	16.4	0.5
6	benzofuran	17.0	8.0	15.5	4.2	16.1	5.3	22.4	12.7
7	benzothiophene	21.0	9.0	18.6	3.9	20.4	6.9	25.5	13.8
8	naphthalene	14.8	1.7	17	1.6	13.7	-0.3	21.9	10.9

21.0 kcal/mol, M06-2X/6-31+G(d,p), Table 8.2) is in line with the previously reported result. More recently, intramolecular competition reactions of vinyl sulfide and phenyl sulfide were modelled in CHCl_3 at the MPW1K/6-31+G(d,p)//M06-2X/6-31+G(d,p) level of theory to investigate the favorable formation of thiophene derivatives.[197] Consistent with experimental findings, the electrocyclization reactions leading to thiophene formation ($\Delta G^\ddagger = 8.3$ kcal/mol, M06-2X/6-31+G(d,p)) was shown to be both kinetically and thermodynamically favored over the formation of benzothiophene ($\Delta G^\ddagger = 16.4$ kcal/mol, M06-2X/6-31+G(d,p)) [197].

Similar to the outcome of the aforementioned intramolecular competition reaction,[197] the free energy of activation for electrocyclization of vinyl sulfide 3 ($\Delta G^\ddagger = 9.9$ kcal/mol, MPW1K/6-31+G(d,p)//M06-2X/6-31+G(d,p), Table 8.2 is shown to be notably lower than that of phenyl sulfide 7 ($\Delta G^\ddagger = 18.6$ kcal/mol, MPW1K/6-31+G(d,p)//M06-2X/6-31+G(d,p)). Considering homocyclization (entries 4 and 8 in Table 8.2), reaction barriers (TS4, $\Delta G^\ddagger = 9.2$ kcal/mol and TS8, $\Delta G^\ddagger = 14.8$ kcal/mol, M06-2X/6-31+G(d,p)) remain between the lowest and highest values and the computational findings for entry 4 in Table 8.2 are in line with our previous study[184] ($\Delta G^\ddagger_{\text{gas}} = 8.5$ kcal/mol, $\Delta G_{\text{rxn}} = -44.5$ kcal/mol, M06-2X/6-31+G(d,p) in gas phase). Hence, in light of previous experimental and computational studies, the computational results presented herein suggest the likelihood of formation of all heterocyclic systems depicted in Table 8.1 via electrocyclization of their corresponding KI derivatives.

Lastly, the energetic consequences of electron-withdrawing Nx-substituents ($-\text{CF}_3$, $-\text{CH}_2\text{CF}_3$,

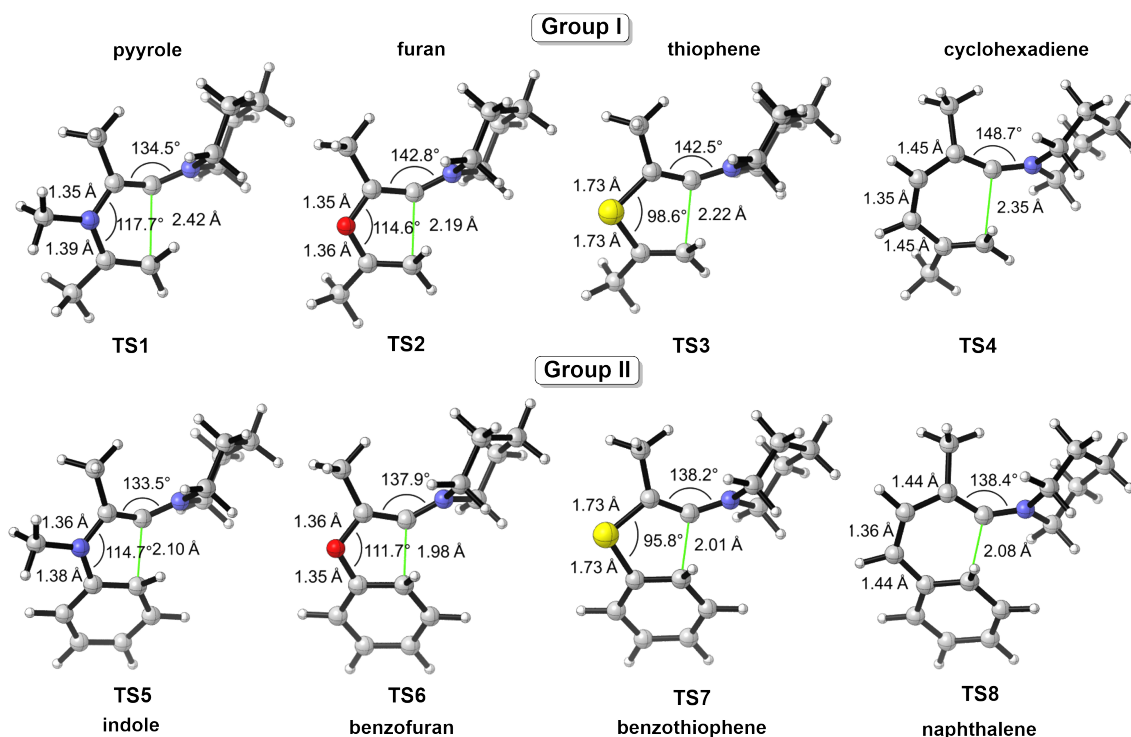


Figure 8.6: Optimized transition state structures (M06-2X/6-31+G(d,p) in CHCl_3 , extra basis set for sulfur atom)

–Ts) on electrocyclization of keteniminiums bearing enamine and aniline moieties (Figures 8.4 and 8.5) were investigated (see Appendix, Figure A.16). Computed data show that EWGs, in particular $-\text{CF}_3$ and $-\text{Ts}$, significantly increase the activation barriers and decrease product stabilities.

8.3.3 Population Analysis and Local Reactivity Descriptors

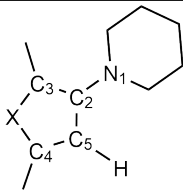
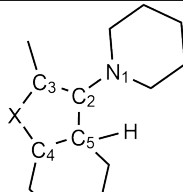
Prior to analyzing the nature of the heterocyclic electrocyclization reactions we investigated the effect of different heteroatoms on the KI reactivity by means of population analysis and local descriptors for all KI's listed in Table 8.1.

Population Analysis

In order to gain insight into the electrostatic nature of the electrocyclization reaction and rationalize the calculated order of activation barriers, NBO 6.0 analysis was performed as shown in Table 8.3. Note that 6π -electrocyclization initially leads to an intermediate (Int) where C5 bears a H atom. Upon deprotonation of C5, aromaticity is established and the end product is obtained. Population analysis results depict considerably larger negative charges on carbon C5, indicating its reactivity towards the positively charged carbon C2. NPA results show that carbon C5 of enamine 1, enol ether 2 and vinyl sulfide 3 substituted KIs leading to pyrrole 9, furan 10 and thiophene 11, respectively, bear approximately two-fold larger negative charges compared to carbon C5 of aniline 5, phenyl ether 6 and phenyl thioether 7 substituted KIs, implying lower

reactivity of the aromatic ring, as expected. Additionally, higher negative charges on carbon C5 were detected in N-heteroatom substituted KIs (enamine 1 and aniline 5) decreasing consistently through O and S heteroatom substituted KIs. Sulfur shows a tendency to donate electrons to the delocalization hence, its positive charge. Evaluation of the NPA charges indicate the keteniminium nature of the reacting species.

Table 8.3: Evolution of NPA atomic charges throughout the electrocyclization reaction. (M062X/6-31+G(d,p)//M062X/6-31+G(d,p) in CHCl₃)

									
					X= N-Me, O, S				
Group I					Group II				
Enamine					Aniline				
Charges	KI	KI-PRC	TS	Int	Charges	KI	KI-PRC	TS	Int
N1	-0.297	-0.330	-0.358	-0.446	N1	-0.298	-0.323	-0.385	-0.478
C2	0.460	0.216	0.247	0.241	C2	0.455	0.186	0.248	0.235
C3	0.159	0.260	0.208	0.054	C3	0.157	0.278	0.197	0.150
X=N-Me	-0.492	-0.394	-0.366	-0.265	X=N-Me	-0.476	-0.381	-0.343	-0.286
C4	0.232	0.204	0.244	0.428	C4	0.176	0.133	0.217	0.332
C5	-0.536	-0.410	-0.451	-0.509	C5	-0.273	-0.226	-0.288	-0.361
Enol ether					Phenyl ether				
Charges	KI	TS	Int		Charges	KI	TS	Int	
N1	-0.290	-0.364	-0.443		N1	-0.285	-0.389	-0.478	
C2	0.325	0.282	0.204		C2	0.336	0.254	0.188	
C3	0.323	0.307	0.186		C3	-0.319	0.322	0.296	
X=O	-0.492	-0.455	-0.366		X=O	-0.491	-0.443	-0.400	
C4	0.309	0.454	0.696		C4	0.265	0.402	0.528	
C5	-0.436	-0.522	-0.556		C5	-0.259	-0.231	-0.404	
Vinyl sulfide					Phenyl sulfide				
Charges	KI	TS	Int		Charges	KI	TS	Int	
N1	-0.303	-0.366	-0.412		N1	-0.304	-0.391	-0.464	
C2	0.412	0.352	0.298		C2	0.417	0.326	0.261	
C3	-0.193	-0.216	-0.332		C3	-0.186	-0.197	-0.216	
X=S	0.310	0.457	0.733		X=S	0.334	0.460	0.603	
C4	-0.161	-0.216	-0.045		C4	-0.204	-0.110	-0.077	
C5	-0.355	-0.458	-0.520		C5	-0.214	-0.314	-0.366	

Local reactivity descriptors

In order to predict local reactivities and rationalize the calculated order of barrier heights for the heterocyclic electrocyclization reactions, the electrophilic Parr function Pk^+ proposed by Domingo et al[96] and the Fukui function fk^+ proposed by Yang and Mortier[97] were calculated.

Pk^+ for carbon atoms C2 and C5, in keteniminium ions of Group I and II, were calculated using NBO atomic spin density with the UM062X/6-31+G(d,p)//M062X/6-31+G(d,p) in $CHCl_3$. The calculation of Fukui indices were performed with M062X/DZP//M062X/6-31+G(d,p) in $CHCl_3$. The computed Pk^+ and fk^+ for C2 and C5 are tabulated in Table 3. Analysis of the Parr and Fukui functions stress that C2 carbon is the most electrophilic center for all reactants in the following order: enamine > enol ether > vinyl sulfide (Group I); aniline > phenyl enol ether > phenyl sulfide (Group II). These findings are directly correlated to the activation barriers and reveal that higher Pk^+ and fk^+ in C2 leads to lower activation barriers. There was no apparent correlation found for C5.

Table 8.4: Calculated Pk^+ and fk^+ for the C2 and C5 carbon atoms of Groups I and II KIs.

Reactants	Pk^+		fk^+	
	C2	C5	C2	C5
Enamine 1	0.714	0.015	0.448	0.002
Enol Ether 2	0.663	0.001	0.439	0.008
Vinyl sulfide 3	0.608	0.005	0.388	0.006
Aniline 5	0.692	-0.001	0.449	0.003
Phenyl Enol Ether 6	0.659	0.002	0.439	0.005
Phenyl sulfide 7	0.592	0.002	0.372	0.006

8.3.4 Nature of the Electrocyclization Reaction of Keteniminium Ions

The structural, energetic and population analysis of keteniminium cyclizations reactions detailed in the previous section does not indicate/validate the pericyclic character of the reactions studied. Herein, we decided to further investigate the true nature of the cyclization reactions under investigation. According to Berney and coworkers, pseudo-pericyclic reactions possess lower activation barriers than pericyclic ones.[245] The significantly lower activation barriers (Table 8.2) for the formation of pyrrole 9 and indole 13 and the non-linear nature of the C3–C2–N1 structure in keteniminiums KI-1 and KI-4 (Figure 8.4) encouraged us to investigate the nature of the reaction in further detail. Therefore, we set out to perform FMO (data not presented here, see Appendix, Figure A.19), AIM, NICS and ACID analysis, for all systems under study, in order to distinguish between pericyclic and (non-planar)-pseudopericyclic reactions.

Atoms in molecules (AIM) Analysis

Atoms-in-molecules (AIM) analysis for transition state structures is a useful method to distinguish the nature of a reaction through the presence/absence of critical points.[238] AIM analysis were performed for transition states (TSs) of Groups I and II; findings indicate that new bond critical points (BCPs, (3,-1)) in TSs were formed as well as ring critical points (RCP) (3,+1), supporting a pericyclic type reaction as illustrated in Figure 5. Moreover, the AIM analysis displays lower density values for Group I when compared to Group II, signifying that newly formed C2–C5 bonds of Group I are weaker, indicative of early transition states and exothermic reactions.

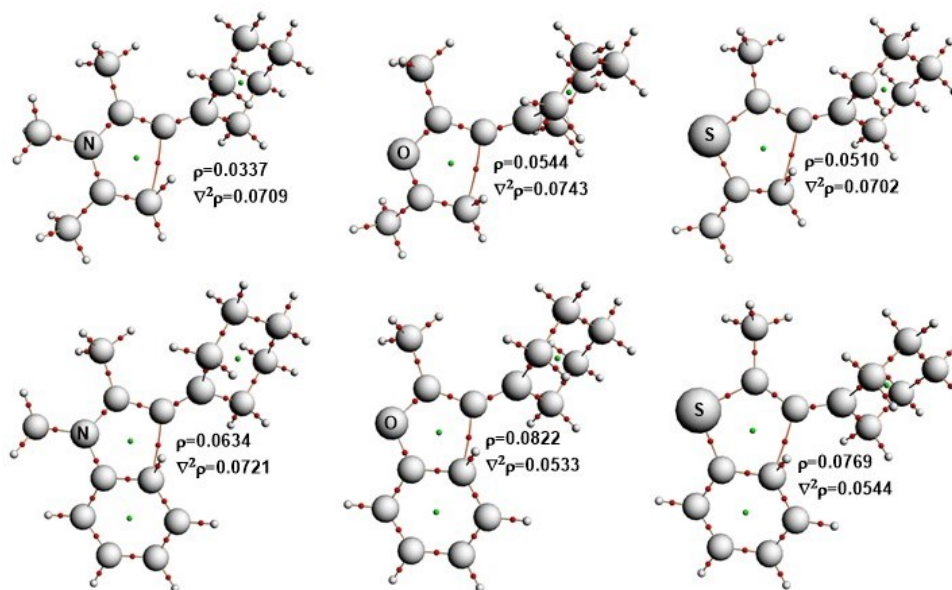


Figure 8.7: AIM analysis of the TS structures for Groups I and II. (M06-2X/ATZ2P//M06-2X/6-31+G(d,p) in CHCl₃, values in a.u).

Nucleus-Independent Chemical Shifts (NICS)

According to Woodward–Hoffmann rules,[246] pericyclic ring closure reactions possess aromatic transition state (TS) structures. NICS introduced by Schleyer et al[235] is a magnetic measure/indicator of aromaticity, particularly for the evaluation of TS aromaticities. In the present study, NICS(-1) values, which are points placed 1 Å below the RCP (since the cyclization occurs along this trajectory, (Figure 8.8), were considered in order to account for π -electron contribution and to avoid the additional sigma (σ) electron contribution in NICS(0). Negative NICS values indicate aromaticity; calculated NICS(-1) values graphed in Figure 8.9 clearly show minima for TSs compared to their corresponding reactants and products, indicating aromaticity in the TS. The aromatic character of the TS confirms the pericyclic ring closure classified as electrocyclozation.[247] Moreover, notably, NICS values of TSs in Group II are lower than the corresponding TSs in Group I. This points to larger aromatic stabilization of the TSs in Group II and is in agreement with our previous work[185] that proposed larger number

of electrons (10π rather than 6π) contribute to the transition state. However, it is important to note that despite the larger aromatic stabilization of the TS, initial disruption of aromaticity still affords larger activation barriers for Group II.

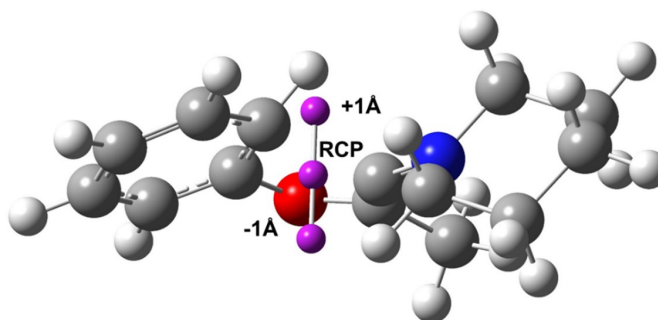


Figure 8.8: One of the representative image of points (Bq ghost atoms) for NICS calculations.

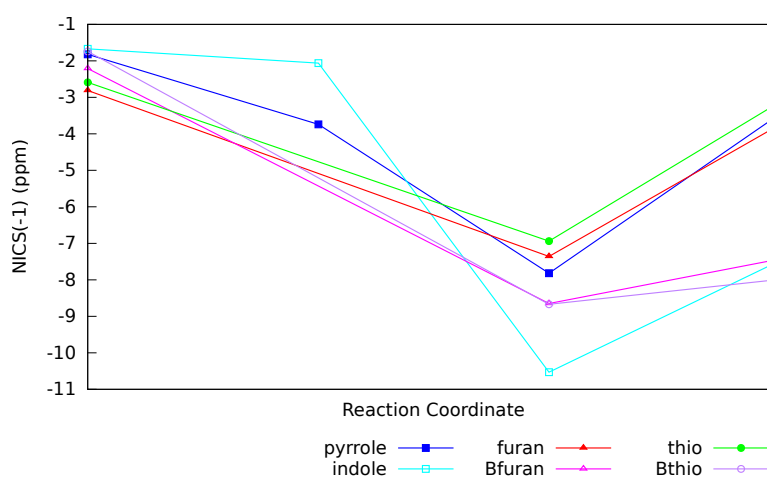


Figure 8.9: Variation of NICS along the reaction coordinates 1 Å below the RCPs for Groups I and II. (M06-2X/6-311++G(d,p)//M06-2X/6-31+G(d,p) in CHCl_3). Note that the electrocyclization initially leads to an intermediate (Int) where C5 bears a H atom. Upon deprotonation of C5, aromaticity is established, and the end product is obtained.

Anisotropy of the Induced Current Density Analysis

Herges and Geuenich developed the anisotropy of the induced current density (ACID) method in order to quantify and visualize electronic delocalization and conjugation [239]. This method is also used for the measurement of aromaticity in order to differentiate the type of the reactions, namely pericyclic and pseudopericyclic reactions [239, 240, 248, 249]. Lemal and coworkers defined the pseudo-electrocyclic reaction as a disconnection in the cyclic array [250]. In the

present study, ACID analysis was carried out to conclusively elucidate the nature of cyclization reactions in Groups I and II. The continuous set of gauge transformation (CSGT) [251, 252] method was applied for the ACID calculations. ACID plots in Figure 8.10 indicate that TS structures do not display any disconnection at isosurface value of 0.03 au. Additionally, diatropic ring currents are known to be present in aromatic systems, where the magnetic field vector is orthogonal to the ring plane leading to clock-wise current. Diatropic ring currents were observed in all ACID isosurfaces of TSs analyzed, indicating the pericyclic nature of the reactions.

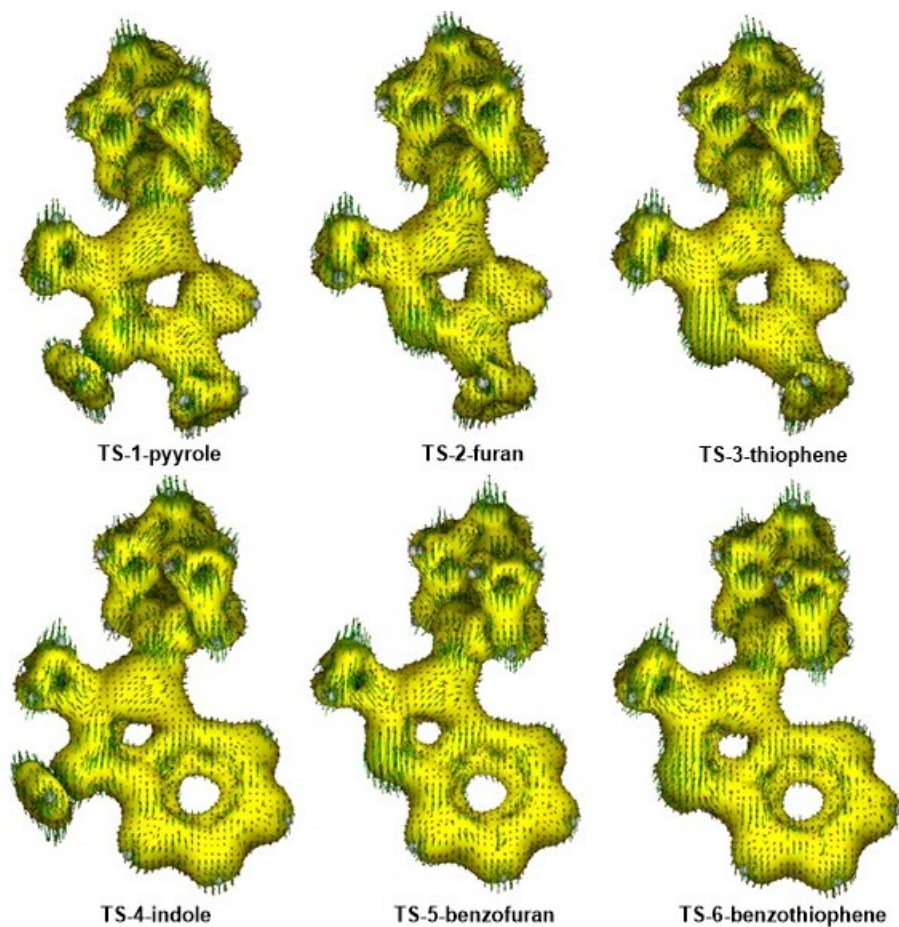


Figure 8.10: ACID plots for the transition states of Groups I and II (M06-2X/6-311++G(d,p)//M06-2X/6-31+G(d,p) in CHCl_3 , extra basis set for S atom, isosurface value 0.03 a.u.).

Moreover, critical isosurface values (CIV) were calculated in order to quantify the delocalization and pinpoint critical values for the topology change from cyclic to noncyclic. Higher CIVs indicate strong delocalization and aromaticity, confirming the pericyclic character of the reaction. CIVs of TSs (TS1-3) in Group I are 0.034, 0.035, and 0.037, respectively; CIVs in Group II are 0.061, 0.053, 0.054 for TS4-6, respectively. Large CIVs both in Group I and II indicate pericyclic character of the reactions (CIV is usually ≤ 0.02 for a typical pseudopericyclic reaction).⁷⁸ Additionally, larger CIVs in Group II are associated with short C2–C5 bond distances (1.98–2.10 Å) leading to higher electron delocalization compared to Group I (2.19–2.42

Å). This outcome is in line with the higher densities and shorter critical distances observed for Group II in AIM analysis. Moreover, higher CIVs for Group II are consistent with larger NICS values, once again pointing towards a 10π -electrocyclization reaction for Group II. Briefly, $6\pi/10\pi$ -electrocyclizations for Groups I/II are characterized as pericyclic reactions, through FMO, QTAIM, NICS and ACID analysis.

8.3.5 Understanding Effect of Substituents on Keteniminium Reactivity

To evaluate the effect of substituents on keteniminium reactivity, a variety of substituted keteniminiums that are experimentally accessible have been selected [185, 197, 253]. Free energy of activation barriers (ΔG^\ddagger) and reaction free energies (ΔG_{rxn}) for $6\pi/10\pi$ -electrocyclizations of keteniminiums in Groups I and II (Table 8.1), are tabulated in Tables 8.5 and 8.6, respectively. Although M06-2X data are tabulated herein, energy refinements at MPW1K, ω B97XD and B2PLYP levels of theory were also performed for all systems (see Appendix, Table S3-8). To be able to systematically check the effect of substituents on vinylic and phenylic moieties, methyl substitution was chosen for the alpha position (C3-Me), for all systems. The effect of substituents at the alpha position will be systematically investigated in a subsequent study. Generally speaking, regardless of the substituents, electrocyclizations of Group I were found to be highly exergonic, making these reactions thermodynamically more favorable. This is also in line with their lower free energies of activation (Table 8.5). Computed data reveal that Group I products are both kinetically and thermodynamically more favored over their Group II counterparts. While the formation of the indole systems in Group II was also found to be slightly exergonic except in the case of ortho- CF_3 and ortho and para -Cl substituents (Table 8.6, entries 8 and 13, respectively). However, electrocyclizations yielding benzothiophenes and benzofurans, showed endergonic reactions, making them less favorable. Substituent positions in Tables 8.5 and 8.6 were given in Figure 8.11.

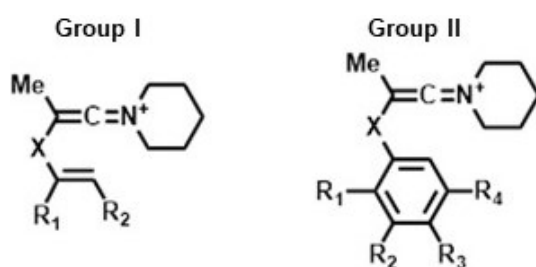


Figure 8.11: R group positions for Groups I and II.

Table 8.5: Effect of substituents on free energy barriers (ΔG^\ddagger), and reaction free energies (ΔG_{rxn}) of 6π -electrocyclizations of KI–Group I. (Free energies in kcal/mol.)

Entry	R1	R2	Enamine		Enol ether		Vinyl sulfide	
			ΔG^\ddagger	ΔG_{rxn}	ΔG^\ddagger	ΔG_{rxn}	ΔG^\ddagger	ΔG_{rxn}
1	CH3	H	3.0	-37.8	6.0	-23.8	11.4	-22.2
2	H	CH3 (<i>E</i>)	2.8	-29.8	10.6	-14.0	14.5	-14.5
3	H	CH3 (<i>Z</i>)	7.0	-33.0	15.6	-14.1	20.2	-15.0
4	H	H	2.9	-35.1	10.5	-16.1	14.3	-18.5
5	Ph	H	3.8	-35.0	8.3	-23.9	13.5	-22.1
6	H	Ph (<i>E</i>)	2.6	-30.6	9.4	-13.4	13.1	-13.8
7	H	Ph (<i>Z</i>)	5.4	-31.1	15.1	-11.5	18.7	-14.0
8	CO2Me	H	6.4	-31.8	12.8	-12.7	15.7	-18.0
9	H	CO2Me (<i>E</i>)	6.0	-24.7	12.6	-8.3	15.4	-10.7
10	CO2Me	CO2Me	7.2	-26.7	16.9	-6.5	17.0	-13.5
11	CN	H	5.3	-32.4	15.9	-9.3	20.0	-14.0
12	H	CN (<i>E</i>)	7.0	-19.3	15.3	-1.7	16.1	-6.7
13	H	CN (<i>Z</i>)	8.0	-22.9	20.1	-1.0	21.1	-7.1

Yield% [197]

80%

95%

72% *E/Z*:80:20

10% *E/Z* 13:87

47%

56% *E/Z*:60:40

58% *E/Z*:67:33

36%

54% *E/Z*:100:0

Table 8.6: Effect of substituents on free energy barriers (ΔG^\ddagger) and reaction free energies (ΔG_{rxn}) of 10π -electrocyclizations of KI-Group II. (Free energies in kcal/mol.)

Entry	Aniline				Phenyl ether			Phenyl sulfide		
	R1	R2	R3	R4	ΔG^\ddagger	ΔG_{rxn}	Yield% [254]	ΔG^\ddagger	ΔG_{rxn}	Yield% [185]
1	H	H	H	H	10.8	-4.9	84%	17.0	8.0	69%
2	H	CH3	H	CH3	9.2	-4.7		13.6	4.8	93%
3	CH3	H	H	H	15.2	-1.9		16.3	6.3	
4	H	CH3	H	H	8.9	-7.5		14.6	4.4	
5	H	H	CH3	H	10.4	-4.9		16.6	7.0	
6	H	H	CF3	H	10.1	-3.8		18.1	9.6	80%
7	H	CF3	H	H	9.6	-3.5		19.6	11.7	
8	CF3	H	H	H	17.2	1.5		18.9	11.9	88%
9	H	H	CN	H	9.9	-3.9		19.3	12.2	47%
10	H	CN	H	H	10.5	-3.1		19.8	12.0	
11	H	Cl	H	H	10.0	-6.0		18.5	9.3	
12	H	H	Cl	H	11.0	-4.1		17.5	10.1	
13	Cl	H	Cl	H	17.8	2.8	91%	20.5	13.3	89%

Role of the substituents in Group I

While each substituent has a different effect on the reactivity itself, the position of the R group plays a potent role on the ease of electrocyclization. In case of R1 and R2, calculations in Table 8.5 demonstrate a general trend, where R1 and R2 with electron donating capabilities (EDG) allow the electrocyclization reaction to proceed with more ease by increasing the electron density around C5 carbon. Moreover, EWG groups ($-\text{CO}_2\text{Me}$, $-\text{CN}$) increase the activation barriers. For all systems, the Z isomer appears to have a higher activation barrier, caused by the steric clash between Z orientation of substituents and the piperidine group (Figure 8). Hence, electrocyclization of E isomers are favored. Activation barriers for Z isomers are also in $\text{CH}_3 < \text{Ph} < \text{CN}$ order.

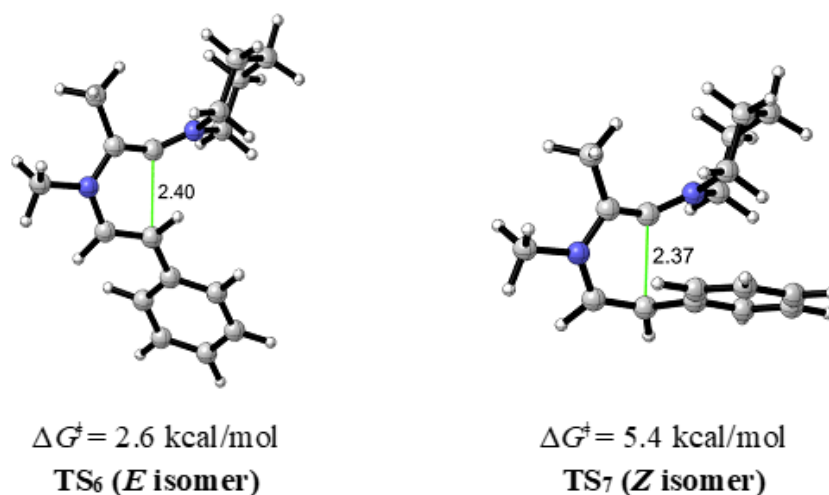


Figure 8.12: Optimized TS structures for the E and Z isomers (entries 6 and 7 in Table 8.5) of enamine systems (Group I). M06-2X/6-31+G(d,p) with IEF-PCM in CHCl_3 ; critical distances in Å.

In case of R1 substituent: For enamine systems, the activation free energy barriers are in order $\text{CH}_3 \approx \text{H} < \text{Ph} < \text{CN} < \text{CO}_2\text{Me}$. On the other hand, the activation barriers leading to furans and thiophenes have increasing orders as follows: $\text{CH}_3 < \text{Ph} < \text{H} < \text{CO}_2\text{Me} < \text{CN}$. Due to the steric hindrance between N-Me and R1, electron donating groups in R1 position slightly increase the barriers compared to furan and thiophene cases, causing the difference in order of reactivities. Apart from electron withdrawing effect, due to steric hindrance, electrocyclization of $-\text{CO}_2\text{Me}$ substituted KI, leading to pyrrole, shows the highest free energy of activation. In electrocyclizations of corresponding KIs leading to furan and thiophene, the highest barriers belong to the cyano ($-\text{CN}$) substituted KI.

In case of R2 substituent: In case of enamine, the effect of the R2 is similar among methyl ($-\text{CH}_3$), phenyl ($-\text{Ph}$) and hydrogen ($-\text{H}$). Similar trends are also consistently observed for enol ether and vinyl sulfide counterparts, except for the phenyl moiety showing the lowest activation barriers. Similar to the R1 effect, EWGs increase the activation barriers for all systems in $\text{CO}_2\text{Me} < \text{CN}$ order. Overall, among Group I ions, activation barriers of all enamine derivatives are significantly lower, followed by enol ether and vinyl sulfide derivatives, respectively.

Role of the substituents in Group II

For Group II, $-\text{CH}_3$, $-\text{CF}_3$, $-\text{Cl}$, $-\text{CN}$ were placed in ortho (o-), para (p-) and meta (m-) positions as depicted in Table 5. The activation barriers of ortho-substituted KIs leading to indoles show an increase in the order: $\text{H} < \text{CH}_3 < \text{CF}_3 < \text{Cl}$, whereas activation barriers for KIs leading to benzofuran and benzothiophene are as follows: $\text{CH}_3 < \text{H} < \text{CF}_3 < \text{Cl}$. The differences stem from the steric hindrance between N-Me and the substituents at o-position. In case of para-substituents, for all systems, the activation barriers are more or less the same. Regarding meta-substituents, the activation barriers of KIs leading to indole are close. The relative order of meta-substituents for electrocyclizations to benzofuran and benzothiophene are $\text{CH}_3 < \text{H} < \text{Cl} < \text{CF}_3 \approx \text{CN}$ and $\text{CH}_3 < \text{CF}_3 \approx \text{H} \approx \text{Cl} < \text{CN}$, respectively. Similar to Group I, activation barrier trends in Group II follow: indole < benzofuran < benzothiophene.

Ultimately, the substitution patterns investigated herein illustrate that the pyrrole systems are the most reactive with the lowest activation barriers, whereas the benzothiophenes are the least reactive with free energies of activation as high as 22.9 kcal/mol (Table 8.6, entry 13). Due to the disruption of aromaticity, free energies of activation for Group II are significantly higher compared to Group I. All in all, it is important to note that among all six heterocyclic systems, the highest barrier (21.0 kcal/mol) is for the formation of 'parent' benzothiophene (Table 5, entry 1), which was already successfully synthesized.¹⁷ Accordingly, the formation of all heterocyclic systems via the $6\pi/10\pi$ -electrocyclization are suggested to be plausible in the light of computational and experimental findings [185, 197, 253].

8.4 Conclusions

In electrocyclization study, structural and energetic analysis, nature of the reactions and the reactivity differences in electrocyclization reactions of keteniminium salts leading to six different heterocyclic systems were computationally examined. The computational results reveal that the 6π -electrocyclization of enamine substituted KI 1 leading to 3-aminopyrroles 9 is favored in Group I, when lowest activation and reaction free energies are considered. Aniline substituted keteniminiums 5 leading to 3-aminoindoles 13 has the lowest free energy of activation in Group II, compared to phenyl ether and phenyl sulfide substituted keteniminiums furnishing the corresponding 3-aminobenzofurans 14 and 3-aminobenzothiophenes 15, respectively. The aromatic moiety in Group II decreases the reactivity compared to the systems in Group I, as expected due to the disruption of the aromaticity in the transition state for cyclization. Notably, the pericyclic nature of the reaction was validated by means of AIM, NICS, ACID analysis, also pointing towards a 10π -electrocyclization for Group II rather than the 6π -electrocyclization observed in Group I. Lastly, among all six heterocyclic systems, the highest barrier is for the formation of benzothiophene 15, which was previously shown to readily form at RT. In line with computational findings, experimental results show that electrocyclization reactions of selected systems in Group II were achieved under mild conditions, suggesting the likelihood of formation of all heterocyclic systems studied herein from their corresponding keteniminium derivatives. Overall, this study is expected to contribute to the understanding of reactivity differences of keteniminium ions and further aid synthetic applications.

Concluding Remarks

This dissertation presents the outcomes of deamidation impact on the structure and function of Bcl-x_L and keteniminium chemistry from KI formation to its reactions.

In the first part of the thesis, we explored deamidation-induced conformational changes in Bcl-x_L to gain insight into its loss of function by performing microsecond-long molecular dynamics (MD) simulations. MD simulation outcomes showed that the IDR motion and interaction patterns have changed notably upon deamidation. Principal component analysis (PCA) demonstrates significant differences between wild type and deamidated Bcl-x_L and suggests that deamidation affects the structure and dynamics of Bcl-x_L. The combination of clustering analysis, H-bond analysis, and PCA revealed changes in conformation, interaction and dynamics upon deamidation. Differences in contact patterns and essential dynamics that lead to a narrowing in the binding groove (BG) are clear indications of deamidation-induced allosteric effects. In line with previous studies, we show that the intrinsically disordered region plays a very important role in the loss of apoptotic function of Bcl-x_L, while providing a unique perspective on the underlying mechanism of Bcl-x_L deamidation-induced cell death. Additionally, we emphasized the importance of using full-length Bcl-x_L in membrane environment as well as the impact of post-translational modification, i.e., deamidation. The findings suggest that interaction pattern change, protein orientation towards membrane and protein-membrane interaction play pivotal role on the structural differences of the protein upon deamidation. Lastly, MD simulations confirmed that unbounded BH3-only peptides are dynamic in water compared to complex systems (bounded state). As a future work, complex systems (Bcl-x_L-BH3-only peptides) will be investigated before and after deamidation both in water and membrane environments.

In the second part of the thesis, keteniminium (KI) chemistry were examined from formation to reactions (electrocyclization and cycloaddition reactions). A wide range of substituents was examined to give insight on their potential contributions to the ease of formation of KIs. The computed data revealed that the reactivity of the starting nucleophilic amides towards the electrophilic triflic anhydride directly affected the ease of formation of the keteniminium salt. Additionally, DFT calculations were performed to rationalize the experimentally observed reactivity difference in the [2 + 2] cycloaddition of keteniminium with alkene and alkyne reactant partners. Calculations verified that the [2 + 2] cycloaddition reaction of keteniminium with alkene/alkyne has a stepwise reaction mechanism. In the competition reactions, computational findings also allowed us to determine favorable kinetic and thermodynamic pathways and investigate the effect of chain length on the competition reaction. Lastly, electrocyclization study presents structural and energetic analysis and the reactivity differences among keteniminium derivatives bearing different substituents leading to six different heterocyclic systems by means

of DFT. The electrocyclization of enamines leading to 3-aminopyrroles was shown to be both kinetically and thermodynamically most favorable. Compared to the systems in Group I, the aromatic moiety in Group II diminishes the reactivity due to the aromaticity disruption in the transition state for cyclization. This study provides insight on reactivity of keteniminium derivatives bearing different substituents and heteroatoms towards electrocyclization reactions. In addition, the true nature of the cyclization mechanism of keteniminium salts were disclosed via a range of different analysis techniques, pointing towards a 10π -electrocyclization for Group II rather than the 6π -electrocyclization observed in Group I.

Taken together, this dissertation provides a unique perspective on the underlying mechanism of Bcl-x_L deamidation-induced cell death. Ketiminium studies will also contribute to the understanding of keteniminium chemistry (formation, reactivity differences, etc.) and further aid synthetic applications.

Bibliography

- [1] Igney, F. H.; Krammer, P. H. Death and anti-death: Tumour resistance to apoptosis. *Nature Reviews Cancer* **2002**, 2, 277–288.
- [2] Trapani, J. A.; Smyth, M. J. Functional significance of the perforin/granzyme cell death pathway. *Nature Reviews Immunology* **2002**, 2, 735–747.
- [3] Martinvalet, D.; Zhu, P.; Lieberman, J. Granzyme A induces caspase-independent mitochondrial damage, a required first step for apoptosis. *Immunity* **2005**, 22, 355–370.
- [4] Singh, R.; Letai, A.; Sarosiek, K. Regulation of apoptosis in health and disease: the balancing act of BCL-2 family proteins. *Nature Reviews Molecular Cell Biology* **2019**, 20, 175–193.
- [5] Adams, J. M.; Cory, S. The BCL-2 arbiters of apoptosis and their growing role as cancer targets. *Cell Death and Differentiation* **2018**, 25, 27–36.
- [6] Brunelle, J. K.; Letai, A. Control of mitochondrial apoptosis by the Bcl-2 family. *Journal of Cell Science* **2009**, 122, 437–441.
- [7] Tait, S. W. G.; Green, D. R. Mitochondria and cell death: outer membrane permeabilization and beyond. *Nature Reviews Molecular Cell Biology* **2010**, 11, 621–632.
- [8] Chipuk, J. E.; Bouchier-Hayes, L.; Green, D. R. Mitochondrial outer membrane permeabilization during apoptosis: the innocent bystander scenario. *Cell death and differentiation* **2006**, 13, 1396–402.
- [9] Warren, C. F. A.; Wong-Brown, M. W.; Bowden, N. A. BCL-2 family isoforms in apoptosis and cancer. *Cell Death & Disease* **2019**, 10, 177.
- [10] Birkinshaw, R. W.; Czabotar, P. E. The BCL-2 family of proteins and mitochondrial outer membrane permeabilisation. *Seminars in Cell & Developmental Biology* **2017**, 72, 152–162.
- [11] Robinson, N. E.; Robinson, A. B. Molecular clocks. *Proceedings of the National Academy of Sciences of the United States of America* **2001**, 98, 944–9.
- [12] Tonie Wright, H.; Urry, D. W. Nonenzymatic Deamidation of Asparaginy and Glutaminy Residues in Protein. *Critical Reviews in Biochemistry and Molecular Biology* **1991**, 26, 1–52.

- [13] Aritomi, M.; Kunishima, N.; Inohara, N.; Ishibashi, Y.; Ohta, S.; Morikawa, K. Crystal Structure of Rat Bcl-x L. *Journal of Biological Chemistry* **1997**, 272, 27886–27892.
- [14] Muchmore, S. W.; Sattler, M.; Liang, H.; Meadows, R. P.; Harlan, J. E.; Yoon, H. S.; Nettlesheim, D.; Chang, B. S.; Thompson, C. B.; Wong, S.-L.; Ng, S.-C.; Fesik, S. W. X-ray and NMR structure of human Bcl-xL, an inhibitor of programmed cell death. *Nature* **1996**, 381, 335–341.
- [15] Cory, S.; Adams, J. M. The bcl2 family: regulators of the cellular life-or-death switch. *Nature Reviews Cancer* **2002**, 2, 647–656.
- [16] Boise, L. H.; González-García, M.; Postema, C. E.; Ding, L.; Lindsten, T.; Turka, L. A.; Mao, X.; Nuñez, G.; Thompson, C. B. bcl-x, a bcl-2-related gene that functions as a dominant regulator of apoptotic cell death. *Cell* **1993**, 74, 597–608.
- [17] Yao, Y.; Nisan, D.; Antignani, A.; Barnes, A.; Tjandra, N.; Youle, R. J.; Marassi, F. M.; Fujimoto, L. M. Characterization of the membrane-inserted C-terminus of cytoprotective BCL-XL. *Protein Expression and Purification* **2016**, 122, 56–63.
- [18] Lee, E. F.; Fairlie, W. D. The Structural Biology of Bcl-xL. *International Journal of Molecular Sciences* **2019**, 20, 2234.
- [19] Raltchev, K.; Pipercevic, J.; Hagn, F. Production and Structural Analysis of Membrane-Anchored Proteins in Phospholipid Nanodiscs. *Chemistry - A European Journal* **2018**, 24, 5493–5499.
- [20] Kale, J.; Osterlund, E. J.; Andrews, D. W. BCL-2 family proteins: changing partners in the dance towards death. *Cell Death and Differentiation* **2017**, 25186, 65–80.
- [21] Kharbanda, S.; Saxena, S.; Yoshida, K.; Pandey, P.; Kaneki, M.; Wang, Q.; Cheng, K.; Chen, Y. N.; Campbell, A.; Sudha, T.; Yuan, Z. M.; Narula, J.; Weichselbaum, R.; Nalin, C.; Kufe, D. Translocation of SAPK/JNK to mitochondria and interaction with Bcl-x(L) in response to DNA damage. *Journal of Biological Chemistry* **2000**, 275, 322–327.
- [22] Zheng, J. H.; Viacava Follis, A.; Kriwacki, R. W.; Moldoveanu, T. Discoveries and controversies in BCL-2 protein-mediated apoptosis. *The FEBS Journal* **2016**, 283, 2690–2700.
- [23] Clem, R. J.; Cheng, E. H.-Y.; Karp, C. L.; Kirsch, D. G.; Ueno, K.; Takahashi, A.; Kastan, M. B.; Griffin, D. E.; Earnshaw, W. C.; Velicuona, M. A.; Hardwick, J. M. Modulation of cell death by Bcl-xL through caspase interaction. *Proceedings of the National Academy of Sciences* **1998**, 95, 554–559.
- [24] Basañez, G.; Zhang, J.; Chau, B. N.; Maksaev, G. I.; Frolov, V. A.; Brandt, T. A.; Burch, J.; Hardwick, J. M.; Zimmerberg, J. Pro-apoptotic Cleavage Products of Bcl-x L Form Cytochrome c -conducting Pores in Pure Lipid Membranes. *Journal of Biological Chemistry* **2001**, 276, 31083–31091.

- [25] Beaumatin, F.; El Dhaybi, M.; Bobo, C.; Verdier, M.; Priault, M. Bcl-xL deamidation and cancer: Charting the fame trajectories of legitimate child and hidden siblings. *Biochimica et biophysica acta. Molecular cell research* **2017**, *1864*, 1734–1745.
- [26] Viehe, H. G.; Buijle, R.; Fuks, R.; Merényi, R.; Oth, J. M. F. Acylation, Alkylation, and Protonation of Alkynylamines. *Angewandte Chemie International Edition in English* **1967**, *6*, 77–78.
- [27] Ghosez, L.; Haveaux, B.; Viehe, H. G. Alkyl and Aryl α -Chloro Enamines. *Angewandte Chemie International Edition in English* **1969**, *8*, 454–455.
- [28] Marchand-Brynaert, J.; Ghosez, L. Cycloadditions of Keteneimmonium Cations to Olefins and Dienes. A New Synthesis of Four-Membered Rings. *Journal of the American Chemical Society* **1972**, *94*, 2870–2872.
- [29] Sidani, A.; Marchand-Brynaert, J.; Ghosez, L. A Convenient Procedure for the Synthesis of Cyclobutanones. *Angewandte Chemie International Edition in English* **1974**, *13*, 267.
- [30] Falmagne, J.-B.; Escudero, J.; Taleb-Sahraoui, S.; Ghosez, L. Cyclobutanone and Cyclobutenone Derivatives by Reaction of Tertiary Amides with Alkenes or Alkynes. *Angewandte Chemie International Edition in English* **1981**, *20*, 879–880.
- [31] Deyrup, J. A.; Kuta, G. S. Deprotonation of a hindered keteniminium salt. *The Journal of Organic Chemistry* **1978**, *43*, 501–505.
- [32] Evano, G.; Lecomte, M.; Thilmany, P.; Theunissen, C. Keteniminium Ions: Unique and Versatile Reactive Intermediates for Chemical Synthesis. *Synthesis* **2017**, *49*, 3183–3214.
- [33] Viehe, H. G. Synthesis and Reactions of the Alkynylamines. *Angewandte Chemie International Edition in English* **1967**, *6*, 767–778.
- [34] Dekorver, K. A.; Li, H.; Lohse, A. G.; Hayashi, R.; Lu, Z.; Zhang, Y.; Hsung, R. P. Ynamides: A modern functional group for the new millennium. *Chemical Reviews* **2010**, *110*, 5064–5106.
- [35] Evano, G.; Coste, A.; Jouvin, K. Ynamides: Versatile Tools in Organic Synthesis. *Angewandte Chemie International Edition* **2010**, *49*, 2840–2859.
- [36] Zhou, B.; Tan, T.-D.; Zhu, X.-Q.; Shang, M.; Ye, L.-W. Reversal of Regioselectivity in Ynamide Chemistry. *ACS Catalysis* **2019**, *9*, 6393–6406.
- [37] Izaguirre, J. A.; Catarello, D. P.; Wozniak, J. M.; Skeel, R. D. Langevin stabilization of molecular dynamics. *The Journal of Chemical Physics* **2001**, *114*, 2090–2098.
- [38] Goddard, T. D.; Huang, C. C.; Meng, E. C.; Pettersen, E. F.; Couch, G. S.; Morris, J. H.; Ferrin, T. E. UCSF ChimeraX: Meeting modern challenges in visualization and analysis. *Protein Science* **2018**, *27*, 14–25.

- [39] Tanriver, G.; Dagoneau, D.; Karadeniz, U.; Kolleth, A.; Lumbroso, A.; Sulzer-Mossé, S.; De Mesmaeker, A.; Catak, S. Keteniminium Salts: Reactivity and Propensity toward Electrocyclization Reactions. *The Journal of Organic Chemistry* **2020**, *85*, 449–463.
- [40] Alder, B. J.; Wainwright, T. E. Phase Transition for a Hard Sphere System. *The Journal of Chemical Physics* **1957**, *27*, 1208–1209.
- [41] Alder, B. J.; Wainwright, T. E. Studies in Molecular Dynamics. I. General Method. *The Journal of Chemical Physics* **1959**, *31*, 459–466.
- [42] Stillinger, F. H.; Rahman, A. Improved simulation of liquid water by molecular dynamics. *The Journal of Chemical Physics* **1974**, *60*, 1545–1557.
- [43] McCammon, J. A.; Gelin, B. R.; Karplus, M. Dynamics of folded proteins. *Nature* **1977**, *267*, 585–590.
- [44] Darden, T.; York, D.; Pedersen, L. Particle mesh Ewald: An $N \log(N)$ method for Ewald sums in large systems. *The Journal of Chemical Physics* **1993**, *98*, 10089–10092.
- [45] Essmann, U.; Perera, L.; Berkowitz, M. L.; Darden, T.; Lee, H.; Pedersen, L. G. A smooth particle mesh Ewald method. *The Journal of Chemical Physics* **1995**, *103*, 8577–8593.
- [46] Berendsen, H. J. C.; Postma, J. P. M.; van Gunsteren, W. F.; DiNola, A.; Haak, J. R. Molecular dynamics with coupling to an external bath. *The Journal of Chemical Physics* **1984**, *81*, 3684–3690.
- [47] Andersen, H. C. Molecular dynamics simulations at constant pressure and/or temperature. *The Journal of Chemical Physics* **1980**, *72*, 2384–2393.
- [48] Ryckaert, J. P.; Ciccotti, G.; Berendsen, H. J. Numerical integration of the cartesian equations of motion of a system with constraints: molecular dynamics of n-alkanes. *Journal of Computational Physics* **1977**, *23*, 327–341.
- [49] Hopkins, C. W.; Le Grand, S.; Walker, R. C.; Roitberg, A. E. Long-Time-Step Molecular Dynamics through Hydrogen Mass Repartitioning. *Journal of Chemical Theory and Computation* **2015**, *11*, 1864–1874.
- [50] Sugita, Y.; Okamoto, Y. Replica-exchange molecular dynamics method for protein folding. *Chemical Physics Letters* **1999**, *314*, 141–151.
- [51] Hansmann, U. H. Parallel tempering algorithm for conformational studies of biological molecules. *Chemical Physics Letters* **1997**, *281*, 140–150.
- [52] Amadei, A.; Linssen, A. B.; Berendsen, H. J. Essential dynamics of proteins. *Proteins: Structure, Function, and Bioinformatics* **1993**, *17*, 412–425.
- [53] Bakan, A.; Meireles, L. M.; Bahar, I. ProDy: Protein dynamics inferred from theory and experiments. *Bioinformatics* **2011**, *27*, 1575–1577.

- [54] Humphrey, W.; Dalke, A.; Schulten, K. VMD: Visual molecular dynamics. *Journal of Molecular Graphics* **1996**, *14*, 33–38.
- [55] Shao, J.; Tanner, S. W.; Thompson, N.; Cheatham, T. E. Clustering molecular dynamics trajectories: 1. Characterizing the performance of different clustering algorithms. *Journal of Chemical Theory and Computation* **2007**, *3*, 2312–2334.
- [56] Jain, A. K.; Murty, M. N.; Flynn, P. J. Data clustering. *ACM Computing Surveys* **1999**, *31*, 264–323.
- [57] Pople, J. A.; Segal, G. A. Approximate Self-Consistent Molecular Orbital Theory. II. Calculations with Complete Neglect of Differential Overlap. *The Journal of Chemical Physics* **1965**, *43*, S136–S151.
- [58] Pople, J. A.; Beveridge, D. L.; Dobosh, P. A. Approximate Self-Consistent Molecular-Orbital Theory. V. Intermediate Neglect of Differential Overlap. *The Journal of Chemical Physics* **1967**, *47*, 2026–2033.
- [59] Pople, J. A.; Santry, D. P.; Segal, G. A. Approximate Self-Consistent Molecular Orbital Theory. I. Invariant Procedures. *The Journal of Chemical Physics* **1965**, *43*, S129–S135.
- [60] Dewar, M. J.; Thiel, W. Ground States of Molecules. 38. The MNDO Method. Approximations and Parameters. *Journal of the American Chemical Society* **1977**, *99*, 4899–4907.
- [61] Dewar, M. J.; Zoebisch, E. G.; Healy, E. F.; Stewart, J. J. AM1: A New General Purpose Quantum Mechanical Molecular Model. *Journal of the American Chemical Society* **1985**, *107*, 3902–3909.
- [62] Stewart, J. J. Optimization of parameters for semiempirical methods II. Applications. *Journal of Computational Chemistry* **1989**, *10*, 221–264.
- [63] Stewart, J. J. Optimization of parameters for semiempirical methods V: Modification of NDDO approximations and application to 70 elements. *Journal of Molecular Modeling* **2007**, *13*, 1173–1213.
- [64] Sousa, S. F.; Fernandes, P. A.; Ramos, M. J. General performance of density functionals. *Journal of Physical Chemistry A* **2007**, *111*, 10439–10452.
- [65] Zhao, Y.; Truhlar, D. G. Density functionals with broad applicability in chemistry. *Accounts of Chemical Research* **2008**, *41*, 157–167.
- [66] Ceperley, D. M.; Alder, B. J. Ground state of the electron gas by a stochastic method. *Physical Review Letters* **1980**, *45*, 566–569.
- [67] Perdew, J. P.; Zunger, A. Self-interaction correction to density-functional approximations for many-electron systems. *Physical Review B* **1981**, *23*, 5048–5079.

- [68] Ortiz, G.; Ballone, P. Correlation energy, structure factor, radial distribution function, and momentum distribution of the spin-polarized uniform electron gas. *Physical Review B* **1994**, *50*, 1391–1405.
- [69] Paier, J.; Hirschl, R.; Marsman, M.; Kresse, G. The Perdew-Burke-Ernzerhof exchange-correlation functional applied to the G2-1 test set using a plane-wave basis set. *Journal of Chemical Physics* **2005**, *122*, 234102.
- [70] Cramer, C. J. *Essentials of Computational Chemistry: Theories and Models*, 2nd Edition | Wiley, 2nd ed.; Wiley, 2004; p 596.
- [71] Lee, C.; Yang, W.; Parr, R. G. Development of the Colle-Salvetti correlation-energy formula into a functional of the electron density. *Physical Review B* **1988**, *37*, 785–789.
- [72] Becke, A. D. Density-functional exchange-energy approximation with correct asymptotic behavior. *Physical Review A* **1988**, *38*, 3098–3100.
- [73] Miehlich, B.; Savin, A.; Stoll, H.; Preuss, H. Results obtained with the correlation energy density functionals of Becke and Lee, Yang and Parr. *Chemical Physics Letters* **1989**, *157*, 200–206.
- [74] Guidon, M.; Hutter, J.; Vandevondele, J. Auxiliary density matrix methods for Hartree-Fock exchange calculations. *Journal of Chemical Theory and Computation* **2010**, *6*, 2348–2364.
- [75] Becke, A. D. Density-functional thermochemistry. III. The role of exact exchange. *The Journal of Chemical Physics* **1993**, *98*, 5648–5652.
- [76] Zhao, Y.; Truhlar, D. G. The M06 suite of density functionals for main group thermochemistry, thermochemical kinetics, noncovalent interactions, excited states, and transition elements: Two new functionals and systematic testing of four M06-class functionals and 12 other function. *Theoretical Chemistry Accounts* **2008**, *120*, 215–241.
- [77] Lynch, B. J.; Fast, P. L.; Harris, M.; Truhlar, D. G. Adiabatic Connection for Kinetics. *The Journal of Physical Chemistry A* **2000**, *104*, 4811–4815.
- [78] Grimme, S. Semiempirical hybrid density functional with perturbative second-order correlation. *Journal of Chemical Physics* **2006**, *124*, 034108.
- [79] Barone, V.; Cossi, M. Quantum Calculation of Molecular Energies and Energy Gradients in Solution by a Conductor Solvent Model. *The Journal of Physical Chemistry A* **1998**, *102*, 1995–2001.
- [80] Cancès, E.; Mennucci, B.; Tomasi, J. A new integral equation formalism for the polarizable continuum model: Theoretical background and applications to isotropic and anisotropic dielectrics. *Journal of Chemical Physics* **1997**, *107*, 3032–3041.

- [81] Marenich, A. V.; Cramer, C. J.; Truhlar, D. G. Universal solvation model based on solute electron density and on a continuum model of the solvent defined by the bulk dielectric constant and atomic surface tensions. *Journal of Physical Chemistry B* **2009**, *113*, 6378–6396.
- [82] Klamt, A.; Schüürmann, G. COSMO: a new approach to dielectric screening in solvents with explicit expressions for the screening energy and its gradient. *J. Chem. Soc., Perkin Trans. 2* **1993**, 799–805.
- [83] Miertuš, S.; Scrocco, E.; Tomasi, J. Electrostatic interaction of a solute with a continuum. A direct utilization of AB initio molecular potentials for the prevision of solvent effects. *Chemical Physics* **1981**, *55*, 117–129.
- [84] Tomasi, J.; Mennucci, B.; Cammi, R. Quantum Mechanical Continuum Solvation Models. *Chemical Reviews* **2005**, *105*, 2999–3094.
- [85] Mennucci, B.; Tomasi, J. Continuum solvation models: A new approach to the problem of solute's charge distribution and cavity boundaries. *The Journal of Chemical Physics* **1997**, *106*, 5151–6158.
- [86] Leach, A. R. *Molecular Modelling: Principles and Applications*, 2nd ed.; Pearson, 2001.
- [87] Reed, A. E.; Weinstock, R. B.; Weinhold, F. Natural population analysis. *The Journal of Chemical Physics* **1985**, *83*, 735–746.
- [88] Contreras-García, J.; Johnson, E. R.; Keinan, S.; Chaudret, R.; Piquemal, J. P.; Beratan, D. N.; Yang, W. NCIPLOT: A program for plotting noncovalent interaction regions. *Journal of Chemical Theory and Computation* **2011**, *7*, 625–632.
- [89] Geerlings, P.; De Proft, F.; Langenaeker, W. Conceptual density functional theory. *Chemical Reviews* **2003**, *103*, 1793–1873.
- [90] Domingo, L. R.; Chamorro, E.; Pérez, P. Understanding the reactivity of captodative ethylenes in polar cycloaddition reactions. A theoretical study. *Journal of Organic Chemistry* **2008**, *73*, 4615–4624.
- [91] Soto-Delgado, J.; Domingo, L. R.; Contreras, R. Quantitative characterization of group electrophilicity and nucleophilicity for intramolecular Diels-Alder reactions. *Organic and Biomolecular Chemistry* **2010**, *8*, 3678–3683.
- [92] Parr, R. G.; Donnelly, R. A.; Levy, M.; Palke, W. E. Electronegativity: The density functional viewpoint. *The Journal of Chemical Physics* **1978**, *68*, 3801–3807.
- [93] Domingo, L. R.; Aurell, M. J.; Pérez, P.; Contreras, R. Quantitative characterization of the global electrophilicity power of common diene/dienophile pairs in Diels-Alder reactions. *Tetrahedron* **2002**, *58*, 4417–4423.
- [94] Domingo, L. R.; Aurell, M. J.; Pérez, P.; Contreras, R. Quantitative characterization of the local electrophilicity of organic molecules. Understanding the regioselectivity on Diels-Alder reactions. *Journal of Physical Chemistry A* **2002**, *106*, 6871–6875.

- [95] Parr, R. G.; Yang, W. Density Functional Approach to the Frontier-Electron Theory of Chemical Reactivity. *Journal of the American Chemical Society* **1984**, *106*, 4049–4050.
- [96] Domingo, L. R.; Pérez, P.; Sáez, J. A. Understanding the local reactivity in polar organic reactions through electrophilic and nucleophilic Parr functions. *RSC Advances* **2013**, *3*, 1486–1494.
- [97] Yang, W.; Mortier, W. J. The use of global and local molecular parameters for the analysis of the gas-phase basicity of amines. *Journal of the American Chemical Society* **1986**, *108*, 5708–5711.
- [98] Takehara, T.; Takahashi, H. Suppression of Bcl-xL deamidation in human hepatocellular carcinomas. *Cancer research* **2003**, *63*, 3054–7.
- [99] Leech, S. H.; Olie, R. A.; Gautschi, O.; Simões-Wüst, A. P.; Tschopp, S.; Häner, R.; Hall, J.; Stahel, R. A.; Zangemeister-Wittke, U. Induction of apoptosis in lung-cancer cells following bcl-xL anti-sense treatment. *International journal of cancer* **2000**, *86*, 570–6.
- [100] Liu, X.; Beugelsdijk, A.; Chen, J. Dynamics of the BH3-Only Protein Binding Interface of Bcl-xL. *Biophysical Journal* **2015**, *109*, 1049–1067.
- [101] Liu, X.; Jia, Z.; Chen, J.; Phys, J.; Chem, B. Enhanced Sampling of Intrinsic Structural Heterogeneity of the BH3-Only Protein Binding Interface of Bcl-xL. *The Journal of Physical Chemistry B* **2017**, *121*, 9160–9168.
- [102] Maity, A.; Yadav, S.; Verma, C. S.; Ghosh Dastidar, S. Dynamics of Bcl-xL in Water and Membrane: Molecular Simulations. *PLoS ONE* **2013**, *8*, e76837.
- [103] Hill, R. B.; MacKenzie, K. R.; Harwig, M. C. The Tail-End Is Only the Beginning: NMR Study Reveals a Membrane-Bound State of BCL-XL. *Journal of Molecular Biology* **2015**, *427*, 2257–2261.
- [104] Chang, B. S.; Minn, A. J.; Muchmore, S. W.; Fesik, S. W.; Thompson, C. B. Identification of a novel regulatory domain in Bcl-x(L) and Bcl-2. *EMBO Journal* **1997**, *16*, 968–977.
- [105] Follis, A. V.; Llambi, F.; Kalkavan, H.; Yao, Y.; Phillips, A. H.; Park, C.-G.; Marassi, F. M.; Green, D. R.; Kriwacki, R. W. Regulation of apoptosis by an intrinsically disordered region of Bcl-xL. *Nature Chemical Biology* **2018**, *14*, 458–465.
- [106] Letai, A.; Kutuk, O. Regulation of Bcl-2 Family Proteins by Posttranslational Modifications. *Current Molecular Medicine* **2008**, *8*, 102–118.
- [107] Yao, Y.; Fujimoto, L. M.; Hirshman, N.; Bobkov, A. A.; Antignani, A.; Youle, R. J.; Marassi, F. M. Conformation of BCL-XL upon membrane integration. *Journal of Molecular Biology* **2015**, *427*, 2262–2270.

- [108] Borrás, C.; Mas-Bargues, C.; Román-Domínguez, A.; Sanz-Ros, J.; Gimeno-Mallench, L.; Inglés, M.; Gambini, J.; Viña, J. BCL-xL, a Mitochondrial Protein Involved in Successful Aging: From *C. elegans* to Human Centenarians. *International Journal of Molecular Sciences* **2020**, *21*, 418.
- [109] Walsh, G.; Jefferis, R. Post-translational modifications in the context of therapeutic proteins. *Nature Biotechnology* **2006**, *24*, 1241–1252.
- [110] Walsh, G. Post-translational modifications of protein biopharmaceuticals. *Drug Discovery Today* **2010**, *15*, 773–780.
- [111] Han, Z.-J.; Feng, Y.-H.; Gu, B.-H.; Li, Y.-M.; Chen, H. The post-translational modification, SUMOylation, and cancer (Review). *International Journal of Oncology* **2018**, *52*, 1081–1094.
- [112] Bobo, C.; Céré, C.; Dufossée, M.; Dautant, A.; Moreau, V.; Manon, S.; Beaumatin, F.; Priault, M. Improved electrophoretic separation to assist the monitoring of bcl-xl post-translational modifications. *International Journal of Molecular Sciences* **2019**, *20*, 5571.
- [113] Deverman, B. E.; Cook, B. L.; Manson, S. R.; Niederhoff, R. A.; Langer, E. M.; Rosová, I.; Kulans, L. A.; Fu, X.; Weinberg, J. S.; Heinecke, J. W.; Roth, K. A.; Weintraub, S. J. Bcl-xL Deamidation Is a Critical Switch in the Regulation of the Response to DNA Damage. *Cell* **2002**, *111*, 51–62.
- [114] Beaumatin, F.; Dhaybi, M. E.; Lasserre, J.-p.; Moyer, M. P.; Verdier, M.; Manon, S.; Priault, M. N52 monodeamidated Bcl - x L properties in vivo and in vitro shows impaired oncogenic. *Oncotarget* **2016**, *7*, 17129–17143.
- [115] Zhao, R.; Oxley, D.; Smith, T. S.; Follows, G. A.; Green, A. R.; Alexander, D. R. DNA damage-induced Bcl-xL deamidation is mediated by NHE-1 antiport regulated intracellular pH. *PLoS Biology* **2007**, *5*, 0039–0053.
- [116] Seng, N.; Megyesi, J.; Tarcsafalvi, A.; Price, P. Mimicking Cdk2 phosphorylation of Bcl-xL at Ser73 results in caspase activation and Bcl-xL cleavage. *Cell Death Discovery* **2016**, *2*, 16001.
- [117] Fujita, N.; Nagahashi, A.; Nagashima, K.; Rokudai, S.; Tsuruo, T. Acceleration of apoptotic cell death after the cleavage of Bcl-XL protein by caspase-3-like proteases. *Oncogene* **1998**, *17*, 1295–1304.
- [118] Robinson, N. E.; Robinson, Z. W.; Robinson, B. R.; Robinson, A. B. A. L.; Robinson, J. A.; Robinson, M. L.; Robinson, A. B. A. L. Structure-dependent nonenzymatic deamidation of glutaminy and asparaginy pentapeptides. *Journal of Peptide Research* **2004**, *63*, 426–436.
- [119] Geiger, T.; Clarke, S. Deamidation, isomerization, and racemization at asparaginy and aspartyl residues in peptides. Succinimide-linked reactions that contribute to protein degradation. *Journal of Biological Chemistry* **1987**, *262*, 785–794.

- [120] Cheng, E. H.; Wei, M. C.; Weiler, S.; Flavell, R. A.; Mak, T. W.; Lindsten, T.; Korsmeyer, S. J. BCL-2, BCL-XL sequester BH3 domain-only molecules preventing BAX- and BAK-mediated mitochondrial apoptosis. *Molecular Cell* **2001**, 8, 705–711.
- [121] Leber, B.; Lin, J.; Andrews, D. W. Still embedded together binding to membranes regulates Bcl-2 protein interactions. *Oncogene* **2010**, 29, 5221–5230.
- [122] Levine, B.; Sinha, S. C.; Kroemer, G. Bcl-2 family members: Dual regulators of apoptosis and autophagy. *Autophagy* **2008**, 4, 600–606.
- [123] Borras, C. et al. Human exceptional longevity: Transcriptome from centenarians is distinct from septuagenarians and reveals a role of Bcl-xL in successful aging. *Aging* **2016**, 8, 3185–3208.
- [124] Yosef, R.; Pilpel, N.; Tokarsky-Amiel, R.; Biran, A.; Ovadya, Y.; Cohen, S.; Vadai, E.; Dassa, L.; Shahar, E.; Condiotti, R.; Ben-Porath, I.; Krizhanovsky, V. Directed elimination of senescent cells by inhibition of BCL-W and BCL-XL. *Nature Communications* **2016**, 7, 11190.
- [125] Vicencio, J. M.; Galluzzi, L.; Tajeddine, N.; Ortiz, C.; Criollo, A.; Tasdemir, E.; Morselli, E.; Ben Younes, A.; Maiuri, M. C.; Lavandro, S.; Kroemer, G. Senescence, apoptosis or autophagy? When a damaged cell must decide its path - A mini-review. *Gerontology* **2008**, 54, 92–99.
- [126] Dho, S. H.; Deverman, B. E.; Lapid, C.; Manson, S. R.; Gan, L.; Riehm, J. J.; Aurora, R.; Kwon, K.-S. S.; Weintraub, S. J. Control of Cellular Bcl-xL Levels by Deamidation-Regulated Degradation. *PLoS Biology* **2013**, 11, 12201901–14924.
- [127] Deverman, B. E.; Cook, B. L.; Manson, S. R.; Niederhoff, R. A.; Langer, E. M.; Rosová, I.; Kulans, L. A.; Fu, X.; Weinberg, J. S.; Heinecke, J. W.; Roth, K. A.; Weintraub, S. J. Bcl-xL Deamidation Is a Critical Switch in the Regulation of the Response to DNA Damage. *Cell* **2003**, 115, 503.
- [128] Ahn, J. S.; Li, J.; Chen, E.; Kent, D. G.; Park, H. J.; Green, A. R. JAK2V617F mediates resistance to DNA damage-induced apoptosis by modulating FOXO3A localization and Bcl-xL deamidation. *Oncogene* **2016**, 35, 2235–2246.
- [129] Fares, M.; Abedi-Valugerdi, M.; Hassan, M.; Potáková, Z. DNA damage, lysosomal degradation and Bcl-xL deamidation in doxycycline- and minocycline-induced cell death in the K562 leukemic cell line. *Biochemical and Biophysical Research Communications* **2015**, 463, 268–274.
- [130] Asakura, T.; Maeda, K.; Omi, H.; Matsudaira, H.; Ohkawa, K. The association of deamidation of Bcl-xL and translocation of Bax to the mitochondria through activation of JNK in the induction of apoptosis by treatment with GSH-conjugated DXR. *International Journal of Oncology* **2008**, 33, 389–395.

- [131] Priya, P.; Maity, A.; Ghosh Dastidar, S. The long unstructured region of Bcl-xl modulates its structural dynamics. *Proteins: Structure, Function, and Bioinformatics* **2017**, *85*, 1567–1579.
- [132] Ryzhov, P.; Tian, Y.; Yao, Y.; Bobkov, A. A.; Im, W.; Marassi, F. M. Conformational States of the Cytoprotective Protein Bcl-xL. *Biophysical Journal* **2020**, *119*, 1324–1334.
- [133] Case, D. A. et al. AMBER 2018. **2018**, University of California: San Francisco, 2018.
- [134] Maier, J. A.; Martinez, C.; Kasavajhala, K.; Wickstrom, L.; Hauser, K. E.; Simmerling, C. ff14SB: Improving the Accuracy of Protein Side Chain and Backbone Parameters from ff99SB. *Journal of Chemical Theory and Computation* **2015**, *11*, 3696–3713.
- [135] Jorgensen, W. L.; Chandrasekhar, J.; Madura, J. D.; Impey, R. W.; Klein, M. L. Comparison of simple potential functions for simulating liquid water. *The Journal of Chemical Physics* **1983**, *79*, 926–935.
- [136] Roe, D. R.; Cheatham, T. E. PTRAJ and CPPTRAJ: Software for processing and analysis of molecular dynamics trajectory data. *Journal of Chemical Theory and Computation* **2013**, *9*, 3084–3095.
- [137] Kabsch, W.; Sander, C. Dictionary of protein secondary structure: Pattern recognition of hydrogen-bonded and geometrical features. *Biopolymers* **1983**, *22*, 2577–2637.
- [138] Pettersen, E. F.; Goddard, T. D.; Huang, C. C.; Couch, G. S.; Greenblatt, D. M.; Meng, E. C.; Ferrin, T. E. UCSF Chimera-A visualization system for exploratory research and analysis. *Journal of Computational Chemistry* **2004**, *25*, 1605–1612.
- [139] Rajan, S.; Choi, M.; Baek, K.; Yoon, H. S. Bh3 induced conformational changes in Bcl-Xl revealed by crystal structure and comparative analysis. *Proteins: Structure, Function, and Bioinformatics* **2015**, *83*, 1262–1272.
- [140] Lee, E. F.; Smith, N. A.; Soares da Costa, T. P.; Meftahi, N.; Yao, S.; Harris, T. J.; Tran, S.; Pettikiriarachchi, A.; Perugini, M. A.; Keizer, D. W.; Evangelista, M.; Smith, B. J.; Fairlie, W. D. Structural insights into BCL2 pro-survival protein interactions with the key autophagy regulator BECN1 following phosphorylation by STK4/MST1. *Autophagy* **2019**, *15*, 785–795.
- [141] Priyadarshi, A.; Roy, A.; Kim, K. S.; Kim, E. E. K.; Hwang, K. Y. Structural insights into mouse anti-apoptotic Bcl-xl reveal affinity for Beclin 1 and gossypol. *Biochemical and Biophysical Research Communications* **2010**, *394*, 515–521.
- [142] Bhola, P. D.; Letai, A. Mitochondria-Judges and Executioners of Cell Death Sentences. 2016.
- [143] Letai, A.; Bassik, M. C.; Walensky, L. D.; Sorcinelli, M. D.; Weiler, S.; Korsmeyer, S. J. Distinct BH3 domains either sensitize or activate mitochondrial apoptosis, serving as prototype cancer therapeutics. *Cancer Cell* **2002**, *2*, 183–192.

- [144] Chen, Z.; Wannere, C. S.; Corminboeuf, C.; Puchta, R.; v. R. Schleyer, P. NICS as an aromaticity criterion. *Chem. Rev.* **2005**, *105*, 3842–3888.
- [145] Leber, B.; Lin, J.; Andrews, D. W. Embedded together: The life and death consequences of interaction of the Bcl-2 family with membranes. *Apoptosis* **2007**, *12*, 897–911.
- [146] Llambi, F.; Moldoveanu, T.; Tait, S. W.; Bouchier-Hayes, L.; Temirov, J.; McCormick, L. L.; Dillon, C. P.; Green, D. R. A Unified Model of Mammalian BCL-2 Protein Family Interactions at the Mitochondria. *Molecular Cell* **2011**, *44*, 517–531.
- [147] Shamas-Din, A.; Brahmabhatt, H.; Leber, B.; Andrews, D. W. BH3-only proteins: Orchestrators of apoptosis. *Biochimica et Biophysica Acta (BBA) - Molecular Cell Research* **2011**, *1813*, 508–520.
- [148] Shamas-Din, A.; Bindner, S.; Zhu, W.; Zaltsman, Y.; Campbell, C.; Gross, A.; Leber, B.; Andrews, D. W.; Fradin, C. tBid Undergoes Multiple Conformational Changes at the Membrane Required for Bax Activation. *Journal of Biological Chemistry* **2013**, *288*, 22111–22127.
- [149] Chi, X.; Kale, J.; Leber, B.; Andrews, D. W. Regulating cell death at, on, and in membranes. *Biochimica et biophysica acta* **2014**, *1843*, 2100–13.
- [150] Hsu, Y. T.; Wolter, K. G.; Youle, R. J. Cytosol-to-membrane redistribution of Bax and Bcl-XL during apoptosis. *Proceedings of the National Academy of Sciences of the United States of America* **1997**, *94*, 3668–3672.
- [151] Todt, F.; Cakir, Z.; Reichenbach, F.; Youle, R.; Edlich, F. The C-terminal helix of Bcl-xL mediates Bax retrotranslocation from the mitochondria. *Cell Death and Differentiation* **2013**, *20131*, 333–342.
- [152] Hausmann, G.; O'Reilly, L. A.; van Driel, R.; Beaumont, J. G.; Strasser, A.; Adams, J. M.; Huang, D. C. Pro-Apoptotic Apoptosis Protease-Activating Factor 1 (Apaf-1) Has a Cytoplasmic Localization Distinct from Bcl-2 or Bcl-XL. *Journal of Cell Biology* **2000**, *149*, 623–634.
- [153] Nijhawan, D. Elimination of Mcl-1 is required for the initiation of apoptosis following ultraviolet irradiation. *Genes & Development* **2003**, *17(1) Nijh*, 1475–1486.
- [154] Edlich, F.; Banerjee, S.; Suzuki, M.; Cleland, M. M.; Arnoult, D.; Wang, C.; Neutzner, A.; Tjandra, N.; Youle, R. J. Bcl-xL retrotranslocates Bax from the mitochondria into the cytosol. *Cell* **2011**, *145*, 104–116.
- [155] Kaufmann, T.; Schlipf, S.; Sanz, J.; Neubert, K.; Stein, R.; Borner, C. Characterization of the signal that directs Bcl-xL, but not Bcl-2, to the mitochondrial outer membrane. *Journal of Cell Biology* **2003**, *160*, 53–64.
- [156] Suzuki, M.; Youle, R. J.; Tjandra, N. Structure of Bax: Coregulation of Dimer Formation and Intracellular Localization. *Cell* **2000**, *103*, 645–654.

- [157] Eswar, N.; Webb, B.; Marti-Renom, M. A.; Madhusudhan, M.; Eramian, D.; Shen, M.; Pieper, U.; Sali, A. Comparative Protein Structure Modeling Using Modeller. *Current Protocols in Bioinformatics* **2006**, *15*, Unit 5 6.
- [158] Maity, A.; Sinha, S.; Ganguly, D.; Ghosh Dastidar, S. C-terminal tail insertion of Bcl-xL in membrane occurs via partial unfolding and refolding cycle associating microsolvation. *Phys Chem Chem Phys* **2016**, *18*, 24095–24105.
- [159] Maity, A.; Sinha, S.; Ghosh Dastidar, S. Dissecting the thermodynamic contributions of the charged residues in the membrane anchoring of Bcl-xL C-terminal domain. *Chemistry and Physics of Lipids* **2019**, *218*, 112–124.
- [160] Vasquez-Montes, V.; Vargas-Urbe, M.; Pandey, N. K.; Rodnin, M. V.; Langen, R.; Ladokhin, A. S. Lipid-modulation of membrane insertion and refolding of the apoptotic inhibitor Bcl-xL. *Biochimica et Biophysica Acta - Proteins and Proteomics* **2019**, *1867*, 691–700.
- [161] Vasquez-Montes, V.; Kyrychenko, A.; Vargas-Urbe, M.; Rodnin, M. V.; Ladokhin, A. S. Conformational Switching in Bcl-xL: Enabling Non-Canonical Inhibition of Apoptosis Involves Multiple Intermediates and Lipid Interactions. *Cells* **2020**, *9*, 539.
- [162] Ryzhov, P.; Yao, Y.; Verdugo, B. B.; Salvesen, G.; Marassi, F. M. Membrane-Mediated Conformational Changes of Cytoprotective BCL-XL Regulate its Activity. *Biophysical Journal* **2020**, *118*, 211a.
- [163] Patriksson, A.; van der Spoel, D. A temperature predictor for parallel tempering simulations. *Physical Chemistry Chemical Physics* **2008**, *10*, 2073–2077.
- [164] Cathcart, K.; Patel, A.; Dies, H.; Rheinstädter, M.; Fradin, C. Effect of Cholesterol on the Structure of a Five-Component Mitochondria-Like Phospholipid Membrane. *Membranes* **2015**, *5*, 664–684.
- [165] Horvath, S. E.; Daum, G. Lipids of mitochondria. *Progress in Lipid Research* **2013**, *52*, 590–614.
- [166] Daum, G.; Vance, J. E. Import of lipids into mitochondria. *Progress in Lipid Research* **1997**, *36*, 103–130.
- [167] Goossens, K.; De Winter, H. Molecular Dynamics Simulations of Membrane Proteins: An Overview. *Journal of Chemical Information and Modeling* **2018**, *58*, 2193–2202.
- [168] Lee, J. et al. CHARMM-GUI Input Generator for NAMD, GROMACS, AMBER, OpenMM, and CHARMM/OpenMM Simulations Using the CHARMM36 Additive Force Field. *Journal of Chemical Theory and Computation* **2016**, *12*, 405–413.
- [169] Jo, S.; Lim, J. B.; Klauda, J. B.; Im, W. CHARMM-GUI membrane builder for mixed bilayers and its application to yeast membranes. *Biophysical Journal* **2009**, *97*, 50–58.

- [170] Dickson, C. J. et al. Lipid14: The amber lipid force field. *Journal of Chemical Theory and Computation* **2014**, *10*, 865–879.
- [171] Tanriver, G.; Monard, G.; Catak, S. Impact of Deamidation on the Structure and Function of Antiapoptotic Bcl-x L. *Journal of Chemical Information and Modeling* **2022**, *62*, 102–115.
- [172] Liu, X.; Dai, S.; Zhu, Y.; Marrack, P.; Kappler, J. W. The structure of a Bcl-xL/Bim fragment complex: Implications for Bim function. *Immunity* **2003**, *19*, 341–352.
- [173] Wilfling, F.; Weber, A.; Potthoff, S.; Vögtle, F.-N.; Meisinger, C.; Paschen, S. A.; Häcker, G. BH3-only proteins are tail-anchored in the outer mitochondrial membrane and can initiate the activation of Bax. *Cell Death & Differentiation* **2012**, *19*, 1328–1336.
- [174] Ashkenazi, A.; Fairbrother, W. J.; Levenson, J. D.; Souers, A. J. From basic apoptosis discoveries to advanced selective BCL-2 family inhibitors. *Nature Reviews Drug Discovery* **2017**, *16*, 273–284.
- [175] Pécot, J.; Maillet, L.; Le Pen, J.; Vuillier, C.; Trécesson, S. d. C.; Fétiveau, A.; Sarosiek, K. A.; Bock, F. J.; Braun, F.; Letai, A.; Tait, S. W.; Gautier, F.; Juin, P. P. Tight Sequestration of BH3 Proteins by BCL-xL at Subcellular Membranes Contributes to Apoptotic Resistance. *Cell Reports* **2016**, *17*, 3347–3358.
- [176] Martin, A. C. R.; Porter, C. T. ProFit Version 3.1. 2009.
- [177] Modi, V.; Lama, D.; Sankararamakrishnan, R. Relationship between helix stability and binding affinities: molecular dynamics simulations of Bfl-1/A1-binding pro-apoptotic BH3 peptide helices in explicit solvent. *Journal of Biomolecular Structure and Dynamics* **2013**, *31*, 65–77.
- [178] Lama, D.; Sankararamakrishnan, R. Molecular dynamics simulations of pro-apoptotic BH3 peptide helices in aqueous medium: Relationship between helix stability and their binding affinities to the anti-apoptotic protein Bcl-XL. *Journal of Computer-Aided Molecular Design* **2011**, *25*, 413–426.
- [179] Yao, Y.; Bobkov, A. A.; Plesniak, L. A.; Marassi, F. M. Mapping the interaction of pro-apoptotic tBID with pro-survival BCL-XL. *Biochemistry* **2009**, *48*, 8704–8711.
- [180] Madelaine, C.; Valerio, V.; Maulide, N. Revisiting keteniminium salts: More than the nitrogen analogs of ketenes. *Chem. Asian J.* **2011**, *6*, 2224–2239.
- [181] Snider, B. B. Intramolecular cycloaddition reactions of ketenes and keteniminium salts with alkenes. *Chemical Reviews* **1988**, *88*, 793–811.
- [182] Ghosez, L.; Mahuteau-Betzer, F.; Genicot, C.; Vallribera, A.; Cordier, J.-F. Enantioselective Vicinal Bis-Acylation of Olefins. *Chemistry - A European Journal* **2002**, *8*, 3411–3422.

- [183] Mahuteau-Betzer, F.; Ding, P.-Y.; Ghosez, L. First [4+2] Cycloadditions Involving the Olefinic Bond of an 'Aldoketeniminium Salt' (=N-Alk-1-enylideneaminium Salt). *Helvetica Chimica Acta* **2005**, *88*, 2022–2031.
- [184] Villedieu-Percheron, E.; Catak, S.; Zurwerra, D.; Staiger, R.; Lachia, M.; De Mesmaeker, A. $6\pi/10\pi$ -Electrocyclization of ketene-iminium salts for the synthesis of substituted naphthylamines. *Tetrahedron Letters* **2014**, *55*, 2446–2449.
- [185] Lumbroso, A.; Behra, J.; Kolleth, A.; Dakas, P.-Y.; Karadeniz, U.; Catak, S.; Sulzer-Mossé, S.; De Mesmaeker, A. Access to functionalized 3-amino-benzothiophenes using keteniminium intermediates. *Tetrahedron Letters* **2015**, *56*, 6541–6545.
- [186] Lumbroso, A.; Catak, S.; Sulzer-Mossé, S.; De Mesmaeker, A. Synthesis of cyclobuteniminium salts derived from aldo-keteniminium salts and study of their reactivity in Diels-Alder reaction. *Tetrahedron Letters* **2014**, *55*, 6721–6725.
- [187] Kolleth, A.; Lumbroso, A.; Tanriver, G.; Catak, S.; Sulzer-Mossé, S.; De Mesmaeker, A. Synthesis of 4-membered ring alkaloid analogues via intramolecular [2+2] cycloaddition involving keteniminium salt intermediates. *Tetrahedron Letters* **2017**, *58*, 2904–2909.
- [188] Lecomte, M.; Evano, G. Harnessing the Electrophilicity of Keteniminium Ions: A Simple and Straightforward Entry to Tetrahydropyridines and Piperidines from Ynamides. *Angewandte Chemie - International Edition* **2016**, *55*, 4547–4551.
- [189] Xu, L.; Yang, P.; Wang, L. Direct functionalization of benzylic and non-benzylic C(sp³)-H bonds via keteniminium ion initiated cascade [1,5]-hydrogen transfer/cyclization. *Organic Chemistry Frontiers* **2018**, *5*, 1854–1858.
- [190] Peng, B.; O'Donovan, D. H.; Jurberg, I. D.; Maulide, N. Dual nucleophilic/electrophilic capture of in situ generated iminium ethers: Towards the synthesis of functionalized amide building blocks. *Chemistry - A European Journal* **2012**, *18*, 16292–16296.
- [191] Lumbroso, A.; Catak, S.; Sulzer-Mossé, S.; De Mesmaeker, A. Cycloaddition of keteniminium with terminal alkynes toward cyclobuteniminium and their use in Diels-Alder reactions. *Tetrahedron Letters* **2014**, *55*, 5147–5150.
- [192] Emamian, S.; Hosseini, S. j.; Ravani, K.-s. Ionic Diels-Alder reaction of 3-bromofuran toward the highly electron deficient cyclobuteniminium cation: a regio- and stereoselectivity, and molecular mechanism study using DFT. *RSC Advances* **2015**, *5*, 98538–98548.
- [193] Kolleth, A.; Lumbroso, A.; Tanriver, G.; Catak, S.; Sulzer-Mossé, S.; De Mesmaeker, A. New access to quaternary aminocyclobutanes via nucleophilic addition on cyclobuteniminium salts. *Tetrahedron Letters* **2016**, *57*, 3510–3514.
- [194] Garro-Helion, F.; Merzouk, A.; Guibé, F. Mild and Selective Palladium(0)-Catalyzed Deallylation of Allylic Amines. Allylamine and Diallylamine as Very Convenient Ammonia Equivalents for the Synthesis of Primary Amines. *Journal of Organic Chemistry* **1993**, *58*, 6109–6113.

- [195] Kolleth, A.; Lumbroso, A.; Tanriver, G.; Catak, S.; Sulzer-Mossé, S.; De Mesmaeker, A. Synthesis of amino-cyclobutanes via [2+2] cycloadditions involving keteniminium intermediates. *Tetrahedron Letters* **2016**, *57*, 2697–2702.
- [196] Kolleth, A.; Müller, S.; Lumbroso, A.; Tanriver, G.; Catak, S.; Sulzer-Mossé, S.; De Mesmaeker, A. Access to 3-aminobenzothiophenes and 3-aminothiophenes fused to 5-membered heteroaromatic rings through 6π -electrocyclization reaction of keteniminium salts. *Tetrahedron Letters* **2018**, *59*, 3242–3248.
- [197] Dagoneau, D.; Kolleth, A.; Lumbroso, A.; Tanriver, G.; Catak, S.; Sulzer-Mossé, S.; De Mesmaeker, A. Straightforward Synthesis of 3-Aminothiophenes Using Activated Amides. *Helvetica Chimica Acta* **2019**, *102*, e1900031.
- [198] Catak, S.; Hemelsoet, K.; Hermosilla, L.; Waroquier, M.; Van Speybroeck, V. Competitive reactions of organophosphorus radicals on coke surfaces. *Chemistry - A European Journal* **2011**, *17*, 12027–12036.
- [199] Goossens, H.; Winne, J. M.; Wouters, S.; Hermosilla, L.; De Clercq, P. J.; Waroquier, M.; Van Speybroeck, V.; Catak, S. Possibility of [1,5] sigmatropic shifts in bicyclo[4.2.0]octa-2,4-dienes. *Journal of Organic Chemistry* **2015**, *80*, 2609–2620.
- [200] Hermosilla, L.; Catak, S.; Speybroeck, V. V.; Waroquier, M.; Vandenberghe, J.; Motmans, F.; Adriaenssens, P.; Lutsen, L.; Cleij, T.; Vanderzande, D. Kinetic and mechanistic Study on p-Quinodimethane formation in the sulfinyl precursor route for the polymerization of poly(p-phenylenevinylene)(PPV). *Macromolecules* **2010**, *43*, 7424–7433.
- [201] Schuchardt, K. L.; Didier, B. T.; Elsethagen, T.; Sun, L.; Gurumoorthi, V.; Chase, J.; Li, J.; Windus, T. L. Basis Set Exchange: A Community Database for Computational Sciences. *Journal of Chemical Information and Modeling* **2007**, *47*, 1045–1052.
- [202] Tomasi, J.; Mennucci, B.; Cancès, E. The IEF version of the PCM solvation method: an overview of a new method addressed to study molecular solutes at the QM ab initio level. *Journal of Molecular Structure: THEOCHEM* **1999**, *464*, 211–226.
- [203] Frisch, M. J. et al. Gaussian 16, Revision A.03. *Gaussian Inc. Wallingford CT* **2016**,
- [204] Fukui, K. The path of chemical reactions - the IRC approach. *Accounts of Chemical Research* **1981**, *14*, 363–368.
- [205] Hratchian, H. P.; Schlegel, H. B. Accurate reaction paths using a Hessian based predictor-corrector integrator. *Journal of Chemical Physics* **2004**, *120*, 9918–9924.
- [206] Hratchian, H. P.; Schlegel, H. B. Using Hessian updating to increase the efficiency of a Hessian based predictor-corrector reaction path following method. *Journal of Chemical Theory and Computation* **2005**, *1*, 61–69.
- [207] Hehre, W. J.; Ditchfield, R.; Pople, J. A. Self—Consistent Molecular Orbital Methods. XII. Further Extensions of Gaussian—Type Basis Sets for Use in Molecular Orbital Studies of Organic Molecules. *The Journal of Chemical Physics* **1972**, *56*, 2257–2261.

- [208] Gonzalez, C.; Schlegel, H. B. Reaction Path Following in Mass-Weighted Internal Coordinates. *J. Phys. Chem* **1990**, *94*, 5523–5527.
- [209] Bickelhaupt, F. M.; Houk, K. N. Analyzing Reaction Rates with the Distortion/Interaction-Activation Strain Model. *Angewandte Chemie - International Edition* **2017**, *56*, 10070–10086.
- [210] Fernández, I.; Bickelhaupt, F. M. The activation strain model and molecular orbital theory: understanding and designing chemical reactions. *Chem. Soc. Rev.* **2014**, *43*, 4953–4967.
- [211] van Zeist, W.-J.; Bickelhaupt, F. M. The activation strain model of chemical reactivity. *Organic & Biomolecular Chemistry* **2010**, *8*, 3118.
- [212] Fukui, K.; Yonezawa, T.; Shingu, H. A Molecular Orbital Theory of Reactivity in Aromatic Hydrocarbons. *The Journal of Chemical Physics* **1952**, *20*, 722–725.
- [213] Fukui, K. Role of frontier orbitals in chemical reactions. *Science (New York, N.Y.)* **1982**, *218*, 747–54.
- [214] Lu, T.; Chen, F. Multiwfn: A multifunctional wavefunction analyzer. *Journal of Computational Chemistry* **2012**, *33*, 580–592.
- [215] Skripnikov, L. V. Chemissian, version 4.60. *Visualization Computer Program* **2018**,
- [216] Legault, C. Y. CYLview, version 1.0b. *Université de Sherbrooke* **2009**,
- [217] Frisch, M. J. et al. Gaussian 09, Revision E.01. *Gaussian Inc. Wallingford CT* **2013**,
- [218] Catak, S.; D’hooghe, M.; De Kimpe, N.; Waroquier, M.; Van Speybroeck, V. Intramolecular π – π Stacking Interactions in 2-Substituted N, N -Dibenzylaziridinium Ions and Their Regioselectivity in Nucleophilic Ring-Opening Reactions. *The Journal of Organic Chemistry* **2010**, *75*, 885–896.
- [219] Boese, A. D.; Martin, J. M. Development of density functional for thermochemical kinetics. *Journal of Chemical Physics* **2004**, *121*, 3405–3416.
- [220] Boydas, E.; Tanriver, G.; D’Hooghe, M.; Ha, H.-J.; Van Speybroeck, V.; Catak, S. Theoretical insight into the regioselective ring-expansions of bicyclic aziridinium ions. *Organic and Biomolecular Chemistry* **2018**, *16*, 796–806.
- [221] Yanai, T.; Tew, D. P.; Handy, N. C. A new hybrid exchange-correlation functional using the Coulomb-attenuating method (CAM-B3LYP). *Chemical Physics Letters* **2004**, *393*, 51–57.
- [222] Domingo, L. R.; Ríos-Gutiérrez, M.; Pérez, P. A DFT study of the ionic [2+2] cycloaddition reactions of keteniminium cations with terminal acetylenes. *Tetrahedron* **2015**, *71*, 2421–2427.

- [223] Domingo, L. R.; Ríos-Gutiérrez, M.; Sáez, J. A. Unravelling the mechanism of the ketene-imine Staudinger reaction. An ELF quantum topological analysis. *RSC Advances* **2015**, *5*, 37119–37129.
- [224] Kolleth, A.; Lumbroso, A.; Tanriver, G.; Catak, S.; Sulzer-Mossé, S.; De Mesmaeker, A. New access to quaternary aminocyclobutanes via nucleophilic addition on cyclobutanium salts. *Tetrahedron Letters* **2016**, *57*, 3510–3514.
- [225] Boeger P, Finding the target site of chloroacetamides: A thorny subject. *Journal of Pesticide Science* **1997**, *22*, 257–262.
- [226] Snoeck, M. Articaine: a review of its use for local and regional anesthesia. *Local and Regional Anesthesia* **2012**, *5*, 23–33.
- [227] Tackie, A. N.; Boye, G. L.; Sharaf, M. H.; Schiff, P. L.; Crouch, R. C.; Spitzer, T. D.; Johnson, R. L.; Dunn, J.; Minick, D.; Martin, G. E. Cryptospirolepine, a unique spiro-nonacyclic alkaloid isolated from *cryptolepis sanguinolenta*. *Journal of Natural Products* **1993**, *56*, 653–670.
- [228] Romagnoli, R.; Baraldi, P. G.; Carrion, M. D.; Cara, C. L.; Preti, D.; Fruttarolo, F.; Pavani, M. G.; Tabrizi, M. A.; Tolomeo, M.; Grimaudo, S.; Di Cristina, A.; Balzarini, J.; Hadfield, J. A.; Brancale, A.; Hamel, E. Synthesis and Biological Evaluation of 2- and 3-Aminobenzo[b]thiophene Derivatives as Antimitotic Agents and Inhibitors of Tubulin Polymerization. *Journal of Medicinal Chemistry* **2007**, *50*, 2273–2277.
- [229] Papakyriakou, A.; Kefalos, P.; Sarantis, P.; Tsiamantas, C.; Xanthopoulos, K. P.; Vourloumis, D.; Beis, D. A Zebrafish In Vivo Phenotypic Assay to Identify 3-Aminothiophene-2-Carboxylic Acid-Based Angiogenesis Inhibitors. *ASSAY and Drug Development Technologies* **2014**, *12*, 527–535.
- [230] Silva, Y.; Reyes, C.; Rivera, G.; Alves, M.; Barreiro, E.; Moreira, M.; Lima, L. 3-Aminothiophene-2-Acylhydrazones: Non-Toxic, Analgesic and Anti-Inflammatory Lead-Candidates. *Molecules* **2014**, *19*, 8456–8471.
- [231] Court, J. J. et al. Discovery of Novel Thiophene-Based, Thumb Pocket 2 Allosteric Inhibitors of the Hepatitis C NS5B Polymerase with Improved Potency and Physicochemical Profiles. *Journal of Medicinal Chemistry* **2016**, *59*, 6293–6302.
- [232] Li, P. et al. Discovery of Novel Allosteric HCV NS5B Inhibitors. 2. Lactam-Containing Thiophene Carboxylates. *ACS Medicinal Chemistry Letters* **2017**, *8*, 251–255.
- [233] Bootsma, A. N.; Wheeler, S. E. Popular Integration Grids Can Result in Large Errors in DFT-Computed Free Energies. *ChemRxiv* **2019**,
- [234] Goossens, H.; Vervisch, K.; Catak, S.; Stanković, S.; D’hooghe, M.; De Proft, F.; Geerlings, P.; De Kimpe, N.; Waroquier, M.; Van Speybroeck, V. Reactivity of Activated versus Nonactivated 2-(Bromomethyl)aziridines with respect to Sodium Methoxide: A Combined Computational and Experimental Study. *The Journal of Organic Chemistry* **2011**, *76*, 8698–8709.

- [235] Schleyer, P. V. R.; Maerker, C.; Dransfeld, A.; Jiao, H.; van Eikema Hommes, N. J. R. Nucleus-Independent Chemical Shifts: A Simple and Efficient Aromaticity Probe. *Journal of the American Chemical Society* **1996**, *118*, 6317–6318.
- [236] Ditchfield, R. Self-consistent perturbation theory of diamagnetism. *Molecular Physics* **1974**, *27*, 789–807.
- [237] Cheeseman, J. R.; Trucks, G. W.; Keith, T. A.; Frisch, M. J. A comparison of models for calculating nuclear magnetic resonance shielding tensors. *The Journal of Chemical Physics* **1996**, *104*, 5497–5509.
- [238] Bader, R. F. W. *Atoms in Molecules: A Quantum Theory*; Oxford University Press: Oxford, 1990.
- [239] Herges, R.; Geuenich, D. Delocalization of Electrons in Molecules. *The Journal of Physical Chemistry A* **2001**, *105*, 3214–3220.
- [240] Geuenich, D.; Hess, K.; Köhler, F.; Herges, R. Anisotropy of the Induced Current Density (ACID), a General Method To Quantify and Visualize Electronic Delocalization. *Chemical Reviews* **2005**, *105*, 3758–3772.
- [241] Glendening, E. D.; Landis, C. R.; Weinhold, F. NBO 6.0 : Natural bond orbital analysis program. *Journal of Computational Chemistry* **2013**, *34*, 1429–1437.
- [242] te Velde, G.; Bickelhaupt, F. M.; Baerends, E. J.; Fonseca Guerra, C.; van Gisbergen, S. J. A.; Snijders, J. G.; Ziegler, T. Chemistry with ADF. *Journal of Computational Chemistry* **2001**, *22*, 931–967.
- [243] Fonseca Guerra, C.; Snijders, J. G.; te Velde, G.; Baerends, E. J. Towards an order-N DFT method. *Theoretical Chemistry Accounts: Theory, Computation, and Modeling (Theoretica Chimica Acta)* **1998**, *99*, 391–403.
- [244] Nishio, M. The CH/ π hydrogen bond in chemistry. Conformation, supramolecules, optical resolution and interactions involving carbohydrates. *Physical Chemistry Chemical Physics* **2011**, *13*, 13873.
- [245] Birney, D. M.; Wagenseller, P. E. An ab Initio Study of the Reactivity of Formylketene. Pseudopericyclic Reactions Revisited. *Journal of the American Chemical Society* **1994**, *116*, 6262–6270.
- [246] Hoffmann, R.; Woodward, R. B. The Conservation of Orbital Symmetry. *Accounts of Chemical Research* **1968**, *1*, 17–22.
- [247] Gupta, N.; Bansal, R. K.; Von Hopffgarten, M.; Frenking, G. 1,5-electrocyclization versus 1,5-proton shift in imidazolium allylides and 2-phospha-allylides: A DFT investigation. *Journal of Physical Organic Chemistry* **2011**, *24*, 786–797.

- [248] Cabaleiro-Lago, E. M.; Rodríguez-Otero, J.; Varela-Varela, S. M.; Peña-Gallego, A.; Hermida-Ramón, J. M. Are Electrocyclization Reactions of (3 Z)-1,3,5-Hexatrienone and Nitrogen Derivatives Pseudopericyclic? A DFT Study. *The Journal of Organic Chemistry* **2005**, *70*, 3921–3928.
- [249] Peña-Gallego, A.; Rodríguez-Otero, J.; Cabaleiro-Lago, E. M. A DFT study of the [4+2] cycloadditions of conjugated ketenes (vinylketene, imidoylketene and formylketene) with formalimine. The pericyclic or pseudopericyclic character from magnetic properties. *Tetrahedron* **2007**, *63*, 4937–4943.
- [250] Ross, J. A.; Seiders, R. P.; Lemal, D. M. An extraordinarily facile sulfoxide automerization. *Journal of the American Chemical Society* **1976**, *98*, 4325–4327.
- [251] Keith, T.; Bader, R. Calculation of magnetic response properties using atoms in molecules. *Chemical Physics Letters* **1992**, *194*, 1–8.
- [252] Keith, T. A.; Bader, R. F. Calculation of magnetic response properties using a continuous set of gauge transformations. *Chemical Physics Letters* **1993**, *210*, 223–231.
- [253] Dagoneau, D.; Kolleth, A.; Quinodoz, P.; Tanriver, G.; Catak, S.; Lumbroso, A.; Sulzer-Mossé, S.; De Mesmaeker, A. Keteniminium Salts as Key Intermediates for the Efficient Synthesis of 3-Amino-Indoles and -Benzofurans. *Helvetica Chimica Acta* **2020**, *103*, e1900217.
- [254] Dagoneau, D.; Kolleth, A.; Quinodoz, P.; Tanriver, G.; Catak, S.; Lumbroso, A.; Sulzer-Mossé, S.; De Mesmaeker, A. Keteniminium Salts as Key Intermediates for the Efficient Synthesis of 3-Amino-Indoles and -Benzofurans. *Helvetica Chimica Acta* **2020**, *103*, e1900217.
- [255] Kučerka, N.; Tristram-Nagle, S.; Nagle, J. F. Structure of fully hydrated fluid phase lipid bilayers with monounsaturated chains. *Journal of Membrane Biology* **2005**, *208*, 193–202.

Appendix A

Supporting Information

A.1 Supporting Information for Bcl-x_L Study in Chapter 4.

A.1.1 Force field parameterization of non-standard iso-aspartate

Amber force field for L-iso-ASP, which is a non-standard amino acid was parameterized with the antechamber and tleap modules as implemented in the Amber program package[133]. Terminal sides of iso-Asp were capped with ACE and NME (ACE-iso-ASP-NME). The optimization and single point calculation were performed at the HF/6-31G(d) level of theory using Gaussian 09 [217] (G09) program package (Rev E.01) (Figure A.1). The restrained electrostatic potential (RESP) charges were obtained using the Merz-Singh-Kollman (MK) scheme (IOP: (6/33=2, 6/42=6)) at the HF/6-31G(d) level. Then the non-standard iso-Asp were replaced on the protein. Topology and coordinate files of DM2-Bcl-x_L were generated using tleap embedded into Amber program package. Table A.1 depicts preparation file to generate iso-Asp mutant (DM2) of Bcl-x_L.

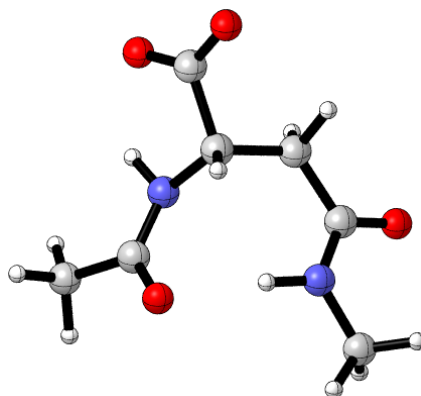


Figure A.1: The optimized structure of ACE-iso-ASP-NME (HF/6-31G(d)).

Table A.1: Preparation file for iso-Asp residue.

0	0	2								
This is a remark line										
frame-last.res										
ISO	INT	0								
CORRECT	OMIT	DU	BEG							
0.0000										
1	DUMM	DU	M	0	-1	-2	0.000	.0	.0	.00000
2	DUMM	DU	M	1	0	-1	1.449	.0	.0	.00000
3	DUMM	DU	M	2	1	0	1.523	111.21	.0	.00000
4	N	N	M	3	2	1	1.540	111.208	-180.000	-0.558004
5	H	H	E	4	3	2	1.011	48.865	-111.983	0.331742
6	CA	CT	M	4	3	2	1.466	89.570	13.373	0.034368
7	HA	H1	E	6	4	3	1.089	109.363	117.013	0.112945
8	C	C	B	6	4	3	1.583	114.386	-3.011	0.758992
9	O1	O2	E	8	6	4	1.256	119.615	-30.611	-0.773907
10	O2	O2	E	8	6	4	1.260	119.489	148.899	-0.773907
11	CB	CT	M	6	4	3	1.537	105.626	-129.178	-0.264114
12	HB1	HC	E	11	6	4	1.090	108.513	51.236	0.057012
13	HB2	HC	E	11	6	4	1.090	109.456	169.906	0.057012
14	CG	C	M	11	6	4	1.491	112.215	-69.502	0.666704
15	OD	O	E	14	11	6	1.232	119.525	112.691	-0.648843
LOOP										
IMPROPER										
CA	H	N	-M							
CA	O1	C	O2							
CB	OD	CG	+M							
DONE										
STOP										

A.1.2 Secondary Structure Analysis

Secondary structure content were calculated using Definition of Secondary Structure Prediction (DSSP) algorithm [137]. Green color in the SS figures presents α helix and 3_{10} helix structures during the simulations.

A.1.3 B-factor coloring

B-factor coloring is based on LIE calculations. In B-factor coloring, blue color represents stable interaction while red color represents unstable interactions.

A.1.4 Distance Analyses for the Combined Trajectories

Distance analysis results herein covers the analysis of the combined trajectories in each system (WT, DM1 and DM2). These results are consistent with the cluster data. In WT a slight narrowing of the binding groove was also detected but was less prominent compared to the DM1 case.

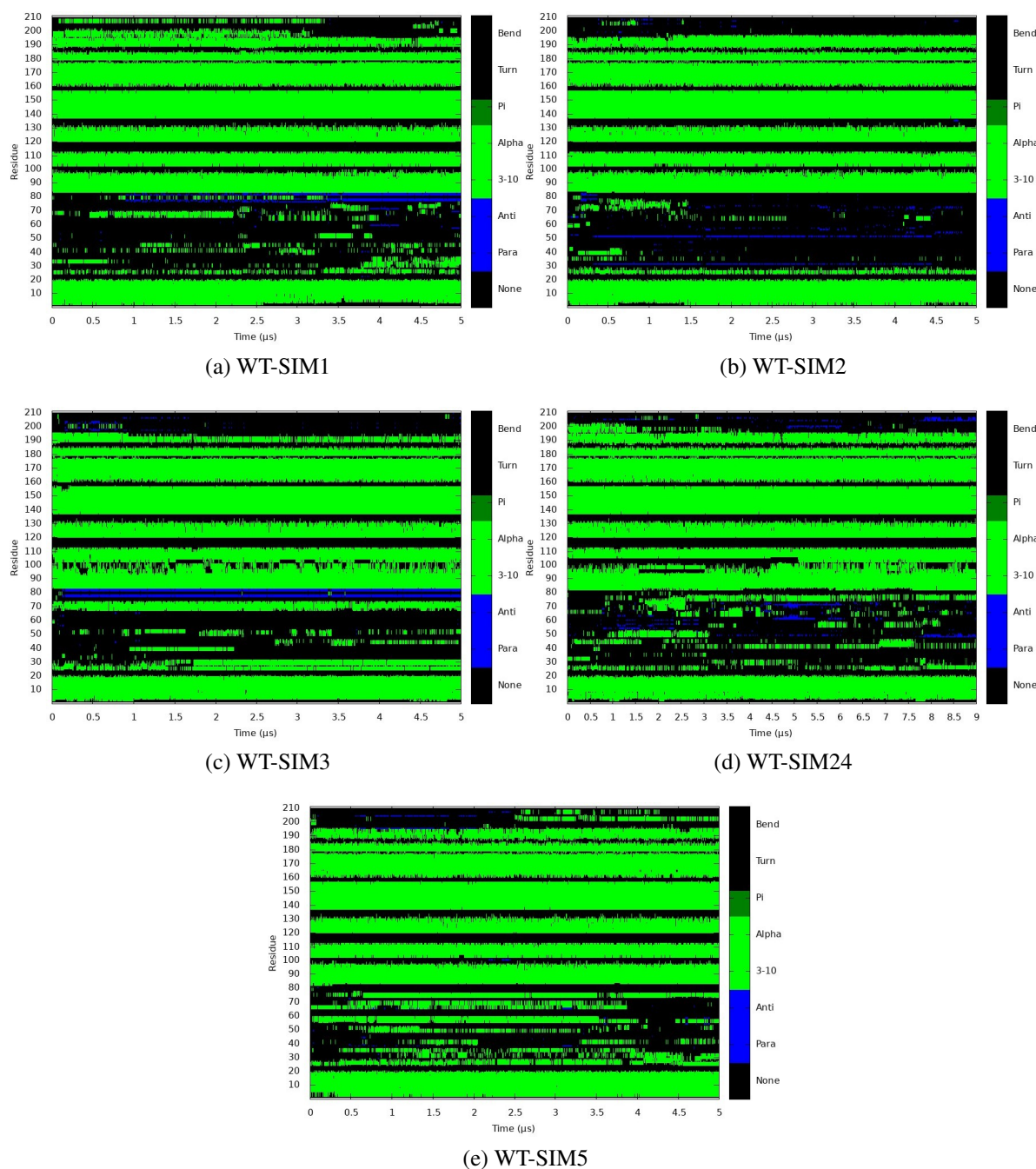


Figure A.2: Secondary structure plots for WT simulations.

A.1.5 Protein (Δ C terminal)-C terminal interactions (residues 196-209) for the Combined Trajectories

In WT, C-terminal part (residues 196-209) is highly flexible/mobile, and it transiently interacts with the IDR and the residues among α 1- α 3 and α 5. In deamidated systems, the C terminal transiently interacts with the bottom side of the groove (particularly, α 2 and J23). The C-

terminal-IDR interaction dramatically diminished compared to WT. Remarkably, the C-terminal residues in DM2 do not interact with $\alpha 1$ and the IDR (except distal IDR residues). In DM2 the C-terminal transiently interacts with $\alpha 8$.

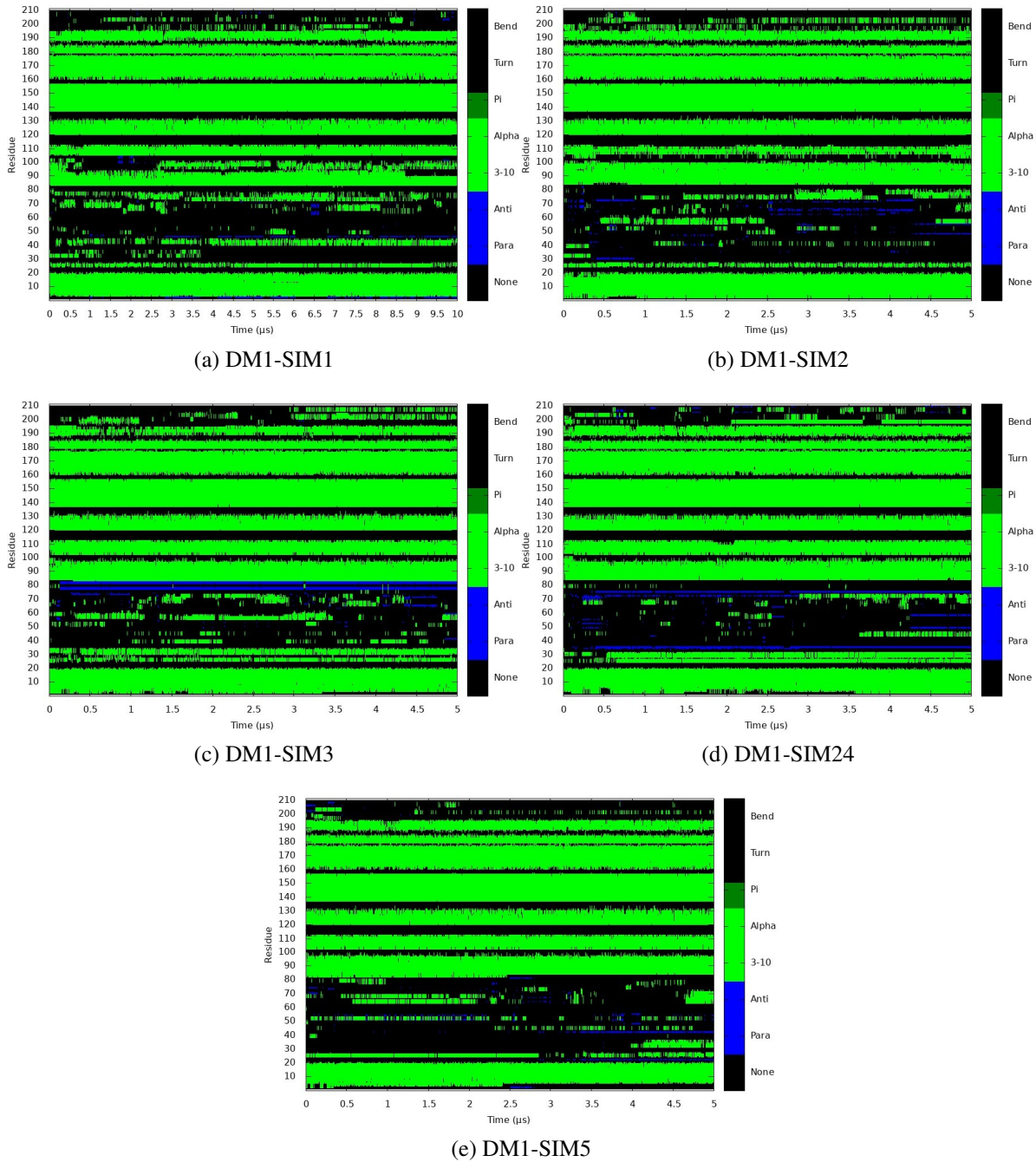


Figure A.3: Secondary structure plots for DM1 simulations.

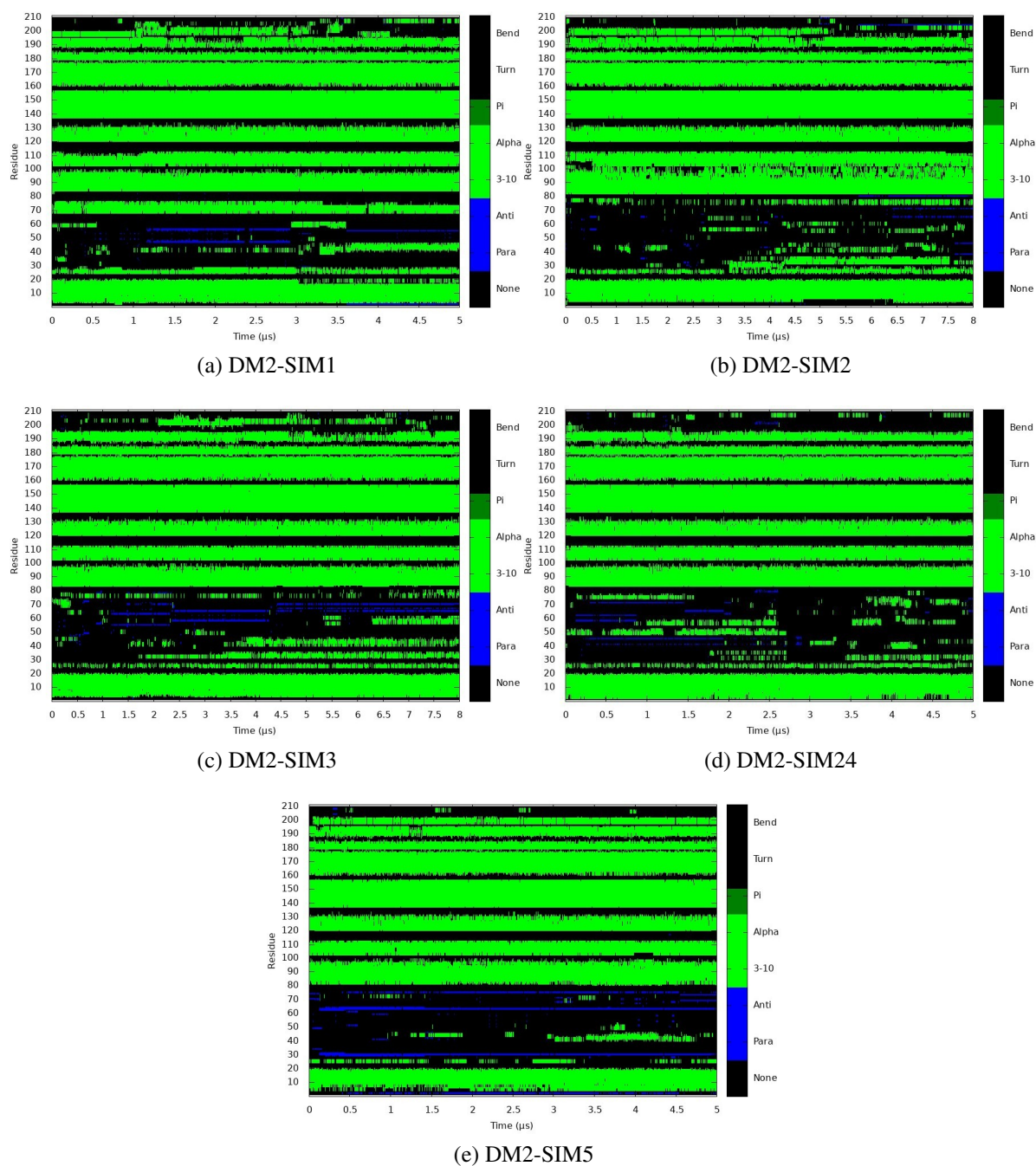


Figure A.4: Secondary structure plots for DM2 simulations.

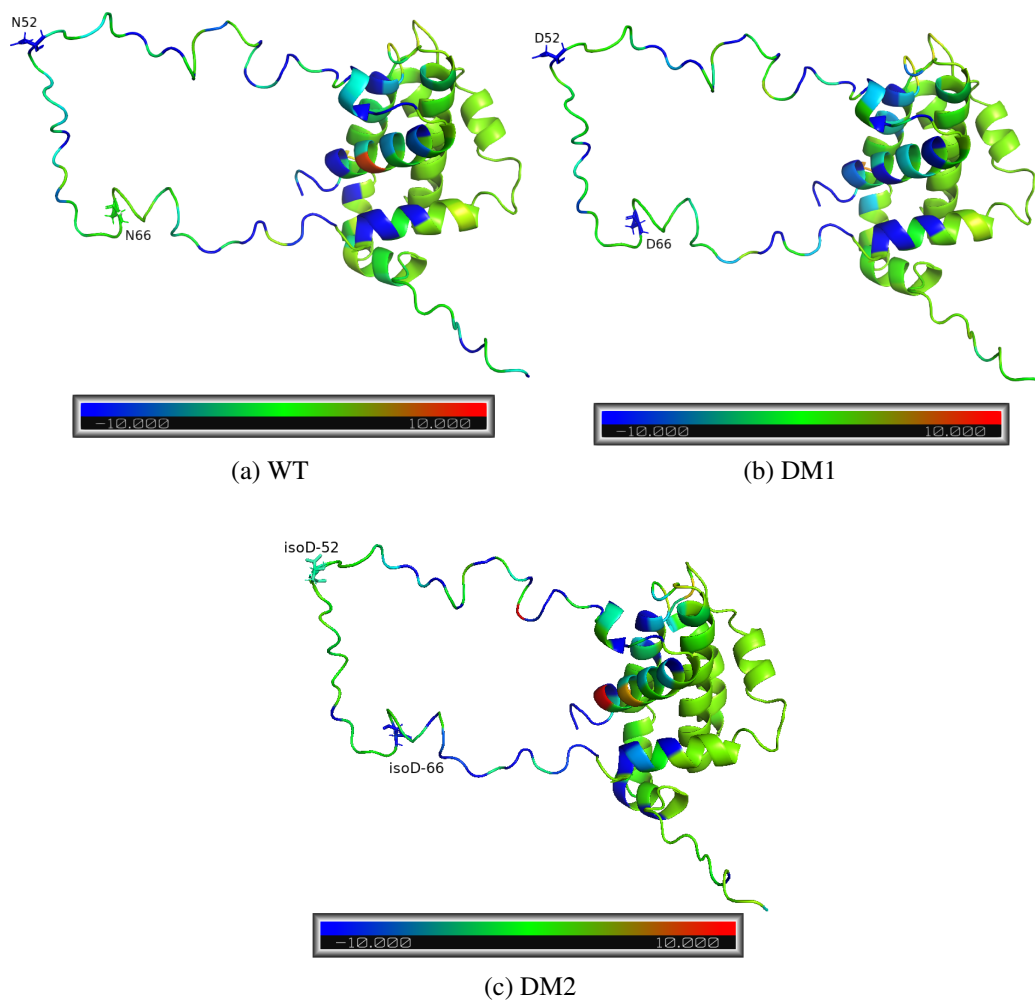


Figure A.5: B-factor coloring based on average LIE calculations between the IDR and protein (ΔIDR) for a) WT, b) DM1, and c) DM2.

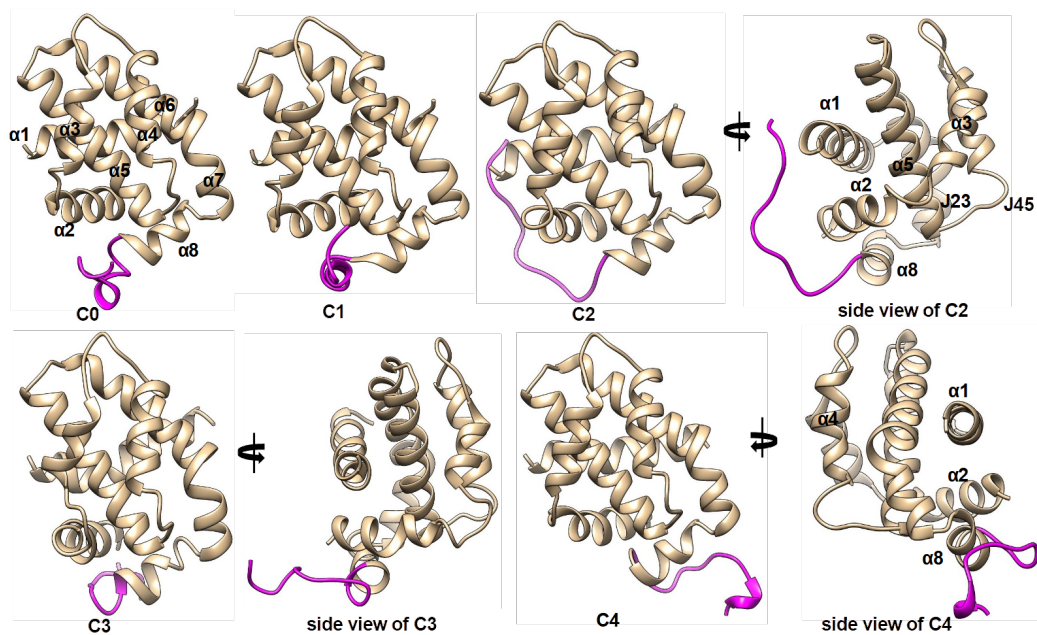


Figure A.6: Representative structures of clusters 0 – 4. (Magenta color refer to the C-terminal part.)

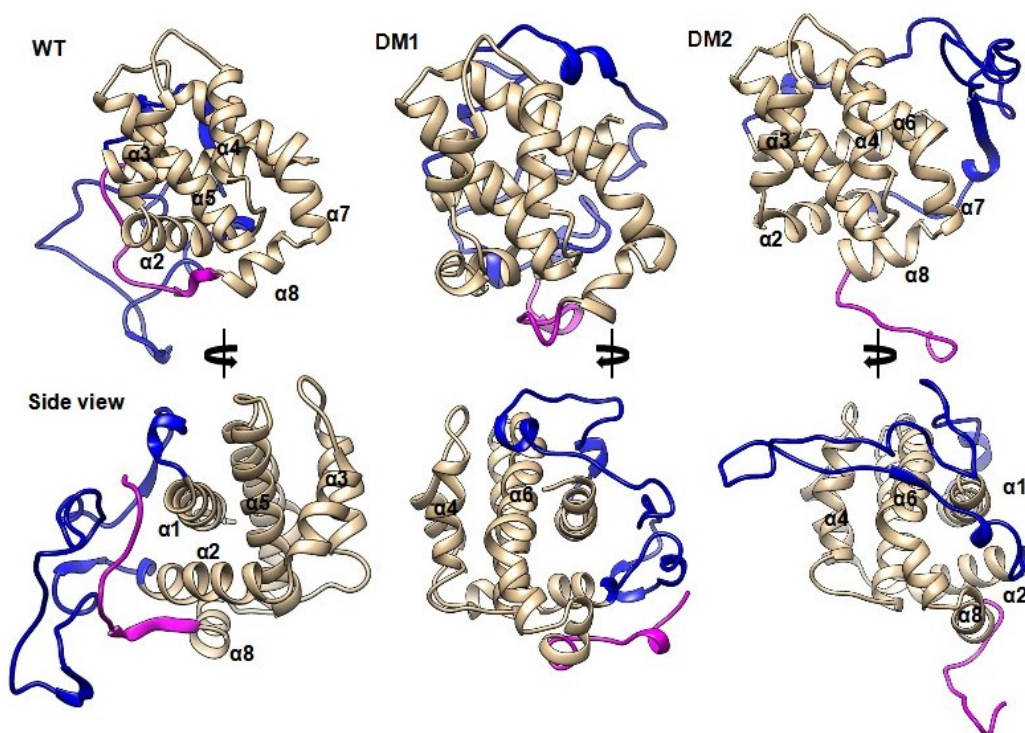


Figure A.7: Front and side views of representative snapshots of each system. (Blue and magenta colors refer to the IDR and the C-terminal part.)

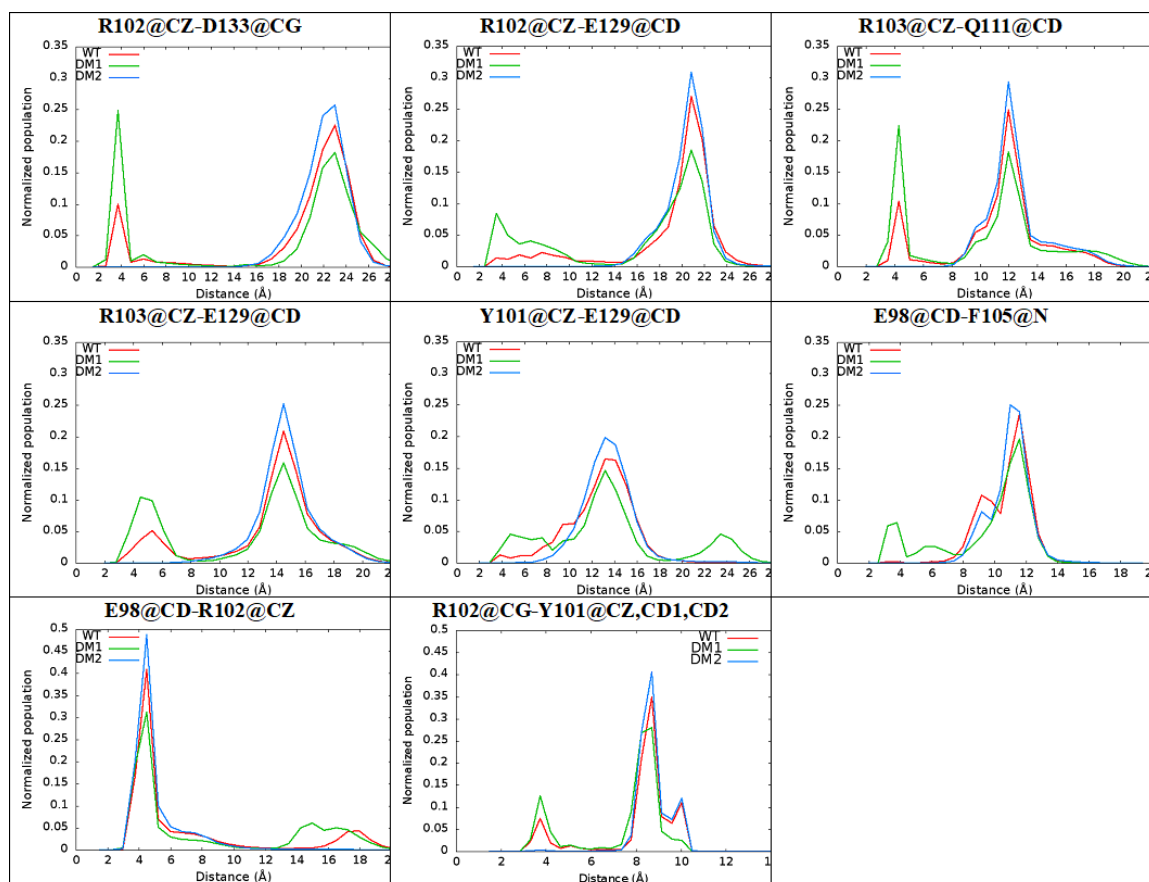


Figure A.8: Distance histogram for the key interactions in the binding groove of WT, DM1, and DM2 simulations.)

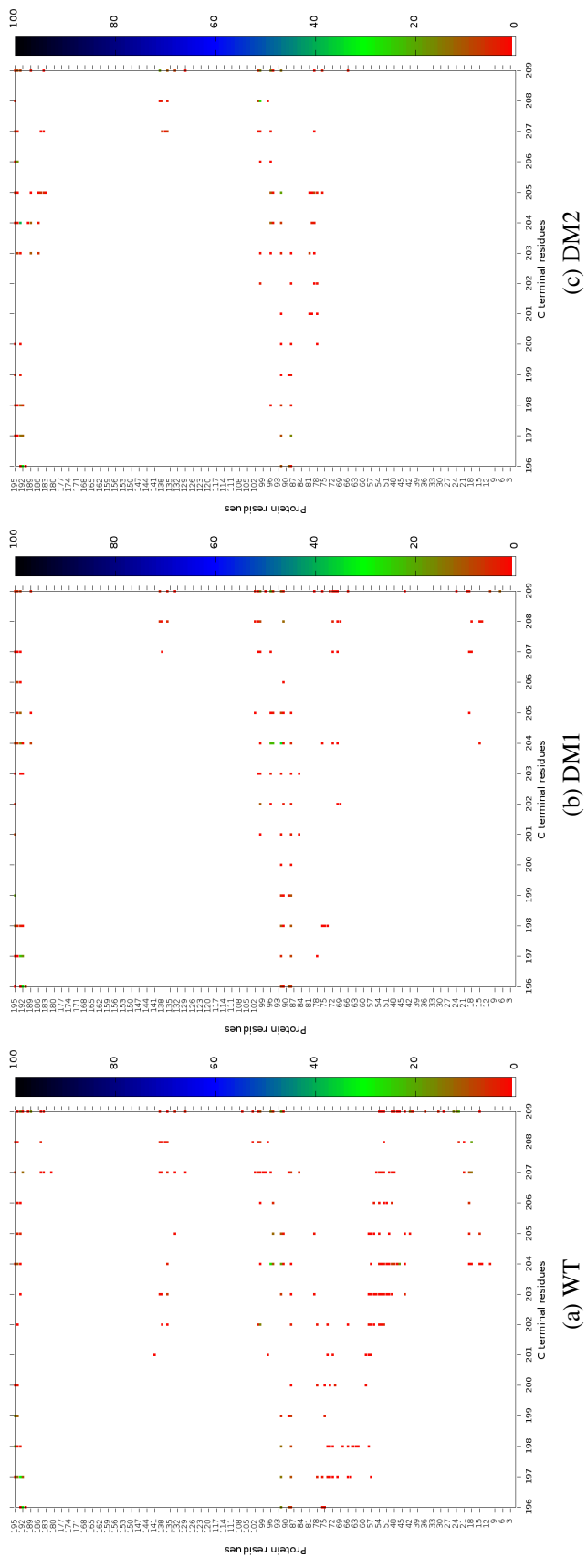


Figure A.9: H-bond interactions plots for the protein (ΔC terminal)-C terminal residues of WT, DM1, and DM2 simulations. The color bars show the contact percentage during the simulations.

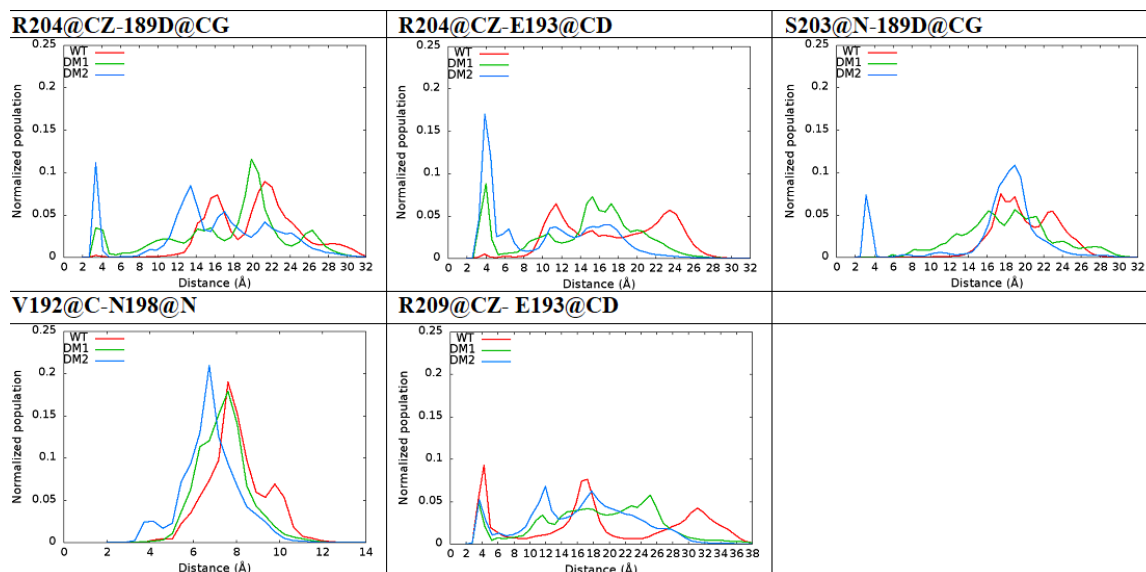


Figure A.10: Distance histogram for the key interactions in the selected H-bonded residues between the C-terminal and $\alpha 8$ of WT, DM1, and DM2 simulations.)

A.2 Supporting Information for Bcl-x_L Study in membrane in Chapter 5.

A.2.1 Area per lipid (APL)

Area per lipid of POPC (16:0 / 18:1) bilayer/membranes was calculated as shown in the formula below and found in the range of 65.8-66.4 Å² within 3% of experimental values [170]. Note that the experimental APL for POPC is 68.3 Å² /lipid11 and 64.3 Å² /lipid [255]. APL was calculated as follows:

$$APL = (boxXdimension) \times (boxYdimension) \div (numberofphospholipidsperlayer) \quad (A.1)$$

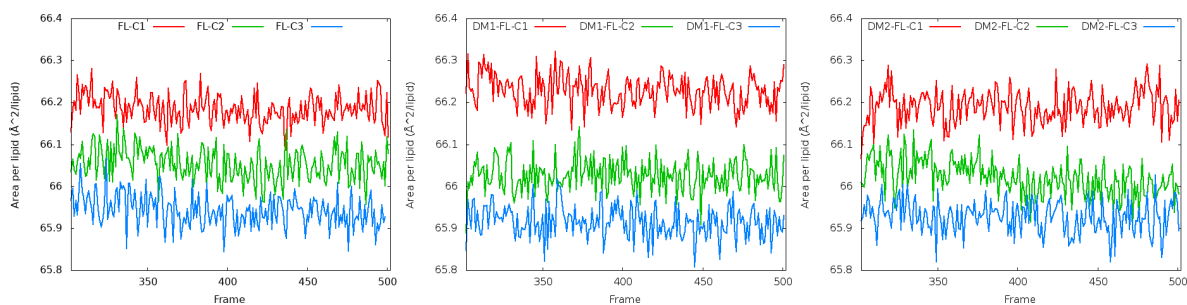


Figure A.11: APL plots for the POPC membranes in equilibrium runs.

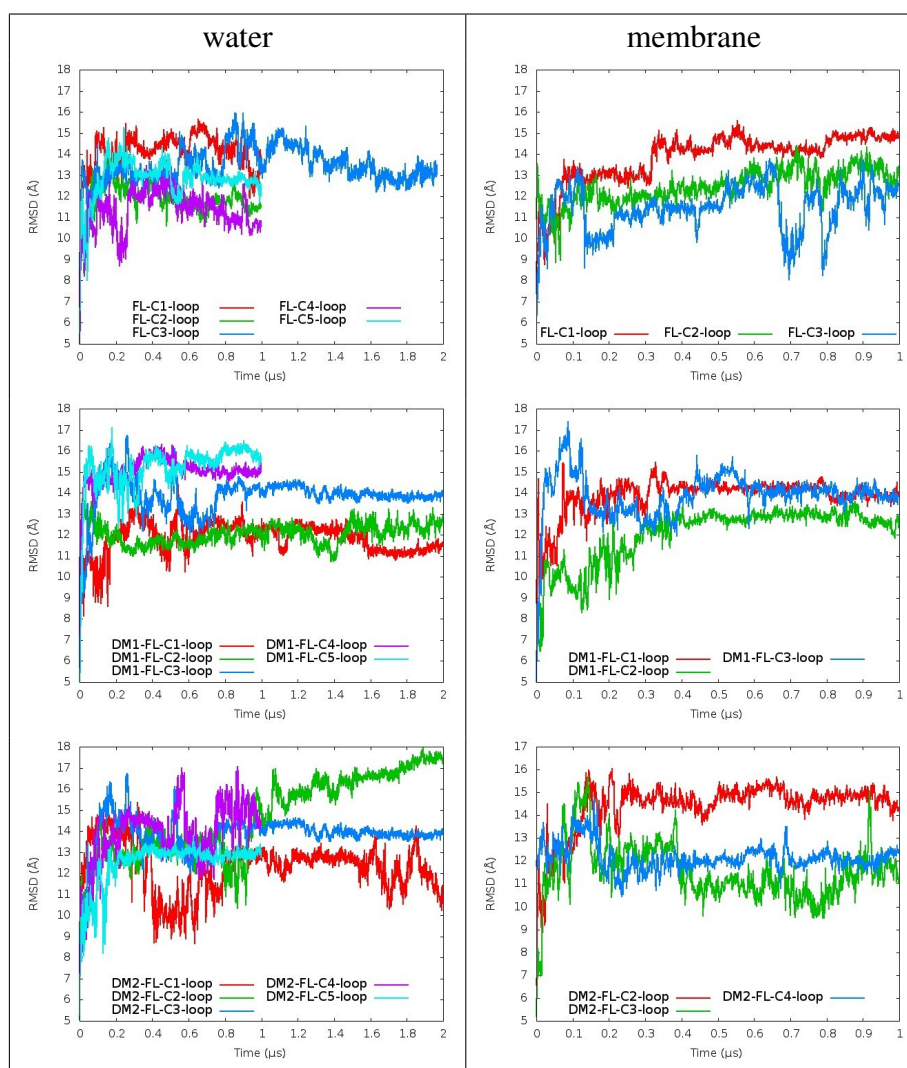


Figure A.12: Backbone RMSD plots for the IDR of FL, DM1 and DM2-Bcl-x_L simulations with respect to initial/built structures. (Every 20 frames)

A.3 Supporting Information for Electrocyclization Study in Chapter 8.

A.3.1 DFT Survey

Besides M06-2X, all calculation in Table A.2 were also performed at the hybrid-GGA B3LYP, hybrid-meta GGA MPWB1K and Second order Møller–Plesset perturbation (MP2). The calculations indicate that even though B3LYP, MPWB1K and MP2 lower the barriers compared to M06-2X optimizations, similar barrier trends were observed regardless of the level of theory. 6-311++G(3df,3pd) extra basis set was used for sulfur atom.

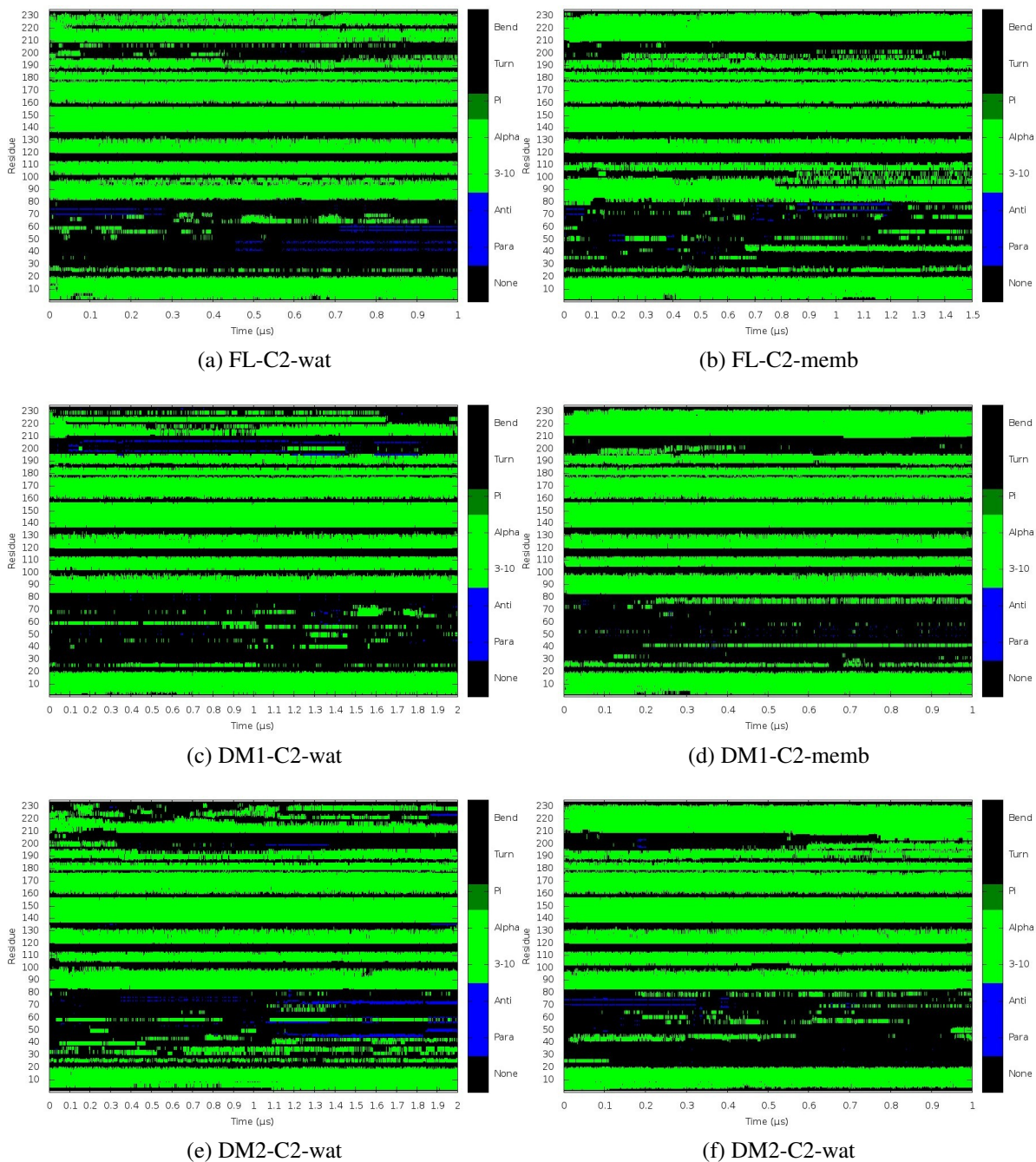


Figure A.13: Secondary structure evolution for the selected FL, DM1 and DM2 simulations in water (wat) and membrane (memb). (Green color presents α helix and 3_{10} helix structures during the simulations.)

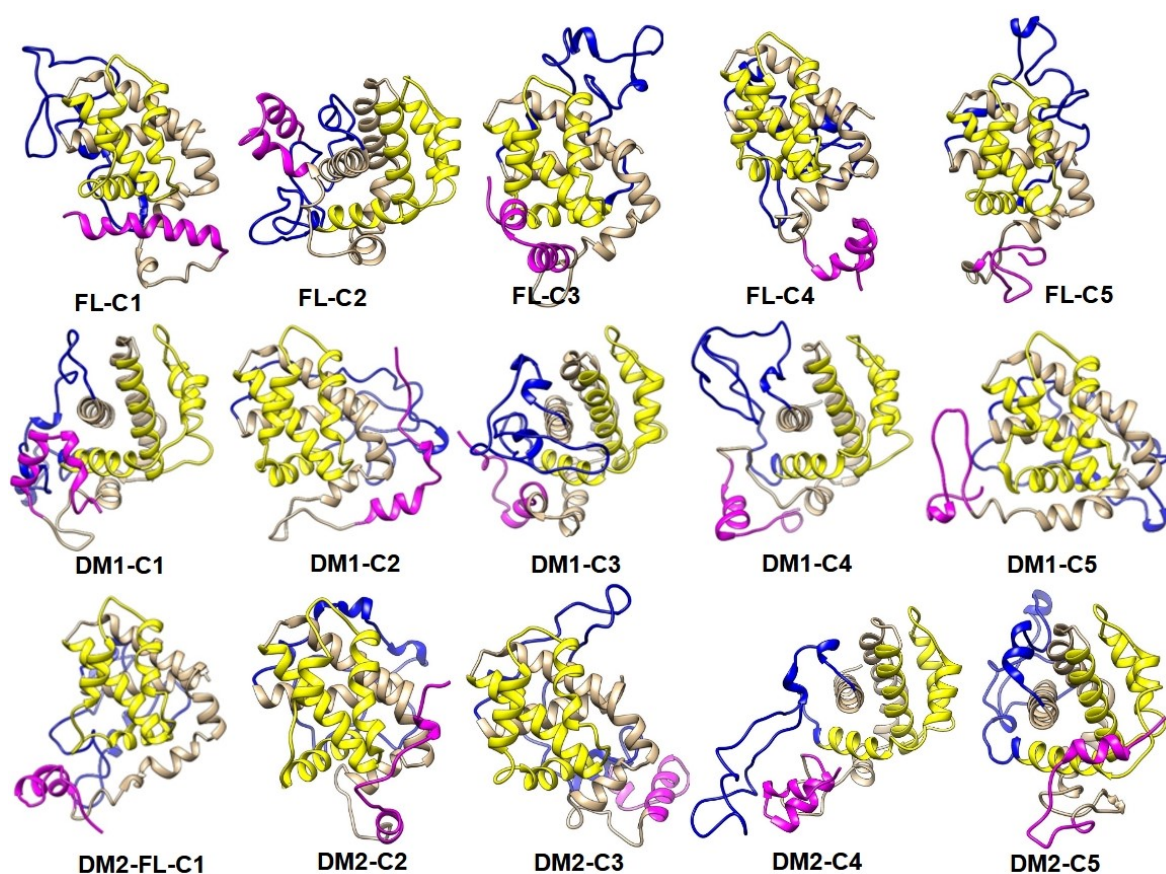


Figure A.14: FL models in water. (Snapshots belong to the last frame of each MD simulation. Blue color denotes loop region (IDR). Magenta and yellow colors present the C-tail and the binding groove, respectively. Water was not shown for clarity.)

Table A.2: Free energy barriers (ΔG^\ddagger), and reaction free energies (ΔG_{rxn}) for 6π -electrocyclization reactions of KIs.

Group I	M06-2X/ 6-31+G(d,p)		B3LYP/ 6-31+G(d,p)		MPWB1K/ 6-31+G(d,p)		MP2/ 6-31+G(d,p)	
	ΔG^\ddagger	ΔG_{rxn}	ΔG^\ddagger	ΔG_{rxn}	ΔG^\ddagger	ΔG_{rxn}	ΔG^\ddagger	ΔG_{rxn}
pyrrole	3.0	-37.8	2.2	-36.1	1.5	-43.0	*	-41.9
furan	6.0	-23.8	6.5	-20.5	5.5	-27.2	3.4	-22.9
thiophene	11.4	-22.2	10.6	-19.4	10.4	-26.8	8.2	-23.4
cyclohexadiene	9.2	-34.8	10.3	-28.6	10.5	-37.1	5.1	-36.6
Group II	ΔG^\ddagger	ΔG_{rxn}	ΔG^\ddagger	ΔG_{rxn}	ΔG^\ddagger	ΔG_{rxn}	ΔG^\ddagger	ΔG_{rxn}
indole	10.8	-4.9	10.2	-3.2	8.8	-9.1	6.1	-7.3
benzofuran	17.0	8.0	15.4	8.5	14.8	3.0	13.6	8.7
benzothiophene	21.0	9.0	20.4	10.6	18.8	4.3	16.0	9.3
naphthalene	14.8	1.7	18.1	8.6	16.2	0.8	6.2	-0.4

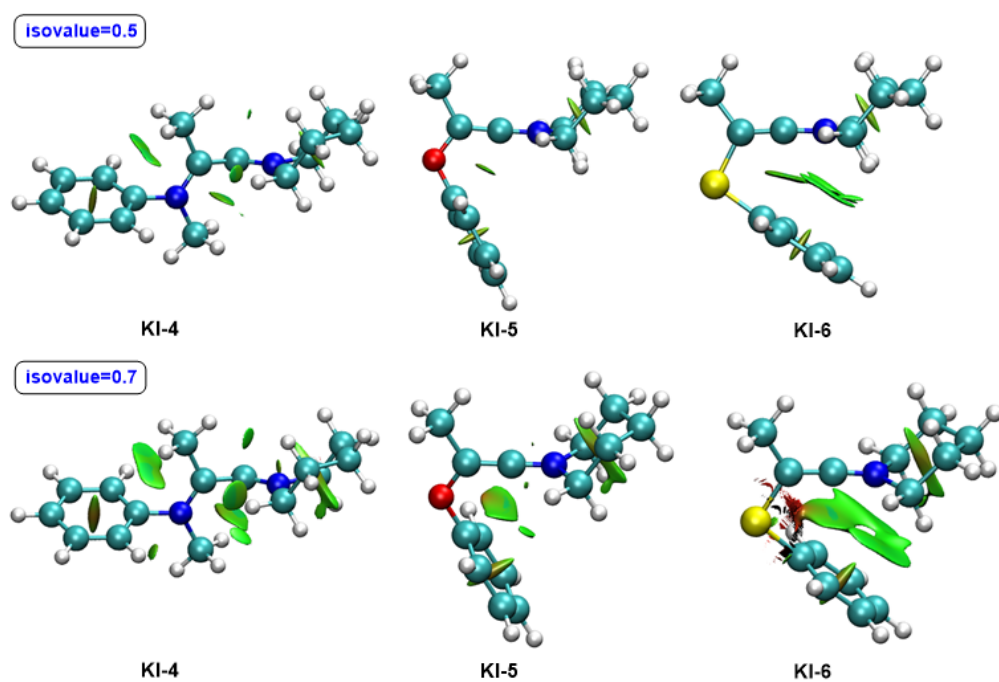
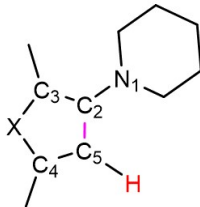
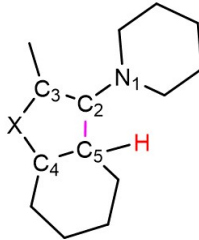


Figure A.15: The non-covalent interaction (NCI) plots of the optimized KI structures. NCI isosurface values= 0.5 and 0.7 au using SCF densities. NCI color scale is $-0.04 < \rho < 0.04$ au.

Note that the electrocyclization initially leads to an intermediate (Int) where C5 bears a H atom. Upon deprotonation of C5, aromaticity is established, and the end product is obtained.

Table A.3: Evolution of distances through the electrocyclization reaction (distances in Å).

<div><div></div><div>X= N-Me, O, S</div><div></div></div>									
Distance	KI ^a	KI-PRC	TS	Int	Distance	KI ^a	KI-PRC	TS	Int
N1-C2	1.25	1.27	1.28	1.36	N1-C2	1.25	1.27	1.29	1.37
C2-C3	1.31	1.39	1.38	1.37	C2-C3	1.31	1.39	1.38	1.37
N-C3	1.42	1.34	1.35	1.44	N-C3	1.42	1.33	1.36	1.41
N-C4	1.42	1.43	1.39	1.30	N-C4	1.42	1.44	1.38	1.32
C4-C5	1.34	1.33	1.35	1.48	C4-C5	1.40	1.39	1.41	1.48
C2-C5	3.34	2.88	2.42	1.51	C2-C5	3.62	4.33	2.10	1.53
Distance	KI	TS	Int		Distance	KI	TS	Int	
N1-C2	1.25	1.28	1.36		N1-C2	1.25	1.30	1.37	
C2-C3	1.32	1.34	1.36		C2-C3	1.32	1.35	1.36	
O-C3	1.34	1.35	1.43		O-C3	1.35	1.36	1.40	
O-C4	1.41	1.36	1.27		O-C4	1.40	1.35	1.31	
C4-C5	1.33	1.36	1.48		C4-C5	1.39	1.41	1.46	
C2-C5	3.11	2.19	1.51		C2-C5	3.22	1.98	1.54	
Distance	KI	TS	Int		Distance	KI	TS	Int	
N1-C2	1.25	1.28	1.35		N1-C2	1.25	1.30	1.36	
C2-C3	1.30	1.34	1.39		C2-C3	1.30	1.35	1.37	
S-C3	1.76	1.73	1.72		S-C3	1.77	1.73	1.73	
S-C4	1.79	1.73	1.62		S-C4	1.78	1.73	1.67	
C4-C5	1.33	1.36	1.49		C4-C5	1.40	1.41	1.47	
C2-C5	3.54	2.22	1.51		C2-C5	3.30	2.01	1.54	
^a KI (Reactant) unless specified is linear.									

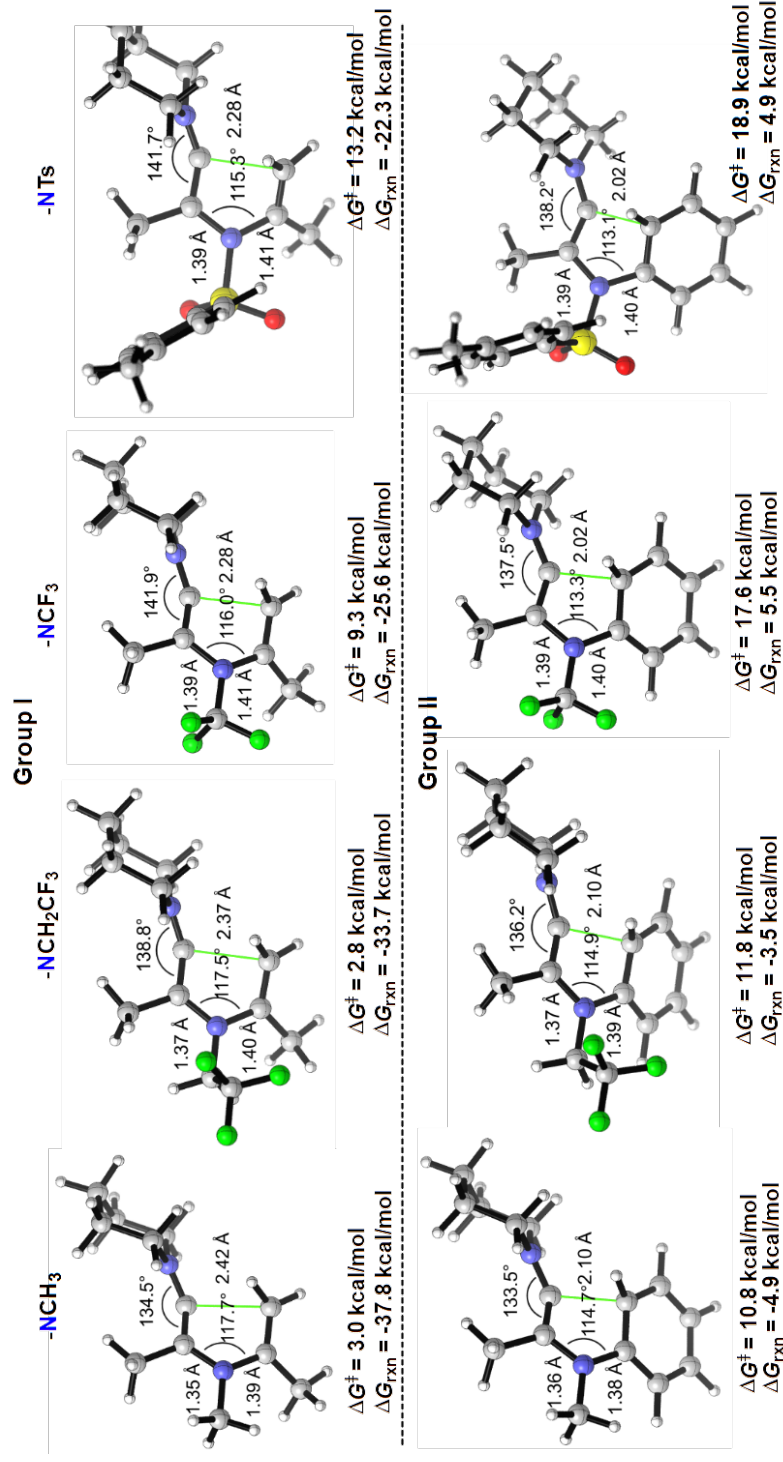


Figure A.16: Optimized TS structures (M06-2X/6-31+G(d,p) in CHCl₃, 6-311++G(3df,3pd) extra basis set for S atom). All energies for the formation of pyrrole and indole derivatives are relative to the pre-reactive conformer (PRC).

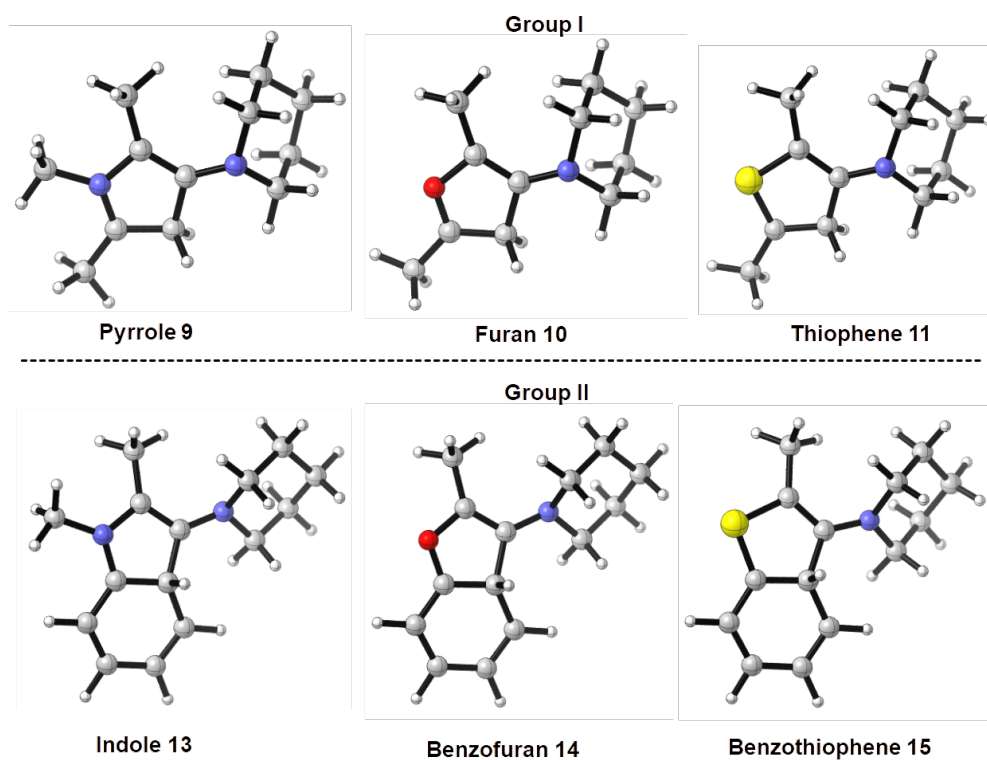


Figure A.17: Optimized INT structures (M06-2X/6-31+G(d,p) in CHCl_3 , 6-311++G(3df,3pd) extra basis set for S atom).

A.3.2 Frontier Molecular Orbitals (FMO) Analysis

According to Woodward-Hoffmann rules,[246] pericyclic ring closure in $(4n+2)\pi$ systems proceeds through a concerted disrotatory motion. FMO analysis of the keteniminiums in Groups I and II show HOMOs of keteniminiums primed for a disrotatory closure.

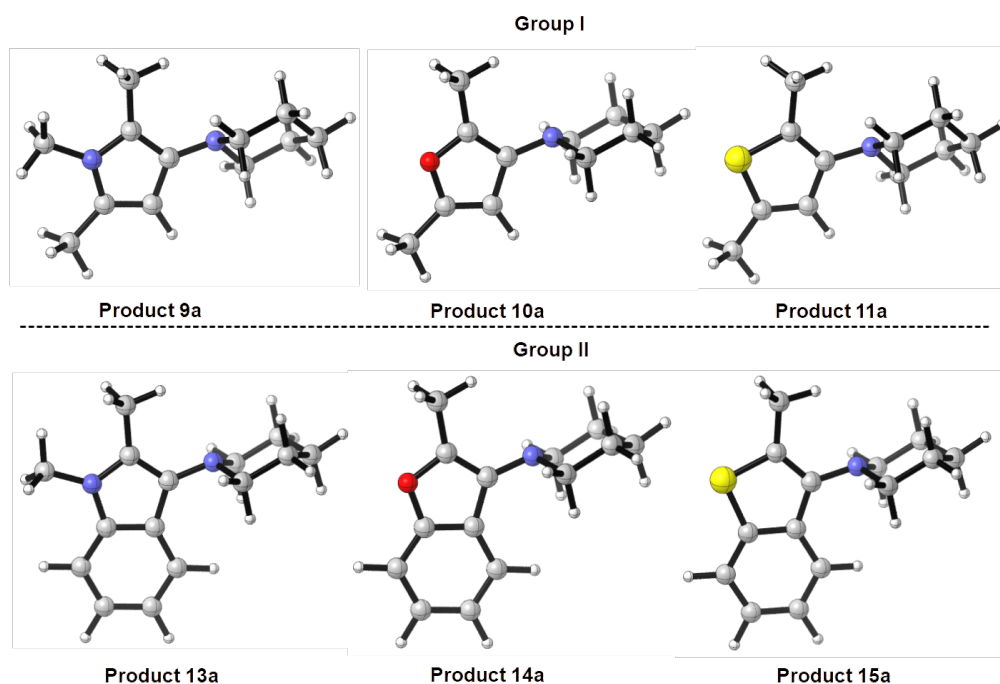


Figure A.18: Optimized end product structures (M06-2X/6-31+G(d,p) in CHCl_3 , for S atom 6-311++G(3df,3pd) extra basis set).

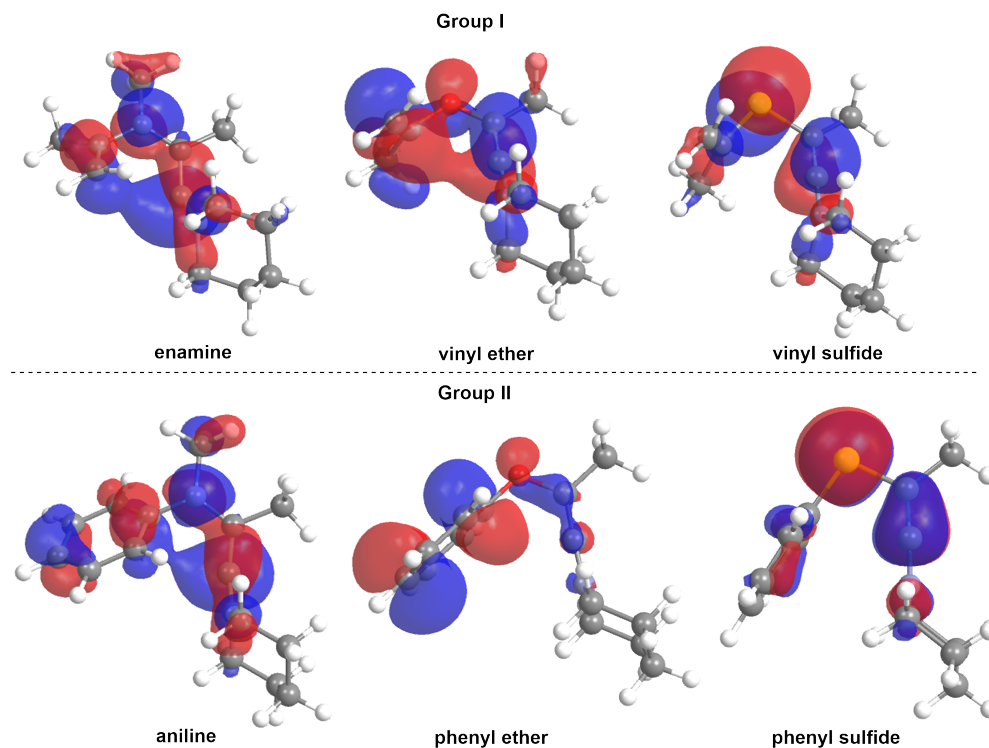


Figure A.19: HOMO of keteniminium ions. (M06-2X/6-311++G(d,p)/M06-2X/6-31+G(d,p) in CHCl_3 , extra basis set for S atom; iso-surface value = 0.03 au).

Appendix B

Publication List

1. Impact of deamidation on the structure and function of anti-apoptotic Bcl-xL.
Tanriver, G.; Monard, G.; Catak, S. *Journal of Chemical Information and Modeling*, 62 (1), 102-115, 2022.
2. Keteniminium Salts: Reactivity and Propensity Toward Electrocyclization Reactions
Tanriver, G., Dagoneau, D., Karadeniz, U., Kolleth, A., Lumbroso, A., Sulzer-Mossé, S., De Mesmaeker, A., Catak, S. *The Journal of Organic Chemistry*, 85 (2), 449-463, 2020.
3. Keteniminium Salts as Key Intermediates for the Efficient Synthesis of 3-Amino-Indoles and -Benzofurans
Dagoneau, D., Kolleth, A., Quinodoz, P., Tanriver, G., Catak, S., Lumbroso, A., Sulzer-Mossé, S., De Mesmaeker, A. *Helvetica Chimica Acta*, 103 (1), e1900217, 2020.
4. Design and Synthesis of Novel Indoline-(Thio)urea Hybrids
Lafzi, F., Kilic, H., Tanriver, G., Avci, O.N., Catak, S., Saracoglu, N. *Synthetic Communications*, 49 (24), 3510-3527, 2019.
5. Straightforward Synthesis of 3-Aminothiophenes Using Activated Amides
Dagoneau, D., Kolleth, A., Lumbroso, A., Tanriver, G., Catak, S., Sulzer-Mossé, S., De Mesmaeker, A. *Helvetica Chimica Acta*, 102 (4), e1900031, 2019.
6. Access to 3-Aminobenzothiophenes and 3-Aminothiophenes Fused to 5-membered Heteroaromatic Rings Through 6π -Electrocyclization Reaction of Keteniminium Salts
Kolleth, A., Muller, S., Lumbroso, A., Tanriver, G., Catak, S., Sulzer-Mossé, S., De Mesmaeker, A. *Tetrahedron Letters*, 59 (34), 3242-3248, 2018.
7. Theoretical Insight into the Regioselective Ring-Expansions of Bicyclic Aziridinium Ions
Boydas, E.B., Tanriver, G., D'hooghe, M., Ha, H-J., Van Speybroeck, V., Catak, S. *Organic and Biomolecular Chemistry*, 16 (5), 796-806, 2018.
8. Synthesis of 4-membered ring alkaloid analogues via intramolecular [2+2] cycloaddition involving keteniminium salt intermediates
Kolleth, A., Lumbroso, A., Tanriver, G., Catak, S., Sulzer-Mossé, S., De Mesmaeker, A., *Tetrahedron Letters*, 58 (30), 2904-2909, 2017.
9. New access to quaternary aminocyclobutanes via nucleophilic addition on cyclobutaniminium salts
Kolleth, A., Lumbroso, A., Tanriver, G., Catak, S., Sulzer-Mossé, S., De Mesmaeker, A., *Tetrahedron Letters*, 57(31), 3510–3514, 2016.
10. Computational Studies on Cinchona Alkaloid-Catalyzed Asymmetric Organic Reactions

Tanriver, G, Dedeoglu, B, Catak, S, Aviyente, V, *Accounts of Chemical Research*, 49(6), 1250–1262, 2016.

11. Synthesis of amino-cyclobutanes via [2+2] cycloadditions involving keteniminium intermediates

Kolleth, A., Lumbroso, A., Tanriver, G., Catak, S., Sulzer-Mossé, S., De Mesmaeker, A., *Tetrahedron Letters*, 57(25), 2697–2702, 2016.

Résumé

Ces dernières années, la chimie computationnelle a joué un rôle important dans la compréhension et la compréhension des propriétés structurales des systèmes (protéines, petites molécules, etc.) en imitant leur environnement. Cette thèse se compose de deux sujets principaux, à savoir la compréhension de l'impact de la désamidation Bcl-x_L au moyen de simulations de dynamique moléculaire (MD) et l'étude du sel de céteniminium (KI) par des méthodes de mécanique quantique (QM). L'étude des modifications post-traductionnelles (PTM) gagne en importance pour comprendre leurs rôles sur la structure et les fonctions des protéines. La désamidation, l'un des PTM, est un commutateur crucial utilisé pour réguler la fonction biologique de Bcl-x_L anti-apoptotique. Dans la première partie de la thèse, les changements conformationnels induits par la désamidation dans Bcl-x_L ont été explorés pour mieux comprendre sa perte de fonction en effectuant des simulations MD. Les résultats de cette étude fourniront une perspective unique sur le mécanisme sous-jacent de la mort cellulaire induite par la désamidation Bcl-x_L. Le sel de céteniminium, analogue azoté du cétène, est un intermédiaire largement utilisé pour la synthèse de divers échafaudages/substances en raison de son électrophilie, de sa réactivité et de sa régiosélectivité plus élevée. Dans la deuxième partie de la thèse, KI a été scruté de la formation à ses réactions impliquées au moyen d'une étude DFT. Les différences de réactivité observées expérimentalement dans les réactions de cycloaddition [2 + 2] et d'électrocyclisation ont été rationalisées via une gamme de techniques d'analyse différentes. Les résultats de cette étude devraient contribuer à la compréhension des différences de formation et de réactivité du KI et faciliter les applications synthétiques.

Mots-clés: Dynamique Moléculaire; Bcl-x_L; apoptose; DFT; Sels de Céténiminium

Abstract

In recent years, computation chemistry plays important role in order to understand and give insight on structural properties of systems (protein, small molecules etc.) by mimicking their environment. This dissertation consists of two main topics, namely understanding impact of Bcl-x_L deamidation by means of molecular dynamics (MD) simulations and investigation of keteniminium salt (KI) by quantum mechanical (QM) methods.

Investigation of post-translational modifications (PTMs) gains importance to understand their roles on structure and functions of proteins. Deamidation, one of the post-translational modifications is a crucial switch used for regulating the biological function of anti-apoptotic Bcl-x_L. In the first part of the thesis, deamidation-induced conformational changes in Bcl-x_L were explored to gain insight into its loss of function by performing molecular dynamics simulations. The outcomes of this study will provide a unique perspective on the underlying mechanism of Bcl-x_L deamidation-induced cell death.

Keteniminium salt, nitrogen analog of ketene is widely used intermediate for the synthesis of various scaffolds/substances due to its higher electrophilicity, reactivity and regioselectivity. In the second part of the thesis, keteniminium salt was scrutinized from formation to its involved reactions by means of DFT study. Experimentally observed reactivity differences in the [2 + 2] cycloaddition and electrocyclization reactions were rationalised via a range of different analysis techniques. The outcomes of this study are expected to contribute to the understanding of formation and reactivity differences of keteniminium salt and aid synthetic applications.

Keywords: Molecular Dynamics; Bcl-x_L; apoptosis; DFT; Keteniminium Salts